Water, energy and residence time modeling in a subalpine critical zone

Aniket Gupta

THÈSE

Pour obtenir le grade de

DOCTEUR DE L'UNIVERSITÉ GRENOBLE ALPES

École doctorale : STEP - Sciences de la Terre de lEnvironnement et des Planètes
Spécialité : Océan, Atmosphère, Hydrologie
Unité de recherche : Institut des Géosciences de lEnvironnement

Modélisation de l'eau, de l'énergie et du temps de séjour dans une zone critique subalpine

Water, energy and residence time modeling in a subalpine critical zone

Présentée par :

ANIKET GUPTA

Direction de thèse :

Didier VOISIN PROFESSEUR DES UNIVERSITES, Université Grenoble Alpes	Directeur de thèse
Jean-Martial COHARD MAITRE DE CONFERENCES, Université Grenoble Alpes	Co-directeur de thèse

Rapporteurs :

Stefan KOLLET
PROFESSEUR, Universität Bonn
Simon GASCOIN
CHARGE DE RECHERCHE HDR, CNRS délégation Occitanie Ouest

Thèse soutenue publiquement le **2 décembre 2022**, devant le jury composé de :

Didier VOISIN PROFESSEUR DES UNIVERSITES, Université Grenoble Alpes	Directeur de thèse
Stefan KOLLET PROFESSEUR, Universität Bonn	Rapporteur
Simon GASCOIN CHARGE DE RECHERCHE HDR, CNRS délégation Occitanie Ouest	Rapporteur
Laurent OXARANGO PROFESSEUR DES UNIVERSITES, Université Grenoble Alpes	Président
Isabelle GOUTTEVIN CHARGE DE RECHERCHE HDR, Météo France	Examinatrice
David GATEUILLE MAITRE DE CONFERENCE, Université de Chambéry	Examinateur

Invités :

Jean-Martial Cohard
PROFESSEUR ASSOCIE, UGA - IGE

dedicated

to

my beloved family

Acknowledgement

I like to express my gratitude towards my supervisor, Prof. Didier Voisin and co-supervisor, Assoc. Prof. Jean-Martial Cohard, Institut des Géosciences de l'Environnement, Université Grenoble Alpes, France, for providing me with the opportunity and valuable guidance throughout the span of this research work. I am thankful to Dr. Basile Hector for continuous support and guidance throughout my PhD tenure. I would also like to thank my geology/geophysics mentor Dr. Marc Descloitres, Dr. Jean-Pierre Vandervaere and Dr. Stéphane Garambois. I want to give special thanks to my Col du Lautaret team, Catherine Coulaud, Romain Biron, Pascal Salze and Lucie Liger, without whom smooth fieldwork would not have been possible. I am also thankful to Prof. Reed Maxwell from Princeton University for his help in model development which I used throughout my PhD.

I extend my sincere regards to my thesis committee- Dr. Isabelle Braud (RiverLy, Lyon) and Dr. Arnaud Foulquier (LECA, Université Grenoble Alpes) for their valuable suggestions and guidance for the completion of PhD thesis. I would also like to acknowledge the Dr. Aurélien DOMMERGUE, director and Dr. Thierry Pellarin, deputy director Institut des Géosciences de l'Environnement, for providing me with administrative assistance throughout my PhD tenure. I want to give special thanks to Mondher Chekki for all kinds of technical support throughout my PhD. I would also like to thank all administrative and technical staff of Institut des Géosciences de l'Environnement who were always with me in the time of trouble.

I would also like to thank the IDEX fellowship from Université Grenoble Alpes, which supported me financially during the PhD for research, training and travelling to scientific conferences. I am also really thankful to the Université Grenoble Alpes and Institut des Géosciences de l'Environnement for providing different technical and research training to enhance my capability.

Lastly, I thank the CHIANTI team for cherishing the various moments throughout the three-year journey. Their love and support helped to recover from all the hurdles during my PhD. I would also like to thank the PHyREV team for their valuable guidance. I would also like to thank my office mate Guillaume Chagnaud for sharing various up and down moments during this long journey. I would also like to thank my fellow lab mates, colleagues, and

most importantly my friends at Université Grenoble Alpes for their discussions, mentoring, constant support and motivation, without which this journey would have been difficult. I also extend my gratitude towards my family for being there and bearing patience with me throughout the period of the research work.

Résumé

L'hydrologie, l'écologie, la géomorphologie et les processus atmosphériques de la zone critique en montagne sont complexes et concernent des échelles temporelles et spatiales très fines. Cette étude a permis de construire un modèle hyper-résolu de la zone critique basé sur des données de terrain pour une petite unité hydrologique proche du "Col du Lautaret", un observatoire de la zone critique en moyenne montagne, afin d'aborder diverses questions relatives aux ressources en eau. L'étude de ce petit bassin versant subalpin (15,28 ha) montre que les rétroactions entre la surface et l'atmosphère sont influencées par la pente et l'orientation du terrain, jusqu'à l'échelle du mètre. Dans ce bassin versant dominé par un régime d'hydrologie nivale, la distribution spatiale de l'accumulation de neige, le transport par le vent et la fonte dépendent tous de la topographie. La distribution des précipitations, y compris le transport de la neige par le vent, est la variabilité spatiale imposée la plus importante pour permettre la simulation de la distribution spatiale de la neige. La distribution spatiale du rayonnement à courtes longueur d'ondes a moins d'impact sur les modèles de fonte dans notre bassin versant principalement orienté vers l'est, mais elle permet de mieux représenter le taux de fonte moyen et l'évapotranspiration. Enfin, la distribution spatiale de la vitesse du vent a peu d'impact mais contribue à améliorer le modèle de fonte lorsqu'elle est combinée avec les autres forçages. Les cinq premiers mètres de la subsurface contrôlent la génération du ruissellement avec un fort couplage surface-subsurface. Une lithologie de subsurface simplifiée, composée de deux horizons, l'un perméable (sableux-limoneux) et l'autre imperméable (roche de base Flysch), n'est pas en mesure de représenter la dynamique du ruissellement événementiel ou saisonnier et le débit de base. Pour capturer le cycle de ruissellement, une conductivité hydraulique variable de la subsurface est nécessaire, séparant les horizons hydrauliques actifs (5 premiers mètres) en 2 couches avec une variabilité latérale. Dans la zone critique de montagne, les écoulements souterrains sont importants et ne peuvent être modélisés en utilisant une conductivité hydraulique constante. Les écoulements de subsurface contribuent non seulement au ruissellement mais soutiennent également la végétation pendant les périodes sèches. Il a été démontré que la fonte des neiges s'infiltre dans la subsurface et, plus tard en été, est utilisée par la végétation pour l'évapotranspiration. La diminution de la période d'enneigement à l'avenir modifiera la période de croissance de la végétation, puis l'ensemble du cycle de l'eau tout au long de l'année, en augmentant l'évapotranspiration avec une période de végétation plus longue et un assèchement de la subsurface. Le temps de séjour de l'eau provenant de la neige et de la pluie diminuera. Ce qui est exporté du bassin versant sous forme de neige ou de pluie sera plus jeune, ce qui signifie que les changements dans le régime de fonte des neiges renderont l'écosystème moins résilient aux périodes de sécheresse.

Mots-clés: Zone critique de montagne, météorologie distribuée, couplage surface-sous-surface, partitionnement neige-pluie, temps de résidence

Abstract

Mountain critical zone hydrology, ecology, geomorphology and atmospheric processes are intricate and occur at very fine temporal and spatial scales. This study builds a data based critical zone model for a small hydrological units close to "Col du Lautaret", a mountain critical zone observatory, to address various water resource issues at hyper-resolution. The study of this small subalpine catchment (15.28 ha) shows that the surface-atmosphere feedback is impacted by slope and aspect, even at meter scales. In such snow-dominated catchment the spatial pattern of snow accumulation, wind transport and melting are all terrain dependant. Precipitation distribution, including snow transport by the wind, is the most important imposed spatial variability to capture the spatial snow distribution. Shortwave radiation spatial distribution impacts less the melting patterns in our mainly East facing catchment but accounts for capturing the average melting rate and evapotranspiration. Finally, wind speed spatial distribution does not produce a significant impact on its own but adds to enhance the melting pattern when combined with other forcings. The first 5m subsurface layer control the generation of runoff with a strong surface-subsurface coupling. Oversimplified subsurface lithology composed of 2 horizons, one permeable (sandy-Loam) and one impermeable (Flysch base rock) are not able to represent either the event or seasonal runoff dynamics and base Flow. To capture the runoff cycle, variable hydraulic conductivity of the subsurface is necessary, separating the active 5m hydraulic horizons in 2 layers with lateral variability. In mountain critical zone, subsurface flows are significant and could not be modeled using a constant hydraulic conductivity. The subsurface flows not only contribute to runoff but also sustain the vegetation in dry periods. It has been shown that the snowmelt percolates to the subsurface and later in summer is used by vegetation for evapotranspiration. Decrease of snow covered period in the future will shift the vegetation period and then the entire water cycle along the year, enhancing evapotranspiration with longer vegetation period and drying subsurface. Residence time for both source from snow and rain decrease. Whatever exports from catchment in the form of snow or rain is younger, which means that changes in the snowmelt regime make the ecosystem less resilient to drought periods.

Keywords: Mountain critical zone, distributed meteorology, surface-subsurface coupling, snow-rain partitioning, residence time

Résumé étendu

Cette étude fait suite aux travaux précédents d'Ilann Bourgeois (Bourgeois et al., 2018b,a), qui a étudié le devenir du nitrate atmosphérique (NO_3^-) déposé sur les prairies subalpines du col du Lautaret. En utilisant la signature $\Delta^{17}O$, qui est unique au nitrate atmosphérique, il a été possible de suivre le nitrate déposé dans l'écosystème qui n'avait pas encore été assimilé et de quantifier quelle fraction ce nitrate non transformé représentait dans les différents réservoirs de l'écosystème. Les résultats montrent que le nitrate atmosphérique non transformé peut représenter jusqu'à 29% du nitrate total à l'exutoire des bassins versants étudiés, avec des valeurs plus élevées lorsque l'eau provient de la fonte des neiges, soit directement, soit éventuellement après un voyage profond en subsurface. Cela met en évidence le contrôle par les flux latéraux et souterrains de la disponibilité du nitrate accumulé en hiver pour l'écosystème et suggère que le bassin versant est saturé en azote pendant la fonte des neiges. En utilisant également la signature $\Delta^{15}N$ du nitrate dans l'aérosol, la neige et l'écoulement de l'eau, Ilann Bourgeois a émis l'hypothèse qu'une partie du nitrate dans l'écoulement de printemps provenait en fait de la nitrification de l'ammoniac atmosphérique dans le manteau neigeux, soulignant ainsi l'importance des processus de la dynamique du manteau neigeux pour la compréhension du cycle de l'azote dans ces bassins versants alpins.

Il avait été émis l'hypothèse que dans un tel bassin versant, le cycle de l'azote est fortement déterminé par la fonte des neiges. En supposant la forte influence du dépôt et de la fonte des neiges dans l'hydrologie du bassin versant, certains de ces paramètres pourraient être expliqués. Par exemple, la quantité élevée de NO_3^- atmosphérique dans le cours d'eau pourrait résulter du temps de résidence de la fonte des neiges dans le bassin versant. La neige fondue avec NO_3^- intacte peut percoler vers la subsurface où cet azote pourrait rester plus longtemps loin de tout processus biologique. Après l'hiver, l'étude d'Ilann suggère également que les changements diurnes du NO_3^- atmosphérique dans le cours d'eau, ne peuvent être induits que par un fort couplage entre la surface et la subsurface. Pendant la journée, le débit du cours d'eau est dominé par le ruissellement direct de la neige fondue (ou de la pluie), mais la nuit, la neige percolée depuis la subsurface réapparaît dans le cours d'eau par le biais de canaux connectés. De même, la concentration atmosphérique de NO_3^- des plantes pourrait également expliquer les flux hydrologiques. Les composantes de

l'évapotranspiration des plantes dominent pendant l'été. Si les plantes absorbent suffisamment l'ancienne fonte des neiges, elles pourraient même absorber le NO_3^- atmosphérique sous une forme inchangée. Bien que le travail d'Ilann ait établi une bonne hypothèse par le biais d'une approche géochimique, elle n'a pas pu être vérifié à l'échelle du bassin versant en raison du manque d'observations hydrologiques détaillées et de modélisation. Certaines questions comme la connectivité surface-sub-surface, la contribution de la fonte des neiges au cours d'eau, l'absorption de la fonte des neiges par la plante et le temps de résidence de la neige dans le bassin versant restent sans réponse pour étayer l'hypothèse.

Les questions soulignées ci-dessus nécessitent des méthodes de surveillance et de modélisation détaillées. La topographie complexe et la rareté des observations limitent l'applicabilité de la plupart des outils de pointe. Dans cette thèse, nous appliquerons les méthodes les plus avancées disponibles pour une étude multidimensionnelle des bassins versants des zones critiques en montagne. L'objectif principal de cette thèse comprendra :

- l'exploration du contrôle météorologique et topographique sur la distribution spatio-temporelle de la neige, et son impact sur les flux hydrologiques dans un bassin versant de moyenne montagne de 15,28 ha au col du Lautaret.
- la construction du modèle hydrologique de subsurface basé sur l'étude géologique et géophysique et les impacts de modèles de subsurface de plus en plus détaillés sur la génération du ruissellement et l'évapotranspiration.
- l'identification des voies d'écoulement et des temps de séjour de l'eau de pluie et de l'eau de fonte des neiges dans le bassin versant, et leur répartition entre le débit et l'évapotranspiration dans les climats actuel et futur.

Pour étudier le comportement complexe de la zone critique et sa sensibilité à différents aspects topographiques, météorologiques et hydrologiques, nous avons choisi un petit bassin versant de 15,28 ha dans une région subalpine des Alpes françaises. Le bassin versant se trouve près du col du Lautaret, à proximité du jardin du Lautaret[1]. La zone se caractérise par sa grande diversité floristique. Le col du Lautaret fait la jonction entre les Alpes du nord et du sud, ce qui explique que la région subisse également l'influence du climat méditerranéen.

[1]https://www.jardindulautaret.com/

Le panorama comprend une riche diversité géologique allant du massif cristallin aux roches et sols sédimentaires. Globalement, cette région est le site idéal pour étudier le climat, l'hydrologie, l'écologie, la géologie et leurs interactions. Afin d'engager le site dans des développements scientifiques, la zone est dédiée au tourisme, à la recherche et à la formation scientifique.

Le bassin versant présente une réponse variable au cours de la seule année hydrologique. L'hiver est dominé par une couverture neigeuse continue, tandis que l'été est dominé par la végétation des prairies. En hiver, la prairie est couverte de neige pendant 5 à 6 mois par an et la distribution spatio-temporelle de la neige au printemps détermine le début et le cycle de la prairie. Outre les prairies, le bassin versant présente également une couverture boisée de 5%, comprenant des mélèzes, des aulnes et des buissons. Nous avons plusieurs types d'observation dans le bassin versant, de la physique à la chimie. Une description détaillée de la surveillance est présentée au chapitre 2. Le débit du cours d'eau pendant le pic de la saison hivernale diminue presque à zéro pendant les températures négatives. En été, le débit du cours d'eau provient du ruissellement direct de la pluie et de la neige et du stockage souterrain peu profond sous forme de sources. La mesure du débit du bassin versant a été mise en place en 2020, ce qui nous laisse une période d'observation limitée.

L'altitude du bassin versant varie entre 2000 et 2200 mètres. La tête du bassin versant est très raide et devient progressivement sub-horizontale dans la partie inférieure du bassin versant. Le bassin versant a également une pente très forte vers l'exutoire (50°) et l'ensemble du bassin versant est principalement orienté vers l'est. La station météorologique Flux'Alp se trouve sur la crête du sud du bassin versant, dans une zone plutôt plate. Selon les données météorologiques 2017-2018 du bassin versant, celui-ci a reçu un total de 1530 mm de précipitations, dont 970 mm de précipitations sèches. La température moyenne pour cette année était de 4 °C avec une température journalière minimale allant jusqu'à -7 °C au mois de février et une température journalière maximale de 14 °C en juillet. Juillet est également le mois le plus sec du bassin versant, mars étant le mois le plus humide. La direction sud-ouest de la vallée est soumise à des vents forts tout au long de l'année. En raison de la latitude élevée, de l'orientation vers l'est du bassin versant et du panorama de haute montagne, le bassin versant connaît une grande variabilité du rayonnement solaire en été et en hiver. Ces aspects du bassin versant seront discutés plus en détail dans le chapitre 2.

Géologiquement, le bassin versant peut être considéré comme la zone externe des Alpes françaises. Sur le bassin versant, la profondeur des sols varie de 20 cm sur les pentes raides à plus de 2 m sur les zones humides plates. Les sols sont riches en argile avec une porosité et une capacité de rétention élevées. Ce sol riche en argile transite lentement vers le socle (Flysch). Le régolithe intermédiaire s'étend jusqu'à 5 m de profondeur aux endroits les plus profonds. La géologie de la région remonte au début de l'ère paléozoïque (300 millions d'années). Le panorama de haute altitude autour du bassin versant comprend le Combeynot et la Meije qui sont principalement constitués de granite et de gneiss de la chaîne hercynienne. Cette chaîne a été profondément érodée depuis lors et l'empiètement de la mer a déposé des argiles, des limons et des calcaires anciens il y a environ 250 millions d'années. Les roches de nature sédimentaire de la région datent de 200 millions d'années à 250 millions d'années ; et font partie de la nappe de Briançon. Plus tard, certains des limons ont été métamorphosés pour donner du schiste noir et un pliage récent, il y a environ 10 millions d'années, soulève les roches sédimentaires de la région. En raison du long épisode de plissement, on peut également remarquer le pli renversé dans la région qui expose la vieille roche au sommet. Notre bassin versant est entièrement situé sur le flanc Est de ce pli, où affleure la formation de Flysch. La partie Est du pli est incliné sub-verticalement vers la partie supérieure du captage (direction Ouest) et sub-horizontalement vers la partie inférieure (direction Est). Cette configuration signifie que l'orientation générale du lit des couches de grès et d'argile de la formation de flysch sous-jacente suit vaguement la topographie du bassin versant. Par conséquent, les caractéristiques géologiques du bassin versant comprennent un sol riche en argile et en limon au sommet, qui passe à la subsurface fortement altérée (régolithe) et conduit finalement au socle ancien au fond sous forme de flysch.

La thèse est organisée en 3 chapitres techniques. Le premier chapitre technique (chapitre 4) décrit la mise en place d'un modèle hydrologique physique entièrement distribué, ParFlow-CLM, sur un terrain montagneux complexe pour modéliser les processus de transfert d'eau dans la zone critique. Notre objectif est de simuler les processus hydrologiques essentiels au fonctionnement d'un tel écosystème. La topographie complexe, les écoulements souterrains et le cycle hydrologique dominé par la neige dans les terrains montagneux constituent un défi du point de vue des mesures et de la modélisation. Ce chapitre étudie la variabilité des processus de surface dans la zone critique et leur rôle dans la perturbation du bilan

hydrologique. La neige joue un rôle important dans ces processus en moyenne montagne. L'approvisionnement en eau, l'agriculture, le cycle de la végétation, le transport chimique et les processus écologiques sont directement affectés par la neige. Cependant, la modélisation de la dynamique spatio-temporelle de la neige et de son impact sur les flux hydrologiques dépend de petites échelles spatiales qui ne sont pas bien représentées dans les composantes hydrologiques des modèles du système terrestre (MSE). Les hétérogénéités dans un tel bassin versant nécessitent une mise à l'échelle des processus à haute résolution spatio-temporelle. Ce chapitre traite de la méthodologie pour modéliser le bilan hydrique dans un terrain aussi complexe, en mettant l'accent sur les processus liés à la dynamique du manteau neigeux qui domine dans le bilan hydrologique. La topographie contrôle la distribution, la fonte et le transport de la neige le long de la pente. La topographie joue un rôle important dans la conduite du flux de fonte de neige de la surface vers la subsurface. Elle contrôle également les échanges de masse et d'énergie avec l'atmosphère. Cependant, à la résolution des MSE, les transferts d'eau dans la zone critique de montagne sont en général trop simplement modélisé et les effets hautes résolution trop peu pris en compte. Ce chapitre abordera les facteurs qui contrôlent la distribution spatio-temporelle de la neige dans un tel bassin versant. Il abordera également l'impact de la distribution spatio-temporelle de la neige sur le flux hydrologique, et les processus de distribution météorologique qui contrôlent la variabilité de la neige dans le bassin versant.

Dans le chapitre 4, nous avons modélisé la variabilité spatiale de la couverture neigeuse sur un petit bassin versant de moyenne altitude et son impact sur le bilan hydrologique en utilisant le modèle 3D de zone critique ParFlow-CLM à 10 m de résolution. À cette fin, nous avons préparé des forçages distribués pour les précipitations (qui imitent le transport de la neige), le rayonnement solaire entrant (qui inclut la fonte différentielle de la neige) et la vitesse du vent pour forcer le modèle. Les principales conclusions de cette étude peuvent être résumées comme suit :

- La distribution des précipitations (y compris la redistribution du vent) a le plus grand impact sur la répartition de la couverture neigeuse dans le bassin versant. Cela conduit à une présence de neige plus longue d'un mois dans le bassin versant lorsque l'on tient compte de la distribution des précipitations dans les simulations par rapport aux simulations qui ne la prennent pas en compte.

- La modulation du rayonnement solaire entrant par la pente locale dans le bassin versant est le deuxième paramètre topographique ayant le plus d'impact sur la fonte ainsi que sur l'évapotranspiration qui a ensuite un impact sur le bilan hydrique du bassin versant.

- La distribution de la vitesse du vent en fonction du terrain induit une certaine variabilité spatiale dans la fonte des neiges simulée au cœur de la période de fonte mais réduit cette variabilité à la fin de la période de fonte.

- La plupart des processus hydrologiques dépendent de la pente, mais cela est simplement pris en compte dans les modèles de surface terrestre et hydrologiques. L'étude quantifie les impacts hydrologiques en termes de fonte, de débit et de dynamique d'évapotranspiration en prenant en compte ou non l'effet de pente. En considérant les modèles de zone critique appliqués aux zones montagneuses, nous recommandons fortement de prendre en compte les effets de pente/aspect à l'échelle sous-grille dans les modèles à grande échelle, surtout lorsqu'ils sont utilisés pour des études hydrologiques. Cela améliorera la représentation spatiale des processus nivaux et de l'évapotranspiration et minimisera les biais dans la gestion des ressources en eau.

Le deuxième chapitre technique (chapitre 5) décrit la sensibilité de la paramétrisation de la subsurface dans le bassin versant étudié. La subsurface dans les bassins versants montagneux joue un rôle actif dans le ruissellement, l'humidité du sol et l'évapotranspiration. Cependant, peu de choses sont connues sur la sensibilité de la subsurface dans la simulation d'un bloc montagneux. Ce chapitre se concentre sur la sensibilité de la sub-surface homogène et hétérogène dans la simulation du ruissellement et la capture des flux de surface comme l'humidité du sol et l'évapotranspiration. La sub-surface dans l'étude est conçue à partir de données géophysiques factuelles et de modèles conceptuels. L'étude examine l'impact de la conductivité hydraulique uniformément répartie par couche ou variable sur la connectivité surface-sub-surface.

Le rôle de la subsurface dans la répartition du flux d'eau et la génération du débit est essentiel pour l'hydrologie des zones critiques, cependant, notre connaissance des caractéristiques de la subsurface est faible compte tenu des grandes hétérogénéités qui comptent pour les processus hydrologiques. Ceci est particulièrement vrai pour les régions d'aquifères de socle comme les zones de montagne où la géologie active a conduit à une structure

souterraine complexe comprenant des plis, des fractures, une érosion importante, etc. Dans cette étude, nous montrons comment un regard croisé par plusieurs méthodes géophysiques et partagé sur une petite unité hydrologique dans les Alpes de moyenne altitude peut aider à construire un modèle de subsurface à des fins hydrologiques. Elle comprend la géologie, la pédologie, l'hydrodynamique de la surface du sol, et de multiples méthodologies géophysiques, à savoir les méthodes électrique, électromagnétique et GPR. À partir des observations in situ, nous avons ensuite établi un modèle physique couplé surface-sous-surface pour explorer le rôle de la subsurface dans la régulation des flux hydrologiques. Les sept expériences conçues comprennent un modèle complexe avec variabilité 3D à partir duquel nous avons dérivé des modèles simplifiés pour lesquels les caractéristiques hydrodynamiques ont été dérivées de mesures sur le terrain. Cinq de ces modèles sont horizontalement homogènes avec un nombre variable d'horizons et de profondeurs. Deux d'entre eux incluent une variabilité horizontale dérivée de l'étude géophysique. Nous avons montré que seules les caractéristiques hydrodynamiques du sol conduisaient à une hydrologie de drainage libre où l'eau de pluie et de fonte s'infiltre profondément et rapidement dans le sol et se déverse continuellement dans le cours d'eau. Nous avons constaté que les deux simulations dans lesquelles nous incluons une couche intermédiaire de régolithe entre le sol et le flysch étaient très proches dans la simulation du ruissellement, de l'humidité du sol et de l'évapotranspiration. Dans ces simulations, le flysch était presque hydrologiquement inactif et ne contribuait pas à l'écoulement, et le régolithe agissait pour maintenir l'écoulement, l'humidité et ensuite la saturation de la surface. A partir de ces deux simulations, les hétérogénéités n'ont pas montré beaucoup de différence en terme de performance pour l'évaluation de la moyenne spatiale, cependant, nous avons soutenu que la simulation hétérogène à trois couches était un peu meilleure pour capturer le cycle de fonte quotidien, le débit de base, l'évapotranspiration et les hétérogénéités de saturation de surface plus contrastées. Enfin, aucune de nos configurations à deux couches n'a été en mesure de produire un débit de base pertinent ou une réponse pertinente aux événements de précipitation. Plus généralement, les modèles d'hydrologie basés sur la physique ont besoin d'informations détaillées sur la subsurface pour simuler les bons processus. Notre étude souligne, d'une part, la nécessité d'une investigation géophysique minimale pour simuler des résultats pertinents à l'échelle du bassin versant et, d'autre part, la nécessité d'une description plus précise de la subsurface pour

mieux simuler la variabilité interne. Notre étude montre que même si nous ne pouvons toujours pas associer la caractérisation nécessaire à n'importe quel modèle de pixels, plus on ajoute de contraintes, plus les résultats obtenus sont robustes. L'inclusion de données distribuées provenant de levés géophysiques, même à une plus grande échelle en utilisant l'observation aéroportée, a donc un fort potentiel pour construire et contraindre de meilleurs modèles de subsurface pour la modélisation de l'hydrologie de la zones critique.

Le troisième chapitre technique (chapitre 6) décrit le comportement du bassin versant en ce qui concerne le temps de résidence. La connectivité surface-sub-surface peut être rapide ou lente en termes de réponse aux flux. L'altération chimique dans la subsurface et l'impact du climat sur la recharge des eaux souterraines peuvent être observés par la modélisation du temps de résidence. Ce chapitre décrit la distribution du temps de résidence dans la subsurface, la distribution du temps de résidence dans la contribution de la source à l'évapotranspiration et à l'exutoire, et le partage de la source vers l'évapotranspiration et à l'exutoire. Le modèle calibré et ajusté a été utilisé à cette fin. Nous montrerons comment ce bassin versant se comporte dans le climat actuel et comment il a le potentiel d'être impacté par un stress climatique.

Le temps de résidence nous donne une image générale de la connectivité hydrologique entre la surface et la subsurface. Avec le modèle ajusté, nous sommes capables de déterminer la distribution du temps de résidence, l'âge de la source et le partage de la source. Ces facteurs dépendent de la configuration de la subsurface et du chemin d'écoulement. Dans un bassin versant de montagne, ces voies d'écoulement partagent dynamiquement dans le temps les sources (pluie et neige) entre l'évapotranspiration et le ruissellement. Avec une couche de subsurface de 118 m de profondeur, nous avons montré que la subsurface profonde ne participe pas activement à l'hydrologie du bassin versant. La plupart des particules anciennes qui se trouvent à des profondeurs supérieures à 40 m présentent des temps de résidence supérieures à 75 ans. Proches de la surface et à l'exutoire, les particules jeunes sont dominantes avec un age moyen de l'ordre de 5ans. La séparation entre le régolithe et le Flysch sépare la subsurface active et la subsurface lente à environ 4,7 mètres sous la surface.

La connectivité surface-sous-surface contrôle la répartition de la neige et de la pluie dans le bassin versant. Dans le bassin versant étudié, on constate que la fonte des neiges domine l'écoulement tandis que la pluie domine l'évapotranspiration. La pluie contribue pour 39%

au ruissellement total, et la neige y contribue pour 61%. Dans le flux d'évapotranspiration, cette répartition est inverse. Dans l'évapotranspiration, la pluie contribue à 77% du flux total alors que la neige ne contribue qu'à 23% du flux total. Cependant, il est démontré que les sources de neige pour les plantes sont généralement de vieilles particules. Ces particules anciennes sont potentiellement sujettes à des altérations chimiques et à des changements climatiques qui pourraient avoir un impact significatif sur l'écosystème de montagne.

L'hydrologie de montagne de moyenne altitude est fortement impactée par le changement climatique car l' isotherme zéro se déplacent vers le haut, transformant les précipitations de neige en pluie et modifiant les régimes de fonte. Cela a déjà un impact sur de nombreux secteurs économiques, notamment l'énergie, l'agriculture et le tourisme, mais aussi sur des processus environnementaux tels que la quantité et la qualité de l'eau, l'écologie végétale et animale, etc. Cette thèse a abordé certaines questions de la communauté scientifique concernant la zone critique de montagne, fondamentalement liée aux hétérogénéités spatiales d'origine topographique : Il a été démontré que les zones critiques de montagne sont hétérogènes et que le processus opère à une échelle beaucoup plus fine que celle à laquelle on pourrait penser. Pour traiter les problèmes sociétaux en montagne, il faut tenir compte de ces processus à échelle fine. L'étude a abordé trois questions majeures dans la zone critique montagneuse, a) L'impact des hétérogénéités de surface, en particulier météorologiques sur les flux hydrologiques. b) L'impact des hétérogénéités de la lithologie sur la génération du ruissellement. c) Le partage des flux hydrologiques et le potentiel impact du changement climatique sur sur ces flux. Cette recherche identifie d'abord certaines limitations des modèles du système terrestre (ESM) dans la mise à l'échelle des processus de la zone critique et montre ensuite la dynamique des flux hydrologiques lorsque les hétérogénéités sont prises en compte. Un modèle de zone critique de 10 m de résolution d'un bassin versant de 15,4 ha a été construit à l'aide du modèle hydrologique Parflow-CLM qui permet de représenter le cheminement des eaux souterraines en 3D, les transferts latéraux des eaux de surface vers les ruisseaux et les rivières et les transferts verticaux par évaporation et évapotranspiration dans un cadre entièrement couplé. La principale conclusion de ce travail basé sur l'étude scientifique de l'hydrologie de surface et de subsurface peut être résumée comme suit :

- La forte variabilité de la topographie en montagne entraîne de grandes variations microclimatiques en termes de précipitations, de rayonnement, de température, de vent,

etc. qui entraînent une variation spatiale des flux hydrologiques tels que les régimes d'accumulation et de fonte de la neige, l'évapotranspiration, le ruissellement, etc. Pour quantifier ces impacts, le modèle a été forcé avec des forçages météorologiques distribués (précipitation, radiation et vent) basés sur la pente et l'orientation. L'étude a montré que la distribution des précipitations avait plus d'impact sur la distribution de la neige tout au long de la saison dans le bassin versant. La distribution du rayonnement à ondes courtes a eu un impact sur les régimes de fonte et d'évapotranspiration. La vitesse du vent a eu un double impact sur la variabilité, une fois par le transport et la redistribution de la neige, que nous avons pris en compte dans la distribution des précipitations en utilisant une topographie du manteau neigeux à la fin de la période d'accumulation de la neige, et une fois par l'effet aérodynamique sur les changements d'énergie, qui n'a eu un impact que lorsqu'il a été combiné avec les autres forçages. Par rapport à la simulation non distribuée, la simulation distribuée montre une augmentation du ruissellement et une diminution de l'évapotranspiration de l'ordre de ∼100 mm. La distribution spatiale de la neige issue de la simulation a été comparée à des images Sentinel à haute résolution. Les résultats ont montré que la couverture neigeuse a duré plus d'un mois de plus pour la simulation distribuée et a montré une erreur moyenne de biais (MBE=0.22) plus faible dans la période de fonte par rapport aux simulations non distribuées (MBE=-0.4). De même, l'évapotranspiration simulée dans le cadre de la simulation distribuée se rapproche beaucoup plus des observations avec un coefficient de régression dont la pente diminue de 1,55 à 1,18. Le forçage météorologique distribué à l'échelle du mètre a un impact sur l'ensemble du cycle saisonnier du bassin versant d'une montagne de moyenne altitude et doit être pris en compte dans la modélisation hydrologique de la zone critique à haute résolution.

- Sept modèles de subsurface ont été construits à partir d'une étude géophysique de terrain afin de quantifier l'impact de configurations de subsurface plus ou moins hétérogènes sur les flux hydrologiques et les bilans hydriques. Ils présentaient 1 à 3 types d'horizons différents (sol, régolithe et Flysch) sur 11 couches. Les résultats ont montré qu'une conductivité hydraulique constante sur un seul horizon de sol n'était pas du tout adaptée pour simuler les comportements hydrologiques d'un bassin versant montag-

neux. Il a également été montré que le passage d'un horizon à deux horizons donnait une meilleure représentation du cycle saisonnier mais n'était pas en mesure de reproduire à la fois la chronologie saisonnière et les réponses à des événements courts tels que des pluies estivales importantes. Les simulations homogènes à trois couches et hétérogènes à trois couches ont pu reproduire les données d'observation à moyenne spatiale du ruissellement (KGE_{np} = 90, 91), de l'humidité du sol (MAPE = 0,23, 0,21) et de l'évapotranspiration (MAPE = 6,66, 6,61). La couche intermédiaire perméable (régolithe) joue un rôle dans le stockage et la libération de l'eau dans les simulations à 3 horizons qui sont capables de capturer l'amplitude du ruissellement, l'humidité du sol et l'évapotranspiration. Enfin, l'hétérogénéité latérale de la subsurface a apporté plus de détails dans les variabilités spatiales du stockage de l'eau et ensuite dans les processus hydrologiques et sont nécessaires pour que les modèles hydrologiques de la zone critique soient également pertinents localement.

- La distribution du temps de résidence dans la subsurface du bassin versant montre que le cycle hydrologique actif du bassin versant est principalement dominé par les particules jeunes. Quelques particules âgées de 5 ans contribuent également de manière significative à l'hydrologie du bassin versant. Beaucoup de vieilles particules dans la subsurface sont le résultat des 125 ans de spinup du modèle qui reste dans la subsurface profonde sans participer activement à l'hydrologie du bassin versant. La pluie domine la composante évapotranspiration tandis que la neige domine la composante ruissellement du flux hydrologique total. La neige contribue 61% au ruissellement et 23% à l'évapotranspiration. La pluie au contribue 39% au ruissellement et 77% de l'évapotranspiration. Cependant, la neige dans l'évapotranspiration provient de précipitations anciennes avec un temps de résidence moyen de $\sim$5 ans. Ces vieilles particules sont porteuses des transformations chimiques et pourraient transporter des nutriments vers les plantes. Les changements climatiques à venir modifieront la répartition de la neige, ce qui pourrait avoir un impact direct sur la répartition de la source de l'évapotranspiration. Cela pourrait exercer une pression sur le fonctionnement et la dynamique de la végétation.

List of Figures

List of Tables

Table of contents

1 Introduction

"We forget that the water cycle and the life cycle are one." — Jacques Yves Cousteau. This maiden statement from the french oceanographer explains that in my writing I am more concerned about the water. The water which rests in the ocean and poles, the water which runs in the mountains and rivers, the water which sustains life in wetlands, and the water on which our human civilization thrives.

1.1 History of water

The history of water is as old as the origin of our planet Earth. The origin of water is linked with the accretion of the nebula which is the only accepted hypothesis for the formation of the earth (Robert, 2001). Since then water has become an integral part of the earth. The cooling of the earth lead to the formation of atmospheric water which fell as rain to form oceans, the primitive form of liquid water on earth. Scientists believe that the first rain fell on earth around 3.8 billion years ago (Graham et al., 2010). This first drop made the foundation for the hydrological cycle on earth. The hydrological cycle, which is driven by solar energy, is responsible for shaping the earth. Water is an essential component for the evolution of both landscape and life forms. As the planet started getting greener, more water became available in the atmosphere through evapotranspiration (green water) (Jewitt, 2006). Exchange from green to blue water and blue to green water became the part of life cycle on the earth. Complexity in the landscape and life forms leads to complexity in the hydrological cycle. Water exchange quantification between ocean, atmosphere, and land, remains the key to understanding the hydrological cycle on the earth (Fig. 1.1).

1.2 History of hydrological sciences

The process of rain hitting the ground has many in between events. A raindrop's journey includes evaporation into the atmosphere, precipitation, surface runoff, evapotranspiration, groundwater recharge, and any possible cycle between these. This interactive cycle from the atmosphere to the deep subsurface is known as Earth's hydrological cycle. Hydrological sciences mainly involve the study of the hydrological cycle and its interaction with several other Earth's components. The hydrological cycle is one of the most intriguing earth cycles

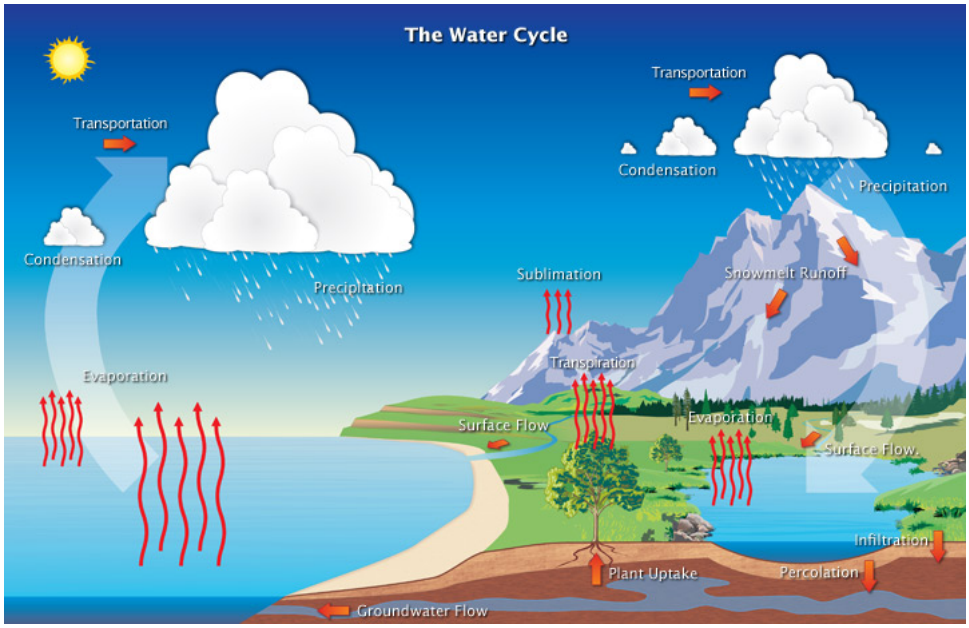

Figure 1.1: Components of the Earth's water cycle (Source: Image courtesy NOAA National Weather Service Jetstream)

and often place at the center of technological to societal aspects.

The history of hydrological studies started more with a philosophical approach. In the past, it was mainly studied for agriculture and flood control. Though the storage, drainage, and flood retaining structures are evident from some oldest civilizations on the earth, however, the development of water studies as sciences started in 15th century (Rosbjerg and Rodda, 2019). The earliest reported scientific study was from Leonardo de Vinci when he measured the streamflow (Pfister et al., 2009). Further developments include the reporting about the origin of springs from rain by Bernard Palissy, and the measuring of rain, runoff and drainage area relationship of Seine River by Pierre Perrault (Deming, 2005; Koutsoyiannis and Mamassis, 2021). These hypotheses later were proved from infiltration experiments. Edmond Halley in 17th century measured the evapotranspiration and reported the hydrological budget for the first time (Koutsoyiannis and Mamassis, 2021; Rosbjerg and Rodda, 2019). However, the foundations of modern hydrological sciences hail from John Dalton in 1802 (Rodda, 2006). He used reliable measurements to report the complete hydrological cycle. In 1831 Henry Palmer designed the instrument to measure the continuous variation of stream height in rivers (Fig. 1.2). Though the book Hydrodynamica was published by Daniel Bernoulli in 1738 about different kinds of flow in open and closed channels. However,

it was in the year 1856 when the fundamental equation of groundwater flow was introduced by Henry Darcy (Darcy, 1856). Later in the 19th century, there was some more development like time of concentration, peak flow design, and mass curve for reservoirs. The first half of the 20th century saw some more basic developments in hydrology. William Green and Gustav Ampt in 1911 provided the description of the soil infiltration and saturation (Green and Ampt, 1911). After 3 years in 1914, Weston Fuller introduced the concept of statistical frequency analysis (Fuller, 1914). One of the major development in this period was the introduction of the concept of flow in unsaturated media from Lorenzo Richards in 1931 (Richards, 1931). Further, Leroy Sherman, in 1932, introduced the concept of unit hydrographs. The impact of pumping on the drawdown of the piezometric surface was formulated by Charles Theis in 1935. And, in 1948 Howard Penman presented the mathematical explanation of the potential evaporation using meteorological variables (Rosbjerg and Rodda, 2019; Koutsoyiannis and Mamassis, 2021).

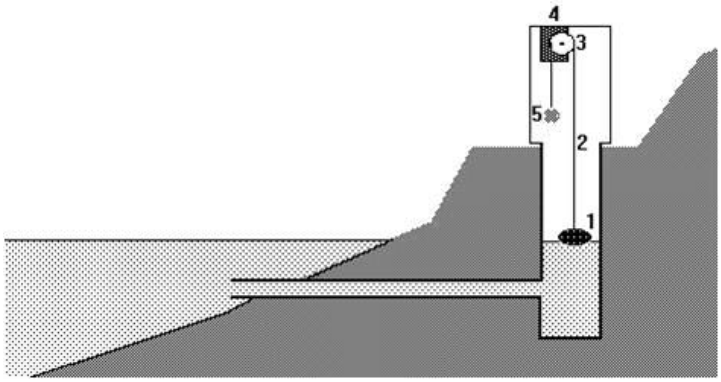

Figure 1.2: Principle of river level measurement developed by Palmer, the system was in widespread use up to 1950 (Source: Encyclopedia of the Environment)

Later in the 20th century, there were many changes in the development of hydrological science. During this period hydrology was recognized as a separate science. Development in computers leads to solving many computationally intense problems in hydrology. All these developments will be discussed in the next section..

1.3 Development of hydrological sciences

The development of hydrological sciences is linked with the development of hydrological modeling methods. Though the concept of hydrological modeling evolved from Mulvaney

(1851) method of calculating the time of concentration. However, it is the year 1960 which marks the major development in the field of hydrology with the evolution of computers. Numerical hydrology, statistical hydrology and big data driven hydrology are some of the areas which gained ample recognition during this period. The development of Soil Conservation Service – Curve Number (SCS-CN) in 1956, and source area contribution reporting were major developments of this period (Lyon et al., 2004; Sivapalan and Blöschl, 2017). Snow hydrology has also been in major development during the same period. In 1960 Matinec developed the degree day approach to calculate snowmelt (Martinec, 1960). Later the energy balance approach for snowpack was developed by Anderson (1968). To be mentioned, the very first representation of the complete hydrological cycle was given by the Stanford Watershed Model (Crawford and Linsley, 1966). Most of the methods till then were based on lumped approaches and the availability of long term streamflow data. Development in infrastructure driven the hydrological sciences more towards the society. Soon it was realized that the current hydrological understanding was not sufficient to tackle issues such as ungauged catchment or contaminant hydrology (Fig. 1.3). This led to the development of physically based models to explain and simulate the natural processes in the watershed. Freeze and Harlan (1969) introduced the idea of a physically-based digitally-simulated hydrological response model. The Richards equation for flow in unsaturated media became the backbone of such kind of model along with the availability of faster computers. Stephenson and Freeze (1974) evaluated this model in a hillslope terrain and reported the difficulty of calibrating a physically based model. Further developments in surface-subsurface coupled models stressed the equal importance of measurement and modeling in calibration. Binley et al. (1989) moreover argued that heterogeneities in soil and vegetation along hillslopes are difficult to handle from point measurements.

Although under-validated, process based distributed hydrological models have been widely used in the end of the 20th century, in particular for assessing the impact of land use, deforestation and urbanisation. This period saw the development of various distributed models like Système Hydrologique Européen (SHE) from joint project between UK, Denmark and France ; Institute of Hydrology Distributed Model (IHDM) in UK ; THALES and CSIRO TOPOG-dynamic model in Australia ; and Integrated Hydrologic Model (InHM) in the USA (Beven, 2011). The above mentioned model differ from each other in term of domain

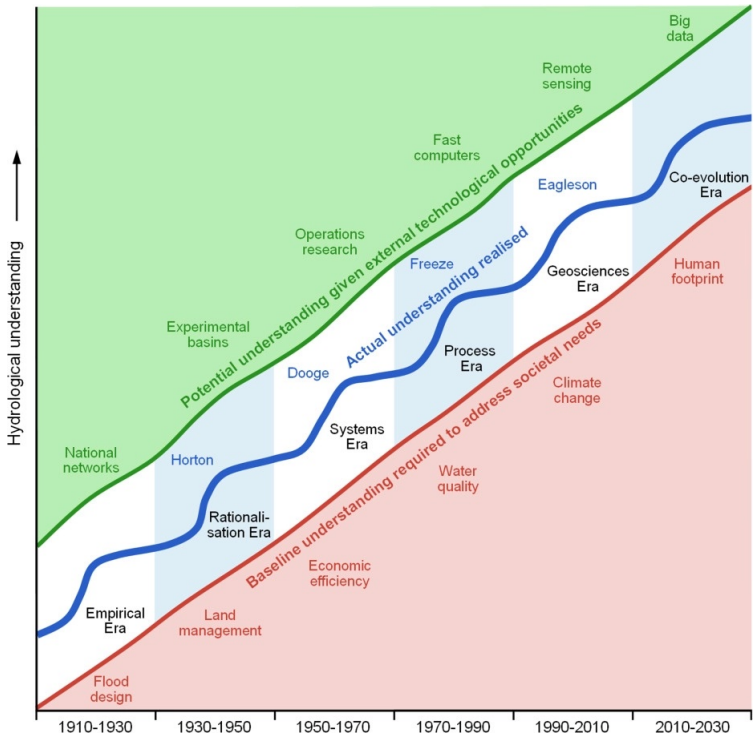

Figure 1.3: Staircase growth of hydrological understanding (Sivapalan and Blöschl, 2017)

discretization and solver enhancement. However, the blueprint of these models were still adopted form the work of (Freeze and Harlan, 1969).

The development of geographical information system (GIS) added much value to the distributed hydrological model. They helped reduce the spatial heterogeneities of various parametrizations by forcing or controlling the models with satellite observations. Advancement in GIS is also a backbone to the development of semi-distributed hydrological models by enabling the aggregation of catchment into separate hydrological response unit (HRU) (Flügel, 1995). In contrast, distributed hydrological models followed a distributed grid approach. Advances in hydrology over the past two decades have been related to improved domain discretization, high-resolution modeling using satellite observation, and improved numerical solvers. A new generation of integrated physics-based hydrological models will be discussed in detail in the next section.

1.4 Process based approach in hydrology

Modern hydrology values representing the physical processes more than just simulating catchment runoff. The concept of the hydrological continuum from the top of the canopy to the

subsurface became the core for the development of integrated hydrological models with increasing complexity (Henriksen et al., 2003; Koch et al., 2016; Shen and Phanikumar, 2010). These complex hydrological models are intended to represent the complete hydrological cycle and its unified components: atmosphere, surface, and sub-surface (Fig. 1.4). The coupling of atmosphere and surface hydrology is common in many models from Earth System Models (ESMs) to catchment scale models. However, integration (coupling) of surface and subsurface into single units is much less common (Fullhart et al., 2019; Clark et al., 2015) although essential to capture outflows, specifically when the Dunnian runoff dominates over the Hortonian runoff (Gilbert et al., 2016). Most models account for the free draining hydrology below the surface. Yet, the subsurface stormflow could be a main runoff mechanism for the steep slope mountainous catchment, hence, accounting for the subsurface becomes extremely important in this kind of terrain.

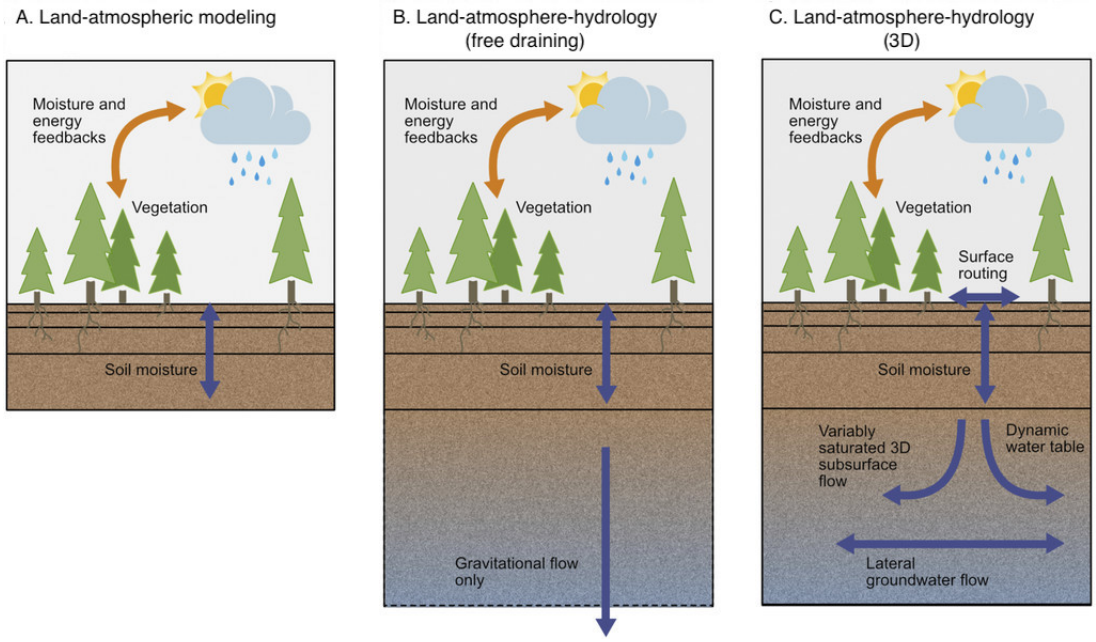

Figure 1.4: Illustration of decoupled subsurface hydrology, coupled 1D hydrology and coupled hydrology with lateral flows (Forrester and Maxwell, 2020)

This kind of model is explicitly the mean to simulate the feedback mechanism along with the runoff routing. The land surface scheme in these models is dedicated to simulating the energy balance, interception, evapotranspiration, soil moisture, snow accumulation, and melting (Kuffour et al., 2020). The subsurface components of these models are meant to simulate vadose zone flow, groundwater flow, and resulting surface runoff (Fig. 1.5. Physical

based models use the natural equation to solve the water and energy balance problem. Hence, these models accurately explain all the physical processes in the catchment. Table 1.1 reviews some of the physical based model and their applications. The empirical details and functioning of such kinds of models will be explained in Chapter 3 with a focus on ParFLOW-CLM.

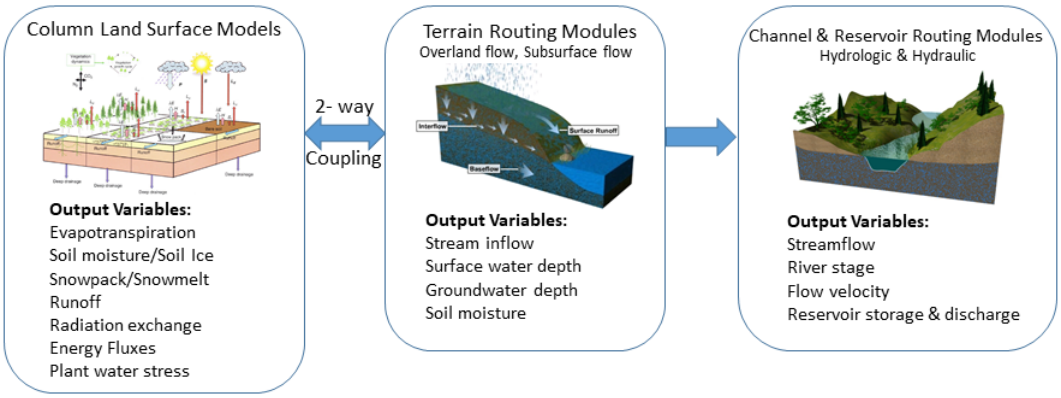

Figure 1.5: Illustration of functioning of coupled hydrological models (Source: WRF-Hydro)

1.5 Water in mountains

About 71 % of the total surface area of the earth is covered with water. If we break down this water then 96.5 % of water is held by oceans, 0.9 % of water is saline (non-oceanic water) and only 2.5 % is freshwater Gleick (1993). Out of this 2.5 % fresh water, 68.7 % water is held in the form of glaciers and ice sheets, 30.1 % as groundwater and 1.2 % includes surface and atmospheric water. Mountains play a very active role in maintaining and perturbing the freshwater system. They are home to glaciers and fresh water on the continent majorly comes from mountain glaciers or springs (Immerzeel et al., 2020), and the groundwater recharge is also largely governed by the mountain snow and ice melt.

Mountains interact with the water cycle in many ways. Agriculture, electricity, fresh water, and reservoirs for example directly thrive on mountain water sources. Snow is central in the mountain-water relationship. Mountains snowpack is crucial from hydrological and ecological points of view. Freshwater originating from mountains fulfils the requirement of 1/6th of the world's population, providing more than 90 % of the total water demand in some watersheds (Liniger and Weingartner, 1998). Seasonal snowpack stores water which

Model	Key method	Application	Reference
WRF-Hydro	Remote sensing based model calibration	Flood forecasting	Silver et al. (2017)
MIKE SHE	Regional climate analysis as forcing	Surface spatial pattern evaluation	Gaur et al. (2022)
TOPMODEL	Multi model analysis for present and future climate	Wetland distribution	Xi et al. (2021)
GeoTOP	Calibration using bulk density optimization	Determination of hydraulic parameter for regolith	Fullhart et al. (2019)
CRHM	Assimilation of gridded snow product	Spatial distribution of Snow water equivalent	Lv et al. (2019)
DHSVM	Application of WRF output in rainfall-runoff modeling	Sediment load of mountainous catchment	Keck et al. (2022)
ParFLOW-CLM	Snow hydrology using observational dataset	Surface-subsurface connectivity	Tran et al. (2020)
ParFLOW-CLM	Conceptual mountain block simulation	Subsurface flow modeling	Rapp et al. (2020)
ParFLOW-CLM	Multimodel gridded datasets	Sensitivity of the mountain front recharge	Schreiner-McGraw and Ajami (2020)

Table 1.1: Review of various physical based distributed models.

later in summer is used for different human needs. Hence, snow in mountains, directly and indirectly, supports the global economy. Along with hydrology, snow also drives the energy budget, biogeochemical processes, ecosystem, and climate. Snow has a large-scale cooling impact on our planet. In winter snow reflects back most of the shortwave radiation and during the melting season, it absorbs the shortwave radiation, hence contributing to cooling of the surface in both cases (Cohen and Rind, 1991). Ecologically, the timing and distribution of flora and fauna are conditioned by onset and disappearance of snow in the year (Esposito et al., 2016; Keller et al., 2005). Furthermore, the climate severely impacts

the vegetation, soil moisture, surface water, and groundwater in these regions. Snow also plays a very crucial role in critical zone functioning in the mountains. The different aspects of the mountain critical zone will be discussed in the next section.

Snow water equivalent (SWE), snow depth, and snow cover are the major parameters to represent the snow distribution across scales (Su et al., 2008). To document these parameters two kinds of approaches are followed. One is to use physical based models of the snow cover force by actual meteorological reanalysis. Another approach is to retrieve these parameters using the satellite method Foster et al. (1996). For example, Crocus, a snowpack simulation model, is used for the application of snow cover forecast and anthropologically induced melting of the snowpack (Tuzet et al., 2020; Vionnet et al., 2019). Similarly, laser scan and optical images are in practice used to estimate the snow depth and snow cover in mountains (Deschamps-Berger et al., 2020; Revuelto et al., 2021a). Few studies also assimilated the data from remote sensing to model the continuous simulation of snowcover (Deschamps-Berger et al., 2022; Revuelto et al., 2021b). Both measurements have their own pros and cons as estimation of these parameters over complex terrains is not easy or announced as an impossible task by some hydrologists. Figure 1.6 shows the global snow depth over the major mountain ranges. It shows that the mountains contribute a lot to store the snow.

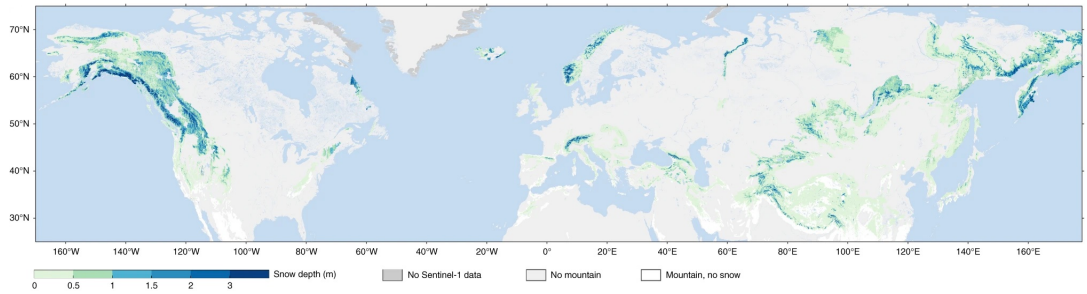

Figure 1.6: Global snow depth distribution over mountains (Lievens et al., 2019).

The Alps are often called the water tower of Europe. In the European Alps, the snow distribution follows a vast climate and topographic variability (Fig. 1.7). European Alps stretch through six major countries: France, Switzerland, Germany, Austria, Italy, and Slovenia (Weingartner et al., 2007; Viviroli et al., 2007). This vast distribution supports the Alpine hydrology along with hydropower generation, fresh water supply, and agriculture. Alps cover an area of 11 % of the total area of the European continent (Vanham, 2012). Figure 1.7 shows the snow cover duration throughout the European Alps which contributes

to more than 40 % of the freshwater supply (Matiu et al., 2021). This snow cover feeds the four largest river basins in Europe i.e. Danube, Rhine, Rhone, and Po. According to Weingartner et al. (2007), on average, 38 % of these four river's discharge is of mountain origin.

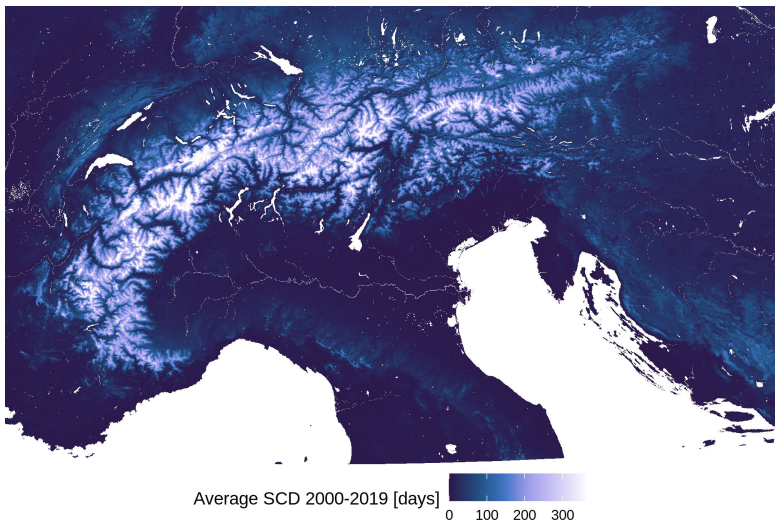

Figure 1.7: Snow cover days over European Alps (Matiu et al., 2021).

Along with such a huge reserve of water the European Alps faces the harsh reality of climate change. The alpine snow depth and snow cover have decreased and will keep doing so in the future. (Breiling and Charamza, 1999; Beniston et al., 2003; Jasper et al., 2004; Vanham and Rauch, 2009). Anthropogenic input like black carbon have increased response to the melting (Réveillet et al., 2022). Studies show that lower elevations of the European Alps usually show a negative trend in snow cover whereas, the higher elevation shows no trend or increasing trend (Fontrodona Bach et al., 2018; Marty et al., 2017; Terzago et al., 2010; Kotlarski et al., 2022). The climatological and hydrological impact on these subalpine critical zone will be discussed in subsequent sections.

1.6 Significance of mountain critical zone

Critical zone is a complex system which couples physical, chemical, biological and geological processes and sustains life at earth's surface (Fig. 1.8). Although we already have a good understanding of critical zone processes, there is still a need to cross disciplinary boundaries to develop an integrated science of the critical zone. The critical zone is essential in terms of

the services it provides to people. Box 1 summarizes the context of critical zones services on societal aspects. Critical zone in mountains include the components from glacier, permafrost, snowcover, snowpack hydrogeology and climate. Contemporary issues related to mountain regions could only be addressed with better understanding of mountain critical zone. Mountain critical zone provide the opportunity to understand the integral behaviour of surface. Biomass production, water storage and transfer, nutrient transportation and biogeochemical alteration are few of the functioning of mountain critical zone (Le Roux et al., 2016; Gao et al., 2018). A vast functioning of these area is also govern from land use practice. Soil plays a central role in critical zone and land use has potential to perturb its functioning. These perturbation mainly affect the water quality/quantity and nutrient transportation from catchment to downstream.

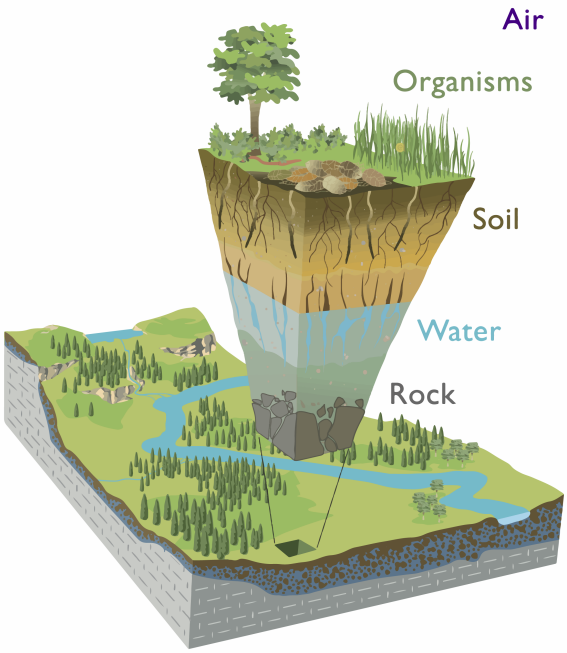

Figure 1.8: Elements of a critical zone

Box 1:

Priority Communications

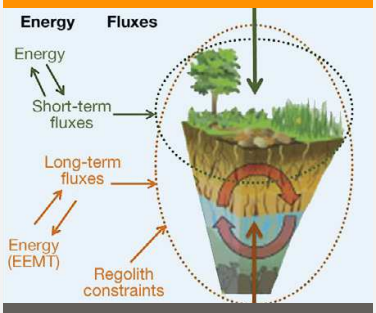

Processes within the critical zone, such as soil formation, support and/or control many ecosystem processes and consequently the supply of products that benefits society. An expanded perspective of ecosystem services that encompasses the critical zone would enable more effective management and allow a more comprehensive valuation of services.

J.P. Field, D.D. Breshears, D.J. Law, J.C. Villegas, R.E. Gallery, and S.A. Papuga, School of Natural Resources and the Environment, Univ. of Arizona; D.D. Breshears, Dep. of Ecology and Evolutionary Biology, Univ. of Arizona; J.C. Villegas, Facultad de Ingeniería, Universidad de Antioquia-Colombia; L. López-Hoffman, School of Natural Resources and the Environment, Udall Center for Studies in Public Policy, Univ. of Arizona; P.D. Brooks, Dep. of Geology and Geophysics, Univ. of Utah; J.C. McIntosh, T. Meixner, G.Y. Niu, and P.A. Troch, Dep. of Hydrology and Water Resources, Univ. of Arizona; J. Chorover, R.A. Lybrand, S.A. Papuga, and C.R. Rasmussen, Dep. of Soil, Water and Environmental Science, Univ. of Arizona; G.A. Barron-Gafford, School of Geography & Development, Univ. of Arizona; G.A. Barron-Gafford, G.Y. Niu, and P.A. Troch, Biosphere 2, Univ. of Arizona; M.E. Litvak, Dep. of Biology, Univ. of New Mexico; and J.D. Pelletier, Dep. of Geosciences, University of Arizona. *Corresponding author (jpfield@email.arizona.edu).

Vadose Zone J.
doi:10.2136/vzj2014.10.0142
Received 9 Oct. 2014.
Accepted 20 Nov. 2014.
Open access

Critical Zone Services: Expanding Context, Constraints, and Currency beyond Ecosystem Services

Jason P. Field,* David D. Breshears, Darin J. Law, Juan C. Villegas, Laura López-Hoffman, Paul D. Brooks, Jon Chorover, Greg A. Barron-Gafford, Rachel E. Gallery, Marcy E. Litvak, Rebecca A. Lybrand, Jennifer C. McIntosh, Thomas Meixner, Guo-Yue Niu, Shirley A. Papuga, Jon D. Pelletier, Craig R. Rasmussen, and Peter A. Troch

Processes within the critical zone—spanning groundwater to the top of the vegetation canopy—have important societal relevance and operate over broad spatial and temporal scales that often are not included in existing frameworks for ecosystem services evaluation. Here we expand the scope of ecosystem services by specifying how critical zone processes extend context both spatially and temporally, determine constraints that limit provision of services, and offer a potentially powerful currency for evaluation. *Context:* A critical zone perspective extends the context of ecosystem services by expressly addressing how the physical structure of the terrestrial Earth surface (e.g., parent material, topography, and orography) provides a broader spatial and temporal template determining the coevolution of physical and biological systems that result in societal benefits. *Constraints*: The rates at which many ecosystem services are provided are fundamentally constrained by rate-limited critical zone processes, a phenomenon that we describe as a conceptual "supply chain" that accounts for rate-limiting soil formation, hydrologic partitioning, and streamflow generation. *Currency*: One of the major challenges in assessing ecosystem services is the evaluation of their importance by linking ecological processes to societal benefits through market and nonmarket valuation. We propose that critical zone processes be integrated into an evaluation currency, useful for valuation, by quantifying the energy flux available to do thermodynamic work on the critical zone. In short, characterization of critical zone processes expands the scope of ecosystem services by providing context, constraints, and currency that enable more effective management needed to respond to impacts of changing climate and disturbances.

Abbreviations: EEMT, Effective Energy and Mass Transfer.

The critical zone is defined as the portion of the Earth's land surface that extends from the lower limit of freely circulating groundwater to the top of the vegetation canopy (NRC, 2001). Functioning of the critical zone determines the rates at which mass and energy are exchanged among the regolith, biosphere, and atmosphere (Lin, 2010; Lin et al., 2011; Chorover et al., 2011; Rasmussen et al., 2011). Processes within the critical zone, such as soil formation, hydrologic partitioning, streamflow generation, and landscape evolution support and/or control many ecosystem processes and, consequently, the supply of products that benefit society. Environmental scientists and economists have addressed the need to link biophysical processes to human well-being through the developing concept of ecosystem services (e.g., Costanza et al., 1997; MEA, 2005; TEEB, 2010), emphasizing how biodiversity, ecological processes, and spatial patterns in the near-surface environment provide services to society. Four categories of ecosystem services were initially identified: (i) *provisioning services* describe the material or energy outputs from ecosystems and include food, water, and other resources; (ii) *regulating services* influence processes such as water quality, flood regulation, and disease regulation; (iii) *habitat or supporting services* consider

The mountain critical zone establishes the bridge between humans and the earth's surface. As the critical zone sustains all life forms in a given area, scarcity and vulnerability come together. The water cycle often plays important role in exploring the critical zone. From ecosystem services to nutrient transport hydrology plays a big role (Brooks et al., 2015; Grant and Dietrich, 2017). The subsurface flow provides the idea of behaviour of porous and fractured media which leads to the overall functioning of the critical zone. However, mountains are not less in facing the global climate change which causes droughts, floods, and impacts on primary productivity. Recent studies suggest that the water cycle in mountains will be strongly affected by climate change (Kohler and Maselli, 2009). And this impact could be much greater with increasing anthropogenic activities. The mountain critical zone and its hydrological dynamics are governed by complex variables: slope, aspect, snow, subsoil fracturing, vegetation cycle length, soil, weathering, erosion (Biggs and Whitaker, 2012; Anderson et al., 2007). Some of these variables depend on climate, creating the potential for feedback between climate change and critical zone evolution in mountains. The hydrological aspect of critical zone and climatic vulnerability will be discussed in detail in the next section.

1.7 Snow hydrological aspects of mountain critical zone

Hydrology and more generally the behaviour of the critical zone is driven in mountains by climatic and topographic gradients, with snowmelt as the dominant source of water (Pelletier et al., 2018; Bales et al., 2006). Right from stream water generation to groundwater recharge, all are governed by snow hydrological response (Fig. 1.9).

The hydrological processes are often studied at the catchment scale, as a functional unit and a well defined box. As explained above the soil plays a central role in the critical zone, modulating the fluxes. Snowmelt first reaches the soil where it gets partitioned into soil moisture, surface runoff, evapotranspiration, and subsurface storage (Chorover et al., 2011). Hence, the persistence of snow plays a central role in the critical zone. Micrometeorology, soil moisture, subsurface storage, Vegetation cycle, and animal grazing are directly affected by snow persistence (Seyfried et al., 2018; O'Geen et al., 2018). Mountainous catchments are generally submitted to a long winter which means long snow cover periods which often last for the complete winter season. Along with holding water for summer runoff and soil moisture, the slow melting gives enough time to percolate to subsurface (Barnhart et al.,

2016). In such catchments, snow is expected to percolate more to subsurface than rain. In the absence of rain, these snow particles sustain streamflow and evapotranspiration. Hence the importance of including a detailed description of the subsurface in critical zone models. However, this subsurface quantification and inclusion in integrated modeling is still debated. Since the last few decades geophysicists and hydrologists are working together to explore the subsurface and include it in hydrological studies (Flinchum et al., 2018; Hector et al., 2015). But, detailed hydrological modeling using these data is still limited and almost unavailable in mountainous catchments. Also, there are various debates about the homogeneous or heterogeneous nature of the subsurface. Certain studies mentioned that a simple homogeneous model can outperform the complex subsurface representation (Claes et al., 2019). Along with lithological layer representation, how deep the subsurface is necessary became a debated question too (Condon et al., 2020). There are studies that estimated that fractures in old rock lead to leaky aquifers and in such regions the subsurface could be much deeper than what we could think of (Stober and Bucher, 1999). These deep circulations mean a longer stay of particles in the subsurface. Snow has more chances to deep percolation hence, they should stay longer in the subsurface and be more prone to biogeochemical alteration. However, rain behaves a bit differently in terms of flow path and travel time (McGuire et al., 2005). The rain along the slope travels faster to reach downstream whereas the snow takes longer time because of its long persistence. This long snow persistence provides enough time to percolate into the subsurface compared to rain. Hence, the decrease or increase in snow amount is directly linked with the subsurface recharge and its partitioning to evapotranspiration and stream outlet component.

Snow and rain transport to the surface and the subsurface in the critical zone depends on slope, aspect, vegetation, porosity, permeability, and regional geology (McDonnell and Beven, 2014; McGuire et al., 2005). The physio-chemical characteristics of water in streams result from the surface and subsurface storage across the critical zone. However, the transient connectivity between different storage makes it complex to quantify. Snowmelt's contribution to stream and its spatio-temporal variability depends upon the hydrological connectivity and residence time. Source, timing, and magnitude are directly controlled by flow paths across the catchment. For example, the higher fraction of young particles in streams indicates shallow and rapid connectivity between the subsurface and surface (Xiao et al.,

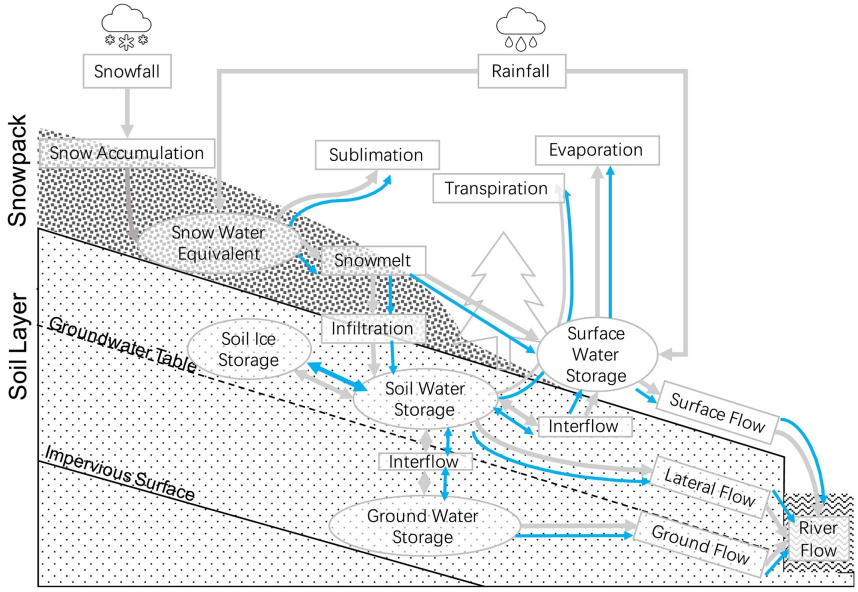

Figure 1.9: Tracing path of snowmelt in mountain critical zone

2022). As the older particle fraction increases in the streamflow, the source particle travels deeper into the subsurface and follows a long path before getting eliminated from the catchment (McGuire and McDonnell, 2010). Similarly, plants take up what is available in the surrounding of their root system. As the youngest water is the closest to the surface, plants usually use the youngest source in the form of rain or snowmelt (Maxwell et al., 2019). However, during the dry season and droughts, they are forced to use older water from deeper soils. In general, along with streamflow control, flow path and residence time also impact plant uptake. These flow paths and residence times are directly controlled by topography and subsurface configuration in the area (McDonnell and Beven, 2014; McGuire and McDonnell, 2010). Non-linearity in storage and discharge relationships is higher for mountain catchments. Partitioning the fluxes based on this non-linearity helps to determine stream chemistry, plant water uptake, discharge concentration, and subsurface behaviour (Soulsby et al., 2015). However, such non-linearity limits the application of analytical methods to solve a such complex problem. Hence, quantifying the source and distribution, especially to evapotranspiration and outflow is a challenging question. The seasonal cycle of the source to evapotranspiration and outflow shows meteorological to geological control. Hence, along with subsurface and topography, the climate has a big role to play in how this partitioning will be impacted in the future.

In mountain, critical zone snowmelt is the dominant component in subsurface recharge

and streamflow generation. Subsurface dynamics and streamflow responses are vulnerable towards the decrease in snow which could shift the partitioning between the runoff, evapotranspiration, soil moisture and subsurface storage (Aygün et al., 2020; McLaughlin et al., 2017). Snow cover shows a global decline, especially for the mid-altitude mountain catchments (Notarnicola, 2020). This could certainly change how snowmelt gets partitioned between those flow components. For example, changing the phase of precipitation from snow to rain could fasten the runoff component which could alter the rate and timing of flux delivery. The partition between rain and snow could have many aspects under future climate change. Some studies suggest that precipitation intensity will increase in the future. However, due to higher temperatures, there will be less snow, then less percolation, and less contribution of deep old water to outflows (Berghuijs et al., 2014). Some warmer areas could experience the complete disappearance of snow by the end of the century. Mountain critical zone is not too much explored and there are still uncertainties in their future behaviour. However, the warmer climate will have two kinds of impact on the mountain's critical zone. The first is the decrease in snow cover, which will decrease the runoff component, subsurface recharge, and limit the plant uptake (Godsey et al., 2018). The second is a faster snowmelt runoff, with shorter travel times decreasing water availability in critical zones (Barnhart et al., 2016). Earlier snow melt will also limit the sustainability of streams in late summer and will create an ecological imbalance. Evapotranspiration is another component which thrives on soil moisture and shallow subsurface storage. Much of these components come from shallow storage of snowmelt. Any shift in snow regime will directly put pressure on vegetation dynamics (Liu et al., 2014). Spatial Heterogeneity in climate, soil, vegetation and geology will result in uneven response of snowmelt across critical zone. Exploring such impact requires the understanding of coupled processes, flow path, and residence time. Critical zone understanding will benefit a lot with the multi disciplinary approach. However, modeling the mountainous critical zone is not handy as it is driven by complex topography and geology which is tough to represent in high spatio-temporal scales. The heterogeneities of critical zone are often neglected in earth system models (ESMs). It is an ongoing debate to find ways to include the small heterogeneities in large scale ESMs. These concepts will be elaborated in the subsequent section.

1.8 Earth system models (ESMs) in mountains

The complexity of the critical zone can be understood only with a high-resolution spatio-temporal approach. Setting up observation at a high spatio-temporal scale is not an easy task hence, modeling and remote sensing are the only approach to monitor the critical zone functioning at a high spatio-temporal resolution as we cannot imagine observing and documenting the surface and subsurface on a range of scale from millimeter or less to thousands of square meter. However, spatial heterogeneities of critical zone processes are often neglected in large-scale hydrological modeling and Earth system models (ESMs).

Underrepresentation of critical-zone processes within ESMs has been a debated topic since the advancement of global and regional-scale modeling (Clark et al., 2015; Fan et al., 2019). Although ESMs succeed in scaling up many land surface processes, they still fail to provide fine-scale energy and mass transfers, and biogeochemical cycling. At regional to global scales, these processes are efficiently represented in ESMs, as they are key to most of their applications such as water stress evaluation, water security management etc. (Masaki et al., 2017; Yang et al., 2019). Yet, the application of these regional-scale models depends much on the geography of the region of consideration. In a broad flat plain, these models are often able to capture the dynamic response of the surface. However, this complexity in mountainous regions is too intricate to capture this response (Fang and Pomeroy, 2020; Zaremehrjardy, 2020; McDonnell and Beven, 2014). With a recent increase in the socio-economic application of ESMs, the scientific community is eager to simulate correctly the water fluxes at different spatial scales. Land surface models (LSMs) are an mandatory component of the ESMs. LSMs are intended to capture the exchange of mass, energy and biogeochemical cycle between Earth's surface and atmosphere (Hurrell et al., 2013; van den Hurk et al., 2011). In a flat region with a homogeneous surface, these LSMs present a high accuracy; however, in sloping terrain, these models often miss micro-scale perturbations (Fan et al., 2019; Kollet and Maxwell, 2008). The micro-meteorology representation in LSMs has improved a lot in the past few decades through dense monitoring. However, due to a lack of surface-subsurface coupling, these models are phased between the predicted and actual land-atmospheric response. Over decades of ESMs and associated LSMs evolution, hydrological processes have mostly been simulated using a one-dimensional approach along the vertical

column (Singh et al., 2015; Song et al., 2020). Bloom in the critical-zone community led to the consideration of surface and subsurface hydrology as a coherent unit. Hence, the vertical and lateral flow concept evolved in integrated hydrological modeling (Liu et al., 2004; Maxwell and Condon, 2016; Overgaard et al., 2006). Maxwell and Condon (2016) argued that evapotranspiration bias, a major flux in land-atmospheric exchange and hydrological budgets, in regional-scale models is due to the under consideration of subsurface lateral flow. Demand in (terms of) applicability of policymakers and end users in terms of water resources and risk predictions forced the modelers to adopt a descriptive terrain-following modeling approach for lateral flows.

Many physical events affect water fluxes in mountainous catchments, such as rain on snow, snow redistribution, differential melting, and slope/aspect. These events are too intricate to catch using modest hydrological tools (Costa et al., 2020; Pomeroy et al., 2007), furthering the need for physically distributed, hyper resolution modeling. Hillslope catchments tend to receive variable radiation and wind variability along the micro-topography; sunlit and sunshade sides of catchments do not behave in the same manner (Fang and Pomeroy, 2020; Pomeroy et al., 2003). It leads to the dominance of complex processes associated with heterogeneities like snow patches during the melting season, redistribution of snow in the catchment, and variable saturation of the surface, which all impact recharge, overland flow responses, vegetation dynamic, and evapotranspiration distribution along slopes. These characteristic responses directly affect the subsurface flow and streamflow in space and time. From per critical-zone perspective, ESMs resolution is usually too coarse to simulate the micro-scale eco-hydrological behaviour. A good number of studies on snowpack simulation have used hyper-resolution distributed observation forcing (Baba et al., 2019; Günther et al., 2019; Vionnet et al., 2012). However, the practice of hyper-resolution distributed observation forcings of multiple meteorological variables in hillslope hydrology is limited.

To conclude the critical zone water cycle is dependent upon the subsurface storage, residence time, flow path, topography, and snow distribution. However, there is a critical knowledge gap to represent these processes with the recent advancements in ESMs. Different observations support the intricate nature of mountainous critical zone catchments. Hence, filling the knowledge gap with the different upscaling processes is needed to enhance the representation of such catchments. This could be achieved by identifying the major sensitive

variables and representing their impact on the water cycle in the critical zone. Then incorporating them into ESMs to represent complete critical zone processes and their responses for simulating ecosystem dynamics.

1.9 Critical zone research site at Col du Lautaret

To study the complex behaviour of the critical zone and its sensitivity towards different topographical, meteorological, and hydrological aspects we have chosen a small 15.28 ha catchment in a subalpine region of the French Alps (Fig. 1.10). The catchment lies close to the Lautaret Pass, in the vicinity of Lautaret garden[2]. The area is characterised by its great floristic diversity. The mountain pass at Col du Lautaret joins the north and south Alps hence, the area also sees influence from the Mediterranean climate. The panorama includes a rich geological diversity from crystalline massif to sedimentary rocks and soil. Overall, this area is the perfect site to study the climate, hydrology, ecology, geology, and their interactions. To engage the site for scientific developments, the area is dedicated to tourism, research, and science training.

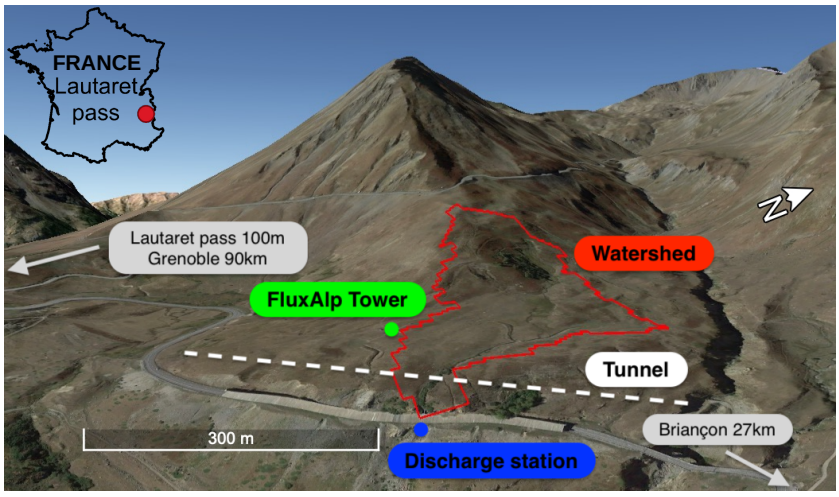

Figure 1.10: Studied catchment at Col du Lautaret.

The catchment shows a variable response during the single hydrological year. The winter is dominated by dense snow cover whereas, the summer is dominated by grassland vegetation (Fig. 1.11). In the winter the grassland is covered with snow for 5 to 6 months per year and spatio-temporal distribution of snow in springs determines the onset and cycle of the

[2]https://www.jardindulautaret.com/

grassland. Along with grassland, the catchment also has a 5 % woody coverage which includes larches, alders ad bushes. We have several kinds of observation in the catchment from physical to chemical (Table 1.2). A detailed description of the monitoring will be included in Chapter 2. The streamflow during the peak winter season decreases close to zero during negative temperatures. In summer the streamflow comes from direct rain and snow runoff and shallow subsurface storage in the form of springs. Discharge measurement of the catchment has been set up in 2020 which leaves us with a limited period of observation.

Figure 1.11: Seasonal contrast at Col du Lautaret.

Surface Flux	Meteo tower (atmospheric variables), FluxAlp (carbon and water vapour flux, eddy cov.)
Hydrological Flux	Stream discharge monitoring, gauge, tunnel leakage monitoring
Chemistry	snow sampling, discharge sampling, high volume sampler (HVS), nitrogen and oxygen isotopes
Others	snow pit, NDVI, live camera

Table 1.2: State of the art monitoring at Col du Lautaret, maintained by numerous collaborators (LECA, IGE, CEN, EDYTEM, ICOS)

The catchment elevation range varies between 2000-2200 meters. The head of the catchment is very steep which gradually becomes sub-horizontal in the lower part of the catchment. The catchment also has a very steep slope towards the outlet (50°) and the whole catchment faces mainly towards the east direction. The Flux'Alp meteorological station lies adjacent to the south of the catchment in a flat zone. According to the 2017-2018 meteorological

data in the catchment, the catchment received a total of 1530 mm of precipitation, out of which 970 mm was dry precipitation. The average temperature for this year was 4 °C with minimum average temperature going as low as 7 °C in February month and a maximum average temperature of 14 °C in July. July is also the driest month in the catchment with March being the moist humid month. The southwest direction of the valley sees strong wind conditions throughout the year. Due to high latitude, east facing catchment and high mountain panorama the catchment sees a large variability in the summer and winter solar radiation. These aspects of the catchment will be discussed in more detail in Chapter 2.

Geologically, the catchment could be regarded as the outer zone of the French Alps. Over the catchment, soil depths range from 20 cm on steep slopes to more than 2 m on flat wetlands. Soils are rich in clay with high porosity and retention capacity. This rich clay soil slowly transits to the hard rock towards the regolith up to 5 m at the deepest locations. Geology in the region date back to the early Paleozoic era (300 million years). The high elevation panorama around the catchment includes the Combeynot and Meije which are mainly made up of granite and gneiss of the Hercynian chain. The chain has been deeply eroded since then and the sea encroachment deposited some old clay, silt, and limestone around 250 million years ago. Sedimentary nature rocks in the area dated 200 million years to 250 million years old; and are part of the Briançon nappe. Later some of the silts were metamorphosed to give black schist and a recent folding around 10 million years ago raises the sedimentary rock in the area. Due to the long episode of folding one can also notice the overturned fold in the area which exposes the old rock at the top. Our catchment itself is entirely on the east flank of this fold outcropping the flysch formation. The east fold limb is tilted sub-vertically towards the upper part of the catchment (west direction) and sub-horizontally towards the lower part (east direction). This configuration means that the general bed orientation of the sandstone and clay layers of the underlying flysch formation loosely follows the watershed topography. Hence, the catchment's geological characteristics include the clay and silt-rich soil at the top which transits to the highly weathered subsurface and finally leads to the old hard rock at the bottom in the form of flysch.

1.10 Background, scientific questions and objective

This study follows on the previous work of Ilann Bourgeois (Bourgeois et al., 2018b,a),who studied the fate of atmospheric nitrate (NO_3^-) deposited on the subalpine prairies at the Lautaret path. Using the $\Delta^{17}O$ signature, which is unique to atmospheric nitrate, it was possible to track the deposited nitrate in the ecosystem that had not been assimilated yet and quantify how much this unprocessed nitrate represented the nitrate in any part of the ecosystem. Results show that unprocessed atmospheric nitrate can represent up to 29% of the total nitrate at the outflow of the watersheds studied, with higher values when water originates from snowmelt either directly or possibly after a deep subsurface travel. This points out the control by lateral and subsurface flows of the availability of the winter accumulated nitrate for the ecosystem and suggests that the catchment is nitrogen saturated during snowmelt. Using also $\delta^{15}N$ signature of nitrate in aerosol, snow, and water outflow (Fig. 1.12), it was hypothesized that part of the nitrate in the springtime outflow actually came from atmospheric ammonia nitrification within the snowpack, thereby underlining the importance of snow processes for the understanding of the nitrogen cycle in those alpine catchments. Finally, it was also possible to directly trace atmospheric nitrate in the plant's leaves and roots, suggesting direct uptake of nitrate by the leaves in the summer months.

He hypothesized that in such a catchment the Nitrogen cycle is dominantly driven by the snowmelt compared to other parameters. Assuming the high influence of snow deposition and melt in the catchment hydrology a few of these might be explained. For example, the high amount of atmospheric NO_3^- in the stream might result from the residence time of snowmelt in the catchment. The snowmelt intact with NO_3^- may percolate to the subsurface where this NO_3^- could stay longer and away from any biological processes. In the post winter season, Ilann's study also suggests the diurnal changes of the atmospheric NO_3^- in the stream which could only be driven by strong surface and subsurface coupling. In the daytime the streamflow is dominated by direct snowmelt runoff (or rain runoff) however, at night time the percolated snow from the subsurface reappears in the stream through connected channels. Similarly, the plant atmospheric NO_3^- concentration could also explain hydrological fluxes. The plant evapotranspiration components dominate during the summer. If plants sufficiently uptake the old snowmelt they could even uptake the atmospheric NO_3^-

in unaltered form. Though Ilann's work established a good hypothesis through a chemical approach, however, due to a lack of detailed hydrological observation and modeling this could not be verified at the catchment scale. Some of the questions like surface-subsurface connectivity, snowmelt contribution to stream, snowmelt uptake by plant, and residence time of snow in the catchment remains unanswered questions to support the hypothesis.

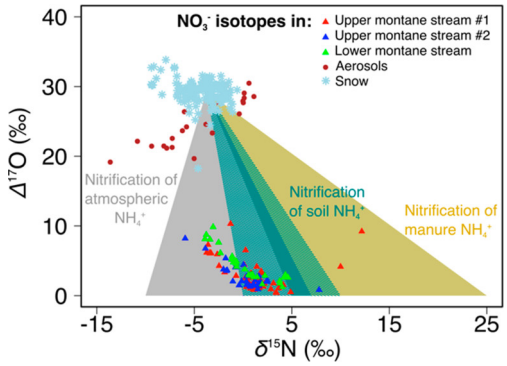

Figure 1.12: Isotope mixing between three sources of NO_3^- in the mountainous catchment (Bourgeois et al., 2018a).

To fulfill the knowledge gap between the previous work and the perspective hypothesis the following scientific questions need to be addressed:

1. How the hydrological fluxes are partitioned between recharge, streamflow and evapotranspiration in a mid-elevation mountainous critical zone catchment at the Lautaret path? What factors do this partitioning depend on? How are impacting snow deposition and snowmelt spatial variability in such a catchment? Does the subsurface variability play an important role in such a kind of catchment?

2. What are the possible flow paths in a mid-elevation mountainous catchment? Which is the most dominant flux in the subsurface? What is the residence time for the rain and snowmelt in the subsurface? What amount of young and old particles are partitioned to the outflow and evapotranspiration? What is the major source of water to streamflow and evapotranspiration? How much old subsurface water is used by plants for their sustainability?

3. What will be the impacts of climate change in mid-elevation subalpine critical zone catchments in terms of water fluxes? How the rain and snow partitioning will be

impacted by climate change? How will the steams be able to sustain the necessary minimum ecological flow in summer despite the reduced snow cover? How water sources partitioning to streamflow and evapotranspiration will change under global warming?

The questions highlighted above need detailed monitoring and modeling methods. The complex topography and scarce observation limit the applicability of most state of the art tools. In this thesis, we will apply the most advanced available methods for a multidimensional study of mountain critical zone catchment. The major objective of this thesis will include:

- the Exploration of the meteorological and topographical control on spatio-temporal distribution of snow, and its impact on hydrological fluxes in a 15ha mid-elevation mountainous catchment at Lautaret Pass.
- the construction of the subsurface hydrological model based on geological and geophysical survey and impacts of more and more detailed subsurface models on runoff generation and evapotranspiration.
- the identification of flow paths and residence times of rain and snowmelt water in the catchment, and their partitioning to streamflow and evapotranspiration in the present and future climates.

From here onwards, the thesis is organised according to the above objectives. **Chapter 2** explains different datasets used in the study for the modeling purpose and validation of results. The same chapter also includes the different types of monitoring in the research site and preprocessing of the datasets. Finally, the meteorological forcing further apply to the model is presented. Extended pre-processing and post-processing of the data till October 2020 are reported in the Appendix I.

Chapter 3 includes the detailed methodology adopted in the study. It details the ParFLOW-CLM model, an integrated physically based coupled hydrological model. The chapter includes the details empirical approaches adopted in the model and its different components including CLM. The same section also mentions the EcoSLIM extension, a Lagrangian particle tracking model, and its functioning with ParFLOW-CLM.

Chapter 4 discusses the first objective of the thesis. The chapter explores the impact of terrain-based distributed meteorology on simulated snow cover and hydrological fluxes for the studied mid elevation mountainous catchment. From a series of ParFlow-CLM simulations with different applied meteorological forcing, the chapter aims at disentangle the impact of some distributed meteorological variables on simulated snow patchiness variability during the springs and on the monthly and yearly water budgets of the catchment.

Chapter 5 discusses the use of geological and geophysical data to build a subsurface model for such a catchment. Then the chapter talks about different conceptual and factual subsurface settings and highlights the improvement in hydrological fluxes due to detailed subsurface inclusion in coupled surface-subsurface hydrological modeling, including vegetation. The chapter also presents a adjusted model for the catchment which will be used for this thesis and further objectives. A few modeling experiences ran for this adjustment are presented in Appendix II to show the sensitivity of the model to various ground characteristic assumptions.

Chapter 6 is more dedicated to the Lagrangian particle modeling in the catchments. The chapter talks about the flow path, residence time, and source partitioning to streamflow and evapotranspiration components. The same chapter also discusses about the shift in the source partitioning and residence time/flow path under global warming.

Chapter 7 presents the synthesis, conclusion, and perspective of the thesis.

2 Data overview

Col du Lautaret is a high mountain pass separating the northern and southern Alps. At an altitude of 2000 meters, the site is mostly grassland that is covered with snow during the cold winter. The area is characterised by its great floristic diversity and is home to more than 200 alpine vegetation across the world. It hosts a botanical garden in its vicinity for preserving the different alpine species carried here from throughout the world. Being at the limit between the northern and southern Alps, the area also sees influence from the Mediterranean climate. The panorama includes a rich geological diversity from crystalline massif to sedimentary rocks and soil. Overall, this area is a perfect site to study the climate, hydrology, ecology, and geology. The site has a typical condition to be recognised as a mountain critical zone research site. To engage the site for scientific developments, the area is dedicated to tourism, research, and science training.

The history of Lautaret garden is associated with the early polar expedition in France. In 1908, Captain Scott and Dr Charcot selected the site for the trial runs of the motorised sled for Antarctica expedition. The site has been later named the Joseph Fourier Alpine Station (Station Alpine Joseph Fourier, SAJF). The SAJF is part of ENVINET, the 'European Network for Arctic-Alpine Multidisciplinary Environmental Research' which has facilitated the creation of a network of Alpine and Arctic stations within the framework of the 5th program of the European Union (1999-2003). In addition, an eco-climate station has been set up next to the Alpine Garden to measure meteorological variables such as temperature, air, and soil humidity, light intensities, direct and reflected, wind speed, and the depth of the snow. Most of the monitoring on the site has started in 2012. It includes the temperature and humidity (CS215, Campbell Sc.), atmospheric pressure (Setra CS100, Campbell Sc.), wind speed and wind direction (Vector anemometer A100LK and W200P, Campbell Sc.), 4 components of net radiation (CNR4, Kipp and Zonen), snow height (SR50A, Campbell Sc.), and NDVI (Normalised Difference Vegetation Index) measured through Skye Instruments SKR1800. Since 2015, the site received eddy covariance sensors composed of the LI-COR LI-7200 closed-path gas analyser and the HS50 Gill 3D sonic anemometer. In 2017 an OTT Pluvio rain gauge was installed at the Flux'Alp weather station. Discharge measurement in the site has started very recently since 2020 and the site still building the quality-controlled

discharge data. Site setup, monitoring, and data processing follow the ICOS[3] standards, and the site has entered this program since 2020.

Data presented here could be divided either according to the type of data (meteorological, geospatial, and climate reanalysis data), or to the use they had in this study (model description, model forcing, or model evaluation). They are presented here according to type, but their use will be specified in each of the following subsections. Shortly, meteorological data majorly come from the automatic weather station and flux tower. Geospatial data either come from in-situ radar and lidar surveys or from satellite images. Climate reanalysis datasets are regional climate model analyses. The site has also been chosen to run the surface-subsurface coupled hydrological model hence a comprehensive forcing dataset for the recent four years (2017-2021) will also be presented

2.1 Geospatial data

Geospatial data are the data that is available at a spatially distributed scale. These kinds of data are important to model the cathment and validate the results from the model. Geospatial data collection techniques in the catchment include the LiDAR survey (laser scan), and satellite data. These data are meant for preparing the Digital Elevation Model (DEM), snow height coefficient, land cover maps, and snow cover maps in the catchment.

2.1.1 DEM

DEM in the catchment is available from the aerial Lidar survey conducted during summer 2012, generating a digital surface model (DSM) with an initial resolution of 0.5 meters $\times$ 0.5 meters horizontal resolution and a 0.1 m vertical one. To produce the DEM from the DSM, first, the tree groves in the watershed have been masked and then the terrain was gapfilled applying the nearest neighbour algorithm, and the resulting DEM upscaled to 10 meters resolution using the minimum of each cell. (Fig. 2.1). This DEM has been used for various purposes including the determination of the snow depth from snow maps, slope processing, creating the terrain following mesh of the model, and defining the actual depth from the surface.

[3]https://www.icos-ri.eu/

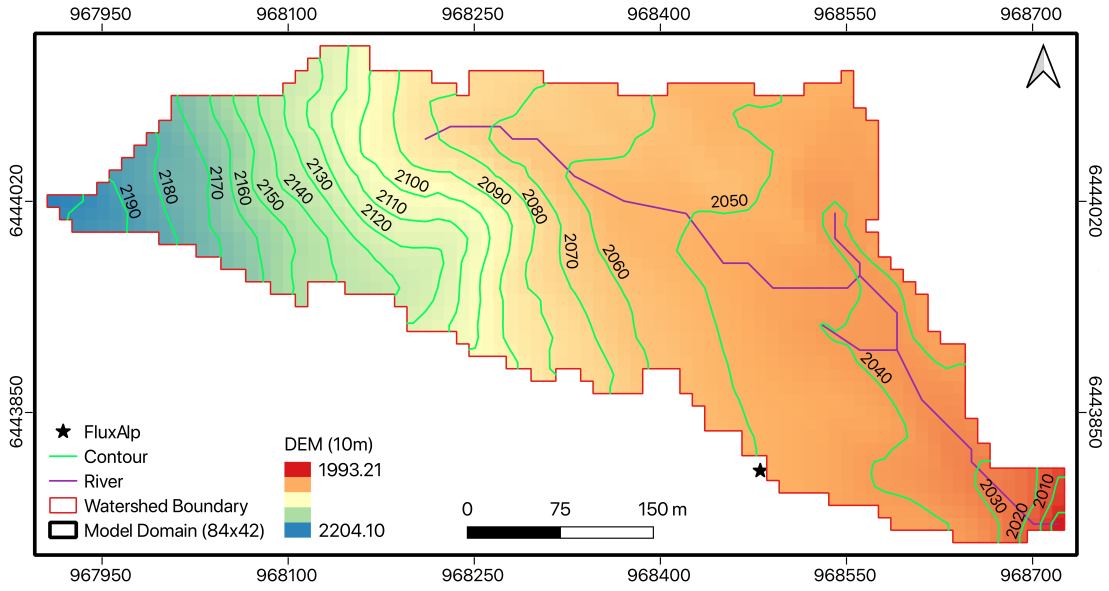

Figure 2.1: Digitial elevation model (DEM) cropped along the catchment boundary (10 meters), DEM is overlain by contour maps and river network in the catchment

2.1.2 Land cover map and Mannings coefficient map

The land cover map of the catchment results from field observations (Fig. 2.2). The catchment is mostly fescue grassland (*Fescuta paniculata*) with *vaccinium* shrubs in the slopes and a 5 % tree cover. These trees include larches (*Larix*), alders (*alnus*) and some rowan trees (*sorbus aucuparia)*. The Manning coefficients in the catchment are assigned using the land cover map. The tree-covered area and river network has been assigned the value 0.05 $m^{1/3}$ s^{-1}, and the rest of the catchment has been assigned the value 0.03 $m^{1/3}$ s^{-1} (Arcement, 1989). This map is part of the initial model description and is used throughout this study.

2.1.3 Soil depth maps

Soil depth and soil structure maps are necessary to describe PARFLOW's simulation domain. In order to investigate those, various geophysical methods were used during a survey led by Romain Noulette in June 2018. This included a combination of Electromagnetic spatial survey, Electrical Resistivity Tomography (ERT), and Ground Penetrating Radar (GPR) transects. The Electromagnetic survey (CMD Explorer, 10000Hz) realised on 96 points in the entire catchment provided maps of apparent soil conductivity integrated over three depths (1m, 2.1m, 3.4m), where apparent conductivity is directly related to several parameters of interest: porosity, saturation degree, conductivity of the groundwater and clay

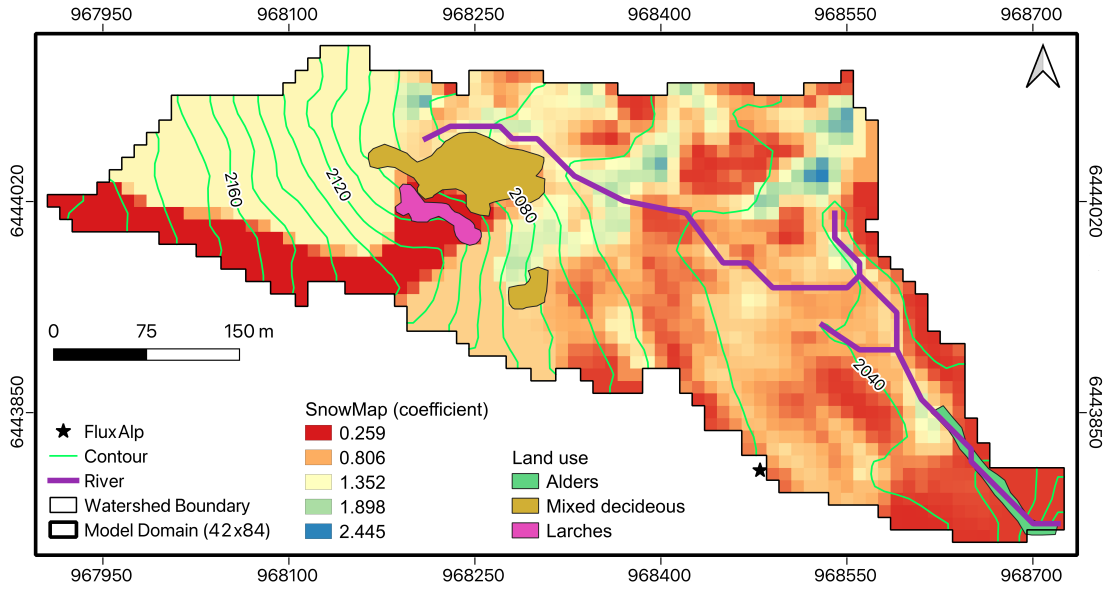

Figure 2.2: Snow depth map on 27 March 2018 cropped along the catchment boundary (10 meters). The snow map coefficient is the relative snow depth compared to snow depth measured at Flux'Alp meteorological station on the same day. The woody cover in the catchment is shown as an opaque mask and the rest of the catchment is dominated by grass.

content providing a calibration with known soils (mcneill electromagnetic 1980). One ERT transect, consisting of 96 2m spaced electrodes along a profile across the lower area of the catchment provided after inversion of the raw data a pseudo-cross-section of apparent resistivity, which was used to calibrate the Electromagnetic survey data. Three GPR profiles, run at different frequencies (250, 500, and 800 MHz) to ensure different penetrations were used to further constrain the interpretations made in the ERT and EM inversions. All this is further developed in chapter 5. The soil depth derived from these different geophysical surveys is shown in figure 2.3. Hydrological conductive soil is not too deep in the catchment however, the intermediate hydraulic conductivity layer goes more than 6 m deep.

2.1.4 Snow height map

A representative snow depth map is used to account for wind-driven snow redistribution (see Chapter 4). This snow map has been obtained by the difference between two Digital Surface Models, with and without snow. The former results from a terrestrial laser scan (TLS) survey conducted on March 27, 2018 (Fig. 2.2). The latter has just been described in the previous sub-section. . This map is available at the resolution of 1 meter $\times$ 1 meter (Revuelto, 2020), and has been upscaled to 10 meters resolution. As the laser scan could

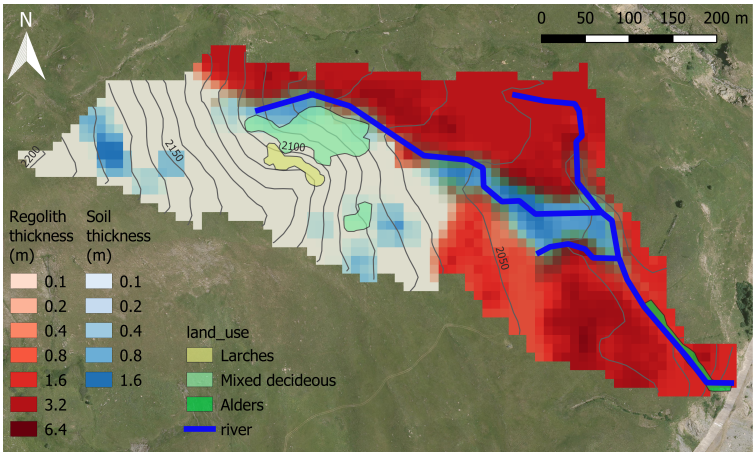

Figure 2.3: Soil and regolith depths derived in the catchment from different geophysical and field surveys.

not reach the upper part of the catchment, the snow depth in this area was given a constant value based on field knowledge.

2.1.5 Snow extent maps

Eight high-resolution images from the Sentinel-2A and Sentinel-2B products from Sentinel-2 mission developed by European Space Agency (ESA) (Drusch et al. (2012); Table 2.1) are used to inform the temporal and spatial variation of snow in the catchment. These images cover different accumulation and melting dates in two different hydrological years (Fig. 2.4). To represent the snow and non-snow pixels from sentinel images we have calculated the normalised snow difference index (NDSI) (Dozier, 1989).

$$NDSI = \frac{Green(band3) - SWIR(band11)}{Green(band3) + SWIR(band11)}, \tag{1}$$

where, 'Green' and 'SWIR' are the corresponding bands in the green and shortwave infrared regions of the satellite, respectively. The green band is represented by 'band 3' and the SWIR band is represented by 'band 11' in Sentinel-2 product. Sentinel 'band 3' was available at 10 m resolution while 'band 11' was at 20 m resolution. NDSI calculation was carried out by resampling 'band 11' at 10 m resolution (Hofmeister et al., 2022). The Sentinel-2 snow pixels were selected with NDSI > 0.4 (Riggs et al., 1994).

	Satellite platform	Date of acquisition	Resolution (m)	Cloud cover (%)	Cloud cover over catchment (%)
1	Sentinel 2B	2017-11-21	10	1.2	None
2	Sentinel 2A	2017-12-06	10	3.3	None
3	Sentinel 2A	2018-05-25	10	12.8	None
4	Sentinel 2B	2018-06-19	10	2.1	None
5	Sentinel 2A	2019-12-06	10	8.6	None
6	Sentinel 2B	2020-02-09	10	5.3	None
7	Sentinel 2A	2020-04-14	10	7.7	None
8	Sentinel 2A	2020-05-04	10	2.2	None

Table 2.1: Images characteristics from ESA's Sentinel-2 mission.

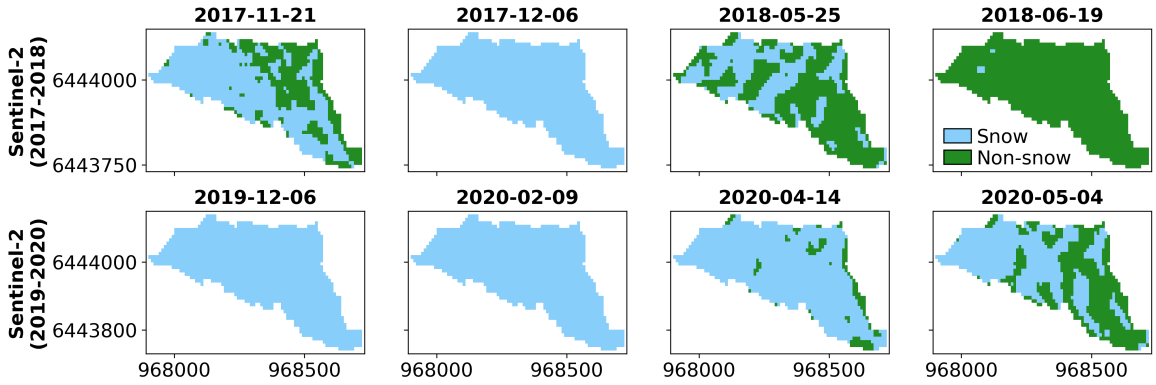

Figure 2.4: Sentinel satellite images acquired at different periods over catchment mask. Snow and non-snow pixels are represented from the NDSI calculation.

2.2 Meteorological data

2.2.1 Primary data

Primary data are the meteorological data directly measured from the weather station. At Col to Lautaret we have a long list of variables which includes the variable from the meteorological station and various in-situ sensors. The list of variables and their years of operation is shown in figure 2.5.

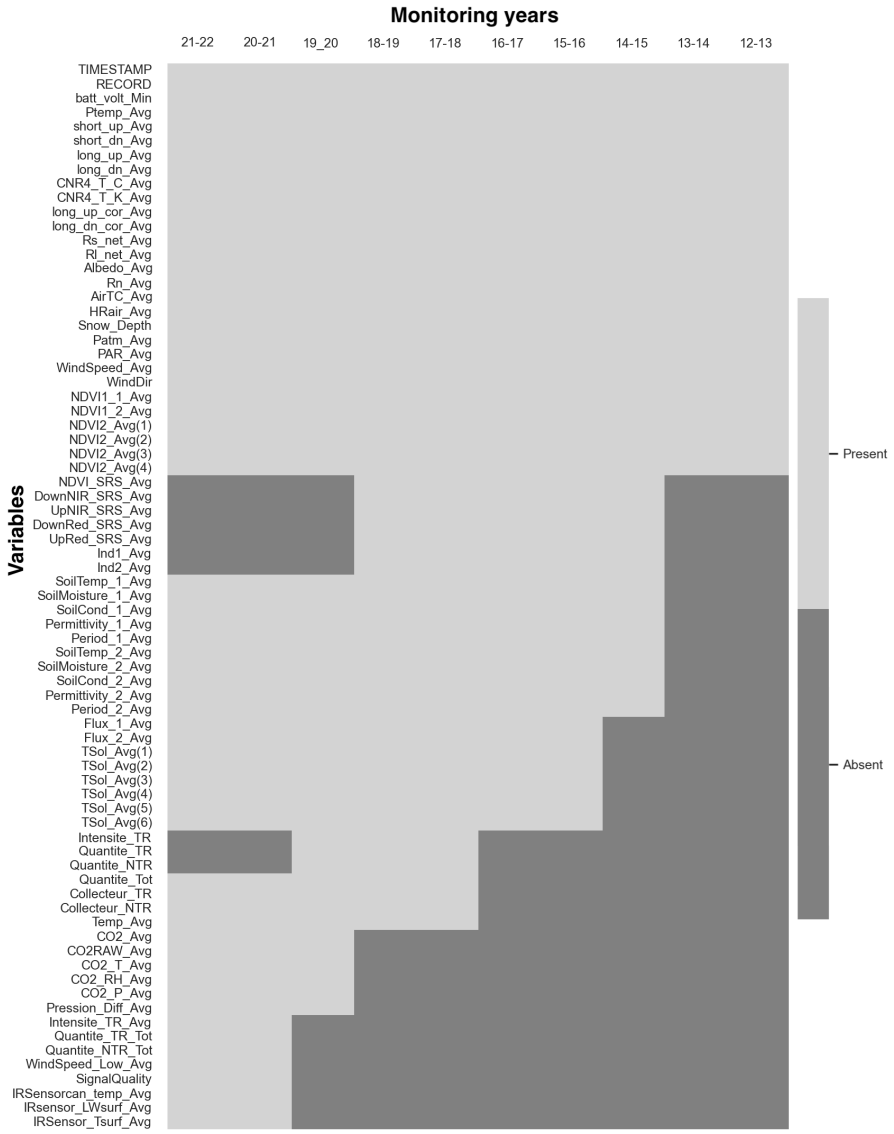

Figure 2.5: List of monitored variables and their operational years at Col du Lautaret

Precipitation

Precipitation monitoring in the catchment started in 2017 with an OTT Pluvio rain gauge. The variables measured from the rain gauge include real-time rainfall intensity (Intensite_TR), real-time accumulated quantity since the last measurement (Quantite_TR), non-real-time accumulated quantity since the last measurement (Quantite_NTR), total accumulated bucket volume (Quantite_Tot), real-time bucket volume (Collecteur_TR) and non-real-time bucket volume (Collecteur_NTR). The real-time data is recorded every 1 minute while the non-real-time data is accumulated over a period of 5 minutes. The precipitation quantity was determined using the 'Quantite_Tot' parameter at the resolution of 30 minutes (Fig.

2.6). The error and gaps were not filled in the raw data set. These gaps at the temporal time scale are very small and will be discussed under the section 'four years of meteorological observation'.

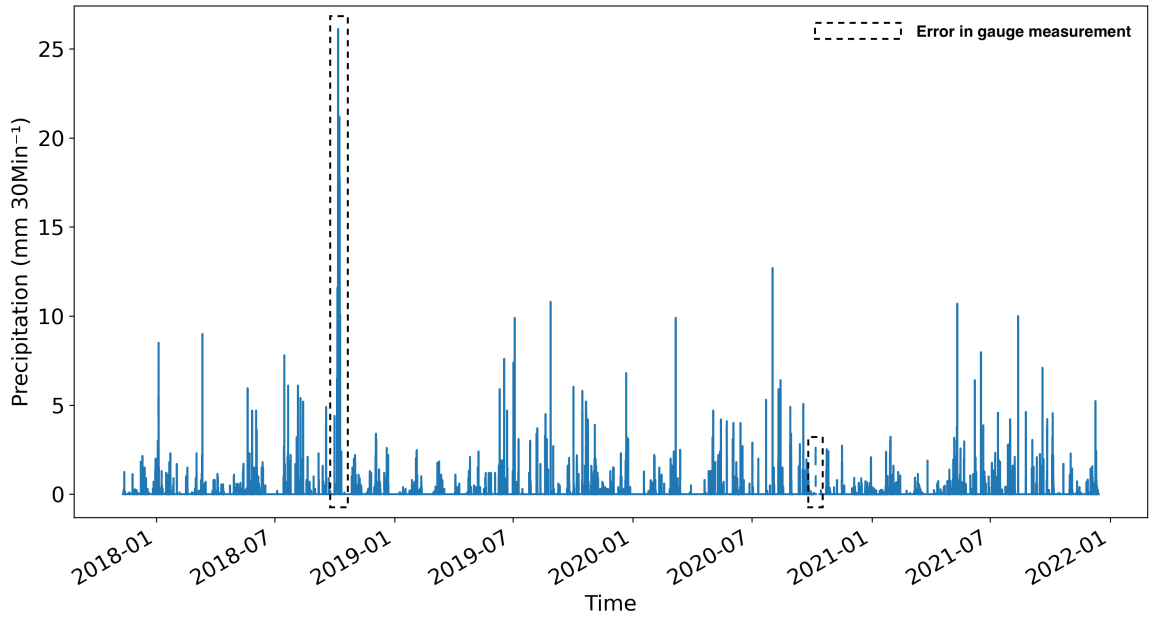

Figure 2.6: Precipitation in the catchment derived from 'Quantite_Tot'

The rain gauge does not have a wind shield since its installation. The wind shield in the rain gauge is installed on 04 May 2021, hence, the precipitation data from the rain gauge has been processed to account for the lack of gauge shield (KLOK et al., 2001). The adopted algorithm follows as:

$$P_{corr}(x_0, y_0) = P(x_0, y_0) * (a + b * u(x_0, y_0)), \tag{2}$$

where, P_{corr} is the corrected precipitation (mm), P is measured precipitation (mm) at observation station, u is the wind speed at observation station in m s^{-1}, a and b are correction factors, and are different for rain ($a = 1.04$, $b = 0.04$) and snow ($a = 1.18$, $b = 0.20$) (Sevruk and WMO, 1986).

Temperature and NDVI

Temperature is measured from the CS215, Campbell Scientific in Kelvin, and the Normalised Difference Vegetation Index (NDVI) is measured from Skye Instruments SKR1800, Campbell Scientific. Temperature and NDVI variation in the catchment is shown in figure 2.7. The

NDVI sensor in the summer gives the vegetation cycle and which is separately used to produce secondary vegetation dataset. The different parameters derived from NDVI and the snow depth sensor will be discussed in the next subsection.

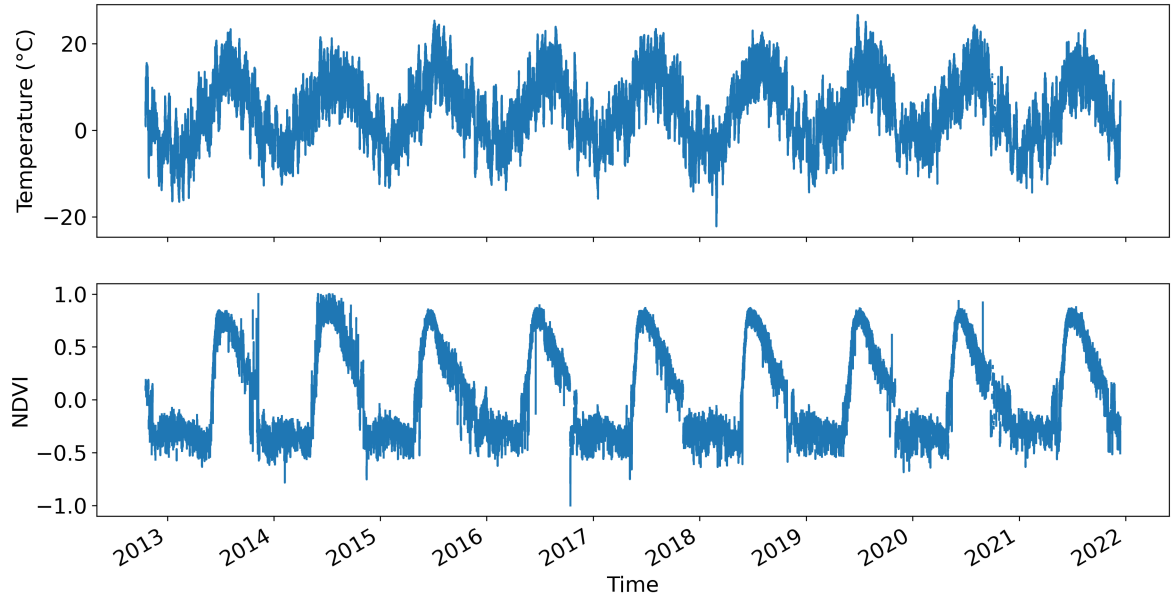

Figure 2.7: Temperature and NDVI data from the catchment.

Evapotranspiration

Evapotranspiration data is measured through the flux tower installed next to the meteo tower at Col du Lautaret. The eddy covariance sensors include the LI-COR LI-7200 close-path gas analyser and the HS50 Gill 3D sonic anemometer. The instrument measures the evapotranspiration flux in W m^{-2}, the daily evapotranspiration cycle from the measurement is shown in figure 2.8. The peak evapotranspiration in the catchment occurs around 12 O'clock in the noon and late evening shows the condensation in the catchment.

2.2.2 Secondary data

Secondary data in the catchemnt includes the vegetation parameters derived from the NDVI and snow depth data. These vegetation parameters include leaf area index (LAI), stem area index (SAI), roughness length (z0) and zero plane displacement (d). First, the vegetation cycle is determined using the NDVI cycle. In order to estimate vegetation height in the catchment, we use the summer values of the snow height sensor. The signal is noisy, with

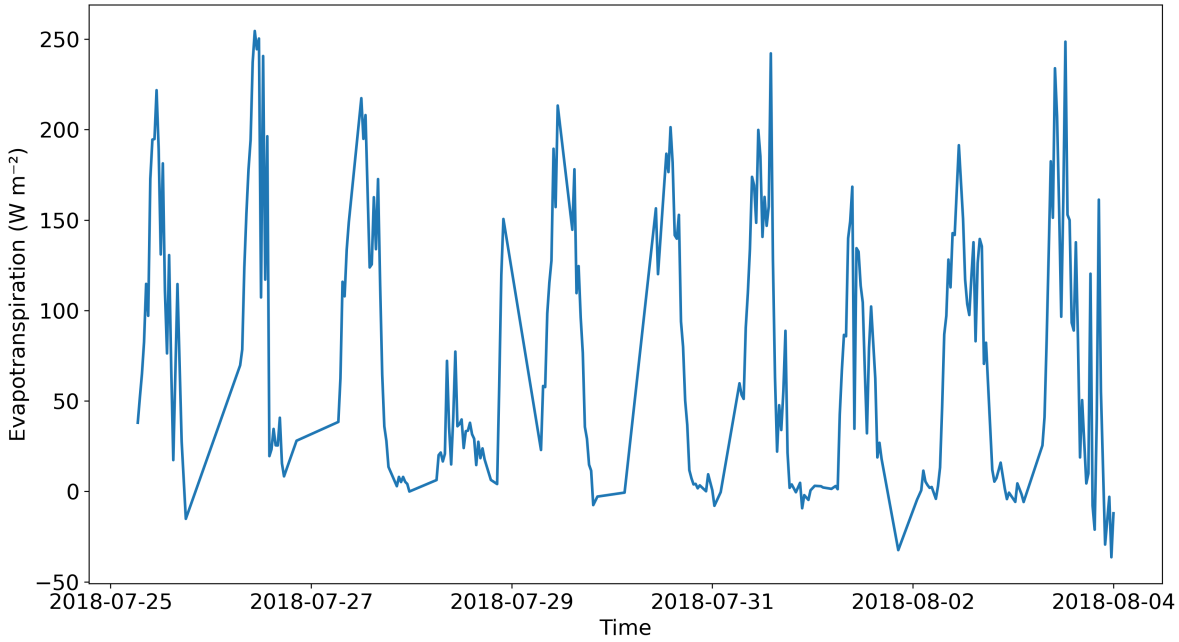

Figure 2.8: Evapotranspiration cycle for 10 days in summer.

multiple in-canopy echoes, and we assume that the highest decile of daily values is representative of the vegetation height on that day. The summer vegetation growth cycle is obtained by interpolating between these well-identified stages. Then LAI is determined from NDVI data using the field measurement while the z0 and d are determined from vegetation height data (Brutsaert (1975); Fig. 2.9).

$$LAI = \frac{0.61 * NDVI}{1.04 - NDVI}, \tag{3}$$

this relationship is developed using the latin hypercube sampling of the parameter space using the field and NDVI sensor data.

$$z0 = \frac{h}{3e}, d = \frac{2}{3}h, \tag{4}$$

where z0 is the roughness length, d is zero plane displacement, h is the vegetation height and e is equal to 2.718.

2.2.3 Four years of meteorological observation

The catchment has the precipitation gauge since 2017. Hence, to run the hydrological model in the catchment the four years of continuous dataset is prepared (Fig. 2.10). The precipita-

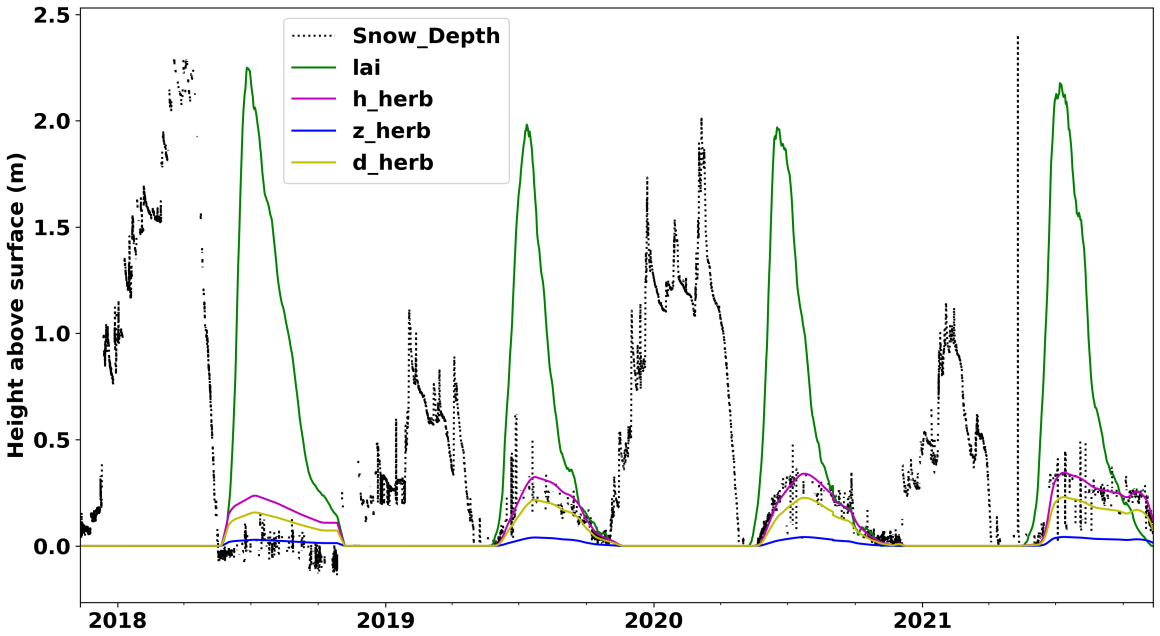

Figure 2.9: Vegetation height (grass) derived from the snow depth data in summer (h_herb). LAI is a function of NDVI measurement. Roughness length (z_herb) and zero plane displacement (d_herb) are functions of vegetation height.

tion in 2017-18 has a missing period of 4 days which was filled from nearby Puy-Saint-Pierre station. The one day gap in September, 2019 is filled with the September mean of that month. Other than these data gaps, the rest of the data gaps were small (1 hour to 2 hour) which were filled using a linear interpolation. The error in 'Quantite_Tot' is cross checked with 'Collecteur_NTR' quantity. These two quantities follow each other and error in any kind of measurement can be cross validated. However, to derive precipitation only 'Quantite_Tot' has been used. The small data gaps in other quantities are also filled with linear interpolation.

The various preprocessing code of the dataset is available under a git repository[4]. The data and code has been not published yet and will be publicly made available after registering DOI.

2.3 Climate reanalysis data

The regional climate reanalysis datasets used in this study belong to ADAMONT CNRM-ALADIN53. ADAMONT is the downscaling method used in the EUROCORDEX project to

[4]https://gricad-gitlab.univ-grenoble-alpes.fr/voisind/fluxalp_data

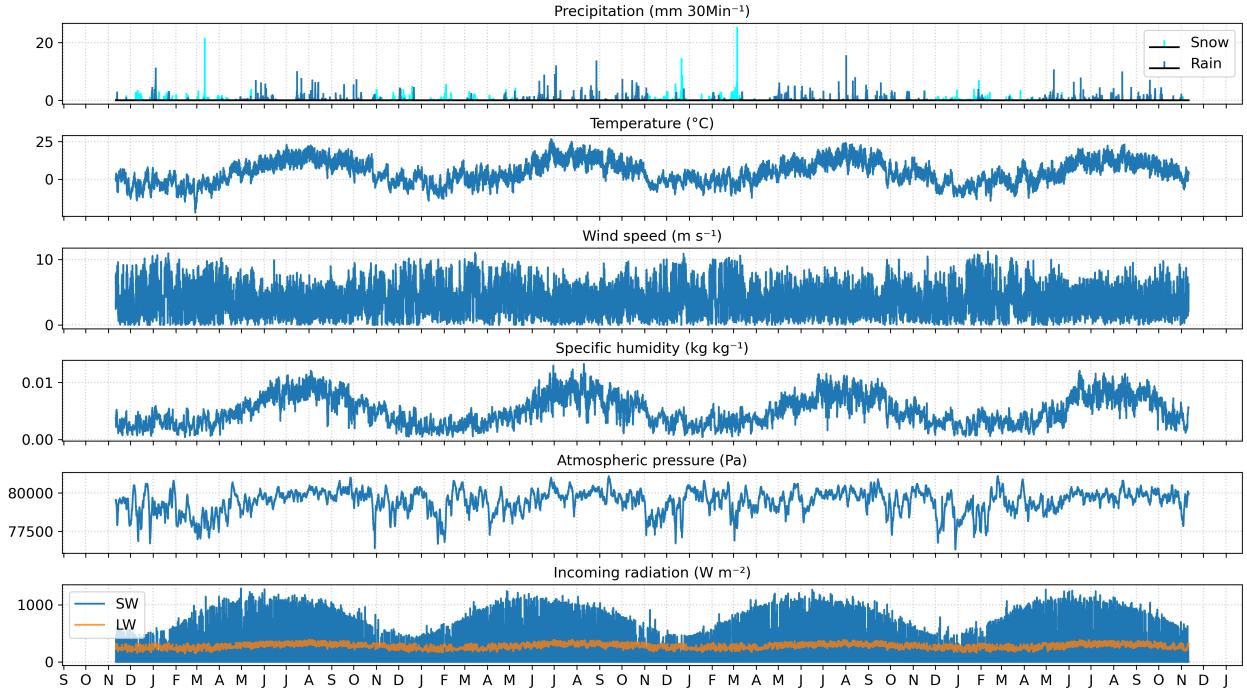

Figure 2.10: Meteorological forcing data for the hydrological model. The hydrological years starts on 11 November 2017 and ends on 10 November 2021.

downscale the regional climate models using quantile-quantile approach (Morin et al., 2021). ALADIN has been used at the CNRM (Centre National de Recherches Météorologiques) as a Regional Climate Model under the name CNRM-ALADIN. These data are forced with SAFRAN (regional-scale meteorological downscaling and surface analysis system) which is a regional climate product for French mountains. The data from SAFRAN is available at hourly temporal resolution for temperature, rain fraction, snow fraction, specific humidity, wind speed, shortwave radiation and longwave radiation. These reanalysis dataset have been acquired for 3 climate scenarios viz. historical (1951-2004), RCPs 4.5 (2021-2099) and RCPs 8.5 (2021-2099) (Fig. 2.11). The datasets are available at each massif scale and has been acquired as presented in Table 2.2. These are used in chapter 6 to explore hydrological behaviour of the catchment under different climate hypothesis

Points RCM	Massif	SAFRAN	LAT	LON	ZS
103	13	Thabor	45.02	6.592	2100

Table 2.2: Grid details of the ADAMONT data extracted for the catchment.

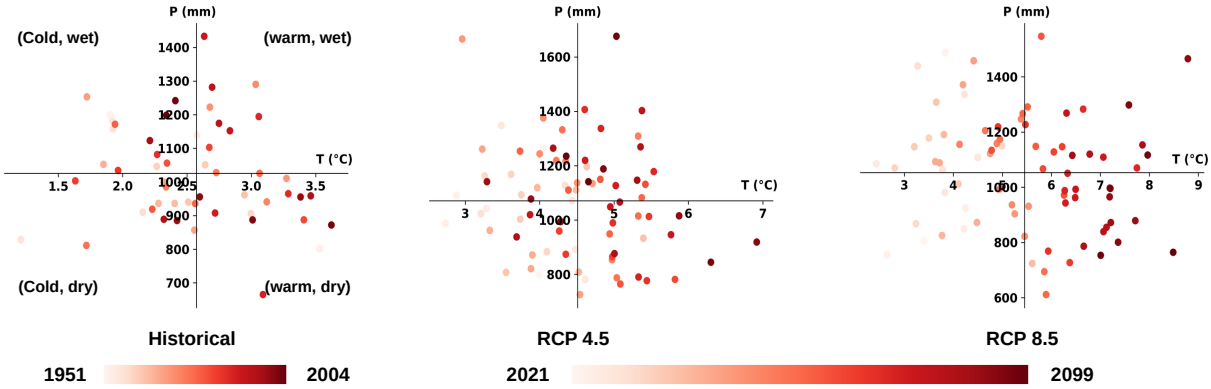

Figure 2.11: Yearly average of temperature and precipitation data for ADAMONT CNRM-ALADIN53 divided into three climate scenarios. Data has been organised into 4 climate regime viz. (cold, wet), (cold, dry), (warm, wet), (warm, dry).

2.4 Discharge data

Discharge data measurement in the catchment started 2020. River runoff ends in an artificial circular concrete pipe. The relationship between the height and flow in pipe was established by 4th degree polynomial using the HEC-RAS hydraulic modeling tool. The site has very few discharge measurement using the salt tracer method. The rating curve for the catchment has been developed with the limited observation (Table 2.3). The fourth degree polynomial fit to develop the rating curve is represented as,

$$-1.0762 * x^4 + 3.6351 * x^3 - 0.8763 * x^2 + 0.0885 * x - 0.0020. \quad (5)$$

Date	Height	Error	Flow ($m^3 s^{-1}$)
14/05/20 15:00	0.26	0.01	0.043
	0.26	0.01	0.038
	0.26	0.01	0.041
10/06/20 13:33	0.166	0.01	0.0068
10/06/20 16:52	0.16	0.01	0.0039
10/06/20 17:12	0.162	0.01	0.0045
25/06/20 17:12	0.11	0.01	0.0021
25/06/20 17:12	0.11	0.01	0.0024
21/09/20 16:40	0.054	0.01	0.00052
21/09/20 16:45	0.056	0.01	0.0005
21/09/20 16:52	0.056	0.01	0.00051
31/03/21 13:15	0.2	0.01	NA
31/03/21 13:34	0.2	0.01	NA
07/04/21 00:00	0.225	0.01	0.012
07/04/21 00:00	0.225	0.01	0.013
05/05/21 08:39	0.225	0.01	0.019
05/05/21 13:28	0.255	0.01	0.020
11/05/21 13:06	0.33	0.01	0.029
07/05/21 09:19	0.262	0.01	0.035

Table 2.3: Salt tracer experiment in the catchment.

3 Methods

The methods for this study revolve around the hydrological modeling of coupled processes and the Lagrangian transport modeling of the flow path and residence time in the subsurface. The hydrological modeling part is achieved with the ParFlow-CLM model and the Lagrangian transport modeling is achieved using EcoSLIM. EcoSLIM relies on the velocity output of ParFlow-CLM to model the trajectories of water through the subsurface. The description of these models will be discussed in the subsequent sections.

3.1 ParFlow-CLM

Interaction between the different processes at the earth's surface lead to the development of integrated hydrological models (IHM). ParFlow-CLM is also a kind of fully distributed surface-subsurface coupled hydrological model. ParFlow-CLM has the capability to model all the physical processes in complex mountainous catchments hence, has been adopted for this study (Jones and Woodward, 2001; Ashby and Falgout, 1996; Kollet and Maxwell, 2006; Maxwell, 2013; Kollet and Maxwell, 2008). The model simulates the surface and subsurface processes from deep subsurface to the top of the canopy (Kuffour et al., 2020). We will develop an understanding of the core functionality of ParFLOW-CLM in the following paragraphs.

3.1.1 Saturated groundwater flow (Darcy's flow)

The saturated groundwater flow is used to solve many of the groundwater problems. Water in aquifers flows through porous media which flows following the hydraulic gradient. With the steady state approximation, the Darcy flow $\vec{q_{sat}}$ in the 3 space directions in saturated media is governed by Darcy's law :

$$\vec{q} = -\bar{\bar{K}}\vec{\nabla}H(x, y, z), \tag{3.1}$$

where $\bar{\bar{K}}$ is hydraulic permeability tensor at saturation $[LT^{-1}]$ which reduces to a constant K diagonal tensor for isotropic media and $H = h - z$ is hydraulic head-potential $[L]$ with h the water pressure $[L]$, ρ the water density, g the gravity and z the vertical coordinate.

Most of the saturated subsurface flows follow this law. However, this equation is not valid when the pores are not completely saturated.

3.1.2 Unsaturated groundwater flow (Richards' equation)

The flow in unsaturated media is represented by Richards' equation derived from the continuity equation expressed as :

$$\frac{\partial(\rho\phi S_W(h))}{\partial t} = \rho.\vec{\nabla}.\vec{q} + Q_s(x,y,z), \tag{3.2}$$

where the left-hand side is the water storage variation in the media with ϕ the porosity and $S(h)$ [.] the water saturation at water load h $[m]$, $\vec{\nabla}.\vec{q}$ is Darcy's flux divergence in the 3 direction of space and Q_s $[kg/m^3 s]$ is the source/sink term as a function of space.

In ParFlow the mixed form of the flow equation is implemented to solve the flow in variably saturated media. It derives from the preceding equation including the extended Darcy's law to the unsaturated zone. The mixed form of Richard's equations is implemented in Parflow as:

$$S_S \frac{\partial S_W(h)}{\partial h}\frac{\partial h}{\partial t} + \phi\frac{\partial(S_W(h))}{\partial t} = \vec{\nabla}.\vec{q} + q_s, \tag{3.3}$$

$$\vec{q} = -k_s k_r(h)\bar{\bar{K}}_{Rel}\vec{\nabla}(h-z), \tag{3.4}$$

where $S_S = s_{sat}.\phi$ is the relative specific storage [.] with s_{sat} the relative water content at saturation [.], S_W [.] is the saturation as function of water load $[L]$,

q is Darcy flux $[LT^{-1}]$, q_s is the source/sink term $[T^{-1}]$, k_s is the saturated hydraulic conductivity $[LT^{-1}]$, k_r [.] is the relative permeability as a function of water load $[L]$, $\bar{\bar{K}}_{Rel}$ is the 3D relative permeability to acccount for anisotropy and z is the depth below the surface $[L]$. In Parflow all terms in the equations are scaled by the permeability units which means that giving a k_s in $[m/h]$ will turn L in $[m]$ and $[T]$ in $[h]$

3.1.3 Overland flow

ParFlow simulates the fully-coupled surface and subsurface flow through the overland boundary conditions. Earlier the model used to be coupled to river routing schemes which made it difficult to represent the physical process in real time. The advancement in the numerical solver lead to the one-to-one coupling of surface and subsurface processes in real time. The shallow overland flow in ParFlow is represented through kinematic wave approximation of shallow water equations. In ParFlow the two-dimensional shallow overland flow is represented as:

$$\frac{\partial \psi_s}{\partial t} = \nabla(\upsilon \psi_s) + q_s, \tag{3.5}$$

where ψ_s is the surface ponding depth $[L]$, t is time $[T]$, υ is the depth-averaged velocity vector $[LT^{-1}]$ and q_s is the general source-sink term. Exclusion of dynamic and diffusive term from the equation gives the momentum equation as:

$$S_{f,i} = S_{o,i}, \tag{3.6}$$

this equation is known as the kinematic wave approximation which hypothesizes that the flowing water level is parallel to the river bed . S_f and S_o represent the friction and topography slopes, respectively and i represents the x and y direction in two dimension. The discharge related to the flow depth as:

$$\upsilon_x = -\frac{\sqrt{S_{f,x}}}{n}\psi_s^{2/3}, \text{ and} \tag{3.7}$$

$$\upsilon_y = -\frac{\sqrt{S_{f,y}}}{n}\psi_s^{2/3}, \tag{3.8}$$

where n is the Manning roughness coefficient $[L^{-1/3}T]$. The overland flow routes horizontally in x or y direction. The direction of overland flow is defined from the D4 flow-routing approach, in which the water flows in either of the four horizontal directions. The direction towards the adjacent cell is determined according to the steepest slope. In ParFlow this overland flow equation is directly coupled to the Richards' equation which means they are solved simultaneously to simulate surface-subsurface transfers. Subsurface to river fluxes can

be either positive or negative according to infiltration capacity and pressure field.

3.1.4 Computational grid (Terrain following grid)

The computational grid in ParFlow is represented by two different grid systems, one is an orthogonal grid and another is a terrain-following grid. Though an orthogonal grid is simple and fast, in complex terrain it leads to many inactive grid cells (above the ground surface). ParFlow terrain-following grid includes the topography in its computational grid architecture. This adaptation transforms Darcy's flow as:

$$q_x = Ksin\Big(\theta_x\Big) + K\frac{\partial p}{\partial x}cos\Big(\theta_x\Big), \text{and} \tag{3.9}$$

$$q_y = Ksin\Big(\theta_y\Big) + K\frac{\partial p}{\partial x}cos\Big(\theta_y\Big), \tag{3.10}$$

where q is the source-sink term in x and y directions, p is the pressure head $[L]$, K is the saturated hydraulic conductivity tensor $[LT^{-1}]$ and θ is the local angle of the topographic slope. The θ_x and θ_y is presented as $\theta_x = \tan^{-1} S_{o,x}$ and $\theta_y = \tan^{-1} S_{o,y}$. This assigns the slope in overland flow as the topographic slope to ease the boundary condition. Terrain following grid matches with the overland flow slope which helps for the flow simulations where the groundwater flow follows the topographic slope.

3.1.5 Subsurface-surface coupling (Common Land Model)

The coupling between ParFlow and other surface models is used to better understand the physical processes at the surface-subsurface boundary or at the surface-atmosphere boundary. ParFlow is unable to account for the surface processes like evapotranspiration or snow dynamics which are usually better accounted for by land surface models. In ParFlow, the coupling with the land surface model solves the purpose of representing the surface processes. This coupling could be achieved either as "offline" where the second model is separately run after generating the output from the first model or as "online" where both models exchange the feedback mechanism in spatial and temporal scales.

The Common Land Model (CLM) is a land surface model designed to simulate mass and energy balance at the surface in ParFlow (Dai et al., 2003). CLM model simulates

the mass, energy, and momentum balance between surface and atmosphere. It includes various parameterization to simulate the radiation budget from radiative characteristics of both the surface and the vegetation), thermal transfers including sensible heat, flux from land characteristics (land cover, soil texture, soil color and thermal properties of soil), water transfers through the vegetation (latent heat flux) from vegetation characteristics (leaf area index, stem area index, zero-plane displacement, roughness length, and root density profile), and the snow dynamic i.e. snow melt, snow depth, and albedo aging). CLM 3.5 is coupled with ParFlow in a modified version. The main one is that it only accounts for one land cover type per pixel. Also, the modified version doesn't simulate the water transfers as ParFlow is calculating them. CLM first solves the surface radiative and energy balance of all the surface and canopy balance to calculate the evapotranspiration flux. This water demand is then prescribed as a sink for Richard's equation. ParFlow thereafter takes care of all subsurface processes and transfers the soil moisture and pressure head to CLM. ParFlow coupled with CLM simulates the subsurface, surface, and canopy processes.

The mass and energy balance at surface in CLM is defined as (Kollet and Maxwell, 2008):

$$R_n(S_m) = H(S_m) + LE(S_m) + G(S_m), \tag{3.11}$$

where R_n is the net radiation $[Wm^{-2}]$, H is the sensible heat $[Wm^{-2}]$, LE is the latent heat $[Wm^{-2}]$, G is the ground heat flux $[Wm^{-2}]$ and S_m is the soil moisture $[kgkg^{-1}]$. All energy exchanges at the surface are the function of the water content of the soil. H is the sum of latent heat flux from vegetation (H_c) and from ground (H_g),

$$H = H_c + H_g, \tag{3.12}$$

$$H_c = \sigma_f L_{SAI} \rho_a c_p r_b (T_c - T_{af}), \tag{3.13}$$

$$H_g = \sigma_f \rho_a c_p C_{soilc} u_{af} (T_g - T_{af}), \tag{3.14}$$

where σ_f is the vagetation fraction [.], L_{SAI} is the stem plus leaf area index $[m^2m^{-2}]$, ρ_a is the intrinsic density of air $[kgm^{-3}]$, c_p is the specific heat of dry air $[Jkg^{-1}K^{-2}]$, r_b is the leaf boundary resistance $[sm^{-1}]$, C_{soilc} transfer coefficient between the canopy air and

underlying ground, u_{af} is the magnitude of wind velocity incident on the leaves [.], T_c is the leaf temperature $[K]$, T_g is the ground surface temperature $[K]$ and T_{af} is the air temperature in canopy space $[K]$.

In CLM, $LE = L_v E$ where L_v is the latent heat of evaporation $[Jkg^{-1}]$ and E is the sum of the evaporation from vegetation, E_c $[kgm^{-2}s^{-1}]$ and from the ground, E_g $[kgm^{-2}s^{-1}]$,

$$E = E_c + E_g, \tag{3.15}$$

$$E_g = \rho_a \frac{q_g - q_a}{r_d}, \tag{3.16}$$

where ρ_a is the intrinsic density of air $[kgm^{-3}]$, q_g is the specific humidity of air at the ground surface $[kgkg^{-1}]$, q_a is the specific humidity of air at reference height z_q obtained from atmospheric forcing $[kgkg^{-1}]$ and r_d is the aerodynamic resistance of evaporation between the atmosphere at z_q $[sm^{-1}]$.

E_c is the sum of evaporation from wet foliage E_w $[kgm^{-2}s^{-1}]$ and transpiration E_{tr} $[kgm^{-2}s^{-1}]$,

$$E_c = E_w + E_{tr}, \tag{3.17}$$

$$E_{tr} = \sigma_f L_{SAI} \delta \left(E_f^{pot}\right) L_d \frac{r_b}{r_b + r_s}, \tag{3.18}$$

$$E_w = \sigma_f L_{SAI} \left[1 - \delta \left(E_f^{pot}\right) (1 - \tilde{L}_w\right] E_f^{pot}, \tag{3.19}$$

where σ_f is the vegetation fraction [.], L_{SAI} is the stem plus leaf area index [.], δ is the step function (one for positive and zero for zero and negative arguments), E_f^{pot} is the potential evaporation from wet foliage $[kgm^{-2}s^{-1}]$, L_d is the dry fraction of foliage surface [.], r_b is the conductance of heat and vapour flux from leaves $[s^{m-1}]$; r_s is the stomatal resistance $[s^{m-1}]$, and $\tilde{L}_w$ is the wetted fraction of the canopy [.].

The ground heat flux, G, is obtained from the one-dimensional transient heat conduction equation,

$$G = \lambda \Delta T, \tag{3.20}$$

where λ is the soil thermal conductivity $[Wm^{-1}K^{-1}]$; and T is temperature in the subsurface $[K]$.

The net radiation, R_n, is expressed as follows,

$$R_n = S_{n,c} + S_{n,g} + L_a^{\downarrow} - L^{\uparrow}, \tag{3.21}$$

where $S_{n,c}$ is the solar radiation absorbed by vegetation $[Wm^{-2}]$, $S_{n,g}$ is the solar radiation adsorbed by the ground $[Wm^{-2}]$, $L_a^{\downarrow}$ is the incoming atmospheric long wave radiation $[Wm^{-2}]$ and $L^{\uparrow}$ is the outgoing long wave radiation $[Wm^{-2}]$.

The parameters in equation 3.21 can be calculated as,

$$S_{n,c} = \sigma_f \sum_{\Lambda,\mu} F_{\Lambda,\mu} S_{\Lambda,\mu}^{\downarrow}, \tag{3.22}$$

$$S_{n,g} = S_n - S_{n,c}, \tag{3.23}$$

$$S_n = \sum_{\Lambda,\mu} (1 - \bar{\alpha}_{\Delta,\mu}) S_{\Lambda,\mu}^{\downarrow}, \tag{3.24}$$

where $S_{n,c}$ is the net solar radiation absorbed by the canopy $[Wm^{-2}]$, $F_{\Lambda,\mu}$ is the fraction of solar radiation absorbed by canopy [.], $S_{\Lambda,\mu}^{\downarrow}$ is the component of the incident solar radiation visible (beam and diffuse), near-infrared (beam and diffuse) $[Wm^{-2}]$, S_n is the net solar radiation absorbed by the surface $[Wm^{-2}]$ $S_{n,g}$ is the net solar radiation absorbed by the ground $[Wm^{-2}]$ and $\bar{\alpha}_{\Delta,\mu}$ is the weighted surface albedo over the grid [.].

3.1.6 Boundary conditions

The surface boundary conditions in ParFlow-CLM is defined from the input meteorological variable. In place of direct meteorological input, the boundary conditions could also be provided from atmospheric models such as Weather Research and Forecasting model (WRF). In the subsurface, the boundary conditions have to be provided for the top, bottom, and side of the domain. At the top, the boundary condition to the subsurface is governed by the overland flow. For the bottom and side of the domain, the boundary condition either be of no flux exchange, constant flux exchange, or variable flux exchange. In the catchment scale hydrological modeling, the boundary condition at the bottom and side of the domain

is often kept with no flux exchange.

3.1.7 Water balance

Water balance in ParFlow is calculated for the subsurface flux (Richards' equation), coupling interface (overland flow), and surface flux (CLM). The storage components in ParFlow include the surface and subsurface while the flux components include the overland flow and evapotranspiration. The water balance in ParFlow is calculated as:

$$\frac{\Delta[Vol_{subsurface} + Vol_{surface}]}{\Delta t} = Q_{overland} + Q_{evapotranspiration} + Q_{source/sink}, \tag{3.25}$$

where $Vol_{subsurface}$ is the subsurface storage $[L^3]$, $Vol_{surface}$ is the surface storage $[L^3]$, $Q_{overland}$ is the overland flux $[L^3T^{-1}]$, $Q_{evapotranspiration}$ is the evapotranspiration flux passed from CLM $[L^3T^{-1}]$ and $Q_{source/sink}$ is the source or sink fluxes in the domain $[L^3T^{-1}]$. The subsurface storage consists of compressible and incompressible storage and is represented as:

$$Vol_{subsurface} = \sum [\underbrace{S(\psi)S_s\psi\Delta x\Delta y\Delta Z}_{\text{compressible}} + \underbrace{S(\psi)\phi\psi\Delta x\Delta y\Delta Z}_{\text{incompressible}}], \tag{3.26}$$

where $S(\psi)$ is saturation as a function of surface pressure $[L]$, S_s is specific storage $[L^{-1}]$, ψ is surface pressure $[L]$ and ϕ is porosity. The surface storage is calculated as:

$$Vol_{surface} = \sum \psi\Delta x\Delta y, \tag{3.27}$$

Finally, the overland flow calculation in x and y direction, respectively, follows as:

$$Q_{overland,x} = \upsilon A = -\frac{\sqrt{S_{f,x}}}{n}\psi_s^{2/3}\psi\Delta y = -\frac{\sqrt{S_{f,x}}}{n}\psi_s^{5/3}\Delta y, \tag{3.28}$$

$$Q_{overland,y} = \upsilon A = -\frac{\sqrt{S_{f,y}}}{n}\psi_s^{2/3}\psi\Delta x = -\frac{\sqrt{S_{f,y}}}{n}\psi_s^{5/3}\Delta x, \tag{3.29}$$

3.2 EcoSLIM

EcoSLIM is a Lagrangian particle tracking model to be run after the integrated hydrological models from the 4D (3D + time) simulated velocity field . for this study we have used EcoSLIM with ParFlow-CLM outputs (Maxwell et al., 2019). EcoSLIM simulates the location of particles (in the snow mantle or in the subsurface) that enter the domain with precipitations and get out through the surface, overland, and evapotranspiration. Integrated over time, this model provides trajectories, flow path, and residence time for particles tagged for snow or rain, when they enter the domain and tagged as evapotranspiration or outflow when they get out. The ParFlow output at the gridded level is directly used by EcoSLIM. This output includes pressure, saturation, subsurface flow velocity, precipitation, and evapotranspiration fluxes from which Ecoslim can calculate particle densities but also water masses. At each time step, the water is inserted, moved or removed based on these ParFlow outputs. It tracks particles in the domain at each specific model time step (ParFlow timestep).

The particles in the EcoSLIM are added in two ways. At the first step, the user-defined particle number is inserted as a constant value. These particles are equally distributed to all numerical cells and tagged as groundwater. These particles are assigned a random location within the cell with the mass of the particle as:

$$m_p = \frac{1}{n_i} \Delta x \Delta y \Delta z \rho \theta S_s, \tag{3.30}$$

where m_p is the mass of each particle $[M]$, n_i is the number of particle inserted, $\Delta x, \Delta y$ and Δz are the cell dimensions $[L]$, ρ is the density of water$[ML^{-3}]$, θ is the effective porosity and S_s is the saturation of water in the cell.

At the second step particles are added through transient simulation when the flux to the subsurface is positive (groundwater recharge from precipitation). The newly distributed mass in a cell is represented as:

$$m_p = \frac{Q_i}{n_i} \Delta x \Delta y \Delta z \rho \theta S_s, \tag{3.31}$$

where Q_i is the flux of new water $[T^{-1}]$ at model timestep Δt $[T^{-1}]$. The number of particles (n_i) is a user-defined value and the same number of particles are added at each time step

when there is a positive flux. A larger number of particles means a better resolution of fluxes. In ideal configurations, when the number of particles is enough, the EcoSLIM outflow and evapotranspiration output match with the ParFlow-CLM flux output.

Inserted particles at each time step are tagged with snow or rain source depending upon input in the ParFlow-CLM domain. Particles are initially assigned with a random age between 0 and the time they were added to the simulation (Δt). After the particles have been initialised in the domain, they moved through the processes of advection, dispersion, and diffusion, depending upon ParFlow-CLM subsurface transient velocities.

The particle movement is approximated with the Ito-Folker-Planck approximation following the advection-dispersion equation as:

$$X_p(t+\Delta t) - X_p(t) = \left[\mathbf{v}_p + \nabla.\boldsymbol{D} + \frac{\boldsymbol{D}}{\theta S_s}.\nabla\theta S_s\right]\Delta t + \boldsymbol{B}.\mathbf{z}\sqrt{\Delta t}, \tag{3.32}$$

where $X_p(t)$ $[L]$ is the location of particle at time t $[T]$, $\mathbf{v}_p$ is the velocity $[LT^{-1}]$, $\boldsymbol{B}$ is defined as $\boldsymbol{B}.\boldsymbol{B^T} = 2D$, $\mathbf{z}$ is random vector with zero mean and unit variance, $\boldsymbol{D}$ is the dispersion tensor approximated as:

$$D \approx (\alpha_T \mathbf{v} + D_e)\boldsymbol{I} + +(\alpha_L - \alpha_T)\frac{\mathbf{vv}}{\mathrm{v}}, \tag{3.33}$$

where α_L and α_T are the longitudinal and transverse dispersivities $[L]$, v is the magnitude of the velocity $[LT^{-}1]$, D_e is an effective molecular diffusivity $[L^2T^{-1}]$. If we neglect microdispersion and include effective molecular diffusion, then Equation (18) can be represented as:

$$X_p(t+\Delta t) - X_p(t) = \mathbf{v}_p\Delta t + \mathbf{z}\sqrt{D_e\mathbf{2}\Delta t} \tag{3.34}$$

Each particle moves independently following first-order advection. Particles are grouped at a certain time interval either decided locally or due to velocity change or due to particles leaving the cell. The age of active particles increases linearly. Thus, EcoSLIM provides variables like location, age, and then flow path and residence time, the particle age when it is getting out. A particle becomes inactive when it leaves the domain either by outflow or overland flow or by evapotranspiration. Particles that reach ponded surface cells (overland

flow) are removed from the EcoSLIM simulation. Evapotranspiration is calculated for each time step as mass equivalent from the ParFlow evapotranspiration file. If the volumetric mass (evapotranspiration) from ParFlow is greater than that of EcoSLIM, the particles are removed through evapotranspiration.

EcoSLIM is used in this work to document i) flow path in the studied catchment to be further validated through hydro-geochemistry (water conductivity, concentration in major element, isotopic ratios, ...) and ii) residence times to feed chemical box models and compare chemical reaction rates and water residence time in the subsurface.

4 Impact of Distributed Surface Meteorology

This chapter describes the set-up of a fully distributed physically based hydrological model, ParFlow-CLM, over a complex mountain terrain to model critical zone processes. The studied area is a small subalpine catchment (15.28 ha) located close to Lautaret pass (2000-2000 meter elevation) in French Alps. We aim to simulate the hydrological processes critical to the functioning of such an ecosystem. The complex topography, subsurface flows, and snow-dominated hydrological cycle in mountain terrain is challenging from measurement to modelling point of view. This chapter investigates the surface processes in the critical zone and their role in perturbing the water balance.

Snow plays an important role in the mountainous critical zone processes. Water supply, agriculture, vegetation cycle, chemical transport, and ecological processes are directly affected by snow. However, modeling the spatio-temporal dynamics of snow and its impact on hydrological fluxes depends on small spatial scales that are not well represented in the hydrological components of Earth System Models (ESMs). Heterogeneities in such a catchment require scaling of the processes in a high spatio-temporal resolution. This chapter discusses the essential methodology to model the water balance in such a complex terrain with a focus on snow processes. In such a catchment major part of the flux is dominated through snow processes. Topography plays an important role in driving the snowmelt flux from surface to subsurface. Topography controls the distribution, melting, and transportation of snow along the slope. It also controls the mass and energy exchange with the atmosphere. However, at the resolution of the mountain critical zone, these processes are merely accounted for in modeling approaches. The chapter will address the factors which control the spatio-temporal distribution of snow in such a catchment. It will also address the impact of spatio-temporal distribution of snow on the hydrological flux, and the meteorological distribution processes which control the snow variability in the catchment. This chapter is based on the following citation:

Gupta, A., Reverdy, A., Cohard, J.-M., Voisin, D., Hector, B., Descloitres, M., Vandervaere, J.-P., Coulaud, C., Biron, R., Liger, L., Valay, J.-G., and Maxwell, R.: Impact of distributed meteorological forcing on snow dynamic and induced water fluxes over a mid-elevation alpine micro-scale catchment, Hydrol. Earth Syst. Sci. Discuss. [preprint],

https://doi.org/10.5194/hess-2021-639, in review, 2022.

Abstract

From the micro to mesoscale, water and energy budgets of mountainous catchments are largely driven by topographic features such as terrain orientation, slope, steepness, and elevation together with associated meteorological forcings such as precipitation, solar radiation, and wind speed. It governs the snow deposition, melting, and transport, which further impact the overall water cycle. However, this microscale variability is not well represented in Earth System Models due to coarse resolutions. This study explores the impact of precipitation, shortwave radiation and wind speed on the water budgets distribution over a 15.28 ha small mid-elevation (2000-2200 m) alpine catchment at Col du Lautaret (France). The grass dominated catchment remains covered with snow for 5 to 6 months per year. The surface-subsurface coupled distributed hydrological model ParFlow-CLM is used at very high resolution (10m) to simulate the impacts on the water cycle of meteorological variability at very small spatial and temporal scale. These include 3D simulations of hydrological fluxes with spatially distributed forcing of precipitation, shortwave radiation, and wind speed compared to 3D simulations of hydrological fluxes with non-distributed forcing. Our precipitation distribution method encapsulates spatial snow distribution along with snow transport. The model simulates the dynamics and spatial variability of snow cover using the Common Land Model (CLM) energy balance module and under different combinations of distributed forcing. The resulting subsurface and surface water transfers are computed by the ParFlow module. Distributed forcing leads to spatially heterogeneous snow cover simulation, which becomes patchy at the end of the melt season and shows a good agreement with the remote sensing images (Mean Bias Error (MBE) = 0.22). This asynchronous melting results in a longer melting period compared to the non-distributed forcing, which does not generate any patchiness. Among the distributed meteorological forcings tested, precipitation distribution, including snow transport, has the greatest impact on spatial snow cover (MBE = 0.06) and runoff. Shortwave radiation distribution has an important impact on reducing evapotranspiration as a function of the slope orientation (decrease in slope between observed and simulated evapotranspiration from 1.55 to 1.18). For the primarily east-facing catchment studied here, distributing shortwave radiations helps generating realistic timing and spatial heterogeneity in the snowmelt, at the expense of an increase in mean bias error (0.06 to 0.22) for all distributed forcing simulations compared to the simulation with only distributed precipitation. Distributing wind speed in the energy balance calculation has a more complex impact on our catchment as it accelerates snowmelt when meteorological conditions are favourable but does not generate snow patches at the end of our test case. It shows that slope and aspect based meteorological distribution can improve the spatio-temporal representation of snow cover and evapotranspiration in complex mountain terrain.

4.1 Introduction

Mountains are natural water reservoirs mitigate the variability of seasonal precipitation through snowpack accumulation. The gradual melting of the snowpack helps meet the demand for freshwater and energy all year long. The warmer climate expected in the near and far future for these mountain regions will impact this mitigation process. Highly variable mountain topography, vegetation, soils, and geological structures affect the water transfer at different scales which makes it difficult for Earth System Models (ESM) to simulate water fluxes in mountain catchments, as they have coarser spatial scale. In particular, topography controls precipitation estimation and uncertainties related to rain/snow partition, snow redistribution, slope/aspect effect, and hill-shading that lead to spatial differences in melting (Costa et al., 2020; Fang and Pomeroy, 2020; Pomeroy et al., 2003, 2007). Fan et al. (2019) argued that variations in topography and catchment aspect can change hydrological fluxes and vegetation dynamics in particular when comparing steep to gentle slopes or north facing to south facing slopes. Therefore, water budget modeling in the mountains is challenging, and the impacts of spatial heterogeneity, like snow depth distribution, calls for specific attention (Blöschl et al., 2019).

Land surface models (LSMs) are an imperative component of the ESMs to capture exchanges of mass, energy, and biogeochemical variables between the Earth's surface and the atmosphere (Hurrell et al., 2013; van den Hurk et al., 2011). However, hydrological flux exchange between surface and subsurface in LSMs is often poorly constrained. The usually applied free draining subsurface approximation is not really adequate to the task. This could also include slope and aspects features (as hill shading) or meteorological subgrid variability (Clark et al., 2015; Fan et al., 2019) or underground horizontal water redistribution (Tran et al., 2020). The spatial variability of hydrological processes and associated variable flux responses are generally too fine to be represented in LSMs when used at several square km resolutions (Song et al., 2020). Bertoldi et al. (2014) mentioned that due to the lack of detailed subsurface characterization, they failed to simulate the heterogeneous soil moisture compared to observation over sloping terrains at 20 m resolution. Similarly, another study acknowledged that precipitation, solar insolation, and wind speed distribution in a hillslope catchment are vital to simulate the spatial heterogeneity in surface hydrological fluxes and

snow dynamics (Sun et al., 2018). Overall, the underrepresentation of subgrid processes within mountain catchment controls the spatio-temporal snow cover, heterogeneous snow melting, and resulting streamflow responses.

Spatially and temporally heterogenous snowmelt in a mid-elevation catchment leads to spatial variation in saturation and pressure head response which affects streamflow at the outlet. Loritz et al. (2021) modeled a 19 km^2 catchment in northern Luxembourg Ardennes low elevation mountains and mentioned the importance of the distribution of rainfall data for the spatial representation of surface and subsurface fluxes. The same study also highlighted that in a snow dominated catchment, the calibration of hydrological models should consider the surface dynamics of snow along with runoff as evaluation variables. Furthermore, evaluating the impact of snow redistribution caused by wind over a catchment is challenging because it involves the hyper-resolution of wind vector (1 m to 100 m) (Marsh et al., 2020; Pomeroy and Li, 2000). Liston et al. (2016) showed the relevance of the physical-statistical distribution of wind field in capturing snow dynamics. Similarly, shortwave radiation plays a significant role from a climatic, hydrologic, and biogeochemistry point of view. Nijssen and Lettenmaier (1999) mentioned that shortwave radiation affects the majority of energy exchanges between land and the atmosphere, including water vapor exchanges. Land surface–radiation interactions rely on terrain, wind speed, and soil moisture, and are often neglected in ESMs. Sampaio et al. (2021) highlighted that the daily/diurnal cycles of heat are also dependent on the surface orientation but are merely taken into account in hydrological modeling. However important, forcing the distribution of only a single variable sometimes is not enough to capture the real catchment behaviour. Combining the terrain-based distribution of precipitation data with solar radiation and wind speed helps to capture spatial patterns of snow melt along the slope, including distribution and redistribution of snow in the catchment (Sun et al., 2018). However, these diverse approaches in hydrological modeling are still limited and merely account for subsurface distribution, hyper-resolution simulation, terrain effect and surface meteorological variable distribution.

In mountainous regions, it is hard to maintain a dense network of weather stations due to the complex terrain (Meerveld et al., 2008; Revuelto et al., 2017; Song et al., 2020). This adds complexity to setting up hyper-resolution distributed models. However, there are proven statistical methods available for distributing the meteorological variables like precipitation,

shortwave radiation, wind speed, temperature, and humidity over the catchment (Liston and Elder, 2006). Many studies focus only on accounting for temperature distributions in the forcings of the model to simulate the spatial variability of fluxes in snow-dominated hillslope catchments (Aguayo et al., 2020; Fang and Pomeroy, 2020). However, these model resolutions remain too coarse to simulate the micro-scale hydrological behaviour. Moreover, only a few studies on snowpack simulation have used hyper-resolution distributed forcing (Günther et al., 2019; Baba et al., 2019; Vionnet et al., 2012). These studies highlighted the importance of meteorological distribution and the need for a hyper resolution modeling framework. Yet, the practice of distributing multiple meteorological forcing in hyper-resolution hydrological modeling of mountainous catchments is limited.

In order to overcome these LSMs limitations and quantify the impacts of fine scale variability on water balance, we used spatially distributed precipitation, wind speed, and shortwave radiation in a unique modeling exercise of the hydrological budget of a small-scale alpine mid-elevation (2000-2200 m) catchment (15.28 ha) for which we have detailed observations on surface and subsurface conditions. We used a hyper resolution subsurface hydrological model (ParFlow) coupled with the Common Land Model (CLM) at 10 m resolution to simulate the hydrological fluxes and spatio-temporal snow cover dynamics. From the perspective of hillslope hydrology we addressed the following points:

- Ability of the hyper-resolution modeling using 3D critical zone model ParFlow-CLM to capture the water/energy fluxes in a sub-alpine snow-dominated catchment.
- Impact on the catchment hydrological fluxes of distributing precipitation, solar radiation and wind speed over the catchment.
- Snow cover spatio-temporal dynamics in a microscale catchment and its role in controlling the water budget.

From onward, the second section presents the study area characteristics. The third section covers the methodology , including the modeling framework and the distribution of the meteorological variables. The fourth section details the domain discretization and model setup. The fifth and sixth sections present the results and discussion, respectively. Finally, the seventh section concludes the study.

4.2 Study Area

4.2.1 Geography and geology

The study area lies in a mid-elevation mountain range in the southern French Alps, near the Lautaret Pass (Fig. 4.1). This micro-scale catchment covers 15.28 ha with elevation ranging between 2000 and 2200 m. It consists of steep slopes facing East in the upper area, and a wetland in the lower area. The catchment is covered by snow for 5 to 6 months per year. The warm season grassland dominates the summer with 5 % woody cover that includes some larches, alders and bushes. Flux'Alp meteorological station lies just on the border of the catchment in a flat zone. Over the catchment, soil depths range from 20 cm on steep slopes to more than 2 m on the flat wetland. Soils are rich in clay with high porosity and retention capacity. This rich clay soil slowly turns into regolith, then hard rock over some transition zone, with thickness up to 5 m at the deepest locations. The base rock is highly fractured "Flysch des Aiguilles d'Arves", a shale-sandstone alternation, with bedding slopes ranging from sub-horizontal to sub-vertical (https://infoterre.brgm.fr/).

4.2.2 Climate

The study area is located in a typical mid-latitude alpine climate. Figure 4.2 shows meteorological observations for the simulated hydrological year starting on 11 November 2017 on the first snowy day to 10 November 2018. The catchment has a long winter season with 5 to 6 months of snowfall (Fig. 4.2a) and snow cover. Flux'Alp meteorological station records a total of 1530 mm year^{-1} precipitation, out of which 970 mm is snow in the studied period. According to 2017-2018 weather data, the site-average temperature is 4 °C. The site temperatures show a strong seasonal contrast, between below-zero winter conditions (-7.4 °C minimum monthly mean in February) and a mild summer (14 °C maximum monthly mean in July) (Fig. 4.2b). Winds higher than 5 ms^{-1} (Fig. 4.2c) are common throughout the year, usually from the South-West direction along the mountain pass (Fig. 4.4a). Temperature and specific humidity follow the same cyclic pattern (Fig. 4.2d). March is the most humid period of the year, while July is the driest. Solar radiation (Fig. 4.2f) varies due to the seasonal cycle, and to shading effects from the southern high mountain range (elevation 3000 - 4000m elevation), which are particularly sensitive in the winter when the sun is lower on

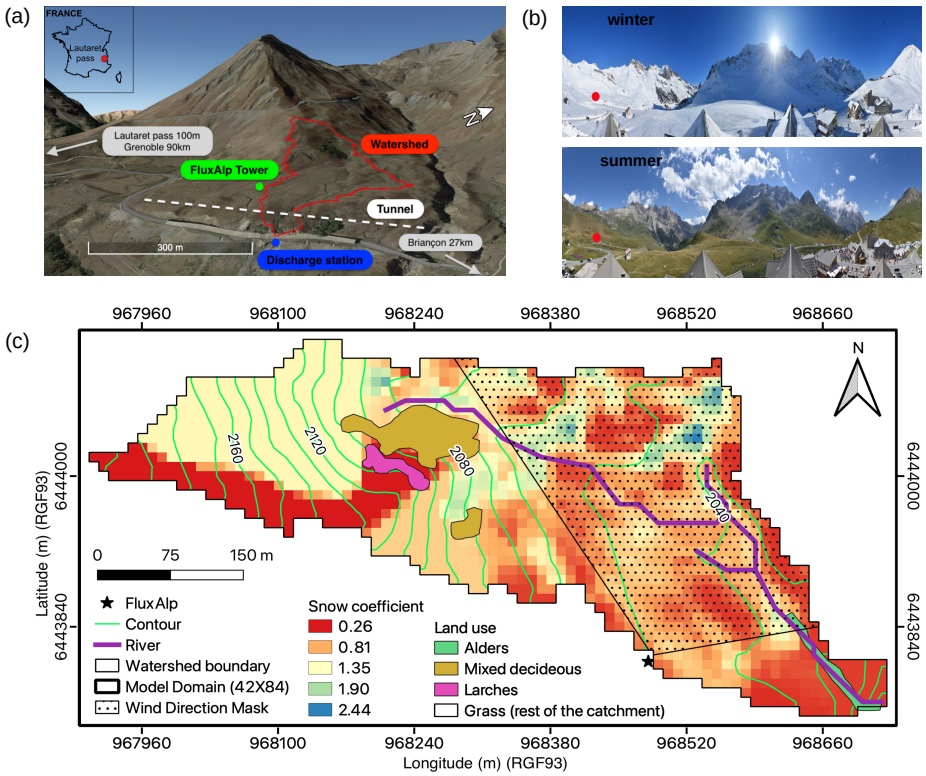

Figure 4.1: (a) Overview of the study area at Col du Lautaret, France, the small subalpine catchment is delineated in red with the outlet at the blue point. The green dot (black star in 4.1(c)) is the Flux'Alp micro-meteorological station. (b) Landscape views of the Lautaret pass area in winter (January) and summer (July). (c) Catchment domain (84 × 42 grid cells at 10 m resolution) with river branches (violet), elevation contours (green), and vegetation. Coloured pixels represent the distributed snow coefficients. The dotted area is the approximated footprint for the daily wind directions considered for ET comparison in (section 4.3.3).

the horizon.

4.2.3 Monitoring

Most of the monitoring on the site has started in 2012. It includes the temperature and humidity (CS215, Campbell Sc.), atmospheric pressure (Setra CS100, Campbell Sc.), wind speed and wind direction (Vector anemometer A100LK and W200P, Campbell Sc.), 4 components of net radiation (CNR4, Kipp and Zonen), snow height (SR50A, Campbell Sc.), and NDVI (Normalised Difference Vegetation Index) measured through Skye Instruments SKR1800. Since 2015, the site received one eddy covariance station composed of a LI-COR LI-7200 close-path gas analyser and a HS50 Gill 3D sonic anemometer. In 2017 an OTT Pluvio weighting rain gauge was installed at the Flux'Alp weather station. Site setup,

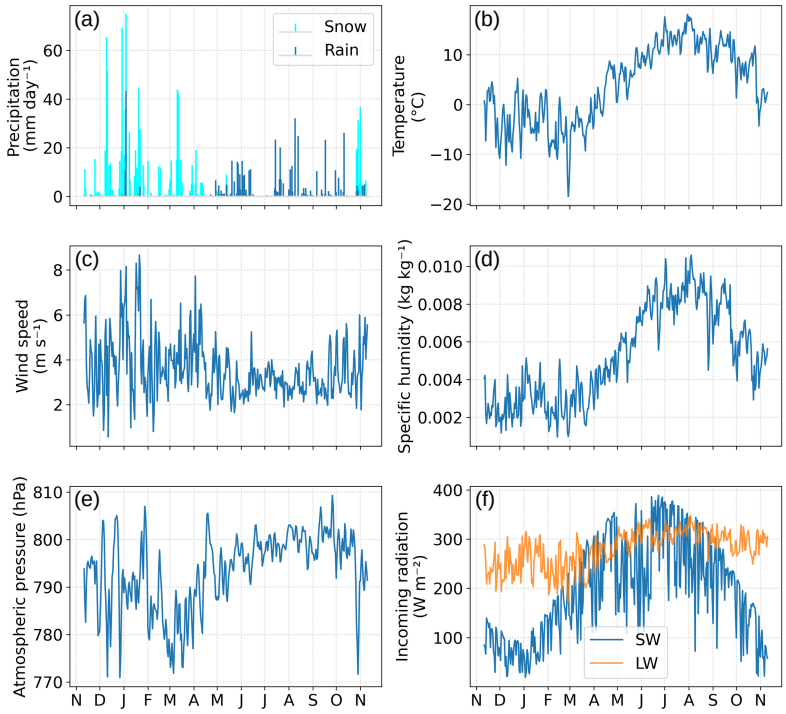

Figure 4.2: Daily meteorological observation at Col du Lautaret for hydrological year 2017-2018: precipitations (a), air temperature (b), wind speed (c), specific humidity (d), Atmospheric pressure (e) and shortwave (SW) and longwave (LW) incoming radiations (f).

monitoring, and data processing follow the ICOS (https://www.icos-ri.eu/) standards. All measured variables are recorded at 15 min time steps and then averaged over 30 min, except precipitation, which is summed. The EddyPro Software was used to process the turbulent fluxes at the same 30 min time step following the ICOS recommendations (Hellström et al., 2016).

4.3 Methodology

4.3.1 ParFlow-CLM (PF-CLM)

In this study, we used ParFlow-CLM, an integrated surface-subsurface coupled hydrological model, to simulate the impact of distributed meteorological forcing on the water transfers (Jones and Woodward, 2001; Ashby and Falgout, 1996; Kollet and Maxwell, 2006; Maxwell, 2013; Maxwell and Miller, 2005; Kollet and Maxwell, 2008). ParFlow is a parallel integrated hydrological model optimised to solve the surface and subsurface exchange of fluxes. ParFlow solves the three-dimensional Richards equation to calculate the water pressure field and

transfer of fluxes between unsaturated and saturated porous media (Jefferson and Maxwell, 2015). Relative permeability and soil retention curves are based on the Van Genuchten relationships (Van Genuchten, 1980). A multigrid-preconditioned conjugate gradient solver and the Newton-Krylov solver for non-linear equations (Kuffour et al., 2020) make the model efficient to run in a parallel computing environment. ParFlow includes a terrain-following grid which eases boundary conditions prescription. It accounts for the surface slope in Darcy's formula, which also eases numerical exchange between subsurface and overland flow. At the model surface, excess of water ($pressure > P_{atm}$) in all saturated cell flows according to the two-dimensional kinematic wave equation (Kuffour et al., 2020). ParFlow then maintains a continuous pressure head value from the bottom to the top of the domain and explicitly calculates fluxes between groundwater and surface water. Infiltration excess (Horton, 1933) or saturation excess (Dunne, 1983) runoff are then generated according to Richards equations. Flow-routing uses the D4 scheme to determine the flow direction based on individual slopes in the x and y direction and has been calculated according to Condon and Maxwell (2019). The CLM (Common land model) is a land surface model designed to compute the land-water-energy exchange between the Earth's surface and atmosphere (Dai et al., 2003). CLM accounts for land cover, surface temperature, soil moisture, soil texture, soil colour, root depth, leaf and stem area, roughness length, displacement height, plant physiology and thermal and optical properties of the medium to calculate the surface energy and water balance. It calculates evapotranspiration as the sum of evaporation, vegetation evaporation, transpiration, and re-condensation. CLM models snow with up to 5 layers, following layer thickness and temperature, water and ice mass in each layer. CLM two-stream radiative transfer scheme accounts for direct and scattered radiation by snow in visible and near infrared wavelengths. In CLM, when pixels cover a large range of elevation, the snow fraction is used to calculate the total snow cover area. In our study snow fraction was assigned 0 (no-snow) or 1 (snow) values. Our horizontal pixel resolution is small enough (10 $\times$ 10 m) that we consider their snow cover to be uniform. This implies that our pixels are either completely covered with or completely devoid of snow. Therefore, CLM can handle the spatial/temporal snow distribution, associated water fluxes (melting, sublimation, infiltration), and evaporative fluxes according to spatial/temporal heterogeneous surface conditions (temperature, water/snow inputs, incoming radiations, wind speed, and vegetation). After

computing the surface exchanges like evaporation, transpiration, snowmelt, and precipitation infiltration to and out of the soil, these are applied as source/sink in the Richards equations. Further information on ParFlow terminology and the model capability is included in the user manual (https://github.com/parflow).

4.3.2 Meteorological distribution

Precipitation

The precipitation data from the rain gauge was first processed to account for the lack of gauge shield (KLOK et al., 2001). The adopted algorithm follows as:

$$P_{corr}(x_0, y_0) = P(x_0, y_0) * (a + b * u(x_0, y_0)), \tag{4.1}$$

where, P_{corr} is the corrected precipitation (mm), P is measured precipitation (mm) at observation station, u is the wind speed at observation station in m s^{-1}, a and b are correction factors, and are different for rain ($a = 1.04$, $b = 0.04$) and snow ($a = 1.18$, $b = 0.20$) (Sevruk and WMO, 1986).

To account for snow cover spatial variability on the catchment domain, $S_c(x, y)$, the precipitation fallen as snow at (x, y) location was calculated using a snow coefficient map $C_s(x, y)$. The snow coefficient map was prepared from the ratio between the measured snow height at the gauge to the snow height measured through the laser scan on the same day (21/02/2018) at the end of the accumulation period (Fig. 4.1). The snow height was calculated from the laser which is the difference of apparent snow height (from laser scan) at the end of the accumulation period and the digital elevation model (DEM) for the surface without snow. The snow DEM and surface DEM were prepared at the resolution of 2 m and were upscaled to 10 m resolution using the minimum of each cell. The $S_c(x, y)$ calculation hypothesizes that distributed snow cover on that date aggregates all spatial heterogeneity of the snow deposition including snow transport (redistribution). It also includes the snow compaction between the date of deposition and the laser scan. Then the corrected precipitation fallen as snow was calculated according to:

$$S_c(x, y) = S_m(x_0, y_0) * C_s(x, y)), \tag{4.2}$$

where, $S_m(x, y)$ is the measured snow precipitation at the observation station. It must be noted that the laser scan didn't cover the upper part of the catchment. Zones not covered by the scanner were each given a fixed value according to our field observation. Moreover, due to the small size of the catchment and the low elevation range (1993 m to 2204 m), precipitation gradients between upper and lower elevations have not been considered and the rain has not been distributed in our study.

Shortwave radiation

The shortwave radiation, $SW_c(x, y)$ was distributed from the observed shortwave radiation measurement, $SW_m(x_0, y_0)$ at the meteorological station considering the sun position and the terrain effect (Liston and Elder, 2006). Equation 4.3 partitions diffuse (30 %) and direct shortwave radiation (70 %) contributions from the observed shortwave radiation, and equation 4.4 accounts for the terrain features based on their orientation which was integrated as a solar cosine function in equation 4.3. The partition of diffuse and direct shortwave radiation was taken from the CLM technical setup (Oleson et al., 2004).

$$SW_c(x, y) = (0.7cosi(x, y) + 0.3) * SW_m(x_0, y_0)), \tag{4.3}$$

$$cosi(x, y) = cos\beta(x, y) * cosZ(x, y) + sin\beta(x, y) * sinZ(x, y) * cos(\mu(x, y) - \xi_s(x, y)), \tag{4.4}$$

SW_c is the corrected shortwave radiation (W m^{-2}) at a coordinate location, SW_m is measured shortwave radiation at the observation station, i is the solar angle function of the slope angle β, the slope southern azimuth ξ_s, sun southern azimuth μ and solar zenith angle Z.

Wind speed

Wind speed was spatialized to better account for the estimation of turbulent fluxes (Liston and Elder, 2006). The wind speed was distributed as

$$W_w(x,y) = 1 + 0.58\Omega_s(x,y) + 0.42\Omega_c(x,y), \tag{4.5}$$

$$\Omega_s(x,y) = \beta(x,y) * cos(\theta(x,y) - \xi(x,y)), \tag{4.6}$$

$$\Omega_c(x,y) = 0.25 \sum (z(x,y) - 0.5(z_i(x,y) + z_j(x,y)))/d, \tag{4.7}$$

$$W_c(x,y) = W_w(x,y) * W_m(x_0,y_0), \tag{4.8}$$

where, W_w is the wind weighting factor at a coordinate location as a function of wind direction slope (Ω_s) and curvature (Ω_c), i and j are the search direction (N-S, E-W, NE-SW, SE-NW), d is 2η for cardinal axes and $2\sqrt{2}\eta$ for others, η is the search distance and, z is the elevation, β is the slope angle, θ is the wind direction and ξ is the slope azimuth. The search distance d for curvature was set to 50 m (Revuelto et al., 2020). Finally, the wind weighting factor (W_w) was multiplied with the wind speed measured (m s^{-1}) at the observation station (W_m) to obtain the terrain corrected wind speed (W_c).

Along with precipitation, shortwave radiation, and wind speed, three more variables are used to force the model: temperature, pressure, and specific humidity. However, as the model was set to a microscale catchment with little elevation variability, we did not distribute these parameters.

4.3.3 Wind direction mask

To compare the simulated evapotranspiration with the observation, a wind direction mask was prepared to approximately represent the Eddy-Covariance station footprint area. As the catchment and the footprint area only partly coincide, we selected simulated pixels in an approximated footprint area based on a wind direction mask (Fig. 4.4) and averaged simulated values over the mask. The wind direction mask was prepared according to the prevailing wind directions towards the Flux'Alp station between the 10 percentile (122.39°) and 90 percentile (260.51°) wind direction. We then compared observed evapotranspiration to the simulated average value over the mask, only when the wind blows from a direction

included in the mask, as this maximises the comparability of simulated and measured values.

4.3.4 Sentinel-2 snow cover

Snowmelt dynamics was compared to Sentinel-2A and Sentinel-2B products from Sentinel-2 mission developed by European Space Agency (ESA) for high resolution satellite imagery (Drusch et al., 2012). We downloaded four Sentinel-2 images out of which two belong to the accumulation period and two to the melting period. These images were selected to show the spatial and temporal distribution of snow in the catchment. For this purpose, we have calculated the normalised snow difference index (NDSI) from the downloaded images as (Dozier, 1989),

$$NDSI = \frac{Green(band3) - SWIR(band11)}{Green(band3) + SWIR(band11)}, \tag{4.9}$$

where, 'Green' and 'SWIR' are the corresponding bands in the green and shortwave infrared region of the satellite, respectively. The green band is represented by 'band 3' and the SWIR band is represented by 'band 11' in Sentinel-2 product. Sentinel 'band 3' was available at 10 m resolution while 'band 11' at 20 m resolution. NDSI calculation was carried out by resampling 'band 11' at 10 m resolution (Hofmeister et al., 2022). The Sentinel-2 snow pixels were selected with NDSI > 0.4 (Riggs et al., 1994). In the model, the snow pixels were selected for snow depth threshold over 1 cm, which is the minimum non zero height for snow.

4.3.5 Performance indicators

Slope

Slope for the linear regression without intercept ($y = \alpha x$) is represented as,

$$\alpha = \frac{\sum_{i=1}^{n}(x_i y_i)}{\sum_{i=1}^{n}(x_i^2)}, \tag{4.10}$$

where, x is observed value and y is predicted value.

R-square (R^2)

R-square or coefficient of determination is defined as,

$$\left[\frac{\sum_{i=1}^{n}(x_i-\bar{x})(y_i-\bar{y})}{\sqrt{\sum_{i=1}^{n}(x_i-\bar{x})^2}\sqrt{\sum_{i=1}^{n}(y_i-\bar{y})^2}}\right]^2, \tag{4.11}$$

where, x is the observed value and y is the predicted value, and $\bar{x}$, $\bar{y}$ are the mean of observed and predicted values, respectively.

Root mean square error (RMSE)

RMSE score is represented as,

$$\sqrt{\frac{1}{n}\sum_{i=1}^{n}(x_i-y_i)^2}, \tag{4.12}$$

where, n in the number of samples and x is observed value while y is predicted value.

Mean bias error (MBE)

MBE score is represented as,

$$\sqrt{\frac{1}{n}\sum_{i=1}^{n}(y_i-x_i)}, \tag{4.13}$$

where, n in the number of samples and y is predicted value while x is observed value. MBE score is represented for the Sentinel-2 images as an average between the spatial similarity of snow and non-snow pixels (mismatch between the image pixels).

4.4 Domain discretization and simulation setup

The surface domain of 15.28 ha was discretized at a horizontal hyper-resolution of 10 m with the total number of 84 × 42 × 11 (longitude × latitude × levels) cells on a terrain following grid (Fig. 4.1). Individual cell height (z-direction levels) varies from 4 cm for the top soil layer to 110 m for the deepest layer (Fig. 4.3a). The model was mainly built and forced using the observations; hence, the input data either belongs to observation data or

data derived from observation. These data include temperature, precipitation, wind speed, short wave, humidity, and atmospheric pressure plotted in figure 4.2. Leaf Area Index (LAI) was calculated from NDVI measurements while Stem Area Index (SAI) was assigned a constant value based on field survey. Displacement height (d) and roughness length (z0) were calculated from the vegetation height following Brutsaert rules (Brutsaert, 1982). The snow height sensor show sensitivity to the grass height when there was no more snow on the ground. We, therefore, used the signal of this sensor when NDVI values were above 0.4 to estimate grass height. LiDAR Digital Surface Model (DSM) of 2 m resolution was available for the catchment and upscaled to 10 m resolution using the minimum of each cell. Upscaled DSM was processed with PriorityFLOW to generate the slope maps in x and y direction (Condon and Maxwell, 2019). The Landcover map was made through field observations while the Manning coefficients were assigned using the landcover map. River pixels were assigned a constant manning value of 0.05 s $m^{-1/3}$ and the rest of the catchment were assigned a constant manning value of 0.03 s $m^{-1/3}$. The lateral and bottom boundary conditions were set to no flow and the surface boundary condition was set at atmospheric pressure that allows fluxes to leave at positive hydraulic head (Kollet and Maxwell, 2006). Hence, the inflow and outflow were restricted to exchange only through the surface. Subsurface was made heterogeneous with three layers consisting of soil, regolith, and flysch with a total of 11 different layers (Fig. 4.3a). The bottom of the domain was set deep enough to accommodate various subsurface water transfers (118 m deep from the surface). The soil physical parameters used in this study include porosity, permeability, soil horizons, and Van Genuchten parameters. The resulting water retention curves were plotted on Fig. 4.3c, d for the three different horizons. They show a reduction of permeability and porosity with depth. Soil horizons distribution (Fig. 4.3b) was determined from an electromagnetic survey measuring apparent electrical conductivity (related to water and clay content) and ground penetrating radar (GPR) measuring soil thickness. Electromagnetic survey was done for the whole catchment however, GPR survey was performed for three transverse profiles across the stream to validate the electromagnetic survey. The soil properties were determined by field permeability experiments and laboratory mercury porosity experiments. Elaboration about the detailed hydro-geological characterization is beyond the scope of this study and will be detailed in a companion paper (Gupta et al., 2022, in preparation). This study is

more focused on surface dynamics due to meteorological variable distribution.

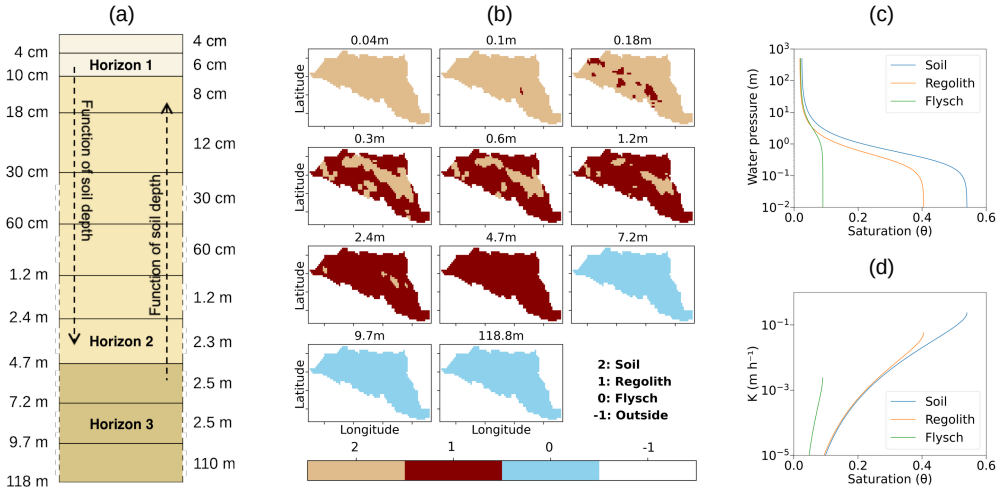

Figure 4.3: Subsurface configuration used for discretizing the domain. (a) The vertical distribution of subsurface layer with thickness (right) and depth (left) of each grid cell. (b) Spatial distribution of subsurface layer including soil (pink), regolith (dark brown) and flysch (blue). These layers vary in their hydro-geological parameters e.g. in terms of conductivity, porosity to the soil transfer functions which are shown in (c- Soil retention curve) and (d- hydraulic conductivity curve).

The model was forced with half-hourly meteorological forcing, however, results were saved at hourly time-step. The Universal Time Zone (UTC) was considered in terms of monitoring and modeling for this study. Before running the actual simulations, a 10-year spin-up run was performed with 'SeepageFace' (no runoff) conditions to bring the model into a hydrological balance. The yearly subsurface storage difference was used to evaluate whether the spin-up had taken the model into equilibrium, which happened at the end of the 10^{th} year. Each simulation was also run for two consecutive years with the same forcing to avoid any imbalance in subsurface storage (Ajami et al., 2014). The different simulations setup for this study are detailed in table 4.1.

All simulations named 1D use forcings that are uniform across the watershed (Table 4.1). Rain is the major hydrological model input hence, we keep the same amount of precipitation input in all simulations (1443.72 mm), which corresponds to the spatial average of precipitation after applying the distribution correction (eq. 4.2). Precipitation is reduced compared to what is measured at the rain gauge station (1531.96 mm) because the precipitation distribution process leads to a non-conservative spatial snow distribution over the catchment. The equal amount of precipitation input leads us to easily see the partitioning between different

hydrological fluxes across the different meteorological forcing simulations. 1D-PM, therefore, corresponds to a classical hydrological simulation for a small catchment when one applies the meteorological forcing directly from a nearby weather station. By contrast, 1D-AM accounts for local terrain slope and aspect according to equation 4.5-4.8, and applies uniformly across the watershed the mean corrected incoming radiation. Therefore, shortwave radiation amount is not the same considering the measured value (yearly averaged shortwave radiation, 1D-AM: 190.8 W m^{-2}) and the mean distributed value (yearly averaged shortwave radiation, 1D-PM: 152.1 W m^{-2}): as the weather station is less shaded than the generally east facing watershed, accounting for slope and aspects reduces the average incoming radiation. Meteorological parameters were further distributed to better analyse their respective influence. Pix-PM, 2D-PD, and 2D-WD all relate to 1D-PM, and used the zenithal solar radiation observation (measured shortwave radiation) directly from the radiation sensor 2D-AD and 2D-SD are related to 1D-AM as they used the same distributed incoming solar radiation, according to equation 4.5-4.8. The latter four proposed simulations were run to quantify the effect of spatially distributed forcing all together or individually (Table 4.1).

Meteorological forcings were distributed according to algorithms described in section 4.3.2. to represent the effects of slope, curvature and aspect on the spatial distribution of those forcings. Figure 4.4 presents snapshots of heterogeneities produced by these algorithms. Even at a micro-scale, one can observe the spatial meteorological variability along the grid after applying equations 4.2-4.8. In Figure 4.4b, for an averaged 0.53 mm snow rate, the distribution algorithm produce large heterogeneities ranging from 0.2 mm to 1.2 mm, with deeper accumulation mainly on lowlands. Similarly for shortwave radiation (Fig. 4.4c) for input radiation of 400.8 W m^{-2} on November 11 at noon, the algorithm reduced the radiation to 349.7 W m^{-2} on average with more than (+/-) 50 W m^{-2} difference depending on the location. In wind speed distribution, there was not so much variation in the spatial mean before and after wind speed distribution. The mean wind speed before and after the spatial distribution was 5.6 m s^{-1} and 5 m s^{-1}, respectively (Fig. 4.4d).

	Precipitation	Shortwave radiation	Wind speed
Pix-PM	Distributed mean	Non-distributed	Non-distributed
1D-PM	Distributed mean	Non-distributed	Non-distributed
1D-AM	Distributed mean	Distributed mean	Distributed mean
2D-AD	Distributed	Distributed	Distributed
2D-PD	Distributed	Non-distributed	Non-distributed
2D-SD	Distributed mean	Distributed	Non-distributed
2D-WD	Distributed mean	Non-distributed	Distributed

Table 4.1: Distributed and non-distributed approach adopted for different simulation.

4.5 Results

4.5.1 Simulations with spatially uniform forcings

1D-PM and 1D-AM represent our reference simulations, with uniform forcings across the watershed (see Table 4.1). Their results were presented in figure 4.5. According to the 1D-PM simulation (Fig. 4.5a) the hydrological year begins with the snow accumulation period until the end of March. December and January were the snowiest periods, with some snowmelt events (magenta line) due to short above zero degree episodes, which generate very little runoff (black line). In April, warmer positive temperatures and rain on snow events generate continuous melting in our simulation and produce the highest river discharge peaks with a strong daily cycle, further intensified by coinciding rain events. This period also increased the subsurface storage which produce a base flow later in May (Fig. 4.5b). In May streamflow show a combination of base flow and snowmelt (snowmelt in May in Fig. 4.5a, subsurface storage decrease in May in Fig. 4.5b).

One of the most important and noticeable points while using non-distributed forcing was the sudden disappearance of the snow at the end of the snowmelt season, which usually not observed in the field. It means that all the pixels behaved in the same way, and there was no noticeable impact on the catchment spatial snow variability when considering a uniform forcing. From June to the beginning of the next snow period, summer rain produce almost instantaneous river response and subsurface storage sustain stream runoff for several months. During this period, one can note a radical change of net radiation because of the land cover

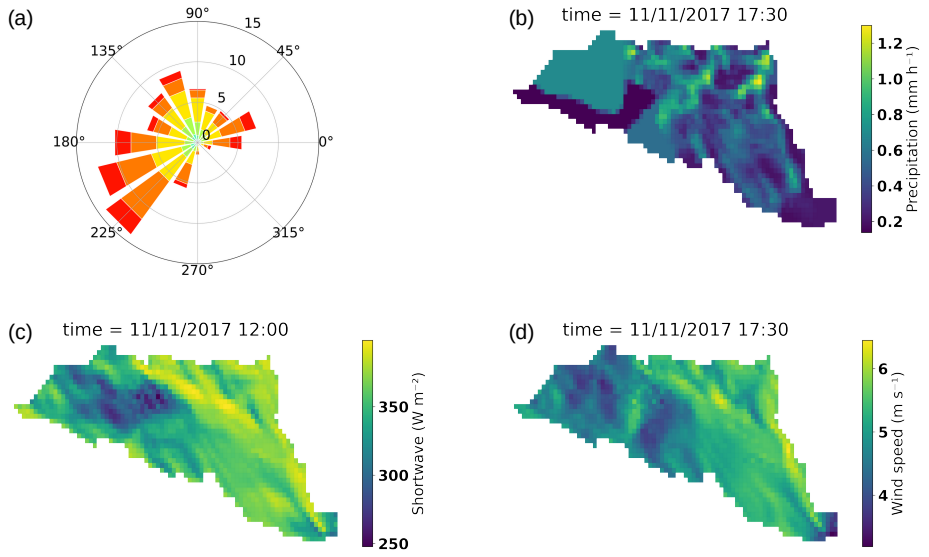

Figure 4.4: (a) Windrose diagram. (b) Precipitation distribution along the catchment. (c) Shortwave radiation distribution over the catchment. (d) Wind speed distribution over the catchment. All are plotted for 11/11/2017 at 5:30 pm and 12:00 pm for shortwave radiation.

change from snow to grass. The net radiation contributes to snowmelt in early spring. Factors responsible for this phenomenon includes higher sun elevation, clear sky conditions, and higher daily temperature.

During winter and spring, the monthly cumulated ET was very small (Fig 4.5b) because of low available energy and complete snow cover. After the complete snowmelt, the model simulated much higher monthly cumulated ET following the LAI cycle. ET at this period was higher than the monthly cumulated rain (June, July, September), which means that ET participates in the extraction of shallow water storage during the summer. This can be seen by the difference in subsurface storage decline between the summer (higher water storage diminution) and the winter (lower water storage diminution). In October one can notice a small increase in the subsurface storage when ET decreases because of vegetation decay. At the end of the hydrological year, the subsurface water storage has a deficit of -0.62 mm, which is much smaller than the annual cycle amplitude.

1D-AM simulation (Fig. 4.5c, d) mostly differs from 1D-PM as precipitation, solar radiation and wind velocity were prescribed using the spatial average of the distributed forcing. This reduces solar radiation from 190.8 W m^{-2} to 152.1 W m^{-2} on average which reduces melting and ET. Snow lasts 9 more days on the ground, runoff increases from 73% to 80% of total precipitation (runoff coefficient, Table 4.2), and infiltration increases by 10.66 mm.

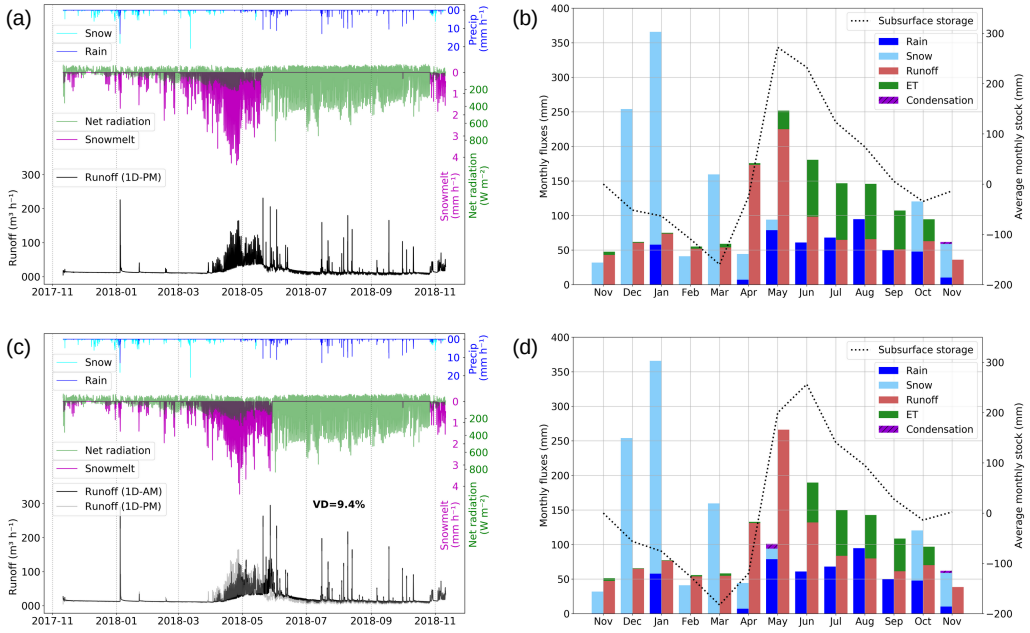

Figure 4.5: (a) Precipitation (rain – blue and snow – light blue), streamflow (black), snowmelt (magenta) and net radiation (green) regimes along the simulation period for only precipitation distributed mean simulation (1D-PM). (b) Monthly water budget for 1D-PM simulation including rain (blue) snow (light blue), Runoff (red), ET (green), and condensation (purple). The Black dotted line is the total subsurface water storage. (c)(d) same as (a) and (b) but for all distributed mean simulation (1D-AM). VD is the volume difference in percentage between plotted simulations.

For similar geomorphology, any reduction in input solar radiation because of catchment orientation or else leads to higher water tables and then higher runoff coefficient. Compared to the 1D-PM simulation this simulation showed reduced runoff peaks in the early melt season which leads to more percolation. Increased percolation leads to higher base flow during the late summer and delays the base flow response by around one month compared to 1D-PM simulation. Runoff in the 1D-AM simulation increases overall by 9.4 % compared to the 1D-PM simulation.

4.5.2 Simulations with spatially distributed forcing

This section present the simulation run with a fully distributed forcing (2D-AD), with its difference from the previous uniformly forced simulations, and the three simulations based on forcings with only one distributed variable (2D-WD, 2D-PD, 2D-SD) to explore the contributions of each individual spatial distribution. Figure 4.6a show that snowmelt lasts longer in 2D-AD simulation, tailing across June and early July, with streamflow decreasing

until even later in July. These snowmelt dynamics were smoother than it was simulated in either uniformly forced simulation (1D-PM and 1D-AM) and correspondingly impacts the net radiation, recharge and streamflow discharge dynamic. In the most intense melt period in May, this resulted in ∼30% lower peak streamflow values in 2D-AD compared to 1D-AM or 1D-PM simulations. However, the resulting annual water budget changed only by 2 % between 1D-AM and 2D-AD simulations, and by -7 % between 1D-PM and 2D-AD simulations. As mentioned in the previous section, time averaged distributed shortwave radiation input was lower in simulation 1D-AM compared to 1D-PM, due to accounting for shading effects. Simulation 2D-AD has the same time average radiation input as 1D-AM and was closer to this simulation in the yearly budget. Small scale distribution of meteorological forcings therefore only adds information on dynamics, and not on yearly budgets. The tailing snowmelt through June generated more percolation to the subsurface, resulting in stronger base flow in late summer, thereby catching up with the total runoff volume simulated in 1D-AM.

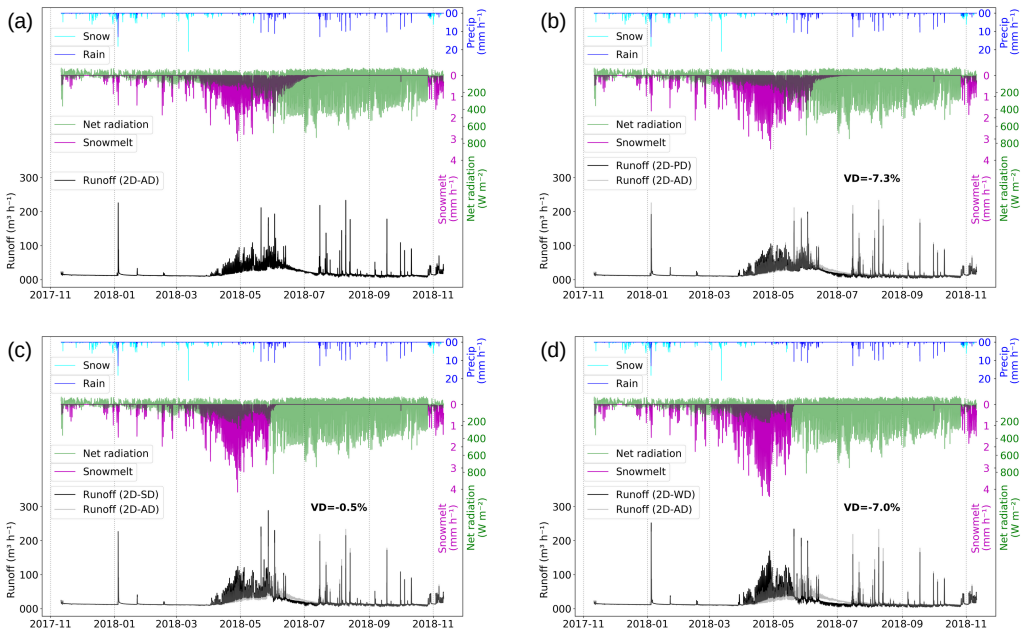

Figure 4.6: Same figure as 5a for (a) all distributed run (2D-AD), (b) only precipitation distributed run (2D-PD), (c) only shortwave radiation distributed run (2D-SD) and (d) only wind speed distributed run (2D-WD). VD is the volume difference in percentage between plotted simulation.

As visible in the results of the simulations with only one distributed forcing (Fig. 4.6b, c, d), the smoother decline in snowmelt resulted from both the precipitation and shortwave

radiation distribution. However, the simulation 2D-WD, where only the wind speed forcing was distributed, did not present such a smooth decline on snowmelt and results were very similar to the non-distributed simulation (1D-PM). The melting period tail length was controlled by the snowpack depth variability (Fig. 4.9a, b) and higher accumulated snow on some pixels. This combines with solar radiation effects, which also produce spatial variability in snowmelt on the catchment even if the snow precipitation was uniformly distributed (Fig. 4.6c). Only wind speed distribution (2D-WD) simulation showed the highest melting regimes from mid-March to mid-May when temperature and incoming radiations were favourable for melting resulting in daily melting peaks larger than 4 mm h^{-1} (Fig. 4.6d). In detail, wind speed distribution show an increase in the melting rate which leads to higher subsurface storage when compared to 1D-PM.

Streamflow differences between simulations basically follow the melting differences. The impact of the late April and early May rain-on-snow period was visible on streamflow on figure 4.6a, b. It must be noted that incoming solar radiation differ between simulations. Due to non-distributed shortwave radiation in 2D-PD simulation, the melting peaks were higher compared to 2D-AD simulation. This resulted in rapid runoff in 2D-PD simulation and less percolation to subsurface which caused a volume difference of -7.3 % compared to 2D-AD simulation. The 2D-WD and 2D-PD simulations showed lower streamflow values compared to 2D-AD and 2D-SD simulations. This happened because for the former two, the catchment receives 38.7 W m^{-2} less radiation than the latter two. The shortwave radiation distribution slowed the melting, which enhanced percolation to the subsurface. This subsurface percolation appeared as the base flow in the late summer. Though the base flow in 2D-SD simulation was lower than 2D-AD, however, due to equal precipitation in all pixels, 2D-SD simulation showed higher early melting peaks (Fig. 4.6c). This counter balance between 2D-AD and 2D-SD simulation showed a volume difference of only -0.5 %. In 2D-WD simulation due to rapid runoff at melting season, the subsurface storage decreased which result in far lower baseflow with volume difference of -7.0 % compared to 2D-AD simulation (Fig. 4.6d). To conclude, the amount of precipitation in a pixel correlated with the snowmelt peaks; however, rapid melting decreases the subsurface storage which result in lowered streamflow. Concerning the late summer period when snow gets melted, these differences were not visible on the streamflow.

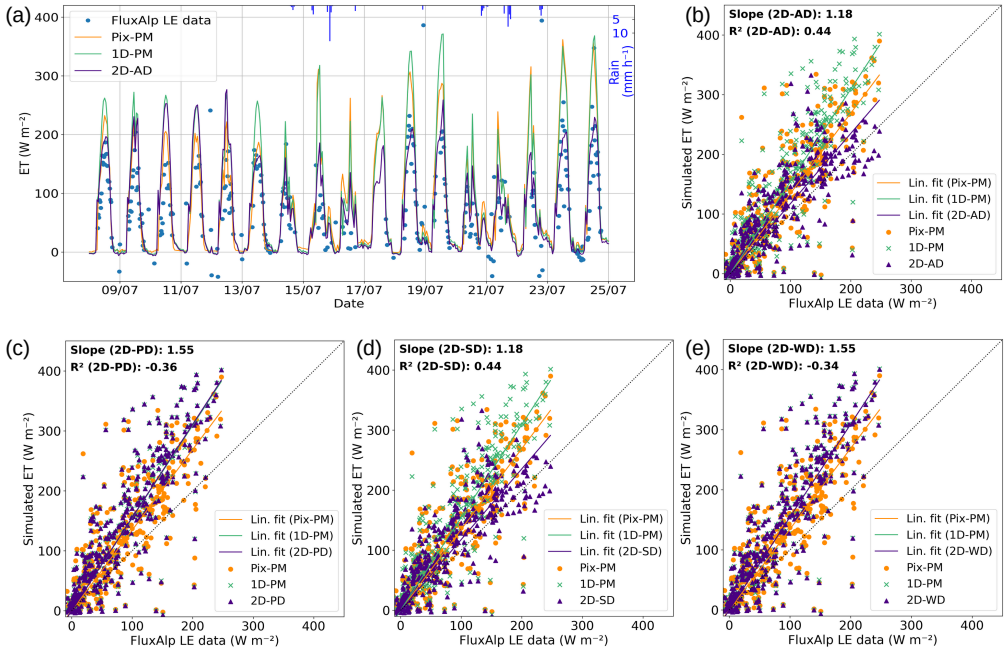

Figure 4.7: (a) Evapotranspiration simulation masked with wind direction mask for 17 days in summer for all distributed run (2D-AD). Scatter plot for the July-August 2018 period for (b) all distributed run (2D-AD), (c) only precipitation distributed run (2D-PD), (d) only shortwave radiation distributed run (2D-SD) and (e) only wind speed distributed run (2D-WD). The slope line represents the corresponding linear fit for the scatter plots, slope value of each simulation highlighted at the top.

Evapotranspiration in the pixel run (orange curve and orange dots) was clearly overestimated compared to observed evapotranspiration as one can see on both the time series and the scatter plots 4.7a, b. Similarly, the non-distributed simulation (green curve and green dots, 1D-PM), and the distributed simulations 2D-PD and 2D-WD have comparable evapotranspiration amplitude (Fig. 4.7c, e). However, 2D-AD and 2D-SD show reduced simulated ET which better matches the observations (Fig. 4.7b, d). This reflects the lower (average) shortwave radiation in the forcings where the solar radiation has been distributed according to the terrain (section 4.4): as the catchment generally faces east, this distribution reduced the direct incoming solar radiation from noon to sunset.

The evapotranspiration in both Pix-PM and 1D-PM overestimated ET compared to observations. First the pixel run (Pix-PM) was supposed to simulate a catchment border (Flux'Alp location) with dryer soil/ground condition (top of a ridge) and the ET observations were supposed to average both the wet zones close to the river and the dryer zones. However, it was not the case in our 2D-AD and 2D-SD simulations. The linear slope in

these two simulations moved much close to the identity line (slope = 1.18) compared to other simulations. This explains that along with subsurface percolation, the shortwave radiation distribution simulated the better ET. In 2D-PD and 2D-WD simulations, the linear slope equals the slope of the pixel run (slope = 1.55) which corresponds to much higher evapotranspiration compared to observation. Shortwave radiation distribution (Fig. 4.7d) showed the most important impact in our measurement area. Shortwave radiation distribution showed the smoothed runoff curve, higher subsurface percolation, increased base flow and increased runoff. The corresponding reduced ET in 2D-SD (and 2D-AD), averaged on the footprint area, also corresponds much better to the observations.

4.5.3 Hydrological budget

Annual water budgets (Table 4.2) show that the shortwave radiation distribution and subsequent ET calculation has large impact. It made a difference of ∼100 mm at the annual budget scale. This increases runoff from 73% to 79% of the total annual precipitation by diverting the difference of flux towards runoff. This also result in the water storage change over the year as explained in previous section. As we started from the same initial conditions for all simulations and additionally run the spinup for another 2 years, it reached more than 10 mm in subsurface storage when SW is reduced (1D-AM, 2D-AD and 2D-SD) and 5.96 mm for 2D-WD simulation. The subsurface storage change remains much smaller than the ET difference and doesn't impact the runoff coefficient.

Simulations	Precipitation (mm)	Runoff (mm)	Runof coef.	ET (mm)	Subsurface storage (mm)
1D-PM	1443.72	1060.74	0.73	372.94	-0.62
1D-AM	1443.72	1159.99	0.80	263.30	10.66
2D-AD	1443.72	1142.30	0.79	266.78	11.68
2D-PD	1443.72	1058.87	0.73	361.48	-0.78
2D-SD	1443.72	1136.39	0.79	269.71	14.98
2D-WD	1443.72	1062.48	0.74	372.23	5.96

Table 4.2: Annual water budget terms in the catchment for different simulations.

Figure 4.8 shows monthly water budgets for 2D-AD and individually distributed simu-

lations. Snow precipitation from November to March do not infiltrate much to fill up the subsurface storage (dotted line). January rain on snow events slightly reduce the subsurface storage. Very similar runoff values were observed up to the end of February among the different scenarios. In contrast, from mid March to June the subsurface storage was replenished by melting (Fig. 4.6) which later increases the runoff. The 2D-WD forcing produced the largest values of recharge (∼430 mm) and the 2D-AD the largest values of streamflow. From May to October, streamflow at the outlet and ET decreased the subsurface storage. Higher shortwave radiations (2D-PD and 2D-WD) led to longer ET periods. One can finally note that reduction in ET because of vegetation senescence in November and beginning of subsurface storage.

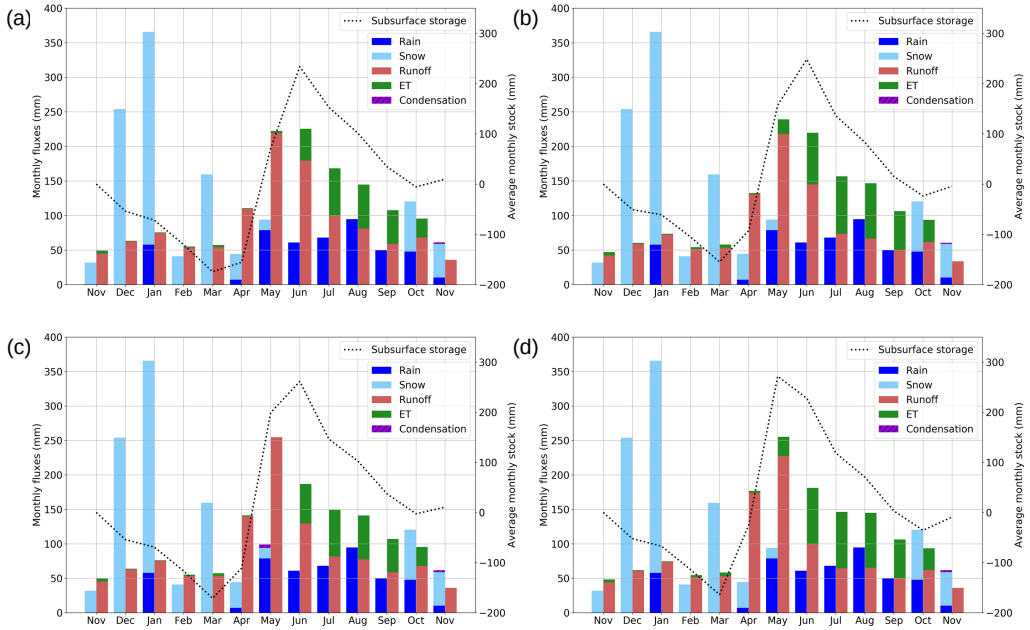

Figure 4.8: Same figure as 5b for (a) all distributed run (2D-AD), (b) only precipitation distributed run (2D-PD), (c) only shortwave radiation distributed run (2D-SD) and (d) only wind speed distributed run (2D-WD).

4.5.4 Snow dynamics

Figure 4.9 shows the temporal dynamics of the snow and the impact on albedo. Snow depth plots for Pix-PM run (purple line) and 1D-PM run (red line) were superimposed. The 1D-PM run show little variability in snow depth (red shading). The dynamics of these two runs is consistent with the observations (black line) although snow height is overestimated during

the initial accumulation period. This was probably because of the rough snow/rain partition temperature threshold and the inability of the snow scheme to account for compaction. The snowmelt dynamic particularly well simulated (snow cover within the Sentinel-2 image acquisition date), especially along the dry period at the end of April. In early May one can note some discrepancies again probably because of our limited ability to separate rain and snow in the precipitation forcing, close to the phase change temperature. This can be seen on the pixel simulated albedo which returned to its maximum snow albedo value at the end of the melting season (0.8), which was not the case in the observations. Concerning simulated albedo, it mostly follow the observations, however, the snow age parameterisation in the model was not adequate enough to simulate the albedo where observation show albedo decrease during melting period.

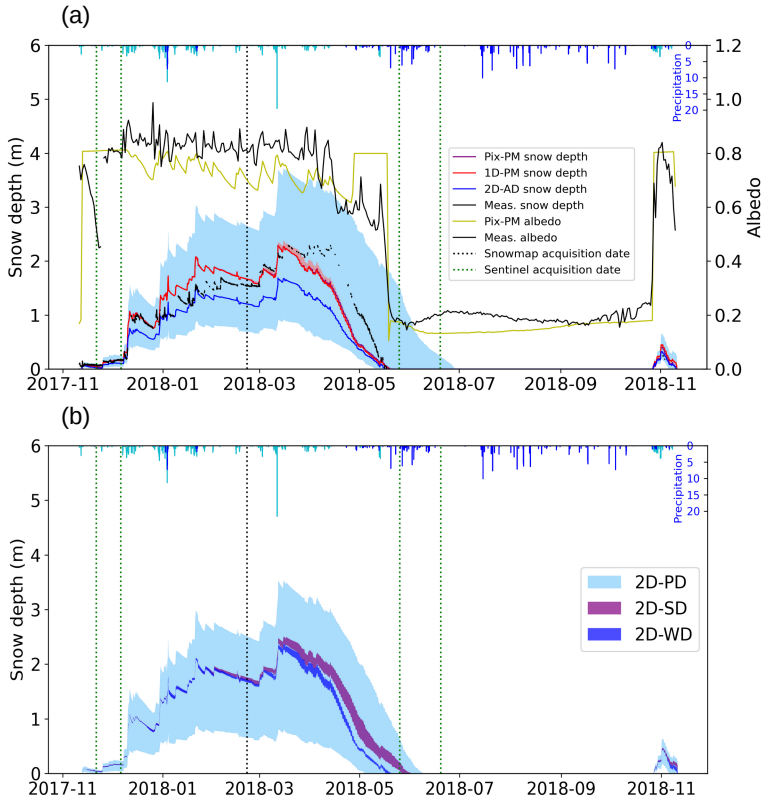

Figure 4.9: (a) Snow depth (left axis) for different simulations compared with observations (black line). Colour lines are the average depth over the catchment and shadings the spatial variability. Right axis: observed (black line) and 1D-PM simulated albedo (yellow line). Averaged precipitation (rain in blue and snow in cyan) are plotted at the top of the graph. (b) same as (a) but for the only precipitation (2D-PD), only shortwave radiation (2D-SD) and only wind speed (2D-WD) distributed run.

In the 2D-AD simulation the snow cover becomes discontinuous early in May and some

pixels stay covered with snow more than one month later compared to the 1D-PM simulation (Fig. 4.9a). Snow depth variability in the watershed, as indicated by the height of the shading in figure 4.9a, increases during the snow accumulation period, then diminishes during snowmelt. This effect can also be seen in the 2D-PD simulation but not in any other distributed forcing simulation (Fig. 4.9b). As 2D-AD and 2D-PD simulations were prescribed the same input precipitation and temperature, this means this effect (the deeper the snow, the faster the melting) was intrinsic to the snow scheme. On the contrary, 2D-SD simulation show a slight increase of depth variability during the melting period.

It can be observed in figure 4.9b that none of the individually distributed simulations show longer snow cover compared to the all distributed simulation (Fig. 4.9a). It indicates that simulating the variability of snow deposition and transport patterns during snow accumulation was not enough to capture the actual behaviour of snow dynamics. It is the combination of precipitation and shortwave radiation distributed forcing that resulted in the longer duration of the snow cover and the development of the typically observed patchiness at the end of the season. Longer snow period resulted from the precipitation spatial variability during accumulation events and differential snow melting resulted from the shortwave radiation spatial distribution. The 2D-WD simulation showed low snow depth variability which was very similar to the 1D-PM simulation at the end of the snow accumulation period (Fig. 4.9b). However, along spring (mid-March to end of April) it produced the same snow depth spatial variability as 2D-SD and higher snowmelt regimes (Fig. 4.9b and 4.6d). Wind speed distribution also result in snow patch through wind transport (accounted for in the snow distribution algorithm). In figure 4.9b, the 2D-WD simulation show a small increase in snow variability compared to 1D-PM simulation. However, the wind distribution favours more spatial dynamics when combined with other forcings.

Spatial distribution of snow cover during the melting period is shown on figure 4.10 for all simulations. On 21st of November first snow events were followed by a partial melting over the catchment (1^{st} row in Fig. 4.10). Our 2D-AD and 2D-PD simulations were partially good at representing this feature, but the simulated melting was overall not enough. Apart from the upper part of the catchment where snow distribution was not well controlled, the early snowmelt is located to the eastern edge of the catchment, a central area aligned with the river left bank and the outlet area. The 2D-AD simulation has more snow cover than 2D-

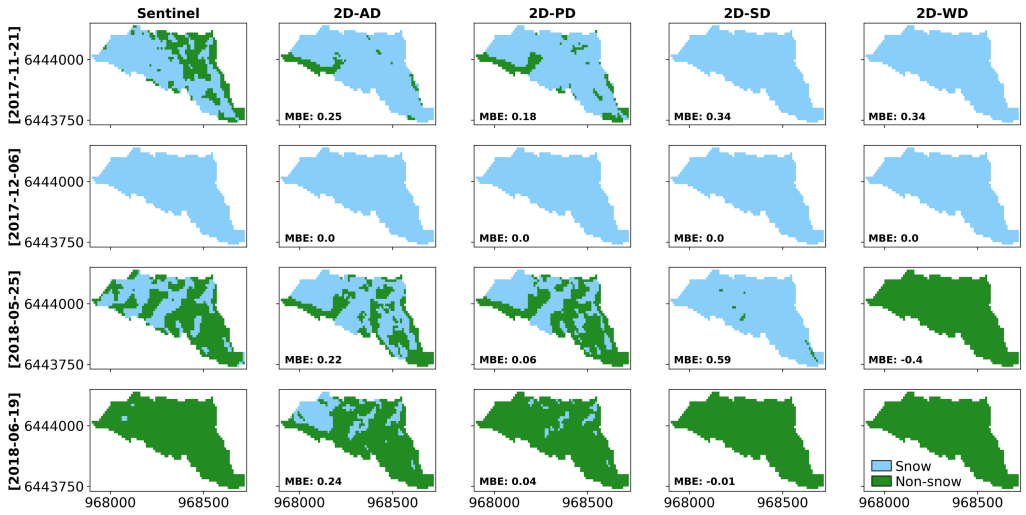

Figure 4.10: Snow map for different simulations compared with the Sentinel-2 images for 4 cloud free images: snow pixels (light skyblue) and non-snow pixel (green). MBE is the mean bias error between the model and Sentinel-2 image.

	Satellite platform	Date of acquisition	Resolution (m)	Cloud cover (%)	Cloud cover over catchment (%)
1	Sentinel 2B	2017-11-21	10	1.2	None
2	Sentinel 2A	2017-12-06	10	3.3	None
3	Sentinel 2A	2018-05-25	10	12.8	None
4	Sentinel 2B	2018-06-19	10	2.1	None

Table 4.3: Images characteristics from ESA's Sentinel-2 mission.

PD because of reduced incoming radiation caused by a reduced solar angle which decrease the melting. On 6th of December, the catchment was completely covered by snow for all simulations. It has to be noted that this date corresponds to early season snow events when the 2D-AD and 2D-PD simulations were able to represent the snow dynamic even for very low snow depth. This means in particular that 1) our model spinup has well initialised the ground temperature profile and its distribution and 2) our distribution algorithm was well adapted, especially for snow deposition. On 25th of May the snow cover has partially melted, developing kind of snow patches typical at this advanced stage of the melting season. Again 2D-PD simulation represents very well the snow pixels to non-snow pixels ratio and the snow distribution (MBE = 0.06). One can see on both Sentinel-2 image and 2D-PD simulation some SW-NE alignment, slightly present on the snow distribution coefficient map

(green/blue pixels on Fig. 4.1c), the timing of disappearance was remarkably well simulated for these pixels. The 2D-AD simulation has more snow cover than 2D-PD simulation and Sentinel-2 image on 25th May (MBE = 0.22). However, we showed (section 4.5.2) that the 2D-AD simulation was better in simulating the snow variability and evapotranspiration compared to 2D-PD simulation. The overestimation in 2D-AD simulation may come from the snow distribution scheme or the albedo scheme of CLM.

Table 4.4 shows the performance indicators for different spatio-temporal variables in the catchment. The goodness of fit for evapotranspiration was better when we distribute shortwave radiation in the catchment. 2D-AD and 2D-SD simulations have better value of slope, R^2 and RMSE. Albedo simulation was more dependent on the snow stay in the catchment. Hence, the simulation where we distribute precipitation (2D-PD) showed better accountability in albedo simulation. Higher R^2 value for albedo in 2D-WD distribution may come from the initial accumulation of a large amount of snow. However, we have shown that snow in this simulation melts quite early compared to other simulations. Finally, precipitation distribution was more important for the spatial snow cover. However, shortwave radiation influence the late melting pattern. In the Sentinel-2 images, the higher performance of 2D-PD simulation than 2D-AD may come from the precipitation distribution itself. Looking at performance indicators together, we could see that 2D-AD was the best simulation which captured the spatial and temporal pattern of evapotranspiration and snow cover in the catchment. It means that precipitation and evapotranspiration need to be distributed together for a more accurate representation of hydrological fluxes.

4.6 Discussion

The presented simulations disentangle the combined effects of precipitation and solar radiation distributions. This makes us able to simulate a realistic patchy snow cover at 10 m resolution (Fig. 4.10) which is a commonly observed phenomenon over mid-elevation mountainous catchments (Revuelto et al., 2020). The Lidar-based snow distribution map is particularly effective for its accurate prediction of distributed snow depth in mountain and forest landscapes as recently suggested (Painter et al., 2016; Hojatimalekshah et al., 2021; Jacobs et al., 2021). We moved one step ahead in using the Lidar map to distribute snow precipitation over the catchment in hydrological models. The all distributed simula-

Variable		Metrics	2D-AD	2D-PD	2D-SD	2D-WD
ET		Slope	1.18	1.55	1.18	1.55
		R-Square	0.44	-0.36	0.44	-0.34
		RMSE	50.77	79.14	50.90	78.41
Albedo		R-Square	0.85	0.88	0.77	0.85
		RMSE	0.12	0.10	0.14	0.12
Snow-cover	MBE	(21 Nov, 2017)	0.25	0.18	0.34	0.34
(Sentinel-2)		(06 Dec, 2017)	0.00	0.00	0.00	0.00
		(25 May, 2018)	0.22	0.06	0.59	-0.40
		(19 June, 2018)	0.24	0.04	-0.01	-0.01
	RMSE	(21 Nov, 2017)	0.63	0.65	0.58	0.58
		(06 Dec, 2017)	0.00	0.00	0.00	0.00
		(25 May, 2018)	0.74	0.75	0.78	0.63
		(19 June, 2018)	0.50	0.23	0.07	0.07

Table 4.4: Statistical metrics for observed and simulated parameter among different simulations (MBE: mean bias error, RMSE: root mean sqare error).

tion (2D-AD), which encapsulates snow distribution (based on snow map) and shortwave radiation distribution (based on small scale terrain), efficiently simulate the snow cover and evapotranspiration spatio-temporal dynamics in our test case. However, this simulation shows a ∼20-day delay in complete snowmelt due to reduced solar radiation, when the solar angle and terrain aspect are taken into account (Fig. 4.9). One reason could be that we might slightly overestimate snow deposition when using the snow coefficient map. Indeed, the yearly spatial average amount of snow/precipitation (1442 mm) is not the same as what is measured with the gauge (1530 mm) and at the moment, we have no means to control the average value we used in this study. This leads to an uncertainty on the cumulated snow amount that could be tuned globally with the snow coefficient map. Another reason might be the lack of melting, which could come from the snow albedo calculation in ParFlow-CLM. Indeed, looking at Fig. 4.9, snow aging reduces too much the albedo during winter months and gives an albedo too high in April when it is re-initialized to its fresh snow value because of very small snowfall events. Those fresh snow episodes also decreased the simulated melt-

ing in the catchment during spring. Both of these defaults should be further corrected with an up-to-date snow scheme and a tuned snow coefficient map for a more precise snow depth distribution.

Our study focuses on the impact of terrain slope and aspect on the simulated spatio-temporal dynamics of snow cover and evapotranspiration in critical zone hydrological models, as this has become a debated issue in recent years (Rush et al., 2021; Parsekian et al., 2021; Fan et al., 2019). However, these are not the only source of variability. Elevation based precipitation distribution (Dahri et al., 2016; Avanzi et al., 2021; Jabot et al., 2012) and land-use based spatial evapotranspiration patterns (Yan et al., 2018; Melton et al., 2021) have also a large impact on mountain hydrology and have been studied extensively in the last few decades. In the studied catchment we considered that land use variability was not the main driver for hydrological responses and temperature differences within the 200 m elevation gradient were partially accounted for through the laser scan map of snow deposition. If one would like to upscale the results to larger catchments with higher land use variability and higher elevation gradients, then temperature variability and land use variability should be accounted for together with terrain slope and aspect.

This study shows large sensitivity of evapotranspiration to incoming solar radiation corrections (decrease in regression slope from 1.55 to 1.18). In the presented results, evapotranspiration spatial average remain larger than observations. The reason to overestimate evapotranspiration could come from our footprint area (Oishi et al., 2008) which is not as precise as it should be. However, it has been highlighted in many studies that comparing simulation of spatially heterogeneous variables with point observation is a difficult task (Pradhananga and Pomeroy, 2022; Zhu et al., 2021; Iseri et al., 2021). In our case, footprint area calculation from Eddypro (Kljun et al., 2004) gave an average peak distance of $\sim$70 m and a 90 % contribution distance of $\sim$400 m for summer months daily hours. These distances are larger than the catchment width in the upwind direction and include areas not simulated. Moreover, the theoretical background of footprint calculation supposes a flat terrain with a fully developed turbulent surface layer. This is not the case in our terrain which is undulating, inducing moisture heterogeneity with some wetlands in the lowlands. For these reasons, we chose a simpler approach for the first order estimation of model performance, but considering soil moisture heterogeneities through wind direction mask (Fig.

4.1). We hypothesize this spatial average is better than a single pixel to compare simulated evapotranspiration series with observations.

ParFlow-CLM is a critical zone physically based model built to closely follow the physics of hydrological processes (Kuffour et al., 2020; Tran et al., 2020). This requires reliable data for forcing, ground, vegetation and hydrology to keep consistency in the model framework while simulating water path with the same accuracy. We chose to work with local observations, from which we built distributed forcing based on the presented algorithm to evaluate the model (Liston and Elder, 2006). The model calibration itself consisted in building the model, which means underground geometries and their associated parameters, only from observations . Building a model from observation is use to enhance our ability to understand the physical processes from hydrological modeling (Sidle, 2006, 2021). However, we don't have spatial observations for each pixel. We then built the model on assumptions that what we measure at a place is also valid for similar places where we do not have measurements. Available observations then restrict ranges to tune the model once we consider embedded parameterization, which explicitly solves melting and evapotranspiration following physical laws. Finally, we forced the model with reliable observed meteorological data. From this approach, we simulated the importance of snow processes and the role of incoming radiation distributions. Indeed, the model has been evaluated against the radiation budget observation (albedo), energy budget observation (latent and sensible heat fluxes), water budget terms including snow cover, the ability of the model to produce baseflow, and snowmelt timing (Table 4.4). Validation with Sentinel-2 images during accumulation and melting period shows that simulations followed the observations in terms of onset and offset of snowcover.

The last remark about the model configuration is that the domain has a no-flow boundary condition on the sides and at the bottom of the domain (Chen et al., 2022; Kollet and Maxwell, 2006). It restricts the option of flux leaving from the domain only through ET and streamflow. In other words, this means that larger scale flow paths (water that enters from the sides of the domain or that gets out through the bottom of the domain) are not simulated although it may exist for high altitudinal mountainous catchments. This subsurface water transfer could also lead to small differences in outlet and evapotranspiration partitioning but it will not change the conclusions of this study. We started some particle tracking calculations from 3D velocity fields produced by ParFlow for our simulations. They show a

very weak percolation and transfer to deep horizons. Most of the water transfers occur in the first 10 layers. It further adds that the flux leaving the bottom of the domain is not so much of a concern.

Importance of critical zone processes in improving the understanding of hydrological cycle is strongly debated (Arora et al., 2022; Wlostowski et al., 2021). These processes often remain unexplored in large scale hydrological models. Fan et al. (2019) recommended to include slope/aspect effect and soil depth in the ESMs to improve the hydrological cycle and its feedbacks on the climate. Our study contributes to this identified issue along with an algorithm to take into account surface heterogeneity. In this study, we precise how slope/aspect impact hydrological budget given spatial variability in the meteorological forcing along with surface to subsurface transfers, and how it can be successfully included in critical zone hydrological modeling. The adopted algorithm efficiently captures the surface heterogeneity in the snow cover and evapotranspiration. The same algorithm also influences the temporal distribution of snowmelt and water balance. The approach of meteorological distribution and cross validation from field observations and Sentinel-2 remote sensing images is also valid for subsequent years in the catchment. This will be presented in the companion paper to be published. This highlights the importance of slope, aspect, and curvature inclusion in hydrological studies.

4.7 Conclusions

Earth system models are gaining ample highlights in socio-economic impact studies. They include more and more processes, including the complete continental water cycle, but still face difficulty to parameterize small scale sub-mesh processes. These processes are crucial in mountain landscapes, both for surface hydrology and their feedback on climate. In this study, we modeled the spatial variability of the snow cover over a small mid-altitude catchment and its impact on the hydrological budget using the 3D critical-zone model ParFlow-CLM at 10 m resolution. For this purpose, we prepared distributed forcings for precipitation (that mimic snow transport), incoming solar radiation (that includes differential snow melting), and wind speed to force the model. The major conclusions of the study could be summarised as:

- Precipitation distribution (including wind redistribution) has the largest impact on

driving the patchiness of the snow cover in the catchment. This leads to one month longer presence of snow in the catchment when accounting for precipitation distribution in simulations compared to simulations ignoring it.

- Modulation of incoming solar radiation by the local slope in the catchment is the second most impacting topographic parametrization for melting as well as for evapotranspiration which then impact the water budget of the catchment.

- Distributing wind speed according to the terrain induces some spatial variability in the simulated snowmelt at the heart of the melting period, but reduces this variability at the end of the melting period.

- Most hydrological processes are slope dependent, but it is merely taken into account in land surface and hydrological models. The study quantifies the hydrological impacts in terms of melting, streamflow, and evapotranspiration dynamic when taking into account, or not, the slope effect. Considering critical zone models applied to mountainous area, we strongly recommend to consider subgrid-scale slope/aspect effects in large scale models, especially when they are used for hydrological studies. It will improve the spatial representation of snow processes and evapotranspiration and minimise biases in water resource management.

4.8 Code and data availability

The published datasets are available at doi.org/10.18709/PERSCIDO.2022.09.DS375, which includes the ParFlow version used in the study, forcing datasets for the non-distributed and all-distributed forcing, input and TCL script to launch ParFlow. The source code for the ParFlow version used in this study is available to clone from:
(https://github.com/aniketgupta2009/treeac-alp-parflow-ver-meteo.git).

4.9 Acknowledgements

A. Gupta, A. Reverdy, J-M. Cohard, designed the experiments and prepared all the necessary inputs to run the model, and A. Gupta performed the simulations. R. Maxwell

and B. Hector developed the model ParFlow-CLM Model version for this study, D. Voisin processed the required meteorological data, M. Descloitres and J-P. Vandervaere provided soil and aquifer properties, C. Coulaud, L. Ligier and R. Biron manage Eddy Covariance micro-meteorological station and all field works at Lautaret Pass, J-G. Valay and D. Voisin brings the necessary support to make this study possible. A. Gupta, J-M. Cohard and D. Voisin analyzed the simulations. A. Gupta and J-M. Cohard prepared the manuscript with contributions from all co-authors.

This research was conducted within the Long-Term Socio-Ecological Research (LTSER) platform Lautaret-Oisans, a site of the European Research Infrastructure eLTER. It received funding from the Lautaret Garden (Univ. Grenoble Alpes, CNRS, LAUTARET, 38000 Grenoble, France), a member of the Zone Atelier Alpes and the eLTER network and from ANR project ANR-15-IDEX-02.

4.10 Synthesis

We have constructed a fully distributed coupled hydrological model in the complex mountainous terrain. The model can solve the fluxes like runoff, evapotranspiration and subsurface variations; and simulates the albedo, snow depth and spatial snow coverage. The chapter focuses on surface meteorological distribution and capturing the impact of distributed forcing adaptation. We have distributed the surface meteorological forcing based on terrain characteristics like slope, curvature and aspect (solar angle). For this purpose we have chosen three meteorological variable viz. precipitation, shortwave and wind. We have shown that our method is able to capture the spatio-temporal distribution of snow in the catchment. We have validated the temporal and spatial snow dynamics with the observed snow depth and Sentinel-2 satellite images, respectively. We have also shown that spatio-temporal distribution of snow affects the hydrological fluxes in subsurface and evapotranspiration. We further investigated that the precipitation distribution has a dominant impact on snow processes in the catchment. Shortwave radiation distribution has impact on evapotranspiration processes and snowmelt processes. Wind distribution on its own doesn't have any direct impact however, it accelerates the snowmelt processes when combined with other variables.

The study highlights the gap in upscaling the processes in large ESMs. We have shown that the heterogeneities in small mountain catchment can produce large difference in flux.

The snowmelt contribution in such a small catchment can vary in its temporal and spatial scale if modeled accurately. And this could creates a flux difference to river, subsurface and soil moisture. The method presented in the chapter is based on local topography hence can be applied to any other geographical location. We further suggest that the along with slope, aspect and subsurface depth, the terrain based meteorlogical processes should be reasonably upscaled to reduce the societal risk through water resource modeling. The chapter develops the foundation for the further study which will incorporate the distributed surface meterological algorithm to model the flow in subsurface and calibrating the model against the discharge data.

5 Impact of subsurface heterogeneity

This chapter describes the sensitivity of the subsurface parametrization in the studied catchment. The subsurface in mountainous catchment plays an active role in stream runoff, soil moisture, and evapotranspiration. However, little is known about the sensitivity of the subsurface in simulating a mountain block. The chapter focuses on the sensitivity of the homogeneous and heterogeneous subsurface in simulating the runoff and capturing the surface fluxes like soil moisture and evapotranspiration. The subsurface in the study is designed on factual geophysical data and conceptual models. The study will investigate the impact of constant and variable hydraulic conductivity on surface-subsurface connectivity.

Distributed meteorological forcing has been adopted to run the simulation for subsurface sensitivity. As snow plays a crucial role in spatio-temporal dynamics of the hydrological fluxes. And we have shown that in distributed forcing simulation the snow lasts longer because of the delay in melting. In view of these points, a few changes in the model have been done from Chapter 4 to better account for albedo compared to observed data. These changes include the albedo tuning from CLM snow age and snow albedo modules.

Snow albedo in CLM is taken from the BATS (Dickinson, 1993) and represented as:

$$\alpha^{\mu}_{sno,\Lambda} = \alpha_{sno,\Lambda} + 0.4 f(\mu)[1 - \alpha_{sno,\Lambda}] \tag{5.1}$$

where function $f(\mu)$ is a factor between 0 and 1 giving the increase of snow albedo due to solar zenith angle exceeding 60°. The diffused albedo is represented as,

$$\alpha_{sno,\Lambda} = [1 - C_{\Lambda} F_{age}]\alpha_{sno,\Lambda,0} \tag{5.2}$$

where, $\alpha_{sno,\Lambda,0}$ is the albedo of the new snow, F_{age} is a transformed snow age accounting for the fractional reduction of snow albedo due to snow aging (increasing grain size and dirt/soot content) and represented as,

$$F_{age} = 1 - \frac{1}{1 + \tau_{sno}} \tag{5.3}$$

where τ_{sno} is an incremental variable depending upon the time steps and represented as,

	Waveband (Λ)	
Parameter	vis	nir
C_Λ	0.2	0.5
$\alpha_{sno,\Lambda,0}$	0.95	0.65

Table 5.1: Snow albedo parameters.

$$\Delta\tau_{sno} = \begin{cases} \tau_0(r_1 + r_2 + r_3)\Delta t & \text{for } 0 < W_{sno} \leq 800 \\ 0 & \text{for } W_{sno} > 800 \end{cases} \tag{5.4}$$

where, Δt is the model time step (T^{-1}), τ_0 is constant equal to 1×10^{-6} (T^{-1}), and W_{sno} is the mass of snow water (ML^{-2}), r_1 represents the effect of grain growth from vapour diffusion,

$$r_1 = \exp\left[5000\left(\frac{1}{T_f} - \frac{1}{T_{snl+1}}\right)\right] \tag{5.5}$$

where, T_{snl+1} is the surface temperature of the top snow layer, r_2 represents the additional effect near and at the freezing of meltwater and r_3 represents the effect of dirt and soot,

$$r_2 = r_1^{10} \leq 1 \tag{5.6}$$

$$r_3 = 0.3. \tag{5.7}$$

In conditions of fresh snowfall, this aging parameter is reduced by a factor depending on the amount of new snow. However, while running the model it has been observed that the snow albedo goes to its highest value because F_{age} factor becomes zero during the peak snowmelt season. Also, the default snow albedo in CLM has a max value of 0.8 ((0.95+0.65)/2) (Table 5.1). However, our field observations show that albedo does go up to maximum values higher than 0.9. To tackle this problem the CLM albedo and snow age parameters are modified according to table 5.2 and the resulting albedo calibration is shown in figure 5.1. The albedo simulation shows that with the original scheme the model fails to simulate the decrease in albedo during the melting period. Albedo attains its maximum

Time step (half-hourly)	$\alpha_{sno,\Lambda,0}$ (vis, nir)	Time step (half hourly)	F_{age} (r_1, r_2, r_3)
$\leq$ 3984	(95, 75)	$\leq$ 2112	(0, NC, NC)
$\geq$ 3985 $\leq$ 5088	(90, 70)	$\geq$ 2113 $\leq$ 3984	(0, NC, 0)
$\geq$ 5089 $\leq$ 6768	(95, 75)	$\geq$ 3985 $\leq$ 6240	(NC, NC, NC)
$\geq$ 6769 $\leq$ 7200	(95, 75)	$\geq$ 6241 $\leq$ 7200	(NC, NC, NC)
$\geq$ 7201 $\leq$ 15264	(85, 65)	$\geq$ 7201 $\leq$ 15264	($F_{age} = 1$)
$\geq$ 15265 $\leq$ 17568	(95, 75)	$\geq$ 15265 $\leq$ 15668	(NC, NC, NC)

Table 5.2: CLM changes to snow albedo and snow age parametrization, time steps are half hourly forcing time steps for model and NC represents no change in the parameter.

value which slows down the melting during early spring. With the newly calibrated albedo, the model simulates better runoff and spatial snow patterns. These aspects will be discussed further in this chapter.

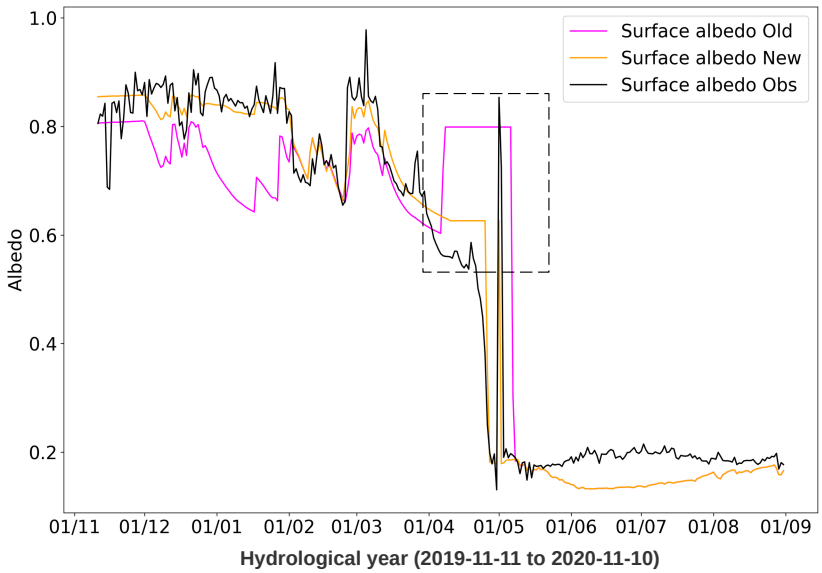

Figure 5.1: Albedo simulation from pixel run after accounting the modification from Table 5.2. In the highlighted box F_{age} parameter forces the albedo to attain its maximum value.

Along with snow albedo and snow age parameters, snow emissivity in 'clm_thermal' module has been changed from 0.97 to 0.98 (field measurement). Finally, the snow map from the Chapter 4 has been also modified for this Chapter. The snow map had been assigned a constant value which was leading to very rapid melting in the head of the catchment. The modified snow map is filling of the undetected pixels using inverse distance weighting (IDW).

First, the border pixel was assigned with the snow coefficient equal to the steep slope in the lower part of the catchment. Then using the IDW methods the data gaps are filled. The modified snow map is shown in figure 5.2.

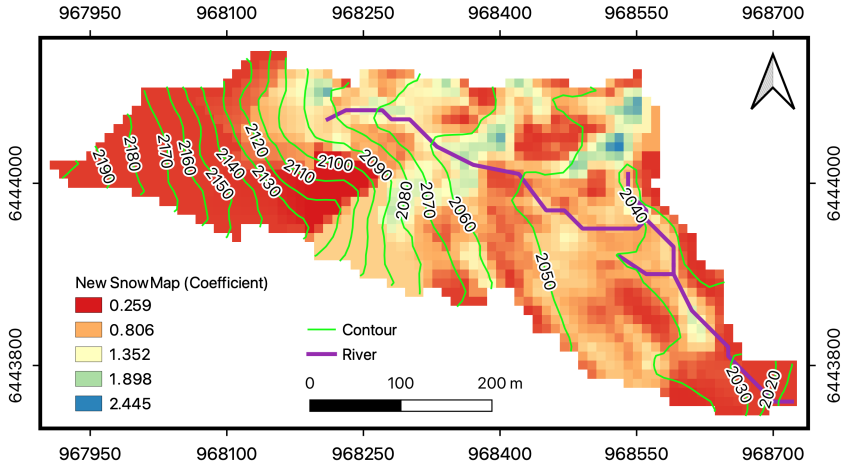

Figure 5.2: Modified snow map coefficient in the upper part of the catchment.

From hereon, this chapter is based on the following citation which is under preparation: Improving hydrological modeling of the critical zone using geophysical data: an example in small scale mountainous catchment, in preparation for Water Resource Research, AGU.

Abstract

As it results from complex geological and pedological processes, the subsurface flow quantification and its role in the hydrological budget is a major issue. In this study, we conducted geophysical and geological surveys to investigate the subsurface and in parallel built conceptual models to represent their subsurface equivalent. The five conceptual models adapt different homogeneous subsurface layers and the two other models adapt heterogeneous layers with varying depths based on the geophysical survey. The geophysics exploration includes geological and pedological characterizations, and electromagnetic and radar surveys. We followed an approach from the simpler to the more complex subsurface configuration. We begin with single-layer subsurface model based on surface hydraulic properties from field data to a three-layer model with constant depth based on geological knowledge and hydraulic properties measured in a tunnel present in the watershed. Then we moved to more complex models with varying layer depth after incorporating the electromagnetic and radar data. For our 15.28 ha alpine catchment at Lautaret pass, the results show that three-layer homogeneous and three-layer heterogeneous models are comparable in runoff (KGE_{np} = 90, 91), soil moisture (MAPE = 0.23, 0.21) and evapotranspiration (MAPE = 6.66, 6.61). This similarly comes from the presence of an active regolith layer located at optimal depth which is responsible for the storage and release of snowmelt. We have argued that conceptual homogeneous models might solve the hydrological purpose only if they were built on reliable geophysical data. The properties of subsurface layers, their thickness, and depth are crucial parameters for constructing a conceptual model. However, we have also shown that the heterogeneous model is slightly better at capturing the snowmelt amplitude, baseflow, evapotranspiration and surface heterogeneities. These small differences might impact the hydrological fluxes in larger catchments or different climatic settings.

5.1 Introduction

Although the importance of subsurface processes for catchment scale hydrology has long been known, quantitative approaches addressing them in realistic hydrological studies have only emerged recently (Rapp et al., 2020; Markovich et al., 2019; Claes et al., 2020). Developing and implementing subsurface models in hydrological studies is the first step to start with the understanding of the Critical Zone (CZ) hydrological response (Claes et al., 2020; Robinson et al., 2008). Porosity, permeability, and suction are the essential hydro-dynamical characteristics that govern the water fluxes in the subsurface from and to the surface (Emerson, 1990; Lofi et al., 2012). These hydro-dynamical parameters are strongly influenced by geology, topography, and surface characteristics such as biosphere, and pedosphere driven by climate (Soulsby et al., 2006; Toth, 1971; Tooth et al., 2002; Kirkby et al., 2002; Rains et al., 2008). However, researchers face two general types of problems when characterizing the subsurface of a catchment. The first one concerns the minimum knowledge relevant for hydrological studies to simulate water flows (Kampf and Burges, 2007; Camporese et al., 2010). This also includes the question of how deep the subsurface should be to account for all flows (Condon et al., 2020). The second is how to characterize the subsurface with cost- and time-effective methods (Binley et al., 2015). As the proper subsurface characterization is extensive and expensive, hydrologists adopt multiple approaches to constrain the subsurface characteristics as much as possible (Robinson et al., 2008; Hubbard and Rubin, 2000).

Among the available methods for subsurface characterization, auger and sieves together with pedotransfer functions provide us with the upper-surface drainage conditions. It includes soil texture and properties, and a first estimation of associated hydrodynamic characteristics (Becker et al., 2018; Obi et al., 2014). These can be accompanied by infiltration experiments, mercury porosimetry, and soil pits, which are considered cost-effective solutions for the upper-surface characterization (Guo et al., 2020; Parsekian et al., 2015; Kuntz et al., 2011). However, these methods are at the plot scale and have to be upscaled to document soil properties variability with depth and horizontal directions at scales of interest (catena, catchment, etc.). Apart from direct methods, geophysical methods provide alternatives to map the underground more deeply and more extensively (Calamita et al., 2019; Hinnell et al., 2010). Most of the available geophysical methods have been used for oil and

mineral exploration (Robinson et al., 2008) or in civil engineering. They are now more and more adapted for hydrological prospecting. Out of the available geophysical methods, the frequency electromagnetic (FEM) and ground penetrating radar (GPR) became important methods for hydrological applications (Kowalsky et al., 2004; Robinson et al., 2008). The FEM method detects changes in permittivity associated with water content in soils, aquifers, and rocks pertaining to their hydro-geological properties (Auken et al., 2006; Spies, 1989). In mapping surveys routine, the method is widely used for giving a qualitative estimate of the ground electrical conductivity, the so-called apparent conductivity using a single separation between the sensors. As a result, FEM provides an estimate of the horizontal variations at a single penetration depth. When several spacings between sensors are used, one can obtain an estimate of the vertical conductivity variation with depth. Thus FEM helps to picture the spatial distribution of ground conductivity which further helps to estimate the soil thickness distribution. This method also helps to subgroup the area of similar conductivity, providing a means for reducing the amount of points measurements (auger, infiltrometers, pits, etc.) by targeting homogeneous zones in the area of interest. FEM has proven to be a decent method for mountainous catchments (Vignoli et al., 2012). In addition, the Ground Penetrating Radar (GPR) method is much more efficient to infer contrasting layers with significant permittivity differences (Kowalsky et al., 2005; Liu et al., 2019). The GPR method is highly recognized especially for deep surface investigation. Resolution and penetration depth depend on the antenna frequency used (Beres Jr and Haeni, 1991; Liu et al., 2019) but also on materials properties. Apart from FEM and GPR method, the electrical resistivity sounding and electrical resistivity tomography (ERT) as well serves as a prominent method for deeper (0-30 m) subsurface characterization. Electrical resistivity sounding is a quick 1D method more suitable for deep vertical exploration whereas the ERT provides a 2D mapping or panels from dozens of electrodes (Auken et al., 2006; Hauck, 2013). As these are all indirect methods, the concept of multi-method characterization of the subsurface is more a practiced idea in geophysical research.

Geophysicists and hydrologists have been teaming up in the last two decades on these issues. Hector et al. (2015) showed the application of gravimetry along with ERT to measure spatio-temporal changes of water storage and how this results in the generation of baseflow in African catchment. Descloitres et al. (2011) measured the actual evapotranspiration using

water table depletion inferred from magnetic resonance sounding and electromagnetic resistivity method. Some studies link soil moisture and infiltration through subsurface processes inferred from electrical resistivity tomography (Lehmann et al., 2013; Batlle-Aguilar et al., 2009). Moghadas et al. (2013) monitored the hydraulic properties of unsaturated zones using the GPR data and assimilate them with a process-based hydrological model. Several other studies have used the subsurface geophysical measurement either to measure hydraulic properties or to force hydrological models like Hydrus (Šimůnek et al., 2016) or others (Hector et al., 2018; Brooks et al., 2015; Francés et al., 2014; Robinson et al., 2008). However, the use of multiple geophysical methods to build the subsurface model and evaluate benefits of each kind of data remains limited.

Every hydrological model cannot benefit from distributed geophysical data. So far, many integrated models have been considering the surface-subsurface as a single unit instead of free-draining subsurface hydrology. One of the earliest models was the Integrated Hydrological Model (InHM) which simulated the integrated hydrology along variable porous media (Freeze and Harlan, 1969). The development of sophisticated computational techniques is turning integrated and coupled hydrology into a more tractable idea. This practice of surface-subsurface coupling was hidden with the models which use streamflow discharge for calibration. On the contrary, models have to represent explicitly and physically the subsurface processes with a gridded representation to be able to account for the observed contrasts and properties revealed by geophysical instruments (Beven, 1990; Baroni et al., 2019; Kuffour et al., 2020). Several hydrological models, among them HYDRUS, ParFlow-CLM, Hydrogeosphere, PIHM, etc., are able to assimilate geophysical data or sometimes simulate geophysical measured variables such as electric conductivity. All these models involve the solving of Richard's equation from surface to subsurface (in variably saturated media). To our knowledge, very few studies built their 3D hydrological model from geophysical data (Hector et al., 2018; Claes et al., 2020) and none of them evaluate the benefits in 3D from any of these data sources. However multi-method characterisation of the underground provides a gold mine of information, from which lithological models have been already extracted at small catchment scale (Hector et al., 2015), regional scale (Knight et al., 2016) up to country scale (Barfod et al., 2016). Geophysical data together with critical zone hydrological model can help in documenting the invisible subsurface flow path (Fan et al., 2019).

In this study, we show how the application of geophysical measurement improves our understanding of subsurface characterization and modeled water fluxes using ParFlow-CLM. We have also shown the necessity of the concept of surface-subsurface coupling and how this could be efficiently achieved through subsurface quantification using geophysical methods. Further onward section two includes a description of the study area and our catchment. Section three is more dedicated to the geophysical explorations achieved in the catchment. Section four has a description of the hydrological model and equations we adopted in this research. This section also includes the domain discretization and simulation setup. Starting from section five onward we will be presenting the results and discussion, section seven concludes the study at the end.

5.2 Study area

The study area is a small mountainous catchment (15.28 ha) in the heart of French Alpes close to the Lautaret pass (Fig. 5.3). The catchment itself lies from 2000 to 2200m ASL. It is mainly facing East. A small stream first collects water to a small clogged area before running down to the discharge station. It is monitored by a meteorological station, a flux tower to measure heat, H_2O and CO_2 turbulent fluxes, a discharge measurement at the outlet along with other in-situ physical and chemical measurement (snow tower, air sampler, dry and wet deposit, conductivity etc.). A tunnel crosses the catchment in its lower half and gives access to the underground regolith for characterisation approximately 3-4 m below the surface. The catchment has a long and chilled winter with a 5 to 6 months snow cover and subsequently develops a grassland in summer used for grazing. The bedrock of the catchment consists of thick turbiditic sandstones/shale alternations known as "Flysch des Aiguilles d'Arves". This paleogene formation overlies a structural unit called "Ultra-Dauphinois", a remnant of the European continental margin mostly subducted during the closure of the Western Thetys ocean at the beginning of the Alps orogen. The regional geodynamics is described in detail in Dumont et al. (2012). Briefly, two major shortening episodes are identified: D2 (N- to NW-directed) and D3 (W directed), with a change from D2 to D3 during the early Oligocene time. Since ∼32 Ma, the previously subsiding areas were uplifted and the syntectonic sedimentation shifted westwards. These general features were confirmed locally in and immediately around the catchment, which is entirely on one flank of a fold of this flysch formation. The fold

axis is oriented along the east-west direction, possibly corresponding to the D2 shortening episode. This fold axis is also tilted sub vertically towards the east in the upper part of the watershed and subhorizontally towards the west in the lower part, possibly in relation to the D3 shortening or the more recent uplifting of the west. This overall configuration means that the general bed orientation of the sandstone/shale alternations of the flysch formation loosely follows the watershed topography. Hence, the catchment's geological characteristics include the clay- and silt-rich soil on top of a highly weathered subsurface and finally the old hard rock at the bottom (flysch).

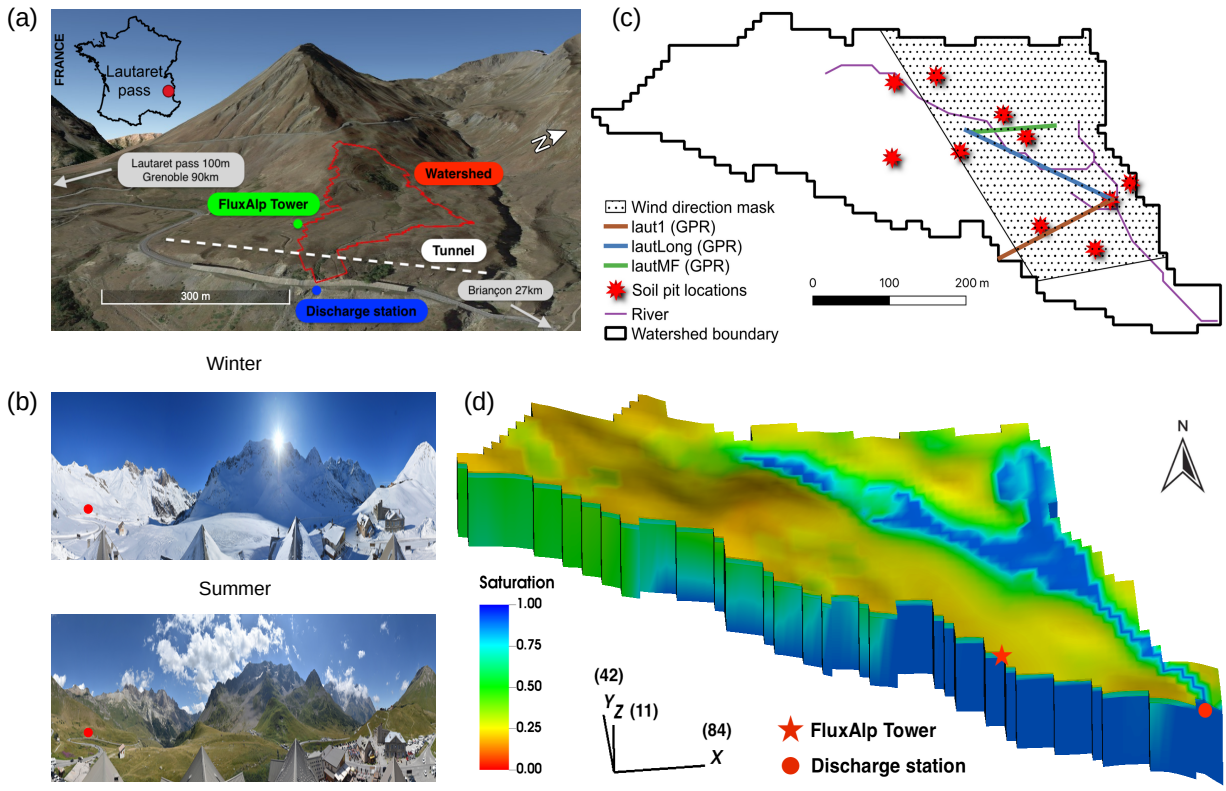

Figure 5.3: (a) Study area close to Lautaret pass (French Alps). The red line delineates the studied watershed Mostly facing East. (b) Seasonal contrast in the catchment (pictures from the Lautaret pass camera (c) locations of soil pits (red dots) and geophysical (colored lines) observations in the catchment along with wind direction mask (shaded area). (d) Initial saturation of simulations after 125 years of spinup.

5.3 Subsurface characterisation

Different methods and instruments used for geophysical investigation are compiled in Table 5.3. The geophysical measurement in the study site could be considered with three different

approaches. We present the methods in the following from the easiest one to get soil information from field campaigns to more specific geophysical methods which required inversion from electromagnetic to hydrodynamic parameters.

Geophysical investigations	Target properties	Method and instruments
Field survey	Porosity	Mercury porosimetry
	Permeability	Infiltration (Lefranc method)
	Density	Mass-volume method
	Humidity	Capacitive sensor
Electromagnetic survey	Soil distribution	EM38 (14500 Hz) and CMD Explorer (10000 Hz)
Electrical survey	Soil thickness and depth	ERT (Wenner and dipole dipole configuration)
Radar survey (GPR)	Deep soil layer	Radar (frequency: 250 MHz, 500 MHz, 800 MHz)

Table 5.3: Summary of the geophysical investigation in the catchment.

5.3.1 Surface soil measurement

Soil measurement includes different kinds of field experiments which could be classified as in-situ point experiments along with soil pit and infiltration experiments. One has to note that, for our study, the locations and distribution of these point experiments have been selected from the FEM and ERT investigations described in the next section.

The soil pits (Fig. 5.4), on average 0.60 meters deep, were analysed for porosity, dry density, and soil texture. The oven method involves the 24 hours soil cube drying at 105°C. The samples from the same pits were brought back to the laboratory for mercury porosimetry to reveal the pore structure and porosity of the samples, and to characterise Vangenuchten suction and permeability functions (Xu et al., 1997). The pressure range of the mercury porosimetry device extends from 3 kPa to 200 MPa, covering a pore range from 400 µm to 6 nm. The permeability test was performed using the Lefranc method (suitable for saturated soil) at a depth of 20 cm with a known tube diameter. Three sets of experiments were performed at 10 different locations (Fig. 5.3) and a precise rate of constant infiltration

function was used to determine the surface permeability at each location.

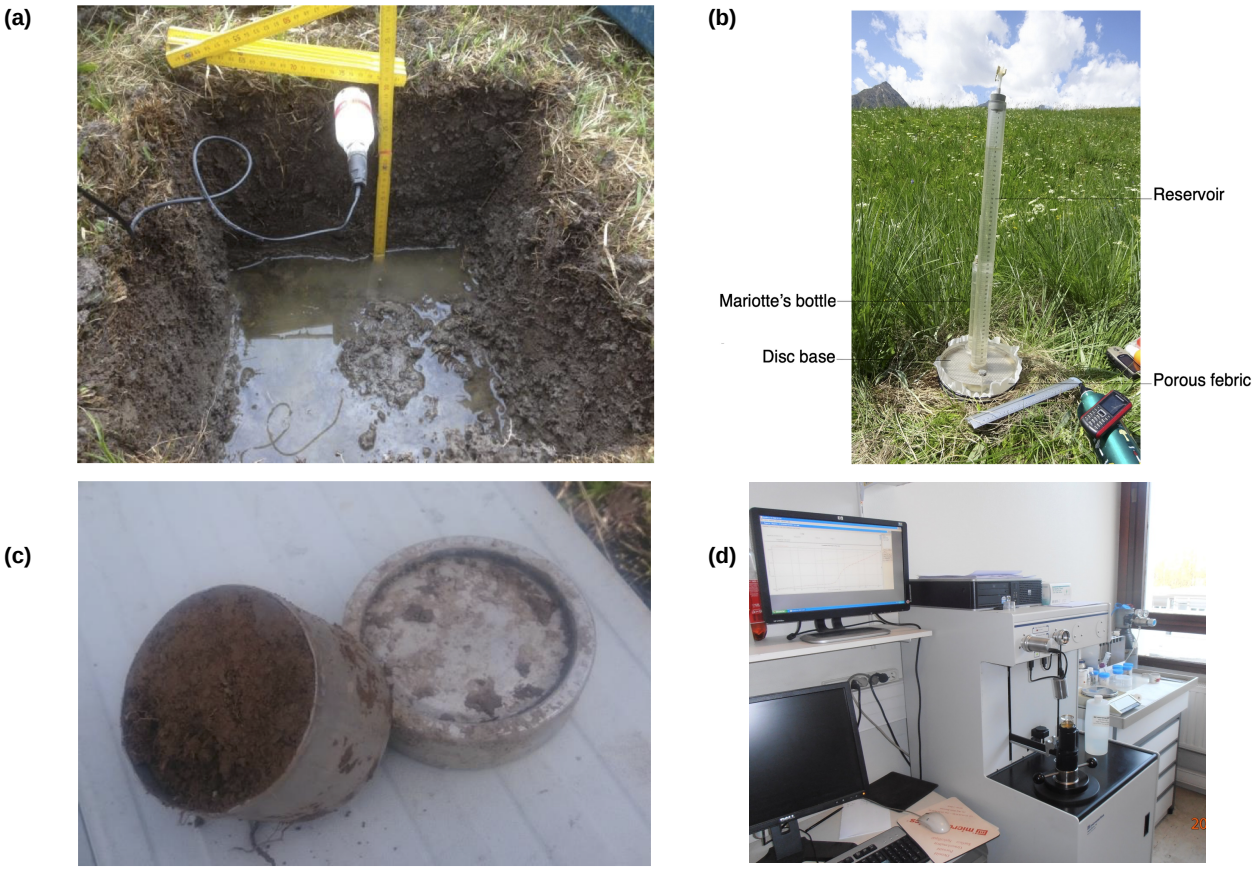

Figure 5.4: Preliminary field survey and experiment (a) Soil pit and humidity measurement (b) Infiltrometer to measure surface permeability (c) Density measurement of soil (d) Mercury porosimetry to measure porosity.

The same soil pits sites were also investigated using electrical sounding for getting a 1D distribution of electrical resistivity using the handheld Syscal Kid resistivity meter (IRIS Instrument). These soundings were performed using the Wenner configuration for a limited depth of investigation. Those 1D resistivity models have been also used to calibrate the Frequency Electromagnetic survey. Data obtained through those surveys were processed using the 1D inversion software (IX1D from Interpex).

5.3.2 Frequency electromagnetic and electrical survey

Electromagnetic surveys were used to get a lateral variation of the apparent soil conductivity transverse to the stream (Fig. 5.5a). The method consists in measuring the electrical apparent conductivity of the soil through the induction principle. A primary magnetic field

generated at the transmitter coil induces low current (eddy current) in conductive parts of the soil. Those eddy currents generate in turn a secondary magnetic field that is recorded with the receiver coil. The separation between the coils adjusts the penetration depth. The apparent conductivity of the soil is directly related to several parameters of interest: porosity, saturation degree, conductivity of the groundwater, and clay content providing a calibration with known soils (McNeill, 1980). Two types of electromagnetic probes were used for the electromagnetic profiling: the EM38 (14500 Hz) from Geonics and the CMD Explorer (10000 Hz) from GF Instruments. Both probes were used in two different modes, one is vertical and one is horizontal. EM38 probe has a simple spacing of 1 m between the transmitting and receiving coils. In vertical mode, the theoretical depth of investigation is 1.5 m and in horizontal mode, it is 0.75 m. It gave us just an overview around the soil pits. The CMD explorer has three coil spacing: 1.48 m, 2.82 m, and 4.49 m. The effective penetrations of each spacing for horizontal mode are 2.2 m, 4.2 m, and 3.4 m; and for horizontal mode, they are 1 m, 2.1 m, and 3.4 m. We finally surveyed the entire catchment with the CMD explorer in horizontal mode at 96 point locations (Fig. 5.5b). The three sets of apparent conductivity data for each coil spacing were transformed into grid maps using the Surfer 9 software. The Kriging method was used to interpolate in a grid format. Calibration was done using an ERT panel (Electrical resistivity tomography) with the Syscal pro resistivity meter (Iris Instrument). It consisted of 96 nos. 2 m spaced electrodes along the laut1 profile (Fig. 5.1). Inversion to a pseudo-cross-section of apparent resistivity was obtained using both Wenner and Dipole-Dipole configurations (Marshall and Madden, 1959; Wenner, 1916), taking into account the topography. Finally, after calibration of CMD explorer data with the ERT panel along the laut1 profile, IX1D software performed the 1D inversion of the calibrated CMD explorer data to convert electrical soil conductivity into actual soil thickness (Fig. 5.5c).

5.3.3 Ground penetrating radar

Ground penetrating radar (GPR) may provide the geometry of electromagnetic contrasts, such as geological horizons in sediments or between sediments and bedrock, with a fine resolution. The method is based on the measurement of the propagation time and amplitude of electromagnetic waves, which are reflected at electromagnetic contrasts and measured between a transmitter and a receiver. In natural environments, the amplitude and velocity

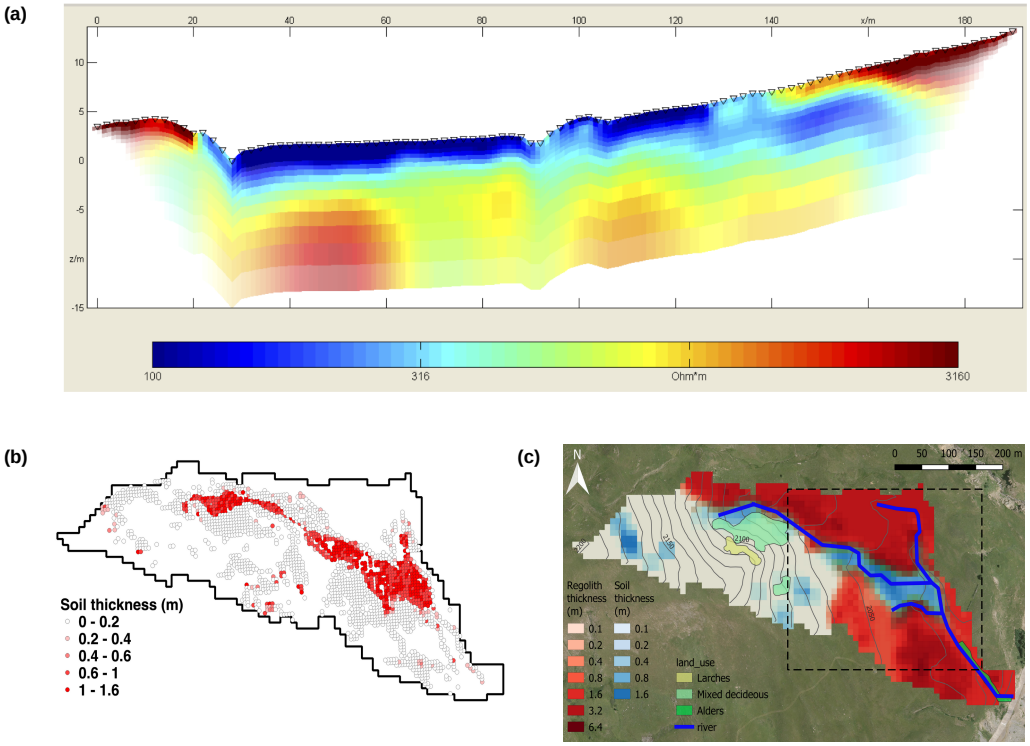

Figure 5.5: Electrical and magnetic survey in the watershed (a) Transverse profile of electrical resistivity tomography (Laut1) (b) Electromagnetic thickness points distribution. red color map indicates the interpreted soil thickness. (c) Soil and regolith thickness map deduced from geophysics survey. The red (resp. blue) color map is for soil (resp. regolith) depth. Dotted box is the area considered in figure 5.12.

of electromagnetic waves are respectively mainly controlled by the electrical conductivity and the dielectric permittivity of layers. In this study the GPR survey was carried out using 250 MHz, 500 MHz and 800 MHz shielded antennas in order to have different resolutions and penetration depths. GPR data are classically processed using zero-phase frequency filters with a band-pass adapted to each antenna frequency, a time squared gain amplification, elevation corrections, and time-to-depth conversions. For the two later processes, a velocity of 10 cm ns^{-1} was used. Three profiles have been done and are plotted in figure 5.3.

5.4 Hydrological modeling

Hydrological modeling in the catchment is performed using the ParFLOW-CLM a surface-subsurface coupled distributed hydrological model (Jones and Woodward, 2001; Ashby and Falgout, 1996; Kollet and Maxwell, 2006; Maxwell, 2013; Maxwell and Miller, 2005; Kollet and Maxwell, 2008). ParfFLOW-CLM simulates the surface water and subsurface water

interaction from simple to complex terrain. The physically based distributed model requires data from surface land use patterns to deep geological maps. Usually, the studied domain is gridded using a terrain-following approach and the model simulates the vertical as well as lateral fluxes. The land surface model (Dai et al., 2003) simulates the surface fluxes in grid column and ParFLOW simulates both vertical and lateral flux transfers at the surface and in the subsurface. Flow in saturated media is governed by Darcy's equation while the flow in unsaturated media is governed by Richards' equation in which relative permeability and suction properties are prescribed using the Van-Genuchten models. The mixed form of equation in variably saturated media is implemented as (Kuffour et al., 2020),

$$S_S S_W(p)\frac{\partial p}{\partial t} + \phi\frac{\partial(S_W(p))}{\partial t} = \nabla q + q_s \tag{5.8}$$

$$q = -k_s k_r(p)\nabla(p - z) \tag{5.9}$$

where S_S is the specific storage and considered in meter units for our study, S_W is the relative saturation as a function of pressure head (p) in meter, q is Darcy flux in m hr^{-1}, q_s is the source/sink term in hr^{-1}, k_s is the saturated hydraulic conductivity in m hr^{-1}, k_r is the relative permeability as a function of pressure head and z is the depth below the surface.

The overland flow in the model is fed by the sum of the saturation excess and the exfiltration, and it is routed using the two-dimensional kinematic wave equation. Overland flow represents the upper surface boundary condition of Richards equation as a function of pressure head. The kinematic wave equation and the Richards equation are solved simultaneously in a fully coupled PDE system. The direction of overland flow is determined by the D4 flow-routing scheme. This scheme allows transferring the flux to a maximum of one next grid which forces ParFLOW to minimize the time step to not allow the flux to travel more than one grid point. If the water travels more than one grid the ParFLOW solver fails and breaks the time step in two until it solves successfully the equations.

ParFLOW-CLM in this study was set up to a complex mountain domain of 84×42×11 (longitude×latitude×depth) grid size with terrain following grid. The model was set at the horizontal hyper-resolution of 10 m. The boundary conditions for the domain were set as no-flow for the bottom and sides of the domain. This leads to source/sink flux exchange only at

the surface of the domain. The model was run for one complete hydrological year (2019-2020) which starts on November 11th, 2019, and ends on November 10th, 2020. Subsurface in the model is divided into three geological types viz. soil, regolith and flysch. The Parflow model is vertically discretized into eleven grid cells distributed according to different combinations of these geological horizons for each simulation. The model is forced half-hourly and the outputs are stored each hour. A distributed meteorological forcing approach is adopted for the catchment and described in detail by (Gupta et al., 2022).

This study is more focused on the subsurface distribution and the associated lateral flows it generates in the catchment. Different kinds of homogeneous and heterogeneous lithological configuration assumptions have been proposed considering the different geophysical surveys conducted in the catchment. They are described in the next section after the analyses of the geophysical survey.

5.5 Results

5.5.1 Hydrogeophysical investigations

Field investigations for the soil layer include the porosity, hydraulic conductivity, density, and humidity. Porosity was measured at soil pit locations. The maximum reported value of porosity from mercury porosimetry was 58 % with an average of 48 % from 6 samples (Table 5.4). Porosity at the surface from soil sample rings was up to 80%. From these measurements, a 60% porosity was chosen considering a 54% soil moisture for saturation. From mercury porosimetry, we also derived Van-Genuchten parameters (Fig. 5.8). However, only consolidated samples were able to be analysed and the results were too sandy compared to field observations and simulation results. Model calibration led us to decrease the n and slightly increase α Van-Genuchten parameters which gave more suction for the soil layer. Hydraulic conductivity was measured at six locations at the surface to be used for the soil horizon and at two locations inside the tunnel to be used for the regolith horizon (Table 5.4). The max reported value at the surface was 332.6 mm hr^{-1} with an average value of 237.43 mm hr^{-1} from the six infiltration tests. In the tunnel the reported values were 276 mm hr^{-1} and 58 mm hr^{-1}.

The average value with two permeability measurements in the tunnel is 167 mm hr^{-1}

Parameter	Calculated values	Adjusted values
Porosity (%)	Soil: 47, 50, 45, 58, 44, 46	Soil: 60
	Regolith: N/A	Regolith: 25
	Flysch: N/A	Flysch: 10
Permeability (mm hr $^{-1}$)	Soil: 332.6, 221, 163, 311, 249, 148	Soil: 237
	Regolith: 276, 58	Regolith: 167
	Flysch: N/A	Flysch: 0.0001
Density (kg m $^{-3}$)	Soil: 1382, 1231, 1310, 1011, 1723, 1230, 1446	N/A
Humidity (%)	Soil: 54, 26, 18, 45, 33, 63, 47	N/A
Van-Genuchten (α,n)	Soil: 2.4, 1.97	Soil: 3, 1.5
	Regolith: N/A	Regolith: 0.16, 1.5
	Flysch: N/A	Flysch: 0.5, 2

Table 5.4: Experimental and adjusted parameters applied for the 3 horizons.

which is slightly less permeable than the surface. Other hydraulic parameters were calibrated according to the literature and calibration procedure. This led us to a very low permeability and porosity (10%) for the flysch horizon and a loamy sand behaviour with a 25% porosity for the regolith horizon (Table 5.4).

The soil depth was deduced from CMD explorer FEM soundings calibrated from the Siscal Pro ERT panel. Figure 5.5a shows a clear contrast between two horizons, one 4 to 5 m deep from the surface with low resistivity (below 300 Ohm.m). It is probably full of water in the river bed and in the peat land area between the two river incisions. Below, the resistivity is much higher, up to 3000 Ohm.m. We interpret it as the flysch bedrock layer introduced earlier. On the slope, right and left sides, a high resistive layer was observed that caps a less resistive area. We interpret it as schist formation that can be also observed higher in the Roche Noire catchment. This could be material transported long ago by the glacier or a schist layer flipped by the tectonic. Whatever this should be hardly fractured, porous, and permeable. We will then consider it as part of the regolith layer.

Figure 5.5b shows the inversion of CMD Explorer data for which 2 resistivity thresholds provided the soil layer depth and the regolith layer depth. If the regolith to flysch transition

was clearly associated with the strong resistivity gradient observed on ERT panel (Fig. 5.5a), it was not so clear for the soil to regolith transition which left us with an uncertainty on the soil layer depth. As a first guess figure 5.5b shows a very contrasted spatial soil depth distribution. The soil depth at river bed and bank locations are 0.3m to more than 2m. On the contrary, on the slopes, we observed very thin soil layers (0.1 to 0.2m).

Although GPR investigations were performed using three different frequency antennas (250 MHz, 500, and 800 MHz), only the lower frequency images were used for penetration depth considerations. The three transverse profiles acquired in the catchment are shown after processing (Fig. 5.6). These profiles show the direct air-waves which propagate with different velocities in different media. The following blue and red lines show where waves have been reflected. The first profile (Laut1) confirms what we interpreted with the ERT cross-section with a bit more detail. At the river and peat land locations, the deepest reflector is 4 to 5 m deep. On the left and right banks, the signal is noisier. These multiple reflections could be interpreted as reflections between two layers or reflections on scattered underground rocks. Other profiles have the same typology.

To conclude, our interpretation of geophysical data led us to consider mainly two layers: Flysch topped by an active 4-5m hydrological layer. Considering CMD explorer, this top layer can be separated in two, what we named the soil and the regolith. This led us to propose several underground configurations from a simple homogeneous soil layer as characterized only by surface properties to a complex 3-layer heterogeneous lithology. The description of these configurations is listed below and plotted in figure 5.7 & figure 5.8,

1. Homogeneous soil (HM-1L-S) inferred from soil pits and infiltration test data

2. Homogeneous shallow soil with flysch (HM-2L-SS), incorporating ERT data with a low 150 Ohm.m electrical conductivity threshold which corresponds to a 0.6 m surface root layer with a large amount of organic matter.

3. Homogeneous deep soil with flysch (HM-2L-DS), incorporating ERT data with a 300 Ohm threshold which corresponds to a 2.4 m surface layer.

4. Homogeneous shallow soil with regolith and flysch (HM-3L-SS) adding tunnel observations to the preceding configurations.

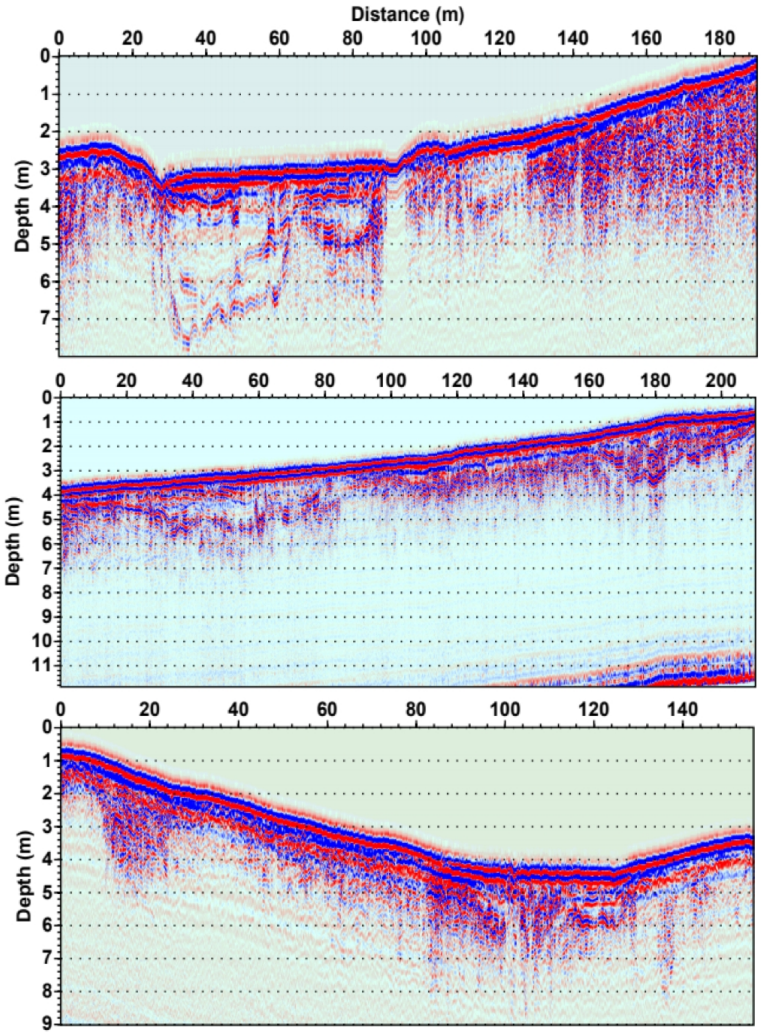

Figure 5.6: GPR profile in the catchment (a) Laut1 (b) LautLong (c) LautMF. Geographical locations are shown in figure 1.

5. Homogeneous deep soil with regolith and flysch (HM-3L-DS) reconsidering soil depth according to GPR data.

6. Heterogeneous shallow soil with flysch (HT-2L-SS) incorporating observed heterogeneity from the distributed thickness from electromagnetic measurements.

7. Heterogeneous deep soil with regolith and flysch (HT-3L-DS), including all the data available and lithological assumptions to complete the setup (Fig. 5.8).

Soil horizons (soil, regolith and flysch) in these simulations are distributed in 10 grid cells for the first 10 m of the subsurface and the deepest layer was made thick enough to

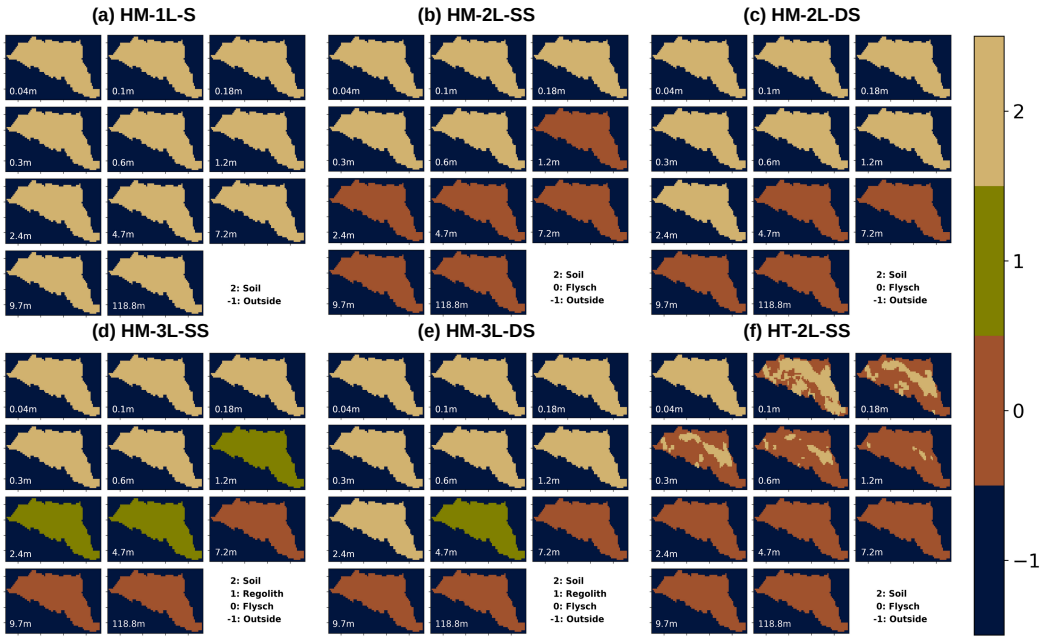

Figure 5.7: Soil (sand color), regolith (green) and flysch (brown) distribution for different simulation setup. Each thumbnail corresponds to modeled horizontal layers

ensure water transmissivity to the outlet, associated with the 200m elevation difference if this matters. The hydraulic properties of the different horizons are first based on observations, then on literature, and then adjusted to get satisfying simulation results. For the soil, the Van-Genuchten parameters have been determined fitted on mercury porosimetry data. The Van-Genuchten parameters for regolith and flysch are taken from observed permeability and porosity in the field, and from the literature. Finally, these values are adjusted in the 7^{th} model within the observation limit. Then, all simulations have been prescribed with the same Van-Genuchten parameters for each layer type, hydrodynamic curves are plotted in figure 5.8c & d.

5.5.2 Model validation

Figure 5.9 shows the streamflow regime in linear scale of the HT-3L-DS simulation to focus more on the high values. This simulation still had a bias in baseflow during the core of the melting season. However, it captures very well early precipitation events and the timing of early melting episodes in mid-March. This is both the result of our subsurface design and of the distributed forcing we applied (Gupta et al., 2022). The model produced also a good daily streamflow variation associated with the daily melting during the melting sea-

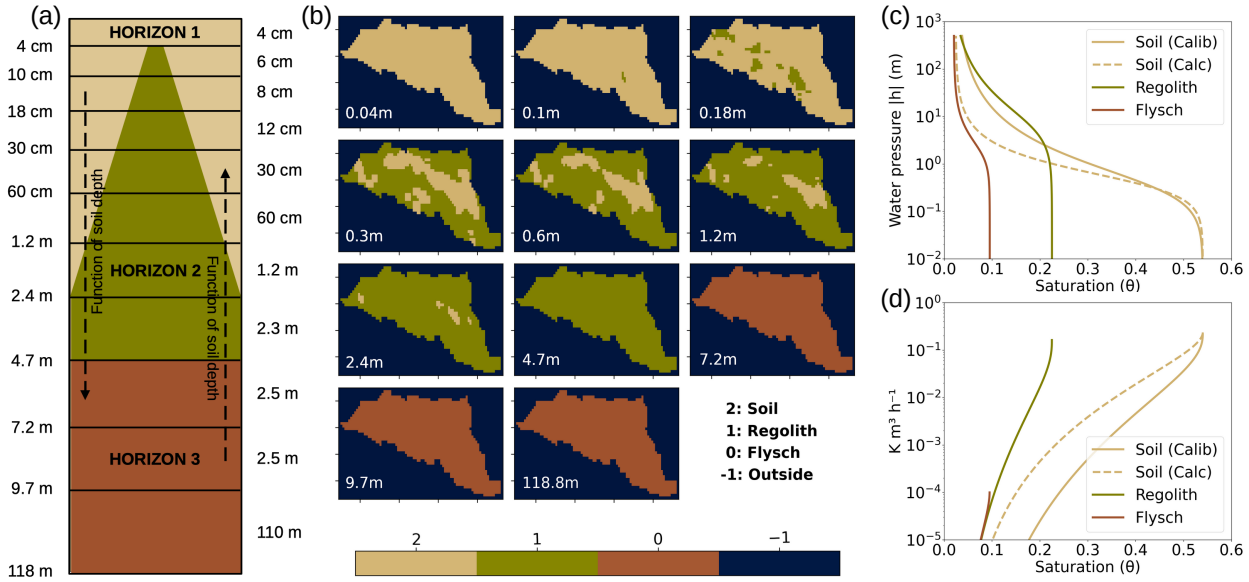

Figure 5.8: Subsurface description of the model built from all measurements (HT-3L-DS) (a) The subsurface is divided into 11 layers of different thickness (b) Soil (sand color), regolith (green) and flysch (brown) vertical (thumbnail) and horizontal (colors) distribution (c) suction and (d) permeability curves as a function of the saturation for soil, regolith and flysch.

son. Simulating accurate time and duration on snowmelt helps to maintain the baseflow in the summer months. The catchment receives a large amount of snow in winter hence, simulating the snowmelt and the way it infiltrates is very important in such kind of environment, which requires carefully managing the snow albedo. After conceptualizing the heterogeneous subsurface distribution the model shows a good agreement with the observed data (KGE_{np}=0.91).

We further evaluated this simulation with different surface observations from the flux station. We used a wind direction masked (Fig. 5.3b) to compare average simulated values with observed values of albedo, soil moisture, evapotranspiration, and snow depth (Fig. 5.10). The albedo in the catchment is well simulated with the RMSE value of 0.09 (5.10a). Low to medium albedo mostly corresponds to the summer season while high albedo belongs to the winter season. As we mentioned that the catchment is mainly driven by the snowmelt hence, precise albedo simulation becomes very important for such a catchment. One can note some overestimation of the albedo during the melting period (blue-green dots) which can partly explain the underestimation of melting. In figure 5.10b surface soil moisture is well simulated during the winter (dark blue dots) and during the fall (yellow-green dots).

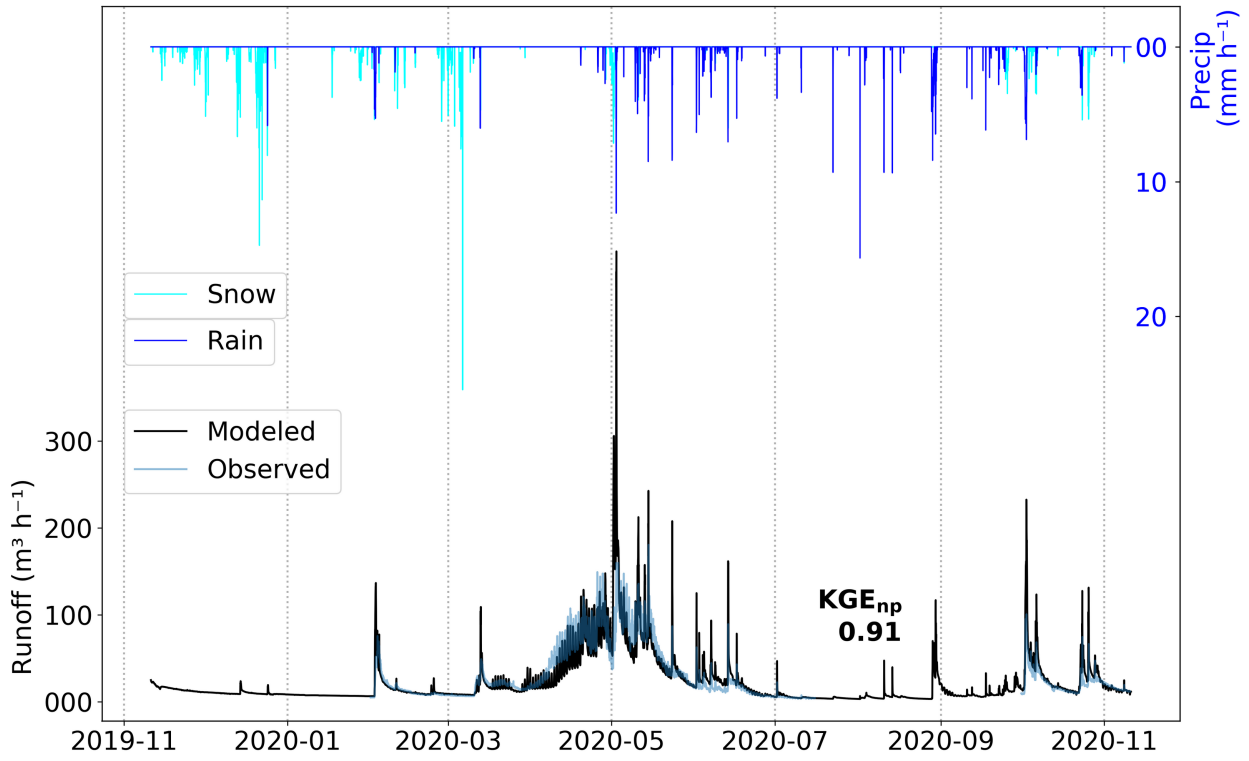

Figure 5.9: Simulated (black) and observed (blue-grey) Streamflow along the simulated 2019-2020 year. The precipitation series is plotted in the upper part of the figure and is separated into the snow (air temperature ≤ 0.3°C) and rain (air temperature > 0.3°C).

On the contrary, it appears too wet during the summer months (green dots) because for the simulated soil moisture values, we averaged dry pixels (on the catchment edge) and wet pixels in the river bed which always remain saturated throughout the year. Hence, the simulated value after averaging the dry and wet zones remain higher in the scatter plot for the summer season. Figure 5.10c compares simulated and observed half-hourly actual evapotranspiration on a simplified footprint area for July and August months. Dot color refers to saturation, the plot is rather scattered both because of uncertainty on the data and potential footprint misalignment because of wind direction changes that we don't take into account in our comparison. This led to a 46.5 W m^{-2} RMSE. Simulated values are 30% higher than observations, especially for dryer soil conditions (dark blue dots). Despite these uncertainties, simulated evapotranspiration can be considered reasonable as observation used to be underestimated (energy budget is not in equilibrium, (Foken et al., 2006)). The second reason can be the overestimation of summer evapotranspiration when soil moisture value is low. In summer, the catchment receives more shortwave radiation compare to winter. In

winter, radiation decreases due to reflection from the snow. As the high radiation in summer is distributed throughout the catchment, the wet zones along the stream evapotranspirate more compared to the dry zones.

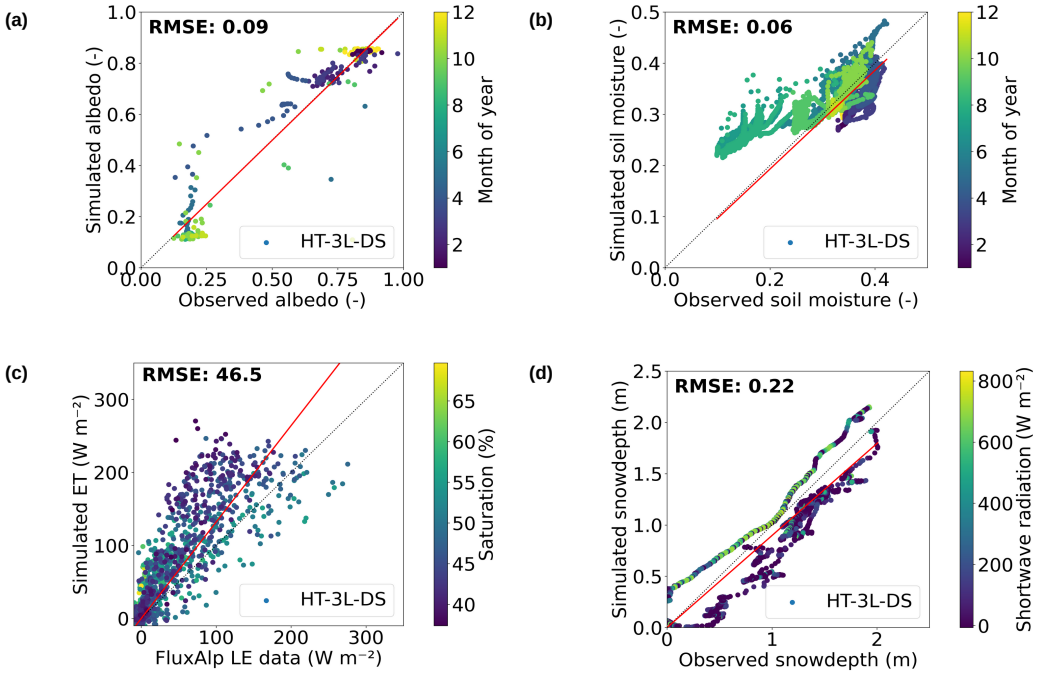

Figure 5.10: Scatter plots of simulated variables vs observed variables, colored as a function of time for the entire year for (a) 10h-14h averaged surface albedo (b) hourly Surface soil moisture. (c) presents evapotranspiration for July and August months colored as a function of saturation and (d) presents snow depth along the snowy period colored as a function of solar radiation. Red lines are the regression line between observed and simulated variables.

Finally, figure 5.10d compares simulated snow depth to observed values. The result shows a very good matching with a low RMSE value of 0.22 m. Colors refer to shortwave radiations, which means that underestimated simulated values correspond to lower shortwave radiations during winter time. The figure tells us that The simulated snow cover period is a bit late compared to the observed snow covered period. Similarly, during the melting period when shortwave radiation is higher (green yellow dots) snow depth is a bit over-estimated which means our simulation is a bit late at melting as it is noted in Gupta et al. 2022.

5.5.3 Sensitivity to underground assumptions from geophysical surveys

Figure 5.11 presents the simulated streamflow for the seven configurations. In the first experiment, we started with a uniform homogeneous subsurface composed only of soil. The

results show that a single homogeneous permeable soil layer is not able to produce the streamflow response to rain and snowmelt events (Fig. 5.11a). This simulation only simulates an average baseflow along the year that filter the all melting seasonal cycle. The second configuration with a permeable soil layer over a non permeable flysch layer (Fig. 5.11b) shows a fast and early response to precipitation events and also reaches very low values in the absence of precipitation or snowmelt. This setup produces a highly intermittent behaviour that either routes rapidly the water towards the stream or drains it rapidly and completely after the melting period. The third simulation resembles the preceding one just moving the depth of the soil layer from 0.6 m to 2.4 m. This simulation shows a better hold in subsurface storage and releases compared to observation and previous simulation (Figure 5.11c). Deepening the soil leads to forming a larger shallow reservoir which sustains the streamflow during the dry season. However, still this simulation drains water too rapidly after each rain event compared to observations. Additionally, this simulation also has a quick and large response to the hydrograph during the precipitation input. These three subsurface configurations didn't produce enough baseflow during the melting period. In the fourth simulation, we introduced a third regolith layer which shows much improvement in streamflow response and baseflow (KGE_{np}=0.89) compared to the above three simulations (Fig. 5.11d). The regolith acts as a reactive layer that holds water longer before releasing it into the stream. Responses to early rain events in February and in fall are particularly well reproduced. One can observe some lack of baseflow in April and a slight excess of baseflow later in June-July at the end of the melting season. The better KGE_{np} in this simulation can be the result of simulating the better drying of the sub-surface after rain events. The fifth homogeneous simulation is the same as the fourth homogeneous simulation except that the soil is made much deeper in this simulation. In this simulation preceding defaults are enhanced and it didn't produce the baseflow at the right time (Figure 5.11e). Water is released much slower during the summer. Also, isolated rain event responses are degraded compared to the HM-3L-SS simulation. This led to a substantial decrease in KGE_{np} value (0.69).

The last two simulations include a heterogeneous soil depth distribution according to the electromagnetic geophysical investigation. The results for the shallow soil layer with variable depth show a very fast response of rain and snowmelt to the stream (Fig. 5.11f). This

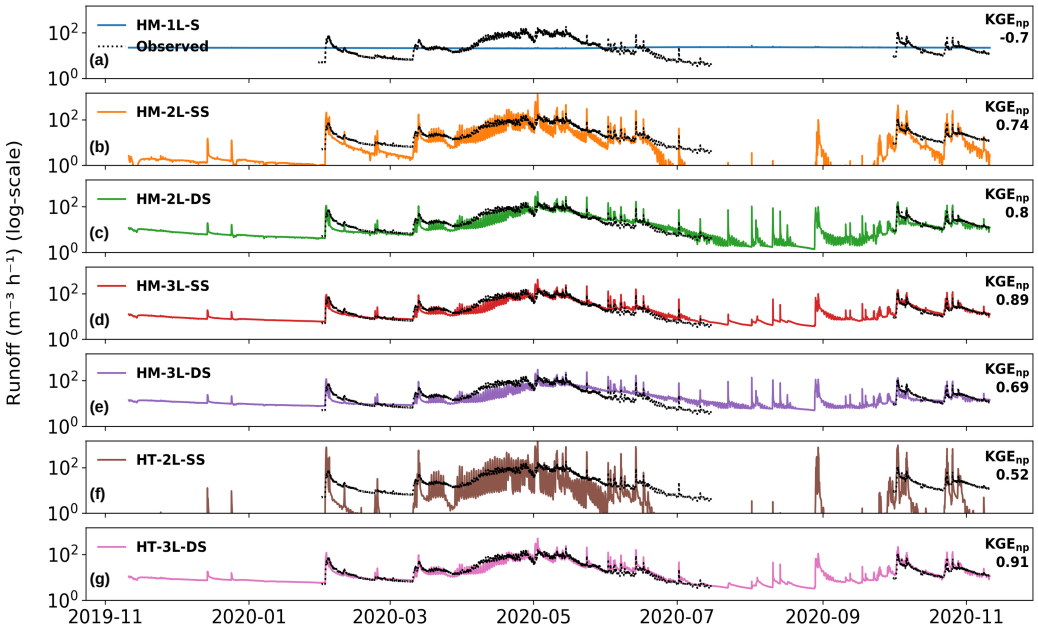

Figure 5.11: Simulated runoff in logscale (colored curves) compared to observed time series (black) for different experimental setups (Table 2). Performance in terms of KGE is plotted on the right side for each.

response is almost similar to the HM-2L-SS simulation (Fig. 5.11b) but with a faster subsurface flow. The final heterogeneous experiment has an increased soil layer depth according to GPR data. The results show that this simulation is really good in capturing the observed streamflow response (KGE_{np}=0.91) including the snowmelt amplitude and duration (Fig. 5.11g). In April the snowmelt amplitude is better compared to HM-3L-SS simulation (Fig. 5.11d). Similarly, in the summer the baseflow matches better with the observed streamflow which is not the case in its counterpart HM-3L-SS simulation. The seven different subsurface model setups lead us to conclude that the heterogeneous 3-layer deep soil (HT-3L-DS) setup that includes all the information we interpreted from geophysical surveys is the most accurate in predicting the observed streamflow response.

Table 5.5 presents some metrics for extra surface variables. It shows these simulations do not present significant differences in surface albedo and snow depth as all the simulations were forced with the same precipitation and radiation forcing. However, the change in subsurface parameters led to changes in surface soil moisture and evapotranspiration estimation. The heterogeneous three-layer simulation (HT-3L-DS) and the homogeneous shallow soil three-layer simulation (HM-3L-SS) show very close scores for surface soil moisture with RMSE value of 0.06 and a MAPE value of 0.23. Homogeneous single-layer simulation (HM-1L-

SS) has better RMSE and MAPE values for evapotranspiration but for the wrong reasons. This simulation dried out faster at the surface leading to less moisture on average which reduced the scatter and the regression slope and then RMSE and MAPE values. All other simulations have less good statistics for the surface soil moisture simulations. In the case of evapotranspiration one could see that the RMSE value is better for HT-3L-DS simulation however, the MAPE value is better for the HM-3L-SS simulations. On average the higher evapotranspiration may lead to better RMSE but accounting for heterogeneities lead to better estimation of MAPE in HT-3L-DS simulation. HM- 3L-SS and HT-3L-DS simulations outperform other simulations in terms of statistical metrics.

	Surface albedo		Soil moisture		Evapotranspirartion		Snow depth	
	MAPE	RMSE	MAPE	RMSE	MAPE	RMSE	MAPE	RMSE
HM-1L-S	0.21	0.09	0.20	0.07	6.18	31.86	0.47	0.22
HM-2L-SS	0.24	0.09	0.42	0.11	7.31	55.45	0.47	0.22
HM-2L-DS	0.23	0.09	0.30	0.08	6.98	49.21	0.47	0.22
HM-3L-SS	0.22	0.09	0.23	0.06	6.66	42.27	0.47	0.22
HM-3L-DS	0.23	0.09	0.27	0.07	6.87	45	0.47	0.22
HT-2L-SS	0.23	0.09	0.32	0.10	7.18	43.73	0.47	0.22
HT-3L-DS	0.22	0.09	0.21	0.06	6.61	46.50	0.46	0.22

Table 5.5: Statistical metrics for simulated surface variables with the different experimental setup.

Surface soil moisture and evapotranspiration depend on the water availability in the subsurface layers. Figure 5.12 illustrates the differences in terms of water stock and moisture availability at the surface for the different simulations. Homogeneous single-layer simulation (HM-1L-S) shows the deep-seated saturated zone compare to other simulations. These simulations don't develop the high saturated river network because of homogeneous infiltration throughout the catchment. The homogeneous single layer and high infiltration lead to a constant runoff exclusively in form of subsurface flow that can be viewed on the extreme right of HM-1L-S plot, if one extrapolates the water table rise to the outlet further right. All other simulations which at least account for two different layers developed surface saturation variability first because of the topography with higher saturation along the river network.

The saturated zone in homogeneous two-layer simulations (HM-2L-SS and HM-2L-DS) varies mainly in terms of water table depth. The deeper the permeable soil layer, the deeper the water table. The deeper saturated zone also led to a drier upper layer (HM-2L-DS). Similarly, homogeneous three-layer simulations (HM-3L-SS and HM-3L-DS) look the same with similar saturation patterns at the surface. The Shallow soil simulation (HM-3L-SS) is a bit drier on the slopes. In depth, for this Fall situation, the soil layer is no more saturated whatever the soil layer depth. One can clearly identify the transition between soil and regolith. The regolith layer has more saturation (light blue color) than the soil layer and is saturated close to the outlet. Among the three-layer homogeneous simulation the HM-3L-SS simulation shows good agreements with the surface soil moisture (RMSE=0.06) and observed runoff (KGE_{np}=0.89). The two-layer heterogeneous simulation (HT-2L-SS) resembles the two-layer homogeneous simulation. Similarly, despite the presence of the saturated flysch layer close to the surface, underground dries rapidly and is then unable to sustain a low underground flow during the summer (Fig. 5.11). This simulation shows a really low RMSE value against the surface moisture (RMSE=0.01).

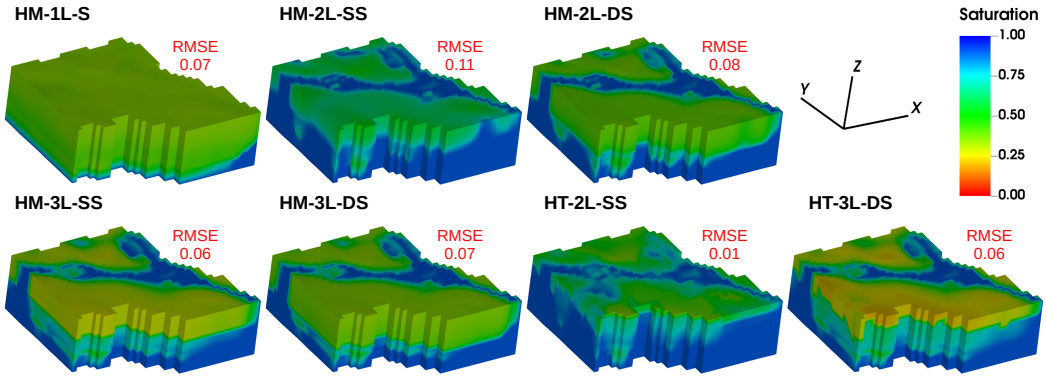

Figure 5.12: 3D Subsurface saturation for initial conditions for the different experimental setup. outlet Z-axis has been scaled (x 10) and zoomed to have a better look at the top soil layers. For each 3D plot, the left and the front side have been cut to plot a cross-section of the saturation. RMSE score represents the comparison of surface soil moisture calculated from saturation to observed soil moisture.

Finally, at the selected date, the three-layer heterogeneous simulation (HT-3L-DS) shows good surface saturation heterogeneities, development of the river network, and an active regolith layer. This simulation shows a good agreement with the surface soil moisture (RMSE=0.06) and observed streamflow (KGE_{np}=0.91). This simulation is different in surface heterogeneities and regolith water content compared to its homogeneous equivalent

(HM-3L-SS). However, these heterogeneities add detail to the simulation and keep strong statistical metrics. In general, the most appropriate simulations are sensitive to soil depth, regolith thickness, and surface saturation.

5.6 Discussion

5.6.1 More geophysical studies for deeper hydrological complexity

Quantifying the role of the subsurface in streamflow response is necessary but difficult to achieve. Subsurface is a blind media for which most of the available data are local and/or are coming from indirect methods. Moreover, the subsurface is very heterogeneous and some tiny features can be responsible for streamflow generation (fractures, preferential flows, karst, sharp permeability gradient, etc. Hence, a high-resolution representation of subsurface properties could be achieved only with a high-resolution geophysical investigation. Claes et al. (2020) argued that simplified geology-based hydrological model can outperform more complex geological representation when using the same numerical model, Hydrus 2D in their study. They use ERT data to map and build the subsurface geometries and report that the over-interpretation of geophysical data can lead to lower hydrological performance in terms of streamflow, recharge, or evapotranspiration. We do agree with this statement considering that our observations are local and indirect. For example, though vertical permeability gradient can be sharp, especially when structured by human activities, various heterogeneities from pore scales to landscape scales in natural environments lead to large difficulties when one has to prescribe a precise depth of a subsurface horizon in a model. In those cases, low vertical resolution can add a fortunate numerical diffusion that can account for depth variability. In the same way, the local 2D ERT panel from Claes et al. (2020) only provides a slice of a 3D complexity and a spatially filtered version of their ERT inversion gave a better average representation of the simulated slope. From our study, we showed that the simplified three-layer homogeneous geology (HM-3L-SS) and the three-layer heterogeneous geology (HT-3L-DS) are on average very similar. However, the construction of such a simpler model was based on multiple geophysical observations and the confidence in these two simulations came from a multi-criteria evaluation from water and energy flux observations. Additionally, as we can see in figure 5.12 (HM-3L-SS & HT-3L-DS), heterogeneous underground enhanced

the spatial variability first induced by the topography, but gave a similar performance for several averaged outputs at the catchment scale. This means that the HM-3L-SS is on average an equivalent catchment model for the HT-3L-DS one, considering three homogeneous layers. We even could be able to tune it, adjusting depths to get closer results on average but losing information and contrast at pixel scale. More generally, this means that being relevant everywhere in the simulated catchment requires representing the actual variability at the model resolution. Geophysical land or airborne ERT or FEM exploration, become some unavoidable and unique tools for such purposes. We also show in this study that the multi-geophysical method approach using local direct in-situ measurement and spatially distributed indirect methods allow us to build step-by-step a consistent subsurface model together with simpler avatars able to give us reliable averaged hydrological dynamics.

5.6.2 Homogeneous v/s heterogeneous

Building a three-dimensional heterogeneous subsurface model is a tough choice because factors like terrain, resolution, and thickness increase the complexity and heterogeneity by manyfold. Hence, working with a conceptual 3D model is often preferred (Markovich et al., 2019; Rapp et al., 2020). Most of them are generally built on average subsurface properties with homogeneous horizontal distribution. Unfortunately, Hartmann et al. (2017) highlighted that the subsurface heterogeneities drive most of the subsurface hydrology but are usually not taken into account in hydrological modeling. Our 15ha study case shows, at that scale, the homogeneous subsurface might be considered for averaged results (HM-3L-SS simulation). However, slightly simpler two-layer subsurface simulations were not able to produce the right streamflow response and the correct water budget. On the other hand, the HT-3L-DS simulation has a better subsurface flow in the dry season, captures better the snowmelt daily cycle and seasonal peak (Fig. 5.9), and enhances spatial heterogeneities (Fig. 5.12) accounting for subsurface heterogeneities. Introducing heterogeneities then shifts processes from a topographically only controlled catchment to a multi-source controlled catchment including climate, vegetation, and subsurface features.

5.6.3 Surface-subsurface coupling

High-resolution critical zone hydrological modeling requires integrated coupled models to simulate surface-subsurface inter-dependencies from aquifers to unsaturated soils and to the atmosphere through vegetation. Such interactive reservoirs and coupled flow could not be achieved by a misrepresentation of the subsurface hydrology (Kuffour et al., 2020; Kollet and Maxwell, 2008; Hector et al., 2018). We have shown that the evolution of runoff in a mountainous catchment is clearly controlled by the subsurface setting (Fig. 5.11). Free drainage hydrology using observed permeability measurements in our test case was not able to provide reliable river runoff (HM-1L-S). More realistically, without the intermediate regolith layer, we were not able to simulate a relevant base flow dynamic (HM-2L-DS, HM-2L-SS) and a correct drying at event scale (HM-2L-DS, HM-2L-DS). Such a catchment has a strong contribution of Dunnian runoff and the subsurface flows govern a large part of the runoff (Weiler et al., 2006). Though we kept the same forcing in all simulations, we simulated huge impacts in hydrological fluxes relying on sub-surface settings. The subsurface setting is also needed for the optimal surface soil moisture estimation (Fig. 5.12) which conditioned Evapotranspiration fluxes, and then the entire water budget. Moving far from reality in a subsurface setting could then lead to wrong partitioning in hydrological fluxes (Blume et al., 2009). Along with infiltration and flows, the subsurface also controls the surface-atmosphere feedback mechanism (Atchley and Maxwell, 2011). This further impacts the vegetation dynamics in the hillslopes. Carroll et al. (2017) highlighted that in hillslope decrease in water availability could lead to a decrease in vegetation health. On mountain slopes, it is really common during drought to see the vegetation turn yellow where the subsurface water availability drops quickly.

5.6.4 Limitations and perspectives

Our study concerns a small hydrological unit of 15ha. It is hard to generalize the results presented for this Lautaret pass catchment, but the study shows our ability to build a subsurface model from geophysical surveys and to identify from a small set of simulations, the necessary information to reach a given level of detail. These simulations also document their limitations when simplifying the subsurface. To be more conclusive on our ability to

constrain sufficiently such physically based 3D hydrological models larger catchment should be considered, using, for example, airborne geophysical data. A second limitation of the study is the lack of distributed data within the catchment to evaluate the relevancy of simulated surface soil moisture or water table depth variabilities. The only distributed data we used was the snow cover variability at the end of the melting season from Sentinel images which have been used in Gupta et al. (2022). They showed a good agreement between the model and the observation. Now the presented simulations can help to identify some locations and periods where and when supplementary measurements could be done. This could be new moisture sensors or new geophysical surveys to evaluate the model more. Although resistivity maps or panels could be calculated from hydrological simulations to make an easier comparison with the observation. At the moment we only show that taking into account subsurface heterogeneities matters for hydrological budgets. About the assumptions we made, one of them is the closed boundary condition at the bottom and sides of the domain. This hypothesizes that no water is leaving the catchment to further downhill outlets and no water enters the catchment from the upper part of the Roche Noire valley, the top of which is 1000 m above. Though we made the subsurface deep enough to account for the deep water path from the top of the catchment to the outlet 200 m below, we finally found that the Flysch layer didn't participate much in the outflow because of its low permeability and its small storage capacity. It seems that streamflow contributions are mainly from the 5 first meters of the subsurface. To evaluate this we started to sample the river for chemistry and isotope analysis to confirm residence times we aim to calculate from our simulations.

5.7 Conclusion

The role of the subsurface in water flux partitioning and streamflow generation is essential for critical zone hydrology, however, our knowledge of the subsurface characteristic is poor considering the large heterogeneities that matter for hydrological processes. This is especially true for hard-rock aquifer regions like in mountain areas where active geology led to a complex underground structure including folds, fractures, major erosion, etc. In this study, we show how a shared cross vision on a small hydrological unit in mid-elevation Alps can help to build a subsurface model for hydrological purposes. It includes geology, pedology, soil surface hydrodynamics, and multiple geophysical methodologies, namely Electric, Electromagnetic

and GPR methods. From in-situ observations, we then have set a surface-subsurface coupled physically based model to explore the role of subsurface setting in regulating the hydrological fluxes. The seven designed experiments include a complex 3D variable model from which we derived a simplified model for which hydrodynamic characteristics were derived from field measurement. Five of those models were horizontally homogeneous with various numbers of horizons and depths. Two of them includes horizontal variability derived from the geophysical survey. We have shown that only soil hydro-dynamic characteristics led to a free drainage hydrology where water from rain and melting percolates deep and fast in the ground and is released continuously to the streamflow. We found that the two simulations in which we include an intermediate regolith layer between the soil and the flysch were very close in simulating the runoff, soil moisture, and evapotranspiration. In those simulations, Flysch was almost hydrologically inactive and didn't contribute to streamflow, and regolith act to maintain the flow, the moisture, and then surface saturation. From these two simulations, heterogeneities did not show much difference in terms of performance for spacial average evaluation, however, we argued that heterogeneous three-layer simulation was a bit better in capturing the daily melt cycle, baseflow, evapotranspiration, and more contrasted surface saturation heterogeneities. Last, none of our 2 Layer configurations were able to produce relevant baseflow or relevant precipitation event response. More generally, physically based hydrology models need detailed subsurface information to simulate the right processes. Our study highlights, on one hand, the necessity of minimum geophysical investigation to simulate relevant catchment scale results and on the other hand, the necessity of more accurate subsurface description to simulate inner variability better. Our study shows that even if we still cannot associate the necessary characterisation to any model pixels the more constraint we add, the more we get. Including distributed data from geophysical surveys, even at a larger scale using airborne observation, have then a high potential to build and constrain better subsurface models for critical zone hydrology modeling.

5.8 Synthesis

The chapter describes the usefulness of the geophysical data in calibrating the hydrological model. Different homogeneous and heterogeneous subsurface simulations conclude that the subsurface controls the hydrological fluxes in a mountain catchment. Results prove that con-

stant hydraulic conductivity fails to simulate the rain-runoff response. These responses drive the soil moisture and evapotranspiration along with stream runoff. Under-representation o spatial and temporal variability of these variables with certainly produce a false conclusion on water resource management. Conceptualization of homogeneous simulations is easy but should be accounted for based on an initial geophysical survey. As far as possible these conceptual models should include variable hydraulic conductivity to modulate the subsurface fluxes. However, to be very accurate in modeling hydrological fluxes the heterogeneous subsurface should be accounted. This heterogeneous subsurface could be either deduced from an in-situ survey or an available airborne geophysical survey at regional scales. Spatial heterogeneity can be modeled only by assimilating more and more available geophysical data.

Using the distributed meteorological forcing and heterogeneous subsurface we have calibrated the ParFlow-CLM for the mountainous catchment. The meteorological distribution approach, albedo calibration and incorporating the geophysical data to model the subsurface are major milestones to reach the calibrated ParFlow-CLM in the catchment. With the final calibrated model all the results shown in Chapter 4 are still valid. The Sentinel-2 images collected for the hydrological year 2019-2020 also show the same pattern (Fig. 5.13). Though we have filled the snow map in the upper part of the catchment it is still not able to catch the actual snow depth and melting. The snow map further needs to be validated either with new laser scans or some in-situ snow probes during the peak accumulation season.

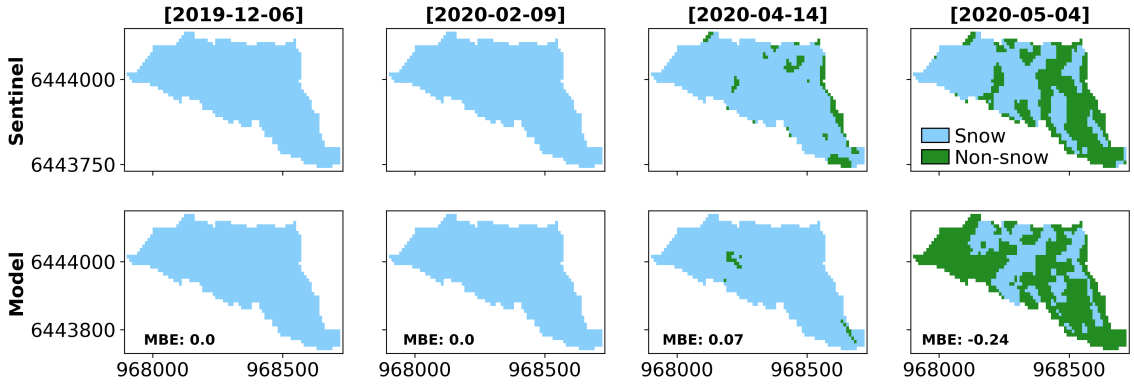

Figure 5.13: Sentinel-2 image spatial pattern. Mean bias error is represented as statistics between the simulated snow and Sentinel-2 snow.

The same approach has also been applied to calibrate the model for continuous four years and the results are included in Appendix A. The model has been successfully calibrated

however, it was not so straightforward to reach. A lot of simulations have been done to reach the final calibrated model. A few of the major simulations are included in Appendix B.

6 Residence time modeling in catchment

Residence time in the subsurface describes the catchment behaviour. The surface-subsurface connectivity could be fast or slow in terms of flux response. Chemical alteration in the subsurface and the impact of climate on the groundwater recharge could be seen through the residence time modeling. This Chapter describes the residence time distribution in the subsurface, residence time distribution of source contribution to evapotranspiration and outlet, and source partitioning of the evapotranspiration and outlet. The calibrated and validated model has been used for this purpose. We will show how that catchment behaves in the present climate and how it has the potential to be impacted under climate stress.

From now onwards, this Chapter is presented in the form of brief communication. This brief communication is under preparation:

Brief Communication: Snow/rain source partitioning and residence time modeling in the subalpine critical zone, in preparation.

Abstract

Residence time distribution in the subsurface shows the catchment behaviour. This behaviour is topographically controlled and driven by snow and rain partitioning at the subsurface. This study shows that snow dominates in the subsurface compared to rain. Most of the particles in the subsurface are young with ∼5 years old particles actively recycled in the subsurface. Results show that plant uptake 23 % of the total snow for evapotranspiration with a mean age of ∼5 years. Snow is the major contributor to runoff accounting for 61 % of the total runoff. The snow age in runoff varies from young to old with younger particles mostly contributing during the melting period.

6.1 Introduction

Residence time and flow path in mountainous catchments are fundamental quantities to describe the hydrological behaviour of the catchment (McGuire and McDonnell, 2010; Zhu et al., 2010). Storage in and release of water from the subsurface sustain the streamflow and vegetation dynamics in dry seasons. In mountainous catchments the connectivity of surface and subsurface controls the hydrological functioning (Thayer et al., 2018). It provides subsurface water to both the streamflow and evapotranspiration fluxes, and partly controls the partitioning between those two components. At the catchment scale usually plants take up the younger water and streamflow can include varying proportions of both younger and old water (Maxwell et al., 2019). How the partition actually occurs depends upon the subsurface setting (Maulé and Stein, 1990). Some study suggests that the vegetation can take up a significant amount of subsurface snowmelt for evapotranspiration in mountains (Sprenger et al., 2022). Subalpine critical zones are more vulnerable to climate change because of their dependence on the snow hydrological regime. Mountainous catchments' behaviour is topographically controlled and exhibits strong dependence on subsurface storage from snowmelt. Depending upon the slope, aspect and climate snowmelt dominates the hydrological cycle in such a catchment. Dominance of snow in mountainous catchment has direct impacts on hydropower production, agriculture and drinking water supply. However, the behaviour of snowmelt and its interaction with the subsurface in these regionsremains too poorly explored.

Storage and groundwater recharge in mountain critical zone depends upon how much snow accumulates in the winter, and how long it stays in the spring. Mountains are vulnerable to global warming as it raises the altitude of the zero celsius isotherm, which changes both

snow/rain partitioning and the amount of snow accumulation, and the onset of snowmelt (Hammond et al., 2019). A low-to-no snow future will significantly impact the groundwater recharge in such regions (Enzminger et al., 2019; Siirila-Woodburn et al., 2021). Snow stays longer in the catchment and has more time to percolate to the subsurface. However, rain after the excess infiltration of soil directly moves along the slope to reach the outlet. This develops a snow dominated reservoir in the subsurface. Later in dry seasons, this reservoir supplies water to streamflow and evapotranspiration . Depending upon the subsurface flow path these contributions could change from young to old water.

In mountains, due to topography-induced heterogeneities, water fluxes really occur at fine spatial and temporal scales. Moreover, slope-induced subsurface flows make integrated approaches, from the top of the canopy to the deep subsurface, quite necessary (Carroll et al., 2018). To address the integrated hydrological behavior of catchments in such regions, we need models coupling surface and subsurface processes. Spatial variability of meteorological fluxes, subsurface heterogeneities, and climate impact makes the hydrological response fluctuate over space and time. High resolution of meteorological distribution and three-dimensional characterization of the subsurface is necessary to calibrate and validate model approaches in such catchments.

This study tries to fill the gap in the hydrological functioning of a complex mountain critical zone through an integrated modeling approach. Literature suggests the strong dependence of evapotranspiration and outlet runoff on subsurface storage. However, the dynamics of these components as a function of residence time is not so much studied. Residence time can provide a broad overview of catchment storage and release along with cyclicity to young and old source contributions to the ecosystem.

6.2 Study area

The study area is a small subalpine catchment (15.28 ha) close to the Lautaret pass in the French Alps. This catchment faces East, with snow on the ground for 5-6 months a year, and therefore a snow-dominated hydrological regime. Vegetation is dominated by a fescue grassland, which contributes significantly to evapotranspiration in the relatively warm summer. The site hosts an extensive monitoring station for critical zone studies. It includes a meteorological station, eddy covariance flux tower, discharge station, snow height sensor,

and time-lapse camera.

6.3 Methods

The study uses the ParFlow-CLM, a surface-subsurface coupled model (Jones and Woodward, 2001; Ashby and Falgout, 1996; Kollet and Maxwell, 2006; Maxwell, 2013; Maxwell and Miller, 2005; Kollet and Maxwell, 2008), for hydrological modeling and EcoSLIM (Maxwell et al., 2019), a Lagrangian particle tracking model, for residence time modeling. ParFlow-CLM is set up at a hyper resolution of 10 m with a total grid size of 84 × 42 × 11 (longitude × latitude × depth). The subsurface is divided into three heterogeneous geological layers viz. soil, regolith and flysch with different hydraulic conductivity. The subsurface characterization has been done using the electromagnetic and ground penetrating radar (GPR) survey. The maximum depth in the model is 118 meters with the first 10 layers extending up to 10 meters. The last layer has been made deep enough to account for all kinds of deep water fluxes.

The model has been forced with distributed meteorological forcing for the simulation year of 2018-2019 (Gupta et al., 2022). The forcing time step is 30 min while the output is written at the hourly time step. The model has been calibrated against the observed discharge, evapotranspiration, snow depth, snow albedo, and soil moisture. In addition to these variables, to capture the spatial distribution of snow on the surface the model has been validated against the Sentinel-2 images (Gupta et al., 2022).

EcoSLIM is dependent on the ParFlow-CLM meteorological input and ParFlow-CLM three-dimensional velocity output. The particle in the subsurface moves through advection, dispersion, and diffusion based on ParFlow-CLM transient velocity. To reach the optimal initial condition ParFlow-CLM and EcoSLIM have been run for 125 years with the same forcing (Appendix C).

6.4 Results

Residence time distribution for a cross-section between latitude 200 meters to 300 meters (6443935 - 6444035 RGF93) is shown in figure 6.1. Rain particles are overlain by the snow particle which means once in the subsurface rain and snow both follow the same path.

The inset figure on the top left shows that snow water dominates over rain water in the subsurface . However, one should note that this represents the water that remains in the subsurface and is different from the partitioning of the total precipitation between outlet and evapotranspiration, as this also includes the fast surface runoff, not accounted for by Ecoslim. Residence time distribution shows that younger water is mostly close to the surface (∼5 m). And this younger water actively contributes to the hydrological cycle of the catchment. The inset figure on the bottom left clearly shows two populations in the simulated subsurface water particles. The first population, younger, dominates the overall population and contains more snow water than rain water. . The second population is older than ∼5 years. These old particles will reappear in the watershed from subsurface flow circulation. Further, these old particles in the model result from the spinup years and do not actively contribute to the catchment hydrology.

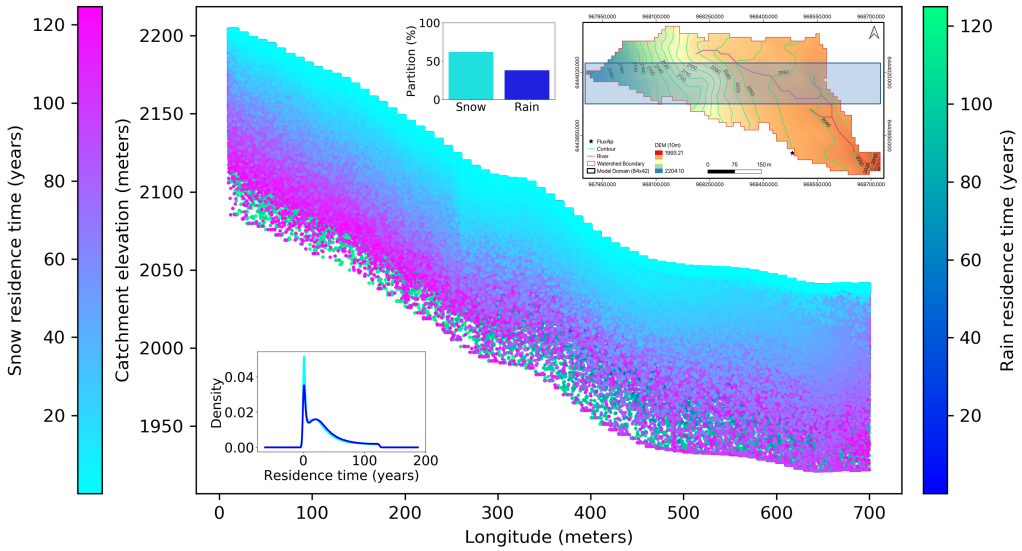

Figure 6.1: Residence time distribution of snow and rain in the subsurface.

Depth variation of residence time shows that the young particles are only close to the surface and the residence time increases as we go deep in the subsurface (Fig. 6.2). Though we have made our surface 118 meters deep, only the first five meters of subsurface actively participates in the hydrological cycle. We could see a sharp transition in the residence time at the regolith and flysch interface. After this interface, the residence time increases depending upon the travel speed in flysch. One could see there are some old particles at top of the surface however, the number of these particles is very low. This will be explained in the next

paragraph. These old particles are either pushed along the river or come from the catchment border where they travel very slowly.

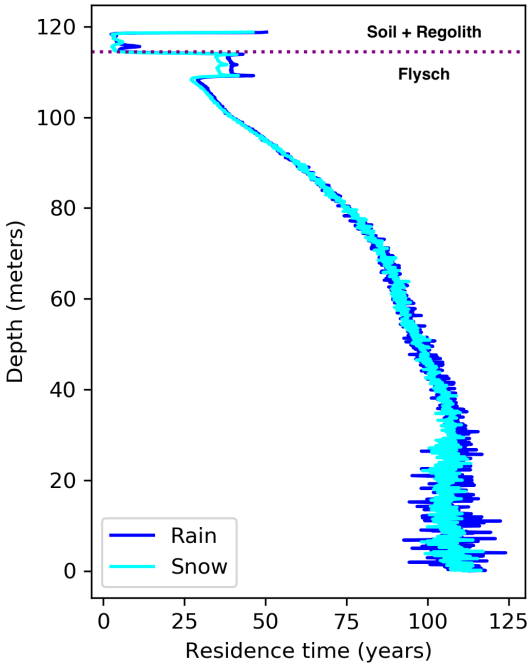

Figure 6.2: Residence time distribution as the function of depth. The regolith and flysch interface lies at 4.7 m below the surface.

Temporal variation of residence time in the catchment shows that old particles actively contribute to the catchment hydrology (Fig. 6.3). In summer, the rain water undergoing evapotranspiration is very young. The high residence time of rain water in winter evapotranspiration is only represented by an insignificant number of particles which only contributes to direct evaporation. In summer time during the peak vegetation activity, the rain water in evapotranspiration is very young. This either comes from wet precipitation or some near-surface source. However, snow contribution to evapotranspiration comes significantly from old snow. This snow water is taken up by plants in absence of rain or during the drier period. Furthermore, the particle number shows that snow water contributes less than rain water to evapotranspiration. In outlet runoff, throughout the year, older rain and snow water dominate. However, their amount is less. Whenever the particles numbers in outlet runoff increase the residence time falls to low values. This explains that too old particles do not actively contribute to the outlet runoff as well. However, during peak discharge time (April and May) close to ∼5 years old particles are significant. Similarly, in evapotranspiration, ∼5 year old particles contribute significantly during the summer.

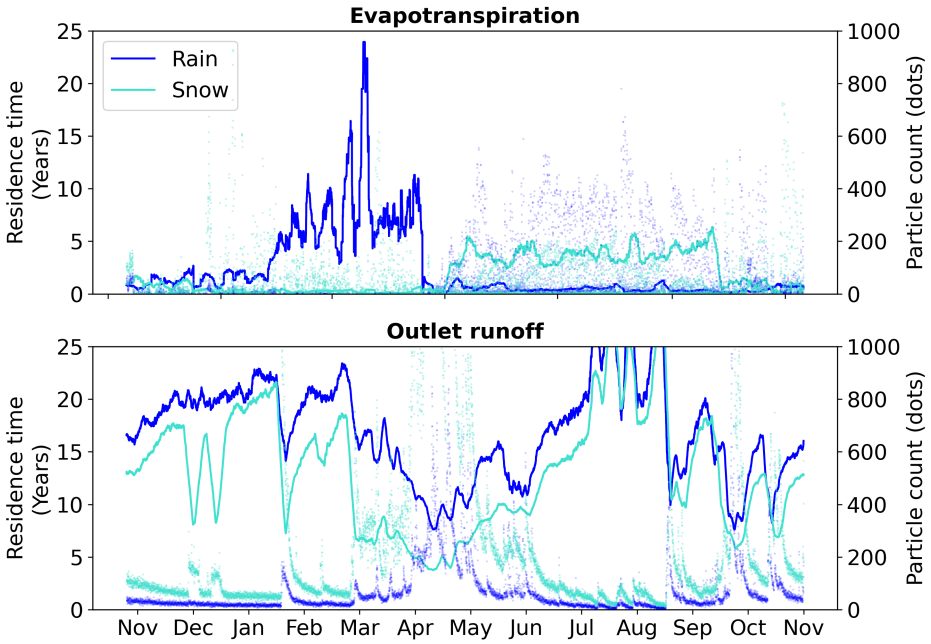

Figure 6.3: Temporal variation of 5 days rolling residence time of the rain and snow to the evapotranspiration and outlet runoff. Particle numbers are plotted with the dots in the corresponding color.

Rain and snow partitioning show that rain contributes more to evapotranspiration whereas snow contributes more to the runoff (Fig. 6.4). Rain contributes 77 % and snow contributes 23 % to the total evapotranspiration. However, in terms of residence time rain contribution is made of younger water, whereas snow contribution is mostly older water. The evapotranspiration period goes from May to November however, some direct evaporation can be seen during the winter period. In the outlet runoff, snow dominates the flux throughout the year. In outlet, rain contributes 39 % whereas snow contributes 61 %.

6.5 Discussion

Residence time gives us a broad picture of hydrological connectivity between the surface and subsurface. With the calibrated model we are able to show the residence time distribution, source age, and source partitioning. These factor depends upon the subsurface setting and flow path. In mountain catchment, these flow paths actively partition the source between evapotranspiration and outlet runoff. With a 118 m deep subsurface layer we have shown that the deep subsurface does not actively participate in catchment hydrology. Most of the old particles are deep seated in the catchment and represent the time spent according to our

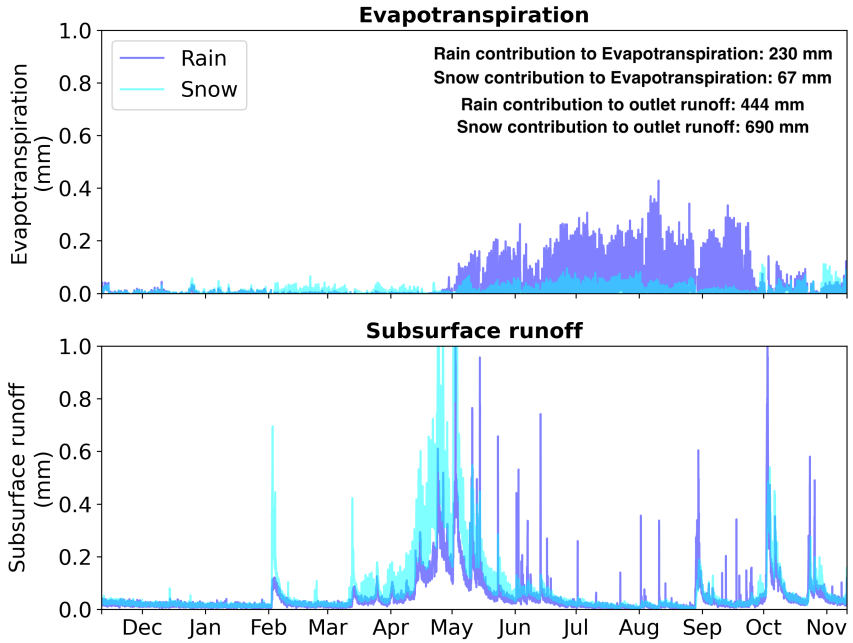

Figure 6.4: Rain and snow source partitioning to evapotranspiration and stream outlet.

model spinup time. Young particles close to the surface and towards the outlet dominate. Flysch separates active and slow subsurface at 4.7 meters below the surface.

6.6 Conclusion

Surface-subsurface connectivity controls the partitioning of snow and rain in the catchment. In the studied catchment it is found that the snowmelt dominates the outflow whereas rain dominates the evapotranspiration. Rain contributes 39 % of the total runoff whereas snow contributes 61 % of the total runoff. In evapotranspiration flux this partitioning is the opposite. In evapotranspiration, rain contribute 77 % of the total flux whereas snow contributes only 23 % of the total flux. However, it has been shown that snow source for plants is usually old particles. This old particle has the potential to be prone to chemical alteration and climate change which could significantly impact the mountain ecosystem.

6.7 Synthesis

The chapter describes the source partitioning and residence time distribution in the subsurface. These results have broad implications for water resource management. The rain and snow distribution in the subsurface is driven by the subsurface setting and the rain/snow

partitioning. Results show that vegetation functioning is dependent on the snow source and uptake of the old snow source during the summer. In the future, changes in snow amount will lead to less percolation to subsurface storage which ultimately impacts the vegetation functioning. In the revised version of the Chapter publication, these climate aspects will be explored as data presented in Chapter 2.

7 General conclusion and perspective

7.1 Conclusion

Mid-elevation range mountain hydrology is strongly impacted by climate change as the zero isotherm is moving up, changing snow precipitation to rain, and changing melting regimes. This already impacts many economic sectors including energy, agriculture, and tourism, but also environmental processes such as water quantities and quality, plant and animal ecology, etc. This thesis addressed some scientific community issues about the mountain critical zone , fundamentally linked to topography driven spatial heterogeneities: a) Impact of surface heterogeneities in driving hydrological fluxes. b) Impact of subsurface heterogeneities in runoff generation c) Hydrological flux partitioning and its impact under climate change. This research first identifies some limitations of Earth System Models (ESMs) in upscaling the critical zone processes and then shows the dynamics of hydrological fluxes when heterogeneities are considered. A 10 m resolution critical zone model of a 15.4 ha catchment was built using the Parflow-CLM hydrological model which allows representing 3D subsurface water path, surface water lateral transfers to streams and rivers and vertical transfers through evaporation and evapotranspiration in fully coupled framework. The major conclusion of this work about surface and, subsurface hydrology could be summarised as:

- The strong topography variability in mountains drives large climate variabilities in terms of precipitation, radiation, temperature, wind, etc. which drives spatial variation of hydrological fluxes such as snow accumulation and melting regimes, evapotranspiration, runoff, etc. To quantify these impacts, the model has been forced with distributed meteorological forcings (precipitation, radiation, and wind) based on slope and aspect. The study found out that distributing precipitation had more impact on the snow distribution all along the season in the catchment. Shortwave radiation distribution had impact on the melting and evapotranspiration regimes. Wind speed impacted the variability twice, once through snow transport and re-distribution, which we took into account in the precipitation distribution using a snowpack topography at the end of the snow accumulation period, and once through an aerodynamical effect on energy exchanges, which had an impact only when combined with the other forcings. Compared

to the non-distributed simulation, the distributed one shows an increase in runoff and a decrease in evapotranspiration of the order of ∼100 mm. Snow spatial distribution from the simulation was compared with high-resolution sentinel images. The results showed that snow cover lasted more than a month longer for the distributed simulation and showed a lower mean bias error (MBE=0.22) in the melting period compared to non-distributed runs (MBE=-0.4). Similarly, simulated evapotranspiration under the distributed simulation get much closer to the observations with a regression coefficient that decrease in slope from 1.55 to 1.18. The conclusion was that distributed meteorological forcing at meter scales impacts the entire seasonal cycle of mid-elevation mountain catchment and has to be taken into account in hyper-resolution critical zone hydrological modeling.

- Seven subsurface models were built based on field geophysical survey to quantify the impact of more or less heterogeneous subsurface configurations on hydrological fluxes and water budgets. They presented in 1 to 3 different horizon types (soil, regolith, and Flysch) on 11 layers. The results showed that constant hydraulic conductivity on one single soil horizon was not suitable at all to simulate hydrological behaviours of a mountainous catchment. It has been also shown that moving from one horizon to two horizons gave a better representation of the seasonal cycle but was not able to reproduce both the seasonal timing and the responses to short events such as important summer rains . The three-layer homogeneous and three-layer hetererogeneous simulations were able to match the spatially averaged observation data of runoff (KGE_{np} = 90, 91), soil moisture (MAPE = 0.23, 0.21) and evapotranspiration (MAPE = 6.66, 6.61). The intermediate permeable layer (regolith) plays a role in storing and releasing the water in the 3 horizon simulations which is able to capture runoff amplitude, soil moisture, and evapotranspiration. Finally, lateral subsurface heterogeneity brought more details in the spatial water storage variabilities and then in hydrological processes and are necessary for critical zone hydrological models to be also locally relevant.

- Residence time distribution in the catchment subsurface shows that the active hydrological cycle of the catchment is mostly dominated by the young particles. A few old particles of ∼5 years of age also significantly contribute to the catchment hydrology.

Many of the old particles in the subsurface are the result of 125 years of model spinup which stays in the deep subsurface without actively participating in the catchment's hydrology. Rain dominates the evapotranspiration components while snow dominates the runoff component of the total hydrological flux. Snow contribution to runoff accounts for 61 % and for evapotranspiration 23 %. Rain contribution to runoff accounts for 39 % and for evapotranspiration 77 %. However, snow in the evapotranspiration comes from an old source with a mean residence time of ∼5 years. These old particles are prone to chemical transformation and could carry nutrients to the plants. Changes in future climate will change the partitioning of snow which could directly impact the source partitioning to evapotranspiration. This could put stress on the functioning of vegetation dynamics.

7.2 Take home messages

- Subsurface configuration matters for CZ hydrological modeling, even at a fine scale, however some simplified configurations (horizontally homogeneous 3 horizons), still built from field observations can be sufficient to represent the average hydrological behaviour of a catchment.

- Hyper resolution CZ hydrological modeling help to validate/invalidate subsurface simplification assumptions.

- Geophysical surveys and field observation are able to provide enough constraints to build hyper resolution CZ model. This opens perspectives for modeling approaches of CZ Observatories and may be further on at much larger scales.

- CZ hydrological Modeling of complex terrain requires adapted resolution climate forcing, especially for snow and radiative distribution in snow-driven mountainous catchments

- Residence time in snow-driven hydrological mountainous catchments is more than a single season, even for very small catchments. Water from melting partly infiltrates the subsurface and can be used by the vegetation and/or to sustain streamflow several

months to several years later. Changes in the snow regime will modify the entire hydrological cycle of these environments.

- Changes in water residence time could also change the geochemistry and vegetation cycle of the catchment.

7.3 Perspective

The study mostly revolves around the data-model approach hence, a lot of time has been invested in building and adjusting the model from observed data such as snow depth, evapotranspiration, streamflow, albedo, etc. This restricted us to deploy broader implications of the model such as changing the catchment aspect, computational optimization, hydrological forecasting, nutrient transport, vegetation dynamics, and many more. As we have a calibrated model of the catchment this has broad implications from the catchment to the regional scale. A few of the potential future studies with this model are included in the following paragraphs.

7.3.1 At catchment scale

Changing the aspect of catchment

In this study, it has been shown that melting and evapotranspiration are dependent on slope and aspect. However, it concerns mainly a single eastward facing slope and the way surface orientation can change melting and evapotranspiration was not completely investigated in our study. It would be a nice study for further research to run a sensitivity study, turning the catchment for 90°, 180°and 270°. This approach will lead to answering a few of the scientific questions like; How the aspect controls melting and evapotranspiration? Does the aspect have control on sources (rain/snow) plants uptake? How the sensitivity of plant evapotranspiration to solar radiation and aspect can change mountain hydrological responses and budgets?

Computational optimization

During the study, it has been found that with a good parametrization, computational cost of the hydrological model can be reduced. In this study, the subsurface was first made very deep,

hypothesizing that large elevation differences would increase transmissivity. However, it has been found that the active subsurface was not so deep. This suggests that the hydrology of the catchment would not change much if the last layer from the subsurface model was removed. taking off the deepest impermeable reservoir (Flysch) might significantly reduce the computational time and even more the spin-up time with a moderate impact on results, and therefore be a good compromise.

Hydrological forecasting

The studied catchment has a 3-day forecasting using the MAR (Modèle Atmosphérique Régional) regional model. These forecast provide all the necessary variables to run the hydrological model. These variables can be distributed using the algorithm shown in this study. Forcing the MAR model output to ParFlow-CLM will develop a hydrological forecasting model in the catchment. This hydrological forecast model can be used for various purposes including snow depth forecasting.

Chemical transport

The EcoSLIM residence time outputs give the opportunity to run and calibrate the nutrient transport model in the catchment. To simulate the nutrient transport in the catchment three types of methods could be adopted,

1. ParFlow-Crunch[5] is nutrient transport model that can be run from ParFlow output. ParFlow-Crunch can solve the transport and chemical reaction separately using an advection solver and a geochemical solver. As we have calibrated the model, it will be the easiest way to model the nutrient transport in the catchment. This model can be run in parallel with ParFlow simulation. Although the model is still under development, it would be worth adopting this approach for nutrient transport modeling.

2. From our simulations one could run some box chemical model using the state variables from Parflow (saturation, pressure, temperature, residence time) and potential sources along the water path. This could give a first guess of how input nitrogen could be transformed along the water path in the catchment and evaluated from Nitrogen isotopic ratios using chemical samples in the atmosphere, in the plants, in the ground, and in the river. Nitrogen

[5]https://doi.org/10.1007/s10596-015-9475-x

isotope data are available for the catchment with yearly nitrogen budget estimates. This data could be verified from the outlet runoff simulation in the catchment. Combining the runoff, source partition, and residence time will give an overall picture of snow transportation in the catchment. The nitrogen isotope data from snow and water samples could be plotted for cross-correlation of chemical transport in the catchment. This will also work as the chemical verification of hydrological model calibration. Further, the flux of different ions from the water samples can be plotted against the snow and rain partitioning. This will lead to concluding which flux is more important for carrying the nutrient load in the catchment. The catchment has a large population of young particles which means there must be chemical similarities in the samples from snow, catchment springs, outlet runoff, and tunnel leakage (Bourgeois et al., 2018a,b; Bourgeois et al., 2019)

3. Common land model (CLM) coupled with ParFlow is an old version. The new version of CLM[6] has many advance dynamic schemes (CLM 5.0). specifically, CLM 5.0 has a carbon and nitrogen cycle which could be forced with nitrogen deposition and atmospheric CO2 concentration observations. The model allows the user to run the spinup to reach the initial chemical concentration at the surface. Coupling the CLM 5.0 model with the ParFlow model will be a long job however, few schemes could be directly coupled with ParFlow as separate modules. This will require first changing the energy balance scheme from two bands to five bands as most of the advanced routines in CLM 5.0 are dependent on five channel radiation scheme. Another advantage of CLM 5.0 could be the dynamic vegetation. This scheme is separated from CLM 5.0 hence, could be directly taken as subroutines in ParFlow.

Further snow scheme

In Chapter 5 it has been shown that the model is not able to capture the albedo, especially during peak snow periods. This could come from various sources which could include ranging from scale issues to model parameterization. In any case, the snow scheme coupled with ParFlow-CLM through CLM 3.5 is very old. This could be the very first step to be taken for the development of the model. CLM 5.0 has a snow scheme from SNICAR model. This SNICAR module has a detailed energy balance of the snow. To start with the snow age scheme from the SNICAR model could be adapted to ParFlow-CLM. However, it will again

[6]https://www.cesm.ucar.edu/models/cesm2/land/

need to change the albedo scheme from 2-channel to 5-channel. Another option exists in the form of the Crocus model (Vionnet et al., 2012). The model has been extensively used for this region and has a very advanced snow scheme. This could be adopted as a separate module for snow albedo and snow aging in ParFlow-CLM.

7.3.2 At regional scale

Surface meteorological distribution and subsurface model can be used to upscale the study for larger catchments. The adjacent Roche Noire catchment has a larger area and similar climate hence, will be suitable to upscale the study (Fig. 7.1). This will allow addressing most of the perspectives listed above in terms of aspect and slope, and in terms of socio-ecological issues. The upscaling to a bigger catchment could be achieved by using the same meteorological distribution and 3-layer homogeneous conceptual model for the subsurface. In the present study due to hyper resolution a lot of time splitting has been encountered during the peak snow period which increases the computational time for the model. Hence, upscaling the study at a lower 50 m resolution will be a good compromise while still modeling the spatial heterogeneities with reasonable computational time. This upscaling will also benefit from a large number of multidisciplinary field observations (Fig. 7.1) to address the multidisciplinary scientific questions arising because of climate change impacts in mid-elevation range mountainous environments.

The result from this thesis and the proposed intermediate scale above can be used to upscale to the mountainous region at any scale. This thesis suggests that the meteorological distribution in the mountain catchment is necessary and should be accounted for depending on slope and aspect. Even at coarser resolution, hydrological modeling will benefit from meteorological distribution based on available high-resolution DEM for the ground level and for the snow surface at the maximum accumulation period from which a snow coefficient map could be deduced. Similarly, depth-varying conductivity could be inferred from air-borne Electromagnetic surveys to constrain subsurface variability. The simulation could be controlled or driven using available soil moisture, temperature remote sensing data along with runoff observation network[7]. This will reduce the error in water resource quantification in mountain catchments. Even the ESMs and large-scale hydrological models will get benefit

[7]https://www.theia-land.fr/en/ceslist/soil-moisture-with-very-high-spatial-resolution-sec/

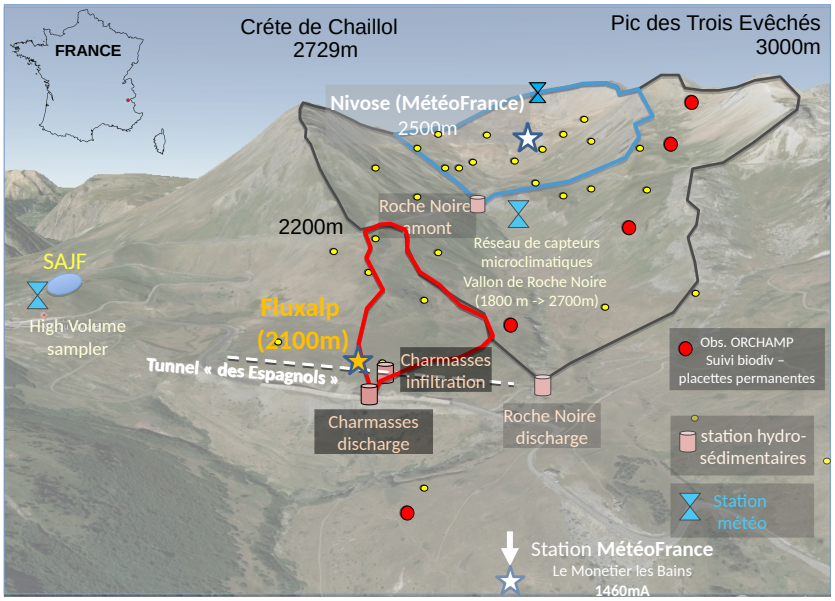

Figure 7.1: Roche Noire catchment (black line) adjacent to the studied Charmasses catchment and the large amount of observations on that catchment including oRCHAMP multiple elevation plots for biodiversity survey (red dots), Flying meadows, hydro-sedimentary river stations (pink cyl.), distributed soil temperature measurements (yellow dots), meteorological stations (blue double triangles), Nivose Météo France snow survey (white stars).

from such kind of approach.

Appendix A - Four years of ParFlow-CLM simulation

This section represent the 4 years of continuous model simulation and validation of approach presented in Chapter 5. Albedo from individual hydrological years has been calibrated by adjusting the snow albedo and snow age coefficients. The resulted albedo calibration is shown in Supplementary figure C1. After calibrating the model using the distributed forcing and subsurface setting from Chapter 5 it has been run for four continuous years. The model run are plotted against the observed discharge and shows good agreement (Fig. C2. This proves that the albedo calibration was essential to validate the model in the catchment.

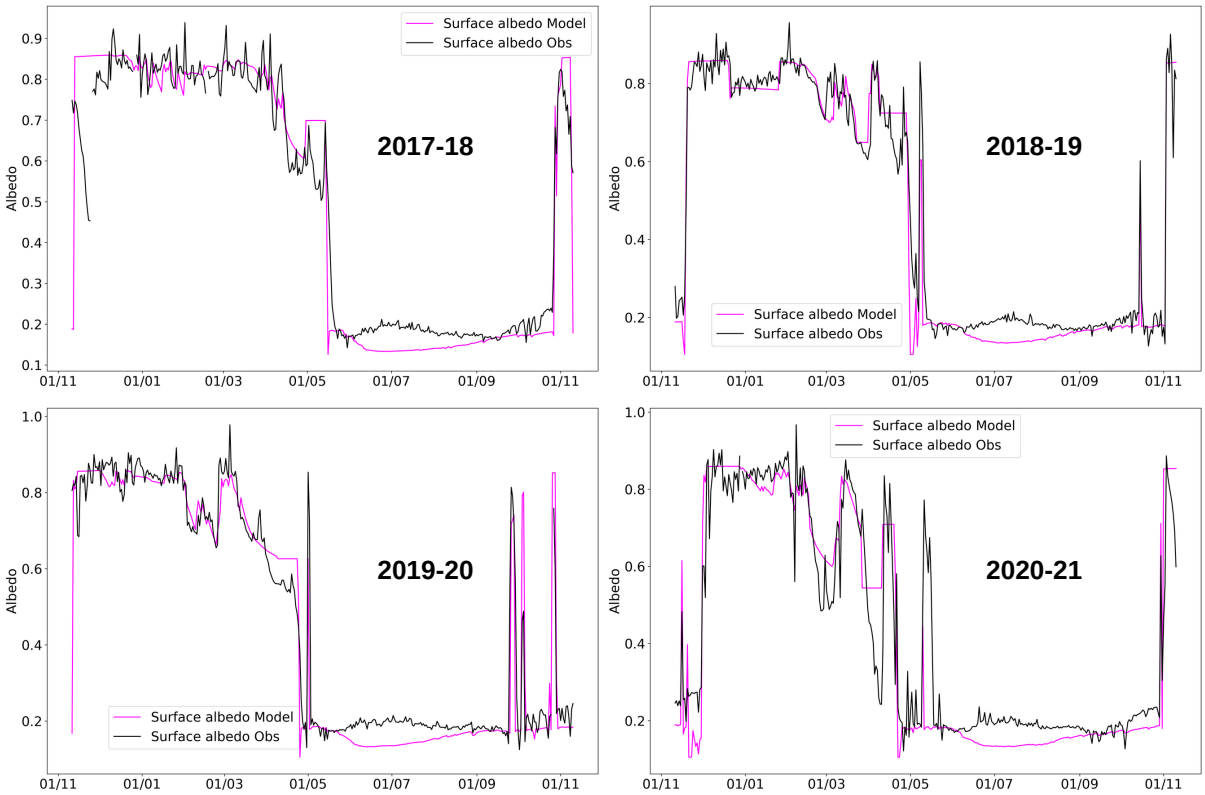

Figure A1: Albedo calibration against the observation for four different hydrological years.

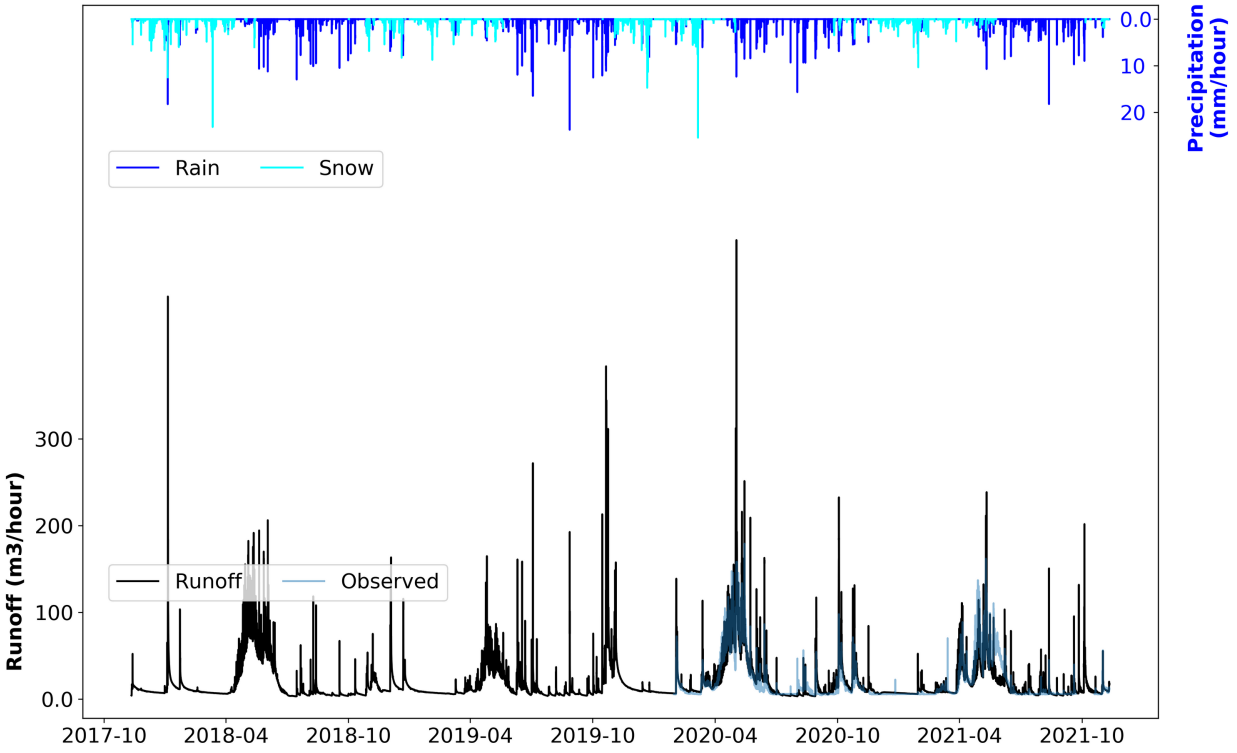

Figure A2: Four years of continuous ParFlow-CLM simulation against the observed discharge.

Appendix B - ParFlow-CLM simulation with various parametrization

This section presents the different sensitivity analysis of subsurface has been done using the three layer heterogeneous model. This section is divided into 3 parts as follow.

Part I: This parts shows the sensitivity of porosity and permeability for the hydrological flux modeling

Part II: This part shows the sensitivity of Van-Genuchten parameters for the hydrological modeling

Part III: This part shows the runoff and evapotranspiration variation for various kind of subsurface parametrization.

Part I

Simulations for porosity and permeability sensitivity

Parflow 2018-2019 simulations

Simulation name: Standard

SoilPerm = 0.237, RegPerm = 0.058, FlyschPerm = 0.00238
SoilPoro = 0.60, RegPoro = 0.45, FlyschPoro = 0.02
SoilAlpha = 2.4, RegAlpha = 0.16, FlyschAlpha = 4
SoilN = 2.67, RegN = 1.56, FlyschN = 2
SoilSRes = 0.04, RegSRes = 0.05, FlyschSRes = 0.04
SoilSSat = 0.9, RegSSat = 0.9, FlyschSSat = 0.9

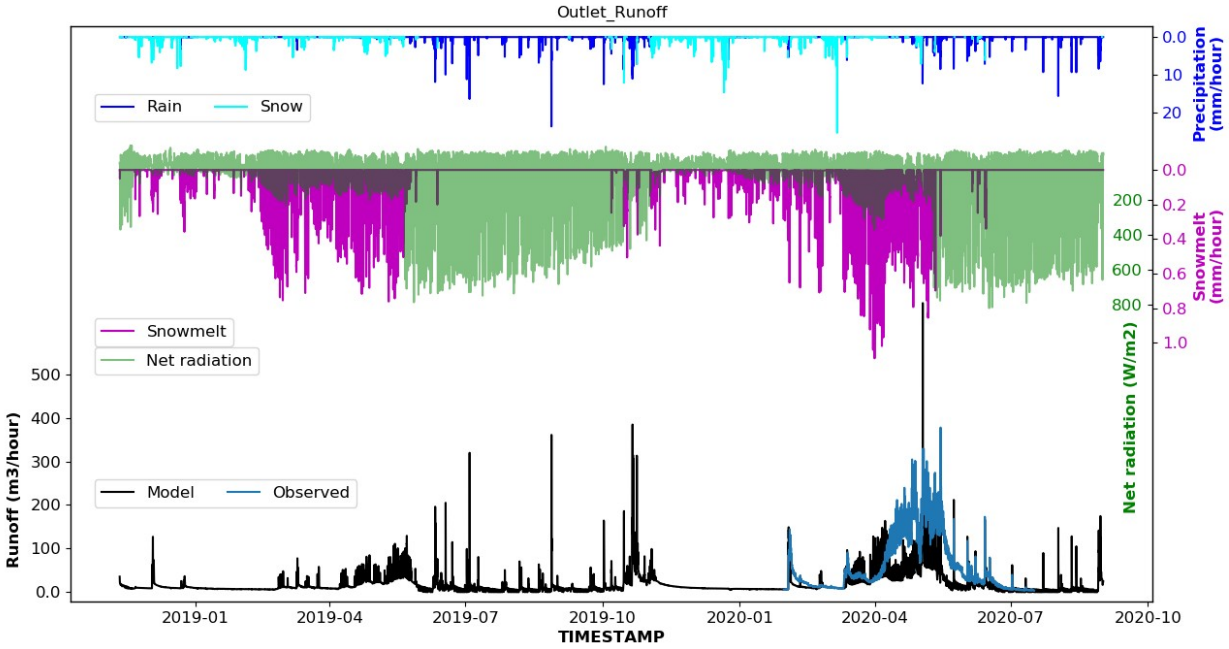

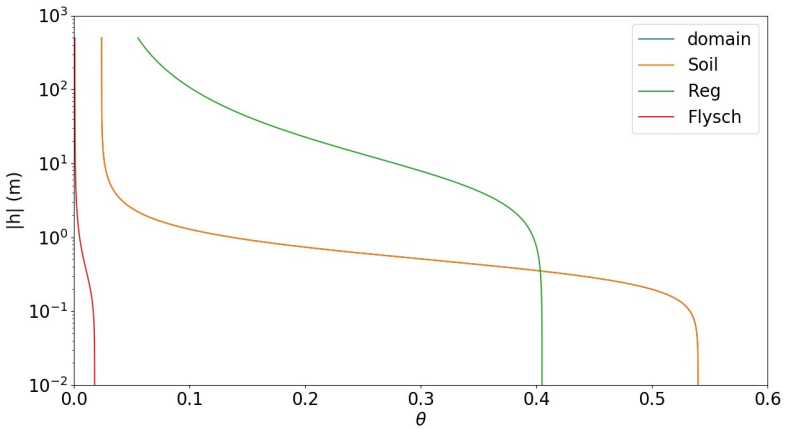

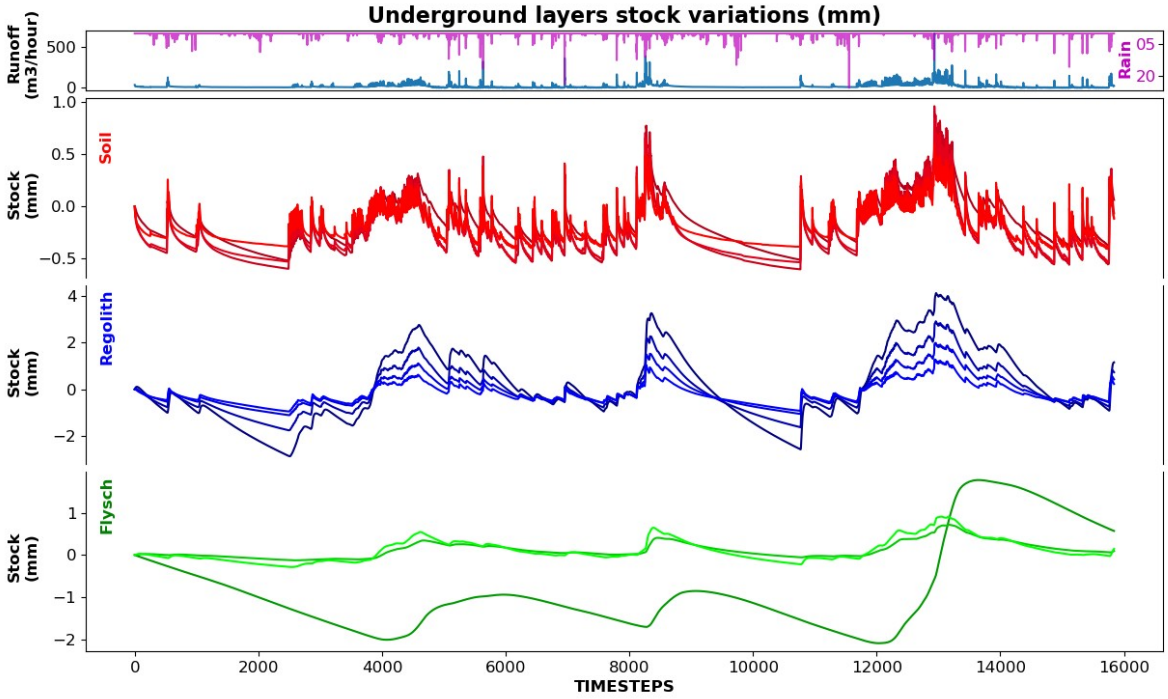
Underground layers stock variations (mm)
Runoff (m3/hour)
500
0
Rain
05
20
Soil
Stock (mm)
1.0
0.5
0.0
−0.5
Regolith
Stock (mm)
4
2
0
−2
Flysch
Stock (mm)
1
0
−1
−2
0
2000
4000
6000
8000
10000
12000
14000
16000
TIMESTEPS

Simulation name: HighRegAlphaN

SoilPerm = 0.237, RegPerm = 0.058, FlyschPerm = 0.00238
SoilPoro = 0.60, RegPoro = 0.45, FlyschPoro = 0.02
SoilAlpha = 2.4, RegAlpha = 1.5, FlyschAlpha = 4
SoilN = 2.67, RegN = 2, FlyschN = 2
SoilSRes = 0.04, RegSRes = 0.05, FlyschSRes = 0.04
SoilSSat = 0.9, RegSSat = 0.9, FlyschSSat = 0.9

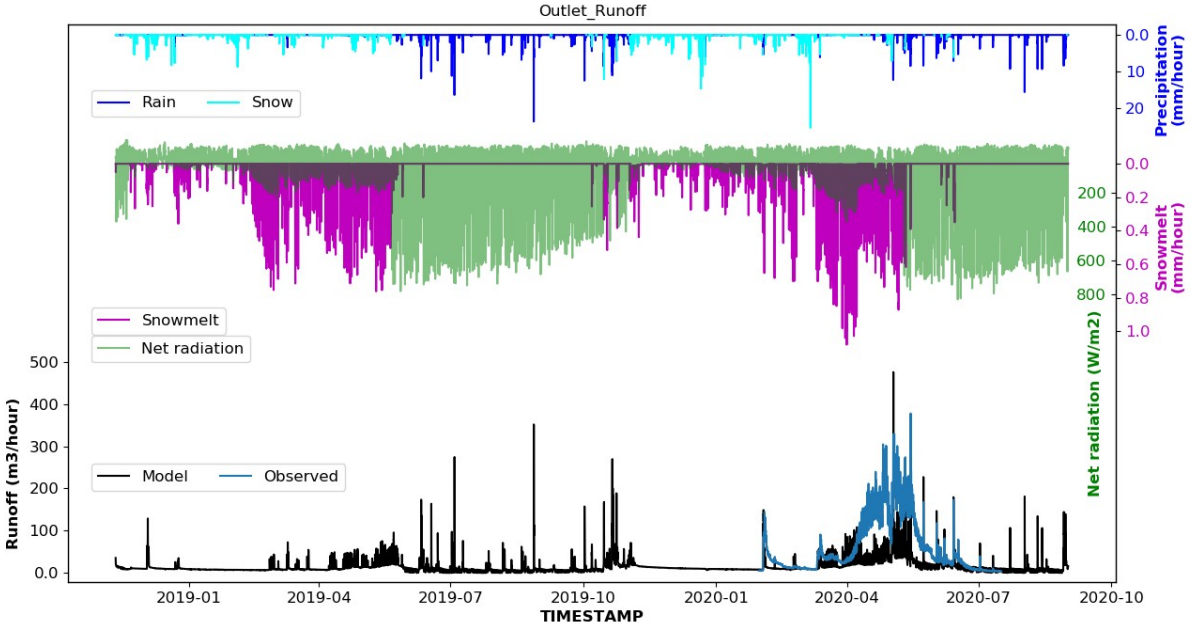

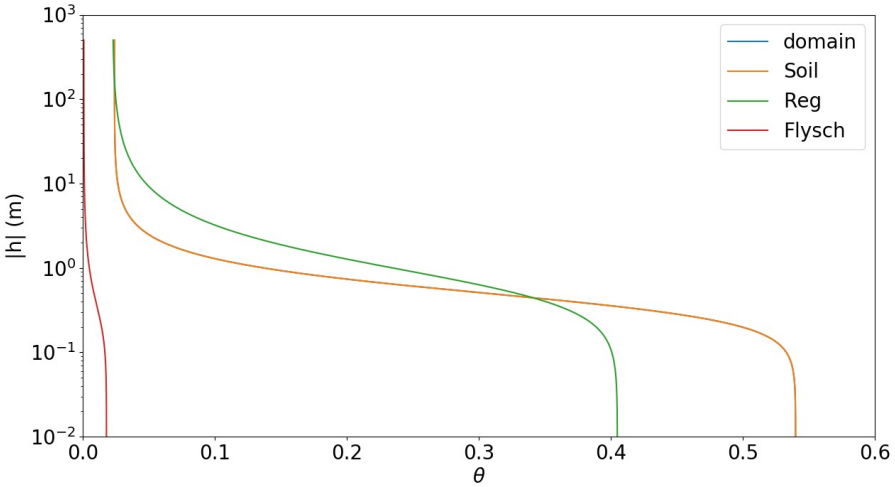

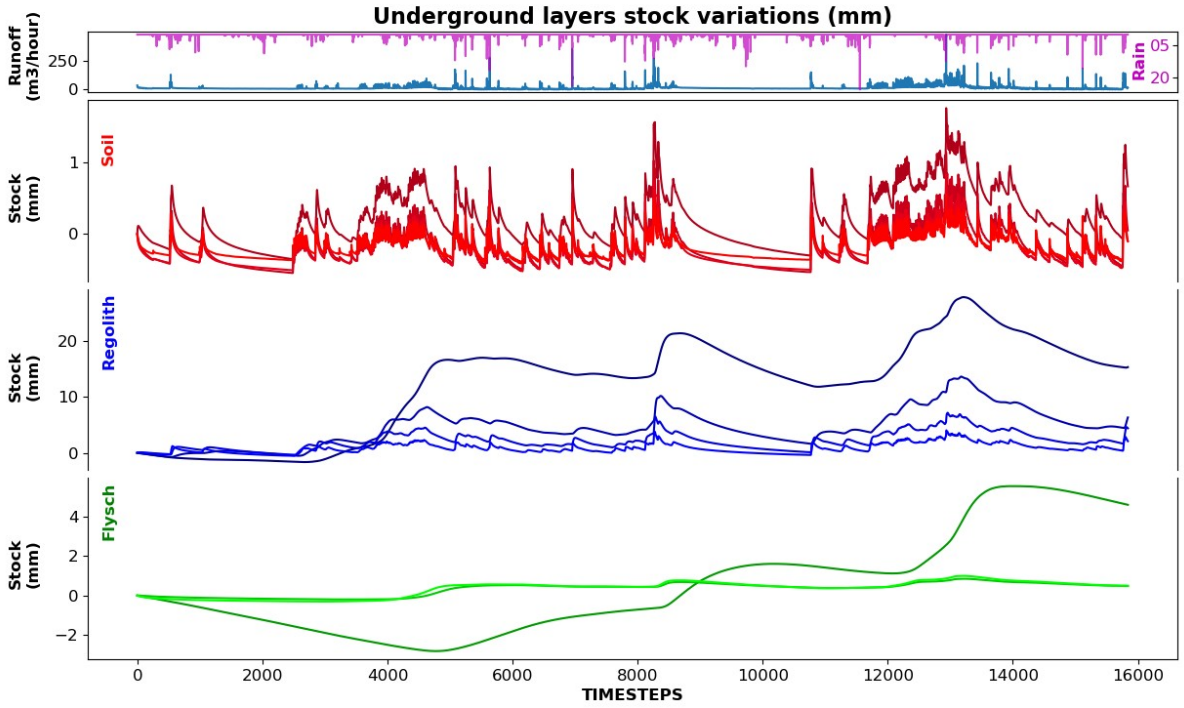
Underground layers stock variations (mm)
Runoff (m3/hour)
250
0
Rain
05
20
Soil
Stock (mm)
1
0
Regolith
Stock (mm)
20
10
0
Flysch
Stock (mm)
4
2
0
−2
0
2000
4000
6000
8000
10000
12000
14000
16000
TIMESTEPS

Simulation name: LowRegSoilAlphaN

SoilPerm = 0.237, RegPerm = 0.058, FlyschPerm = 0.00238
SoilPoro = 0.60, RegPoro = 0.45, FlyschPoro = 0.02
SoilAlpha = 1.5, RegAlpha = 1.1, FlyschAlpha = 4
SoilN = 1.8, RegN = 1.4, FlyschN = 2
SoilSRes = 0.04, RegSRes = 0.05, FlyschSRes = 0.04
SoilSSat = 0.9, RegSSat = 0.9, FlyschSSat = 0.9

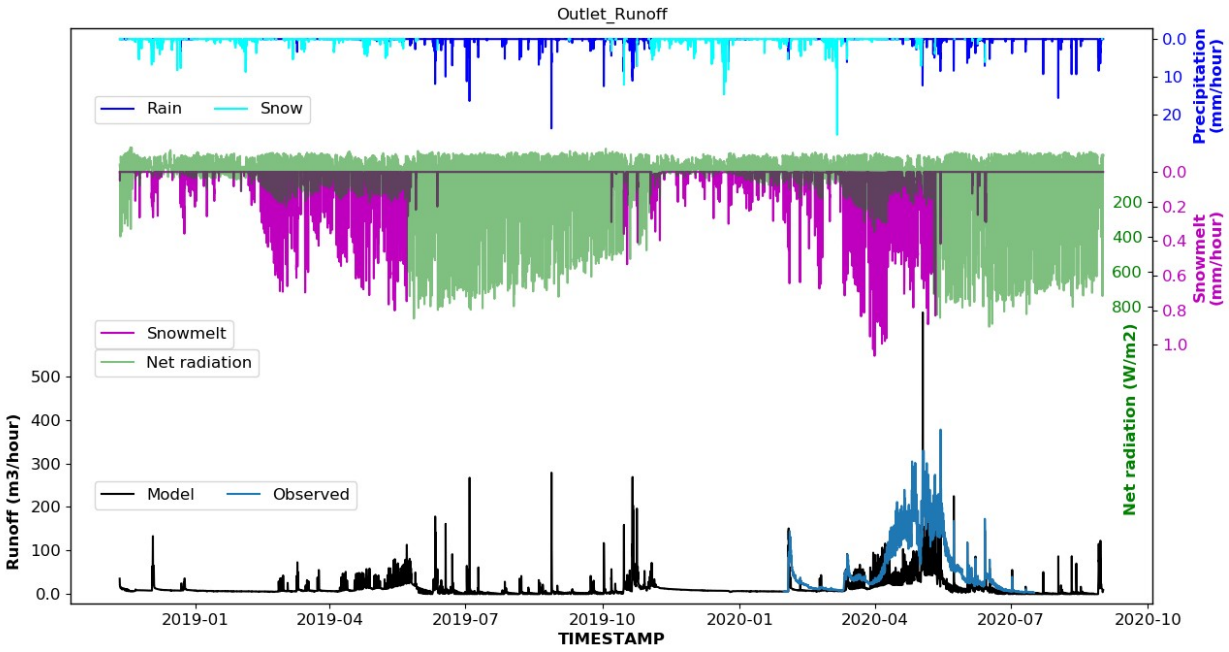

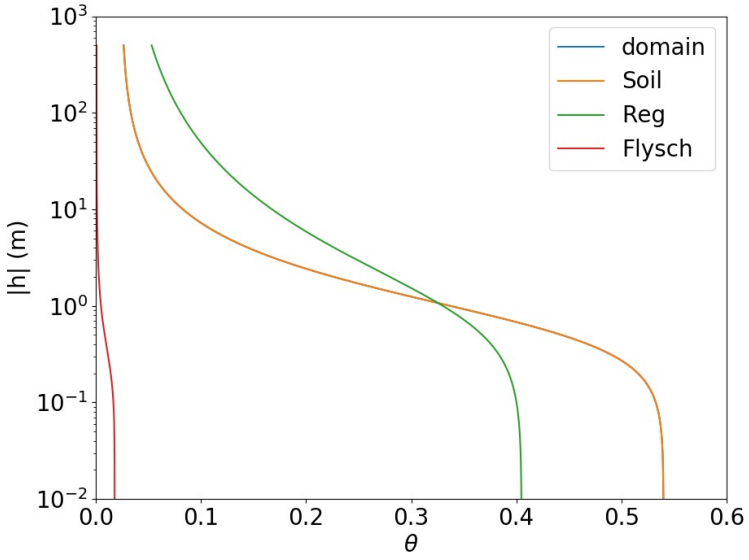

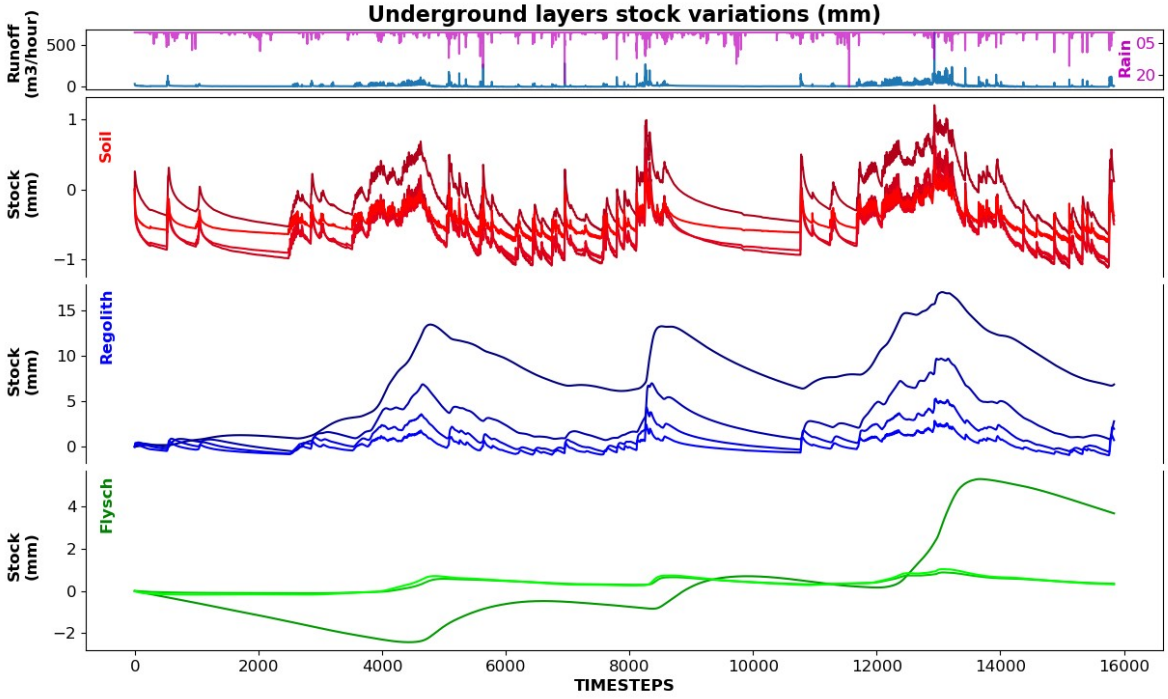
Underground layers stock variations (mm)
Runoff (m3/hour)
500
0
Rain
05
20
Soil
Stock (mm)
1
0
−1
Regolith
Stock (mm)
15
10
5
0
Flysch
Stock (mm)
4
2
0
−2
0
2000
4000
6000
8000
10000
12000
14000
16000
TIMESTEPS

Simulation name: LowSoilHighRegPerm

SoilPerm = 0.148, RegPerm = 0.276, FlyschPerm = 0.00238
SoilPoro = 0.60, RegPoro = 0.45, FlyschPoro = 0.02
SoilAlpha = 2.4, RegAlpha = 0.16, FlyschAlpha = 4
SoilN = 2.67, RegN = 1.56, FlyschN = 2
SoilSRes = 0.04, RegSRes = 0.05, FlyschSRes = 0.04
SoilSSat = 0.9, RegSSat = 0.9, FlyschSSat = 0.9

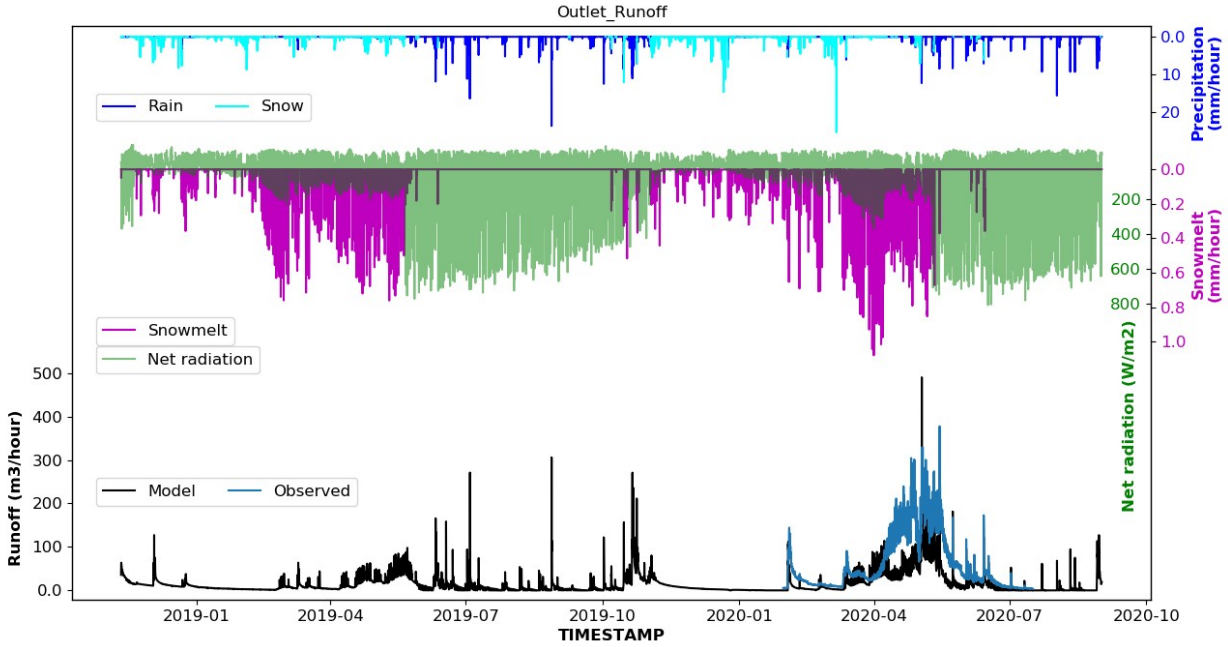

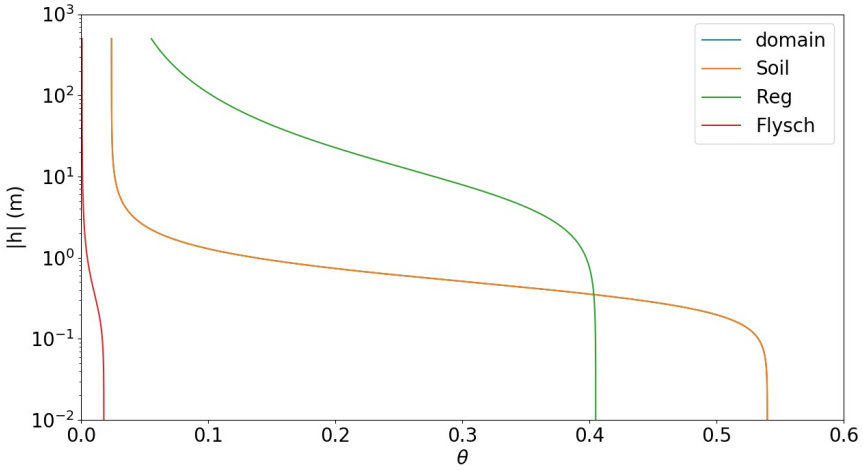

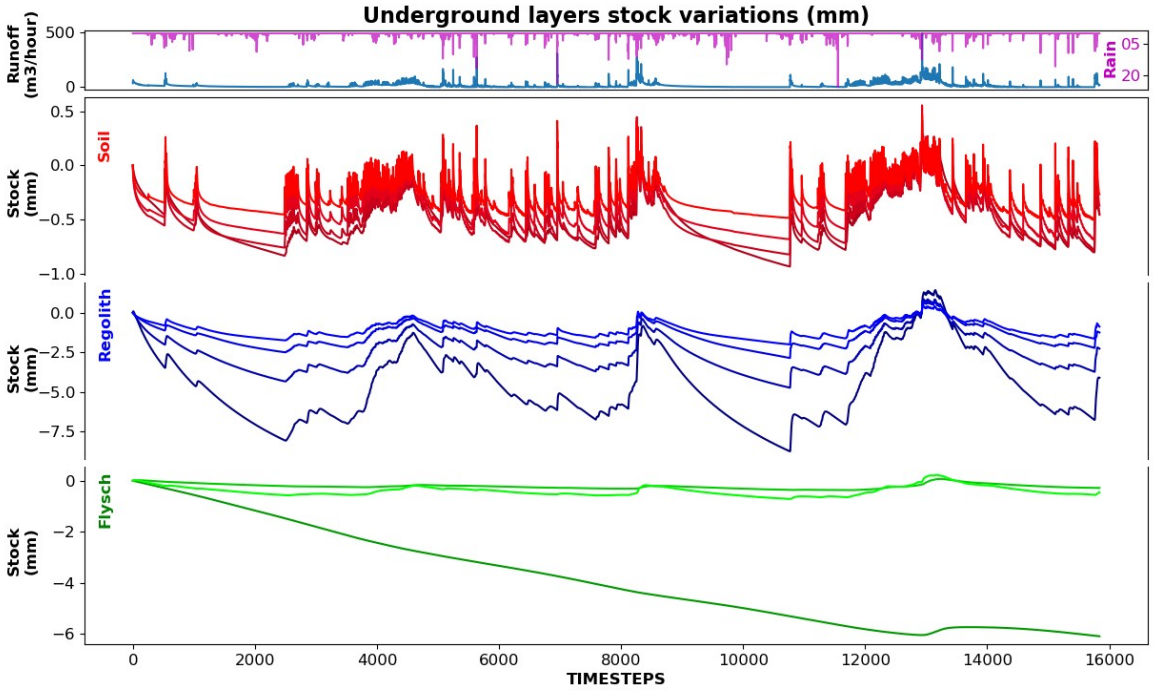
Underground layers stock variations (mm)
Runoff (m3/hour)
500
0
Rain
05
20
Soil
Stock (mm)
0.5
0.0
−0.5
−1.0
Regolith
Stock (mm)
0.0
−2.5
−5.0
−7.5
Flysch
Stock (mm)
0
−2
−4
−6
0
2000
4000
6000
8000
10000
12000
14000
16000
TIMESTEPS

Simulation name: ActivatingReg

SoilPerm = 0.237, RegPerm = 0.158, FlyschPerm = 0.00238
SoilPoro = 0.60, RegPoro = 0.45, FlyschPoro = 0.02
SoilAlpha = 2.4, RegAlpha = 0.16, FlyschAlpha = 4
SoilN = 2.67, RegN = 1.56, FlyschN = 2
SoilSRes = 0.04, RegSRes = 0.05, FlyschSRes = 0.04
SoilSSat = 1, RegSSat = 1, FlyschSSat = 1

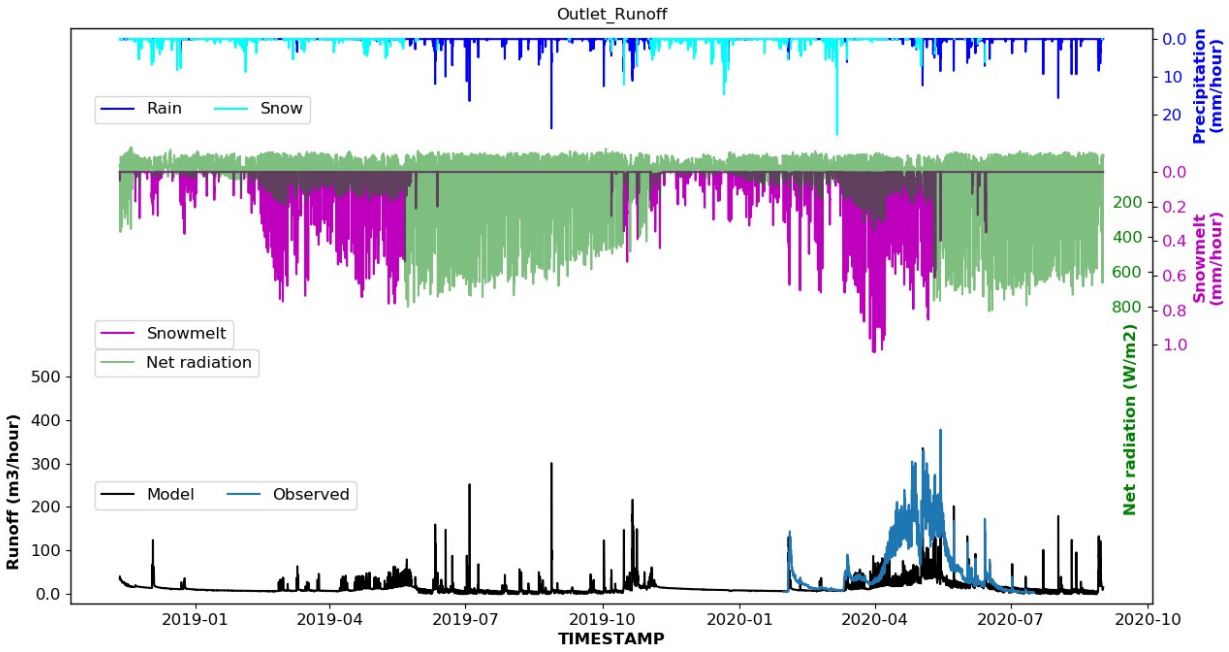

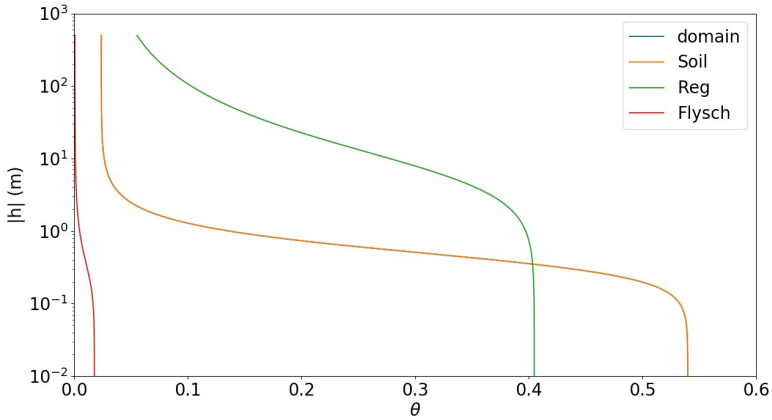

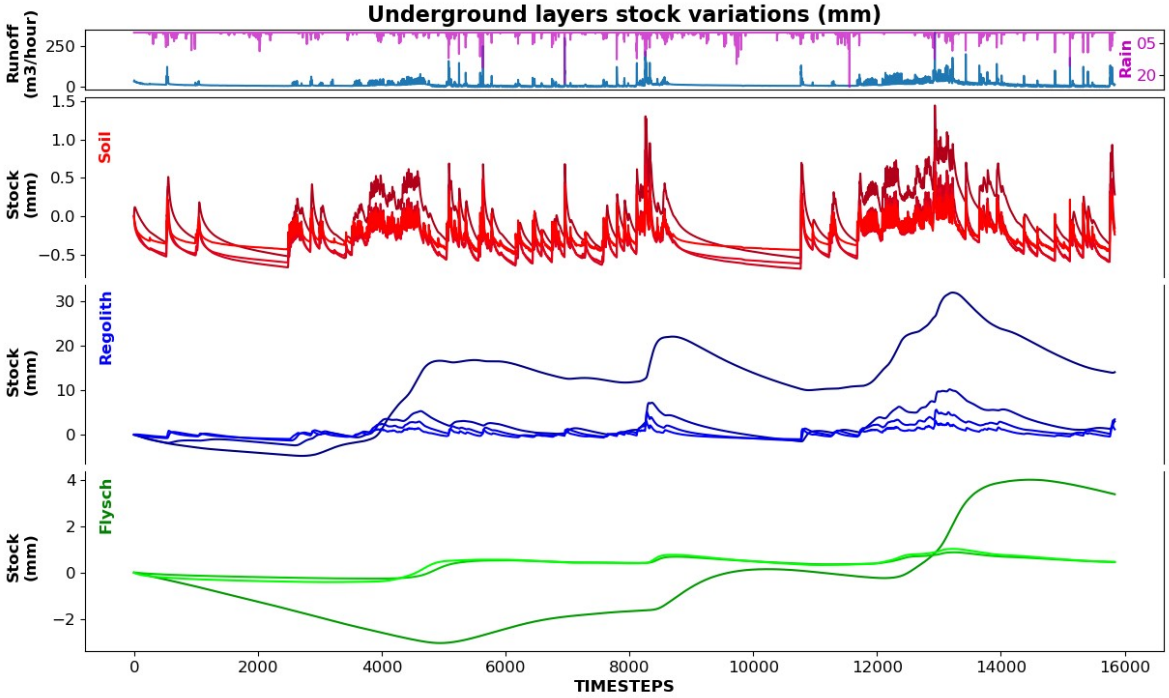
Underground layers stock variations (mm)
Runoff (m3/hour)
250
0
Rain
05
20
Soil
Stock (mm)
1.5
1.0
0.5
0.0
−0.5
Regolith
Stock (mm)
30
20
10
0
Flysch
Stock (mm)
4
2
0
−2
0
2000
4000
6000
8000
10000
12000
14000
16000
TIMESTEPS

Simulation name: ActivatingFlysch

SoilPerm = 0.237, RegPerm = 0.058, FlyschPerm = 0.0238
SoilPoro = 0.60, RegPoro = 0.45, FlyschPoro = 0.3
SoilAlpha = 2.4, RegAlpha = 0.16, FlyschAlpha = 4
SoilN = 2.67, RegN = 1.56, FlyschN = 2
SoilSRes = 0.04, RegSRes = 0.05, FlyschSRes = 0.04
SoilSSat = 1, RegSSat = 1, FlyschSSat = 1

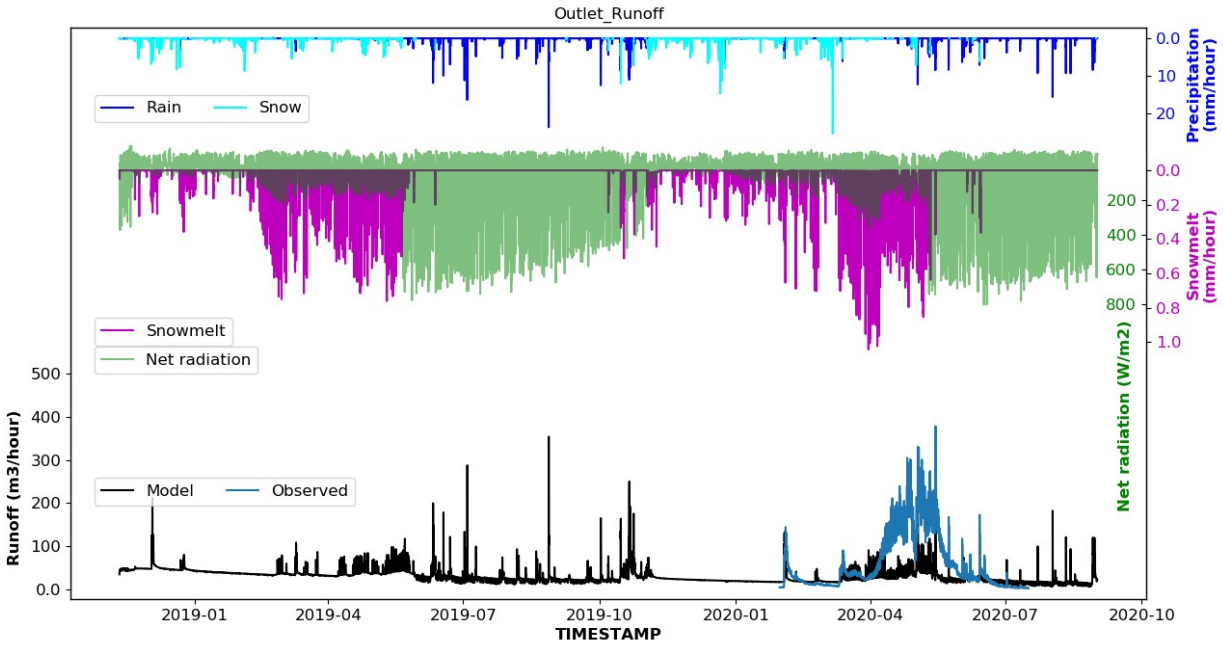

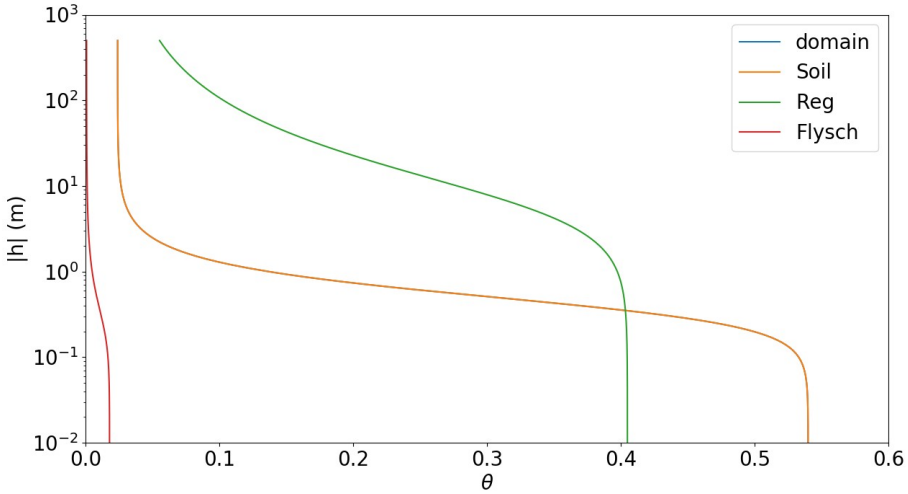

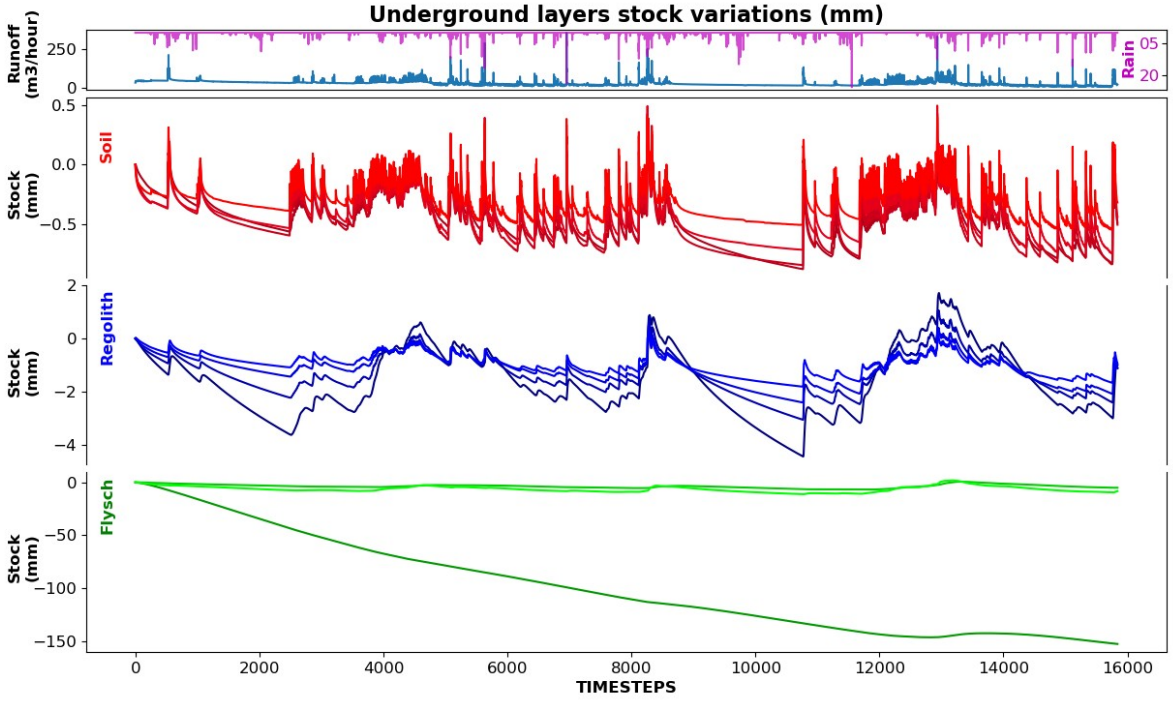
Underground layers stock variations (mm)
Runoff (m3/hour)
250
0
Rain
05
20
Stock (mm)
Soil
0.5
0.0
−0.5
Stock (mm)
Regolith
2
0
−2
−4
Stock (mm)
Flysch
0
−50
−100
−150
0
2000
4000
6000
8000
10000
12000
14000
16000
TIMESTEPS

Simulation name: LowSoilHighRegPermMediumRegAlphaN

SoilPerm = 0.148, RegPerm = 0.276, FlyschPerm = 0.00238
SoilPoro = 0.60, RegPoro = 0.45, FlyschPoro = 0.1
SoilAlpha = 2.4, RegAlpha = 1.1, FlyschAlpha = 4
SoilN = 2.67, RegN = 1.4, FlyschN = 2
SoilSRes = 0.04, RegSRes = 0.05, FlyschSRes = 0.04
SoilSSat = 0.9, RegSSat = 0.9, FlyschSSat = 0.9

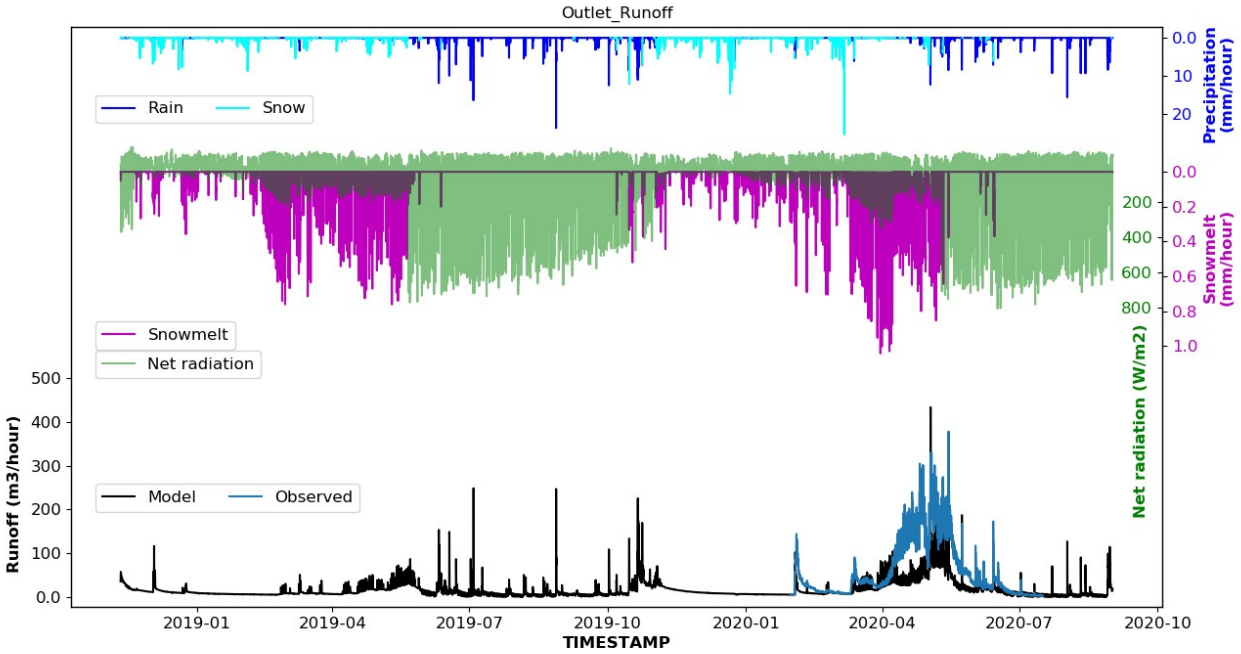

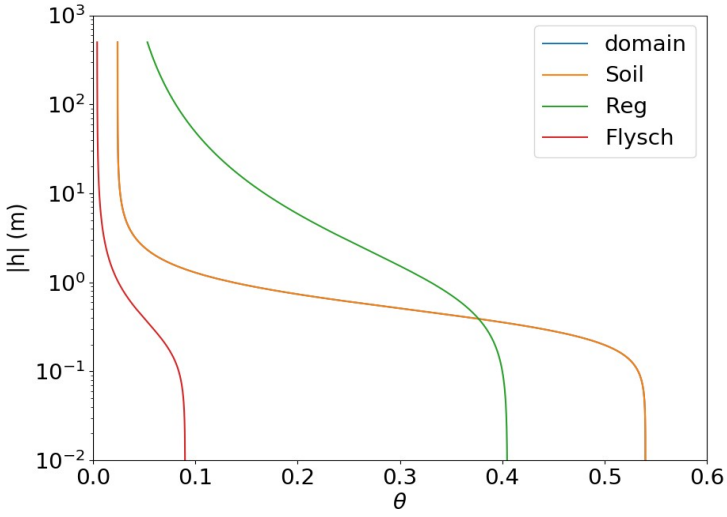

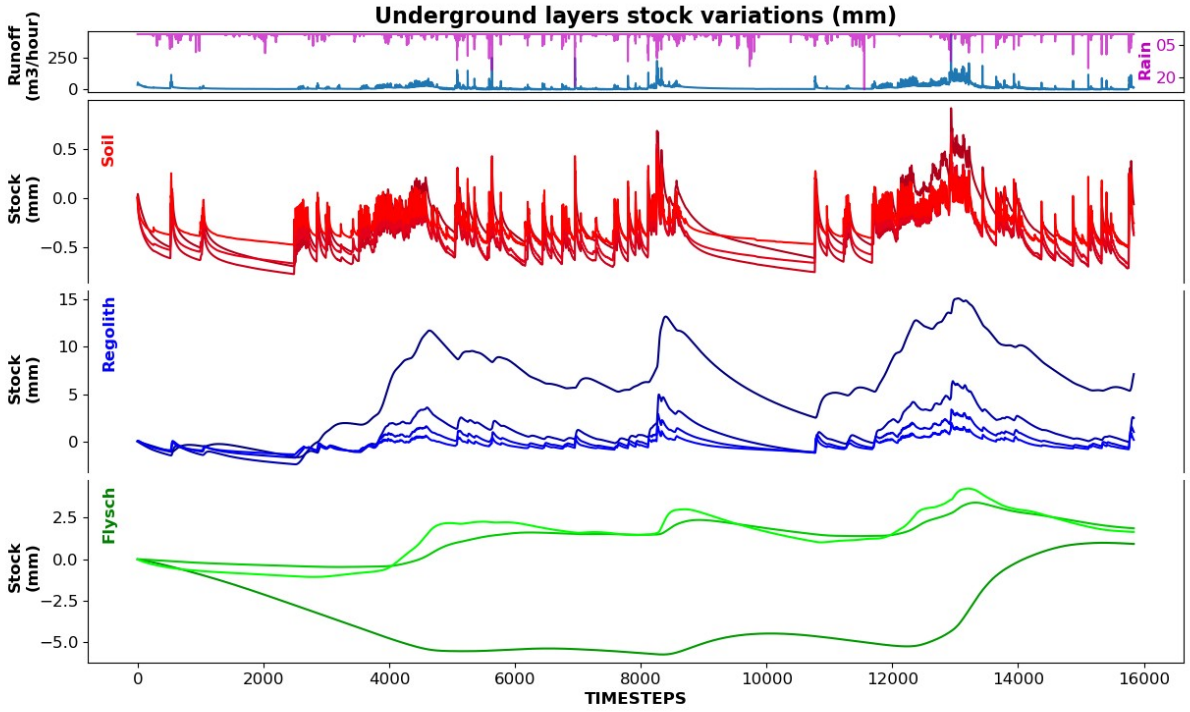
Underground layers stock variations (mm)
Runoff (m3/hour)
250
0
Rain
05
20
Soil
Stock (mm)
0.5
0.0
−0.5
Regolith
Stock (mm)
15
10
5
0
Flysch
Stock (mm)
2.5
0.0
−2.5
−5.0
0
2000
4000
6000
8000
10000
12000
14000
16000
TIMESTEPS

Simulation name: SoilRegSameLowPerm

SoilPerm = 0.148, RegPerm = 0.148, FlyschPerm = 0.00238
SoilPoro = 0.60, RegPoro = 0.45, FlyschPoro = 0.02
SoilAlpha = 2.4, RegAlpha = 0.16, FlyschAlpha = 4
SoilN = 2.67, RegN = 1.56, FlyschN = 2
SoilSRes = 0.04, RegSRes = 0.05, FlyschSRes = 0.04
SoilSSat = 0.9, RegSSat = 0.9, FlyschSSat = 0.9

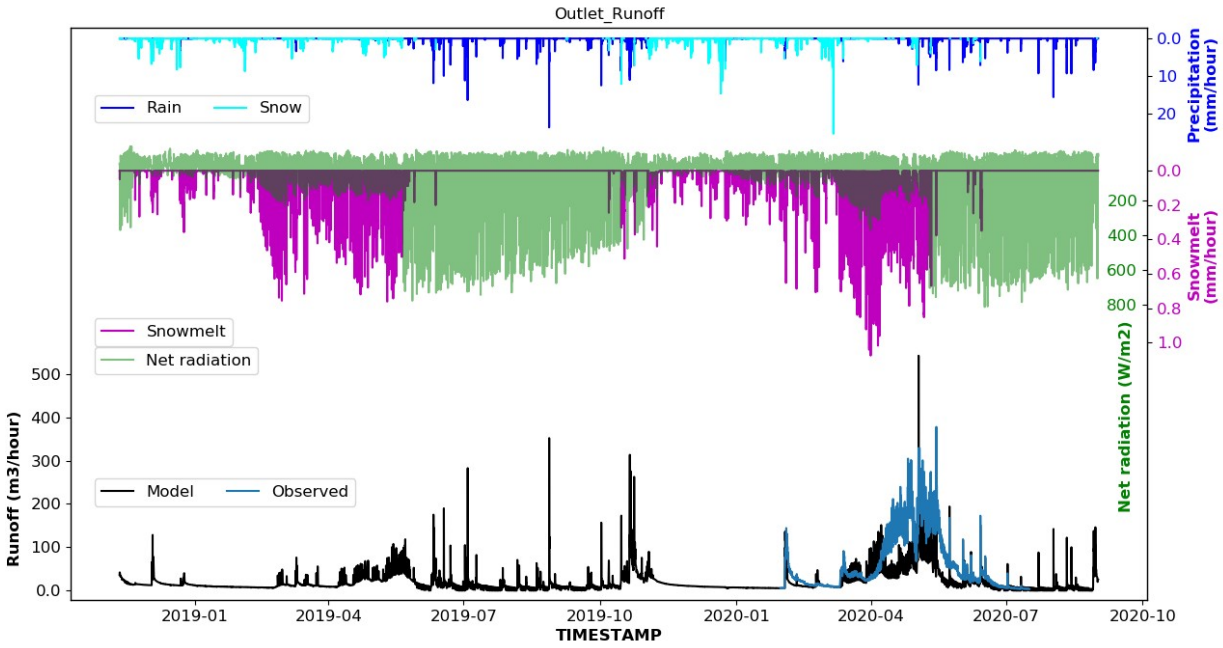

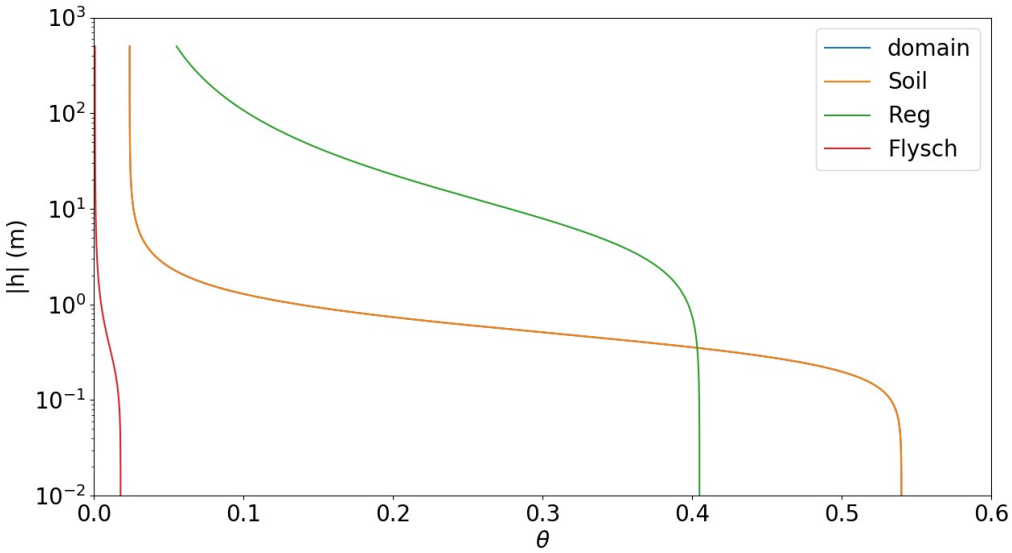

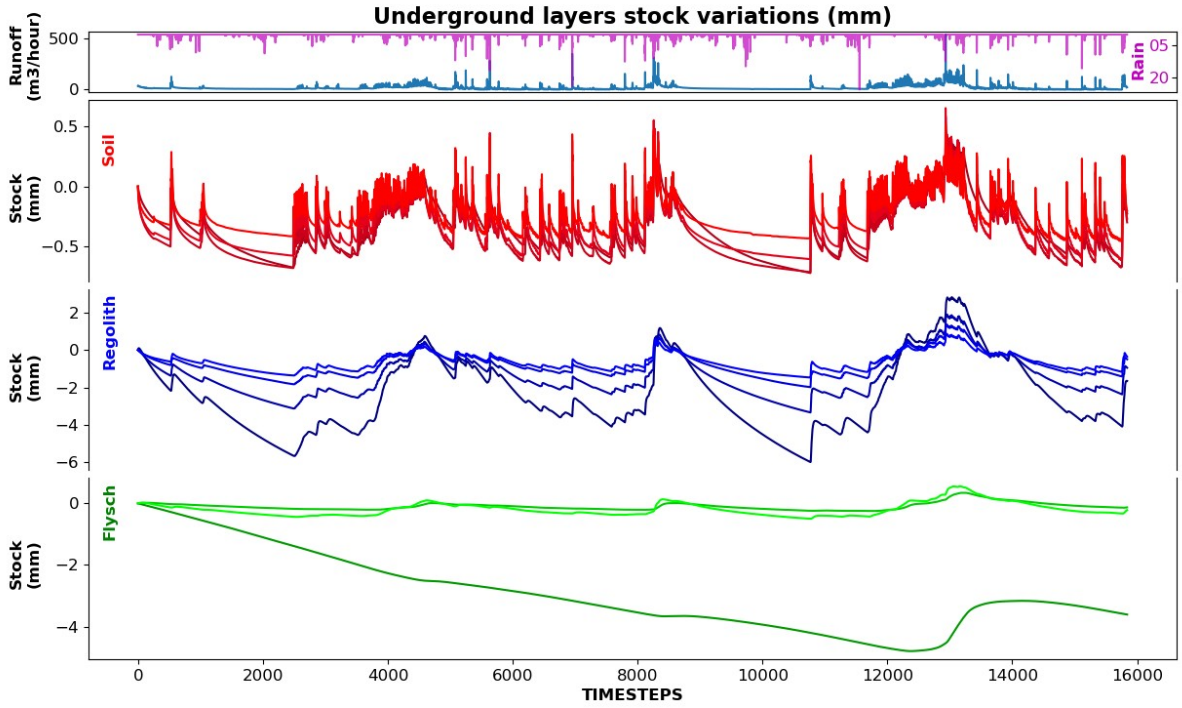
Underground layers stock variations (mm)
Runoff (m3/hour)
500
0
Rain
05
20
Soil
Stock (mm)
0.5
0.0
−0.5
Regolith
Stock (mm)
2
0
−2
−4
−6
Flysch
Stock (mm)
0
−2
−4
0
2000
4000
6000
8000
10000
12000
14000
16000
TIMESTEPS

Simulation name: SoilRegSameFlyschPerm0.058Poro0.02HighRegAlphaN

SoilPerm = 0.237, RegPerm = 0.237, FlyschPerm = 0.058
SoilPoro = 0.60, RegPoro = 0.45, FlyschPoro = 0.02
SoilAlpha = 2.4, RegAlpha = 1.1, FlyschAlpha = 4
SoilN = 2.67, RegN = 1.4, FlyschN = 2
SoilSRes = 0.04, RegSRes = 0.05, FlyschSRes = 0.04
SoilSSat = 0.9, RegSSat = 0.9, FlyschSSat = 0.9

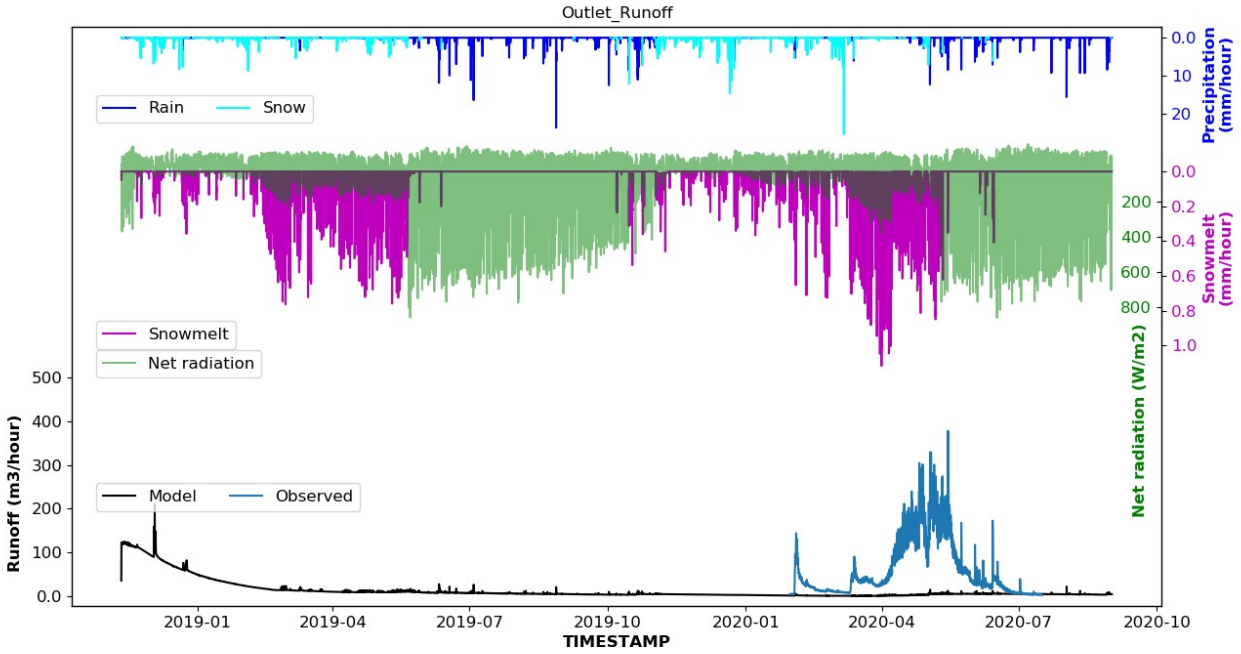

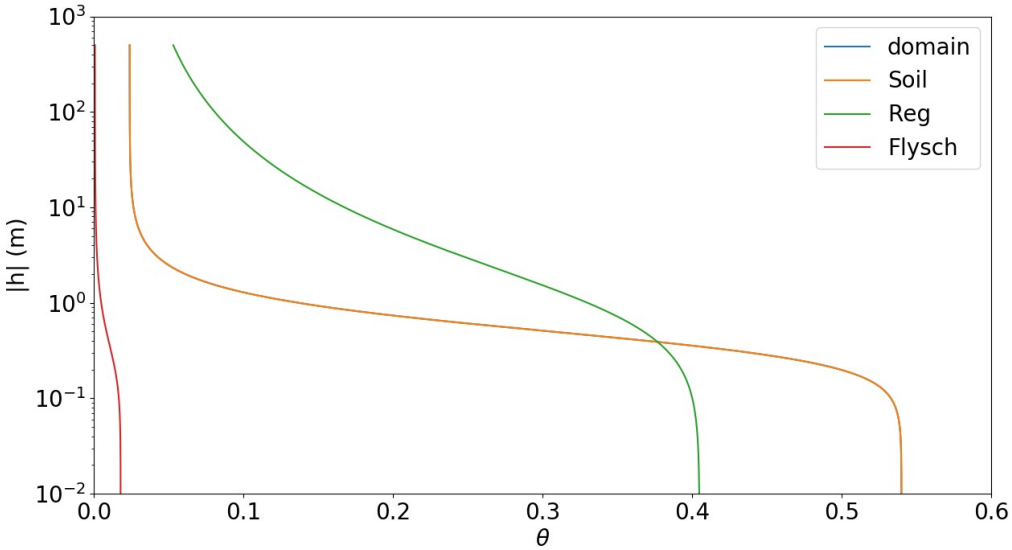

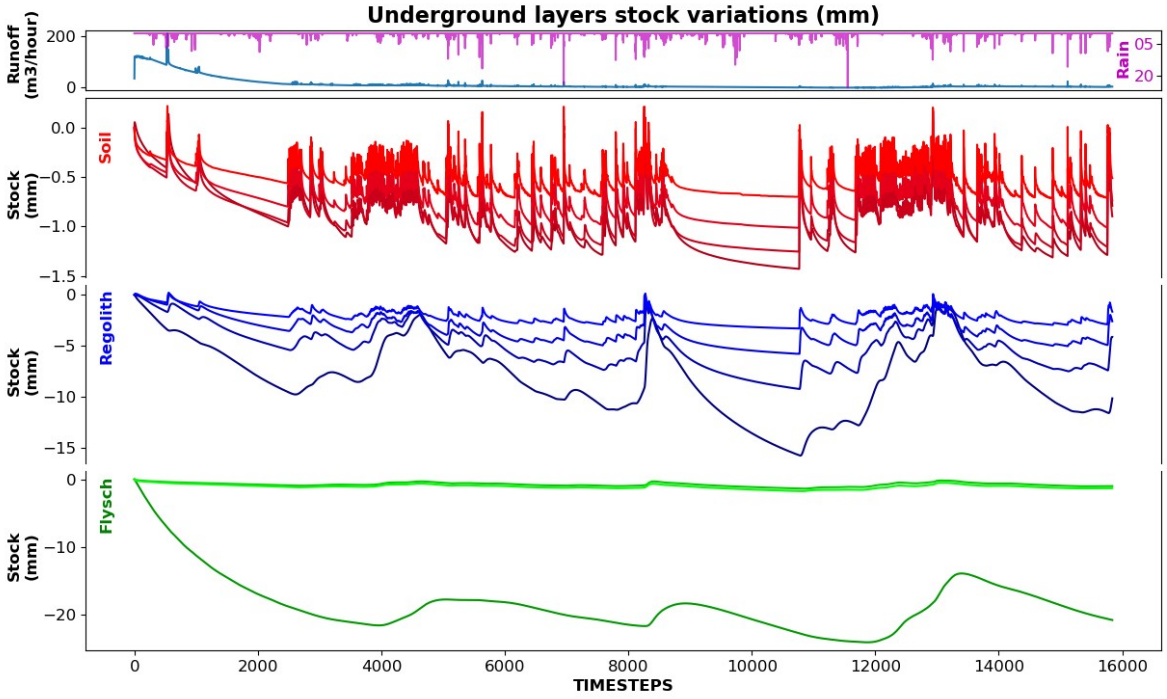
Underground layers stock variations (mm)
Runoff (m3/hour)
200
0
Rain
05
20
Soil
Stock (mm)
0.0
−0.5
−1.0
−1.5
Regolith
Stock (mm)
0
−5
−10
−15
Flysch
Stock (mm)
0
−10
−20
0
2000
4000
6000
8000
10000
12000
14000
16000
TIMESTEPS

Simulation name: SoilRegSameFlyschPerm0.058Poro0.02HighRegAlphaN_ST1

SoilPerm = 0.237, RegPerm = 0.237, FlyschPerm = 0.058
SoilPoro = 0.60, RegPoro = 0.45, FlyschPoro = 0.02
SoilAlpha = 2.4, RegAlpha = 1.1, FlyschAlpha = 4
SoilN = 2.67, RegN = 1.4, FlyschN = 2
SoilSRes = 0.04, RegSRes = 0.05, FlyschSRes = 0.04
SoilSSat = 0.9, RegSSat = 0.9, FlyschSSat = 0.9

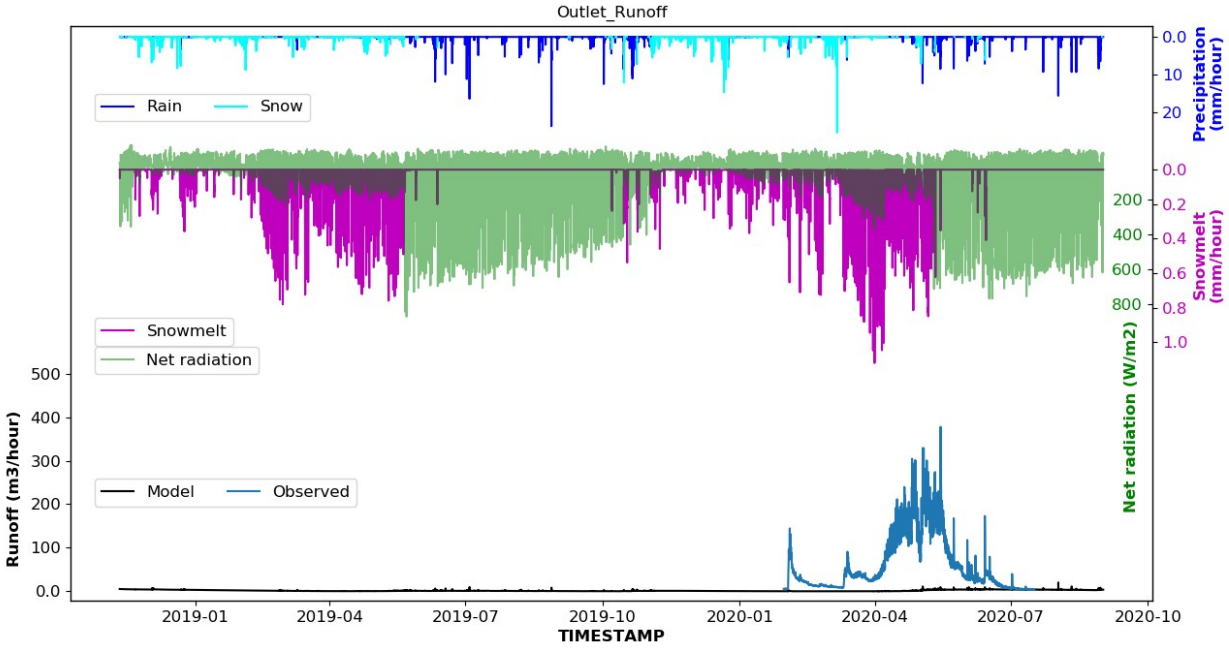

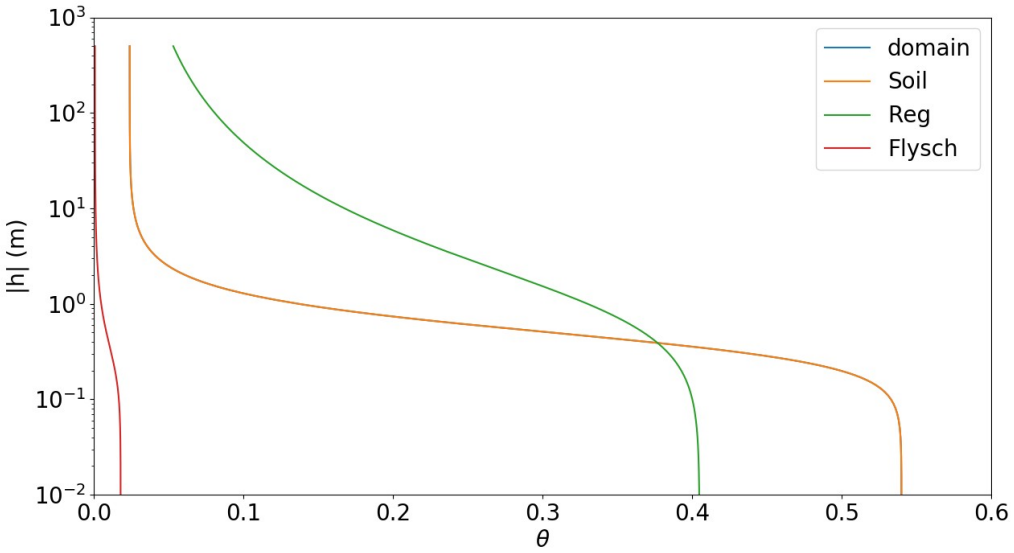

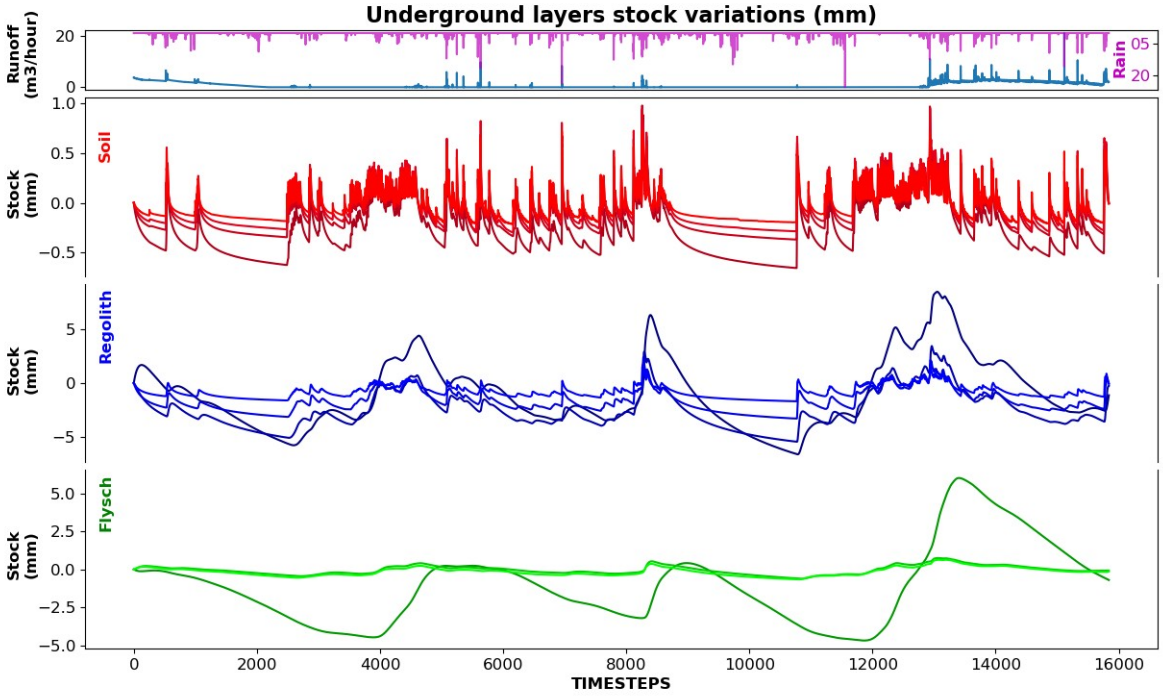
Underground layers stock variations (mm)
Runoff (m3/hour)
Rain
Soil
Regolith
Flysch
Stock (mm)
TIMESTEPS

Simulation name: SoilRegSameFlyschPerm0.058Poro0.02

SoilPerm = 0.237, RegPerm = 0.237, FlyschPerm = 0.058
SoilPoro = 0.60, RegPoro = 0.45, FlyschPoro = 0.02
SoilAlpha = 2.4, RegAlpha = 0.16, FlyschAlpha = 4
SoilN = 2.67, RegN = 1.56, FlyschN = 2
SoilSRes = 0.04, RegSRes = 0.05, FlyschSRes = 0.04
SoilSSat = 0.9, RegSSat = 0.9, FlyschSSat = 0.9

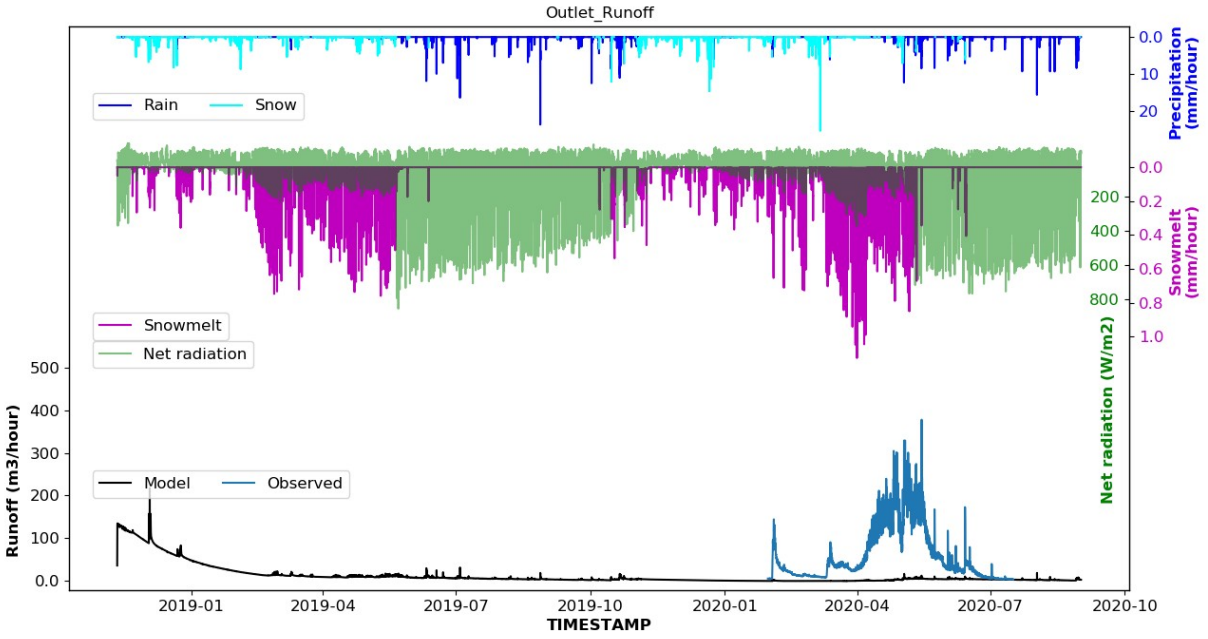

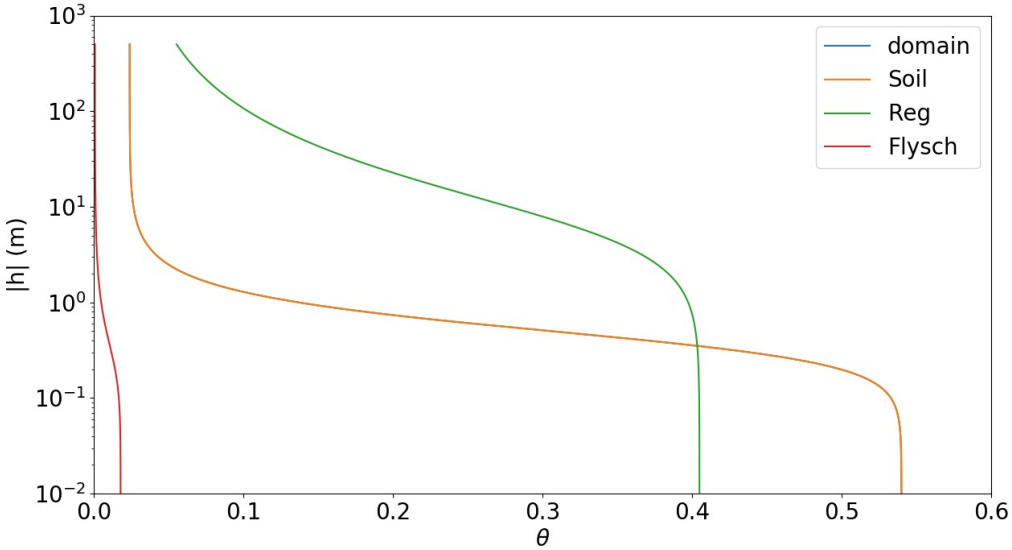

Simulation name: SoilRegSameFlyschPerm0.058Poro0.02_ST1

SoilPerm = 0.237, RegPerm = 0.237, FlyschPerm = 0.058
SoilPoro = 0.60, RegPoro = 0.45, FlyschPoro = 0.02
SoilAlpha = 2.4, RegAlpha = 0.16, FlyschAlpha = 4
SoilN = 2.67, RegN = 1.56, FlyschN = 2
SoilSRes = 0.04, RegSRes = 0.05, FlyschSRes = 0.04
SoilSSat = 0.9, RegSSat = 0.9, FlyschSSat = 0.9

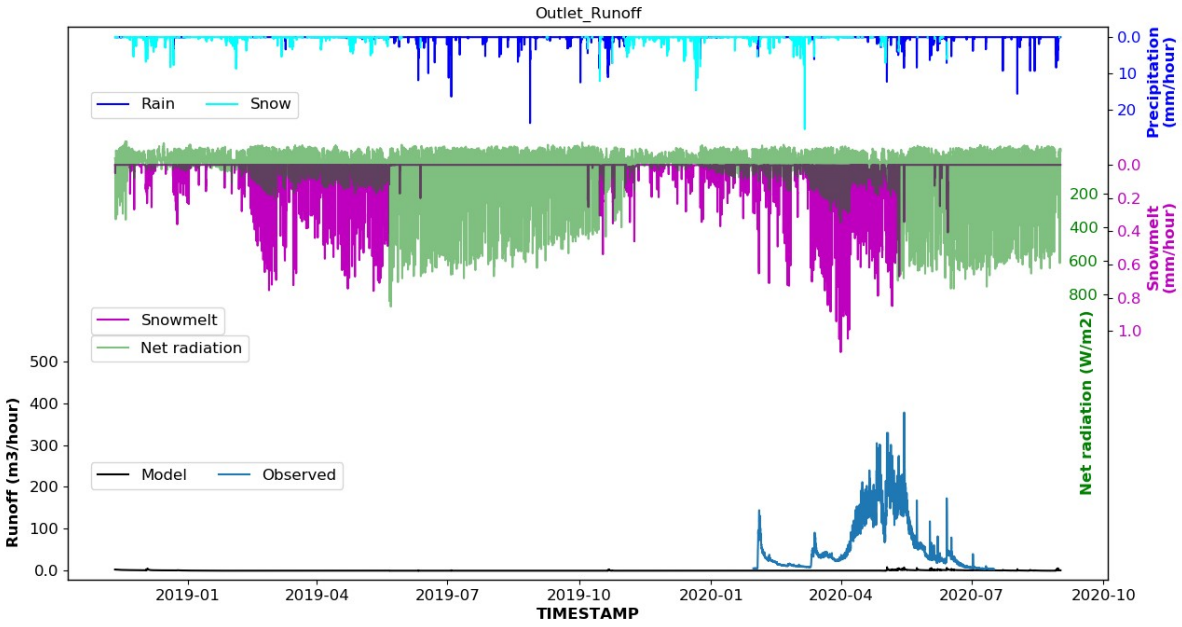

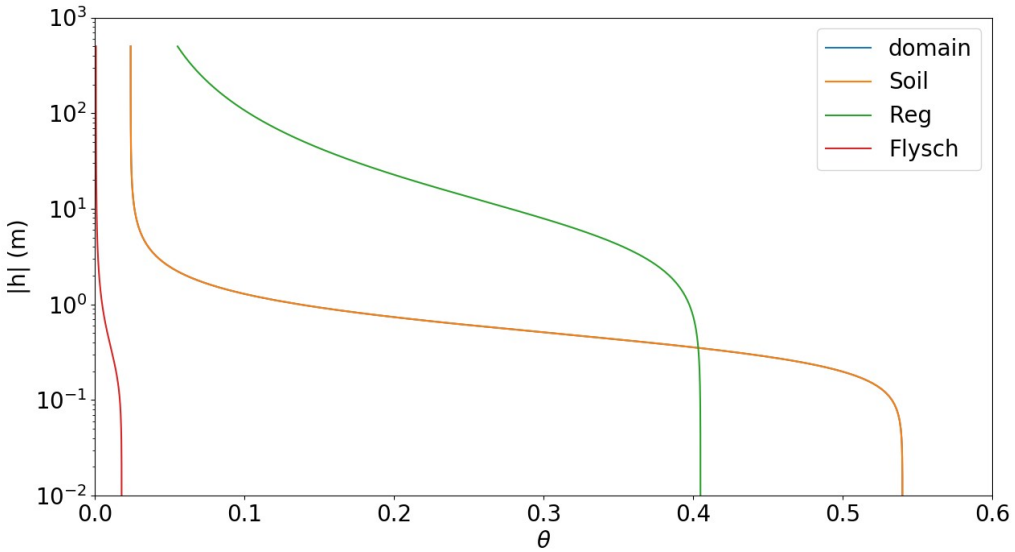

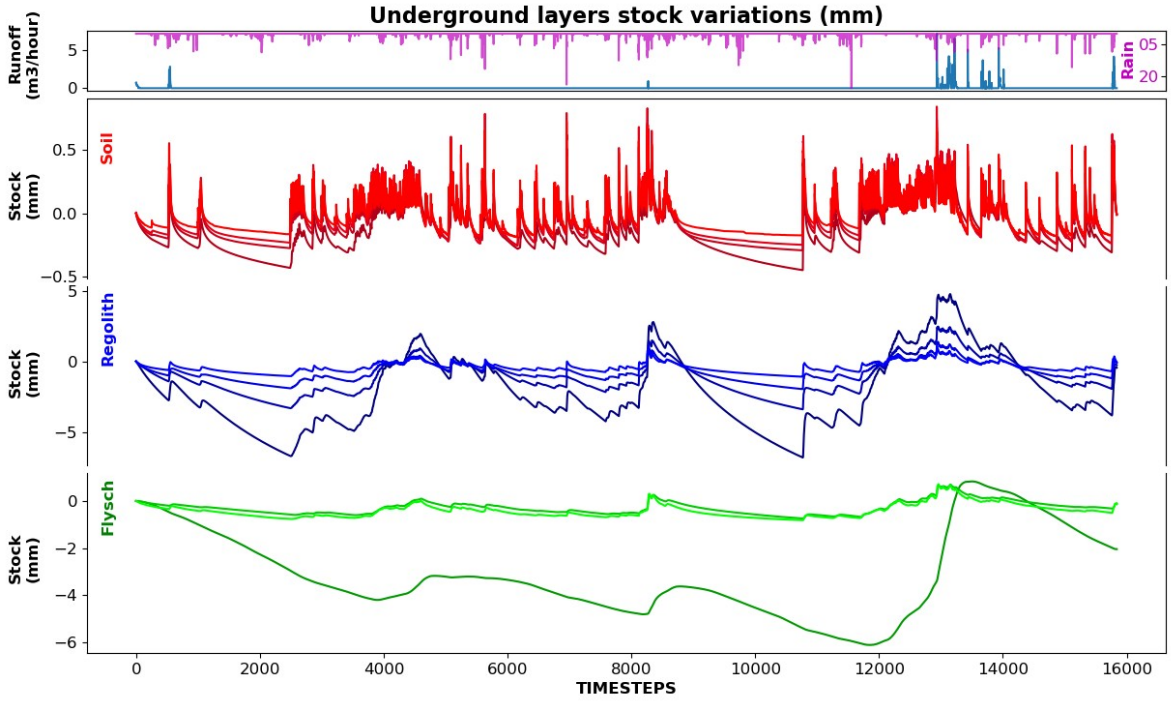
Underground layers stock variations (mm)
Runoff (m3/hour)
Rain
Soil
Regolith
Flysch
Stock (mm)
TIMESTEPS

Simulation name: SoilPerm0.148RegPer.0.058

SoilPerm = 0.148, RegPerm = 0.058, FlyschPerm = 0.00238
SoilPoro = 0.60, RegPoro = 0.45, FlyschPoro = 0.02
SoilAlpha = 2.4, RegAlpha = 0.16, FlyschAlpha = 4
SoilN = 2.67, RegN = 1.56, FlyschN = 2
SoilSRes = 0.04, RegSRes = 0.05, FlyschSRes = 0.04
SoilSSat = 0.9, RegSSat = 0.9, FlyschSSat = 0.9

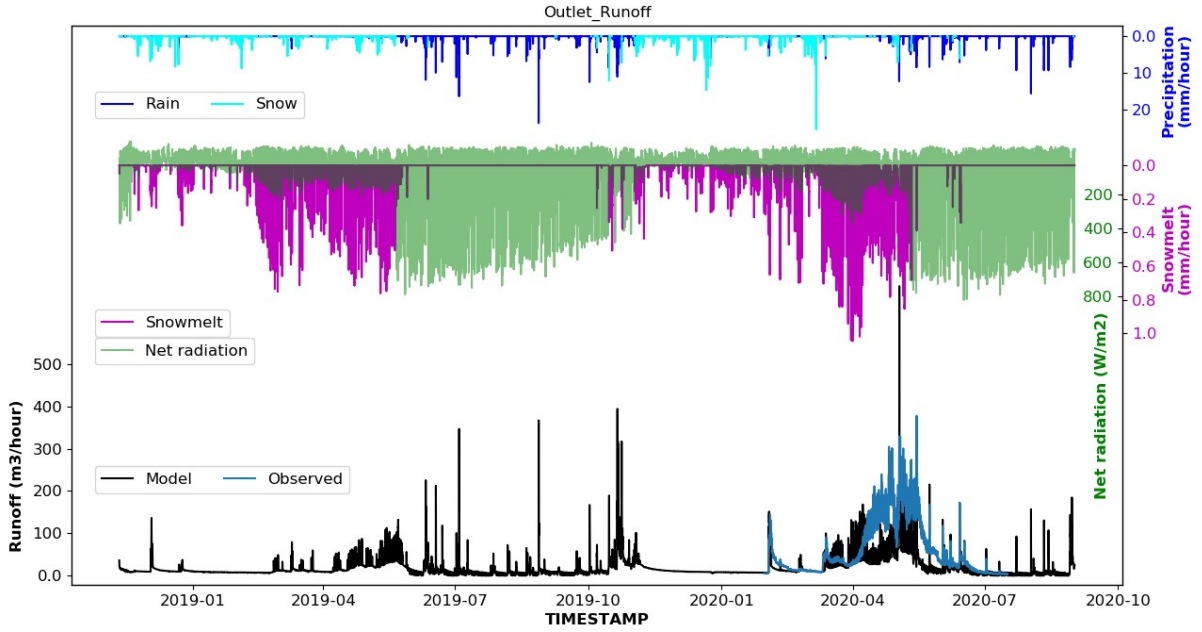

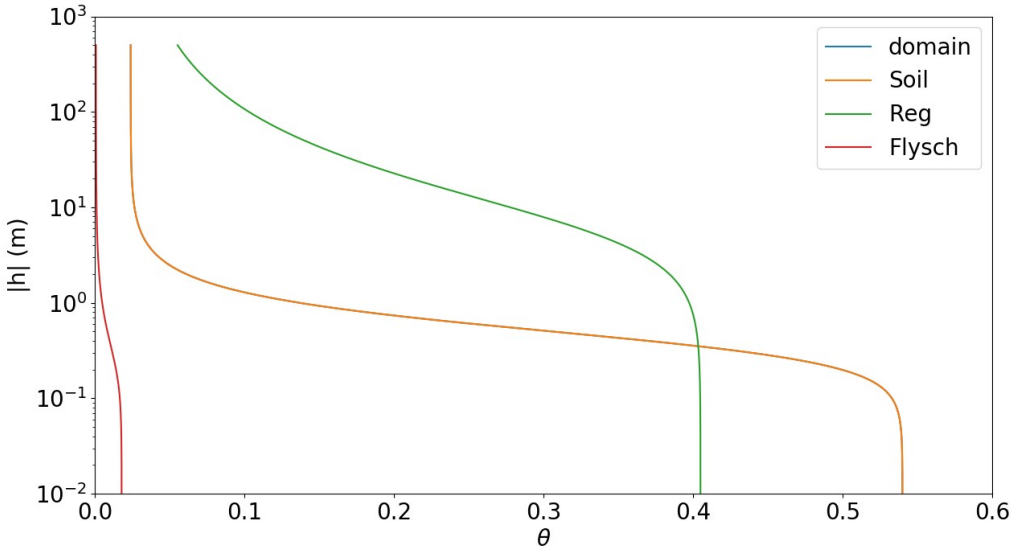

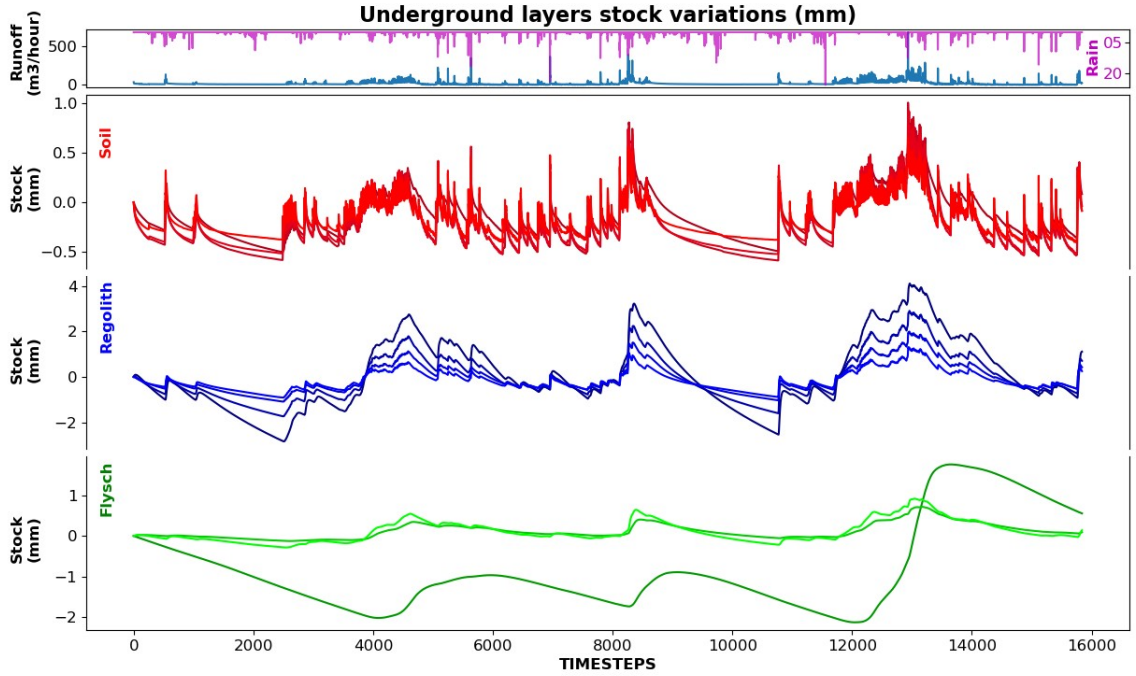
Underground layers stock variations (mm)
Runoff (m3/hour)
500
0
Rain
05
20
Soil
Stock (mm)
1.0
0.5
0.0
−0.5
Regolith
Stock (mm)
4
2
0
−2
Flysch
Stock (mm)
1
0
−1
−2
0
2000
4000
6000
8000
10000
12000
14000
16000
TIMESTEPS

Simulation name: SoilPerm0.148RegPer.0.058HighRegAlphaN

SoilPerm = 0.148, RegPerm = 0.058, FlyschPerm = 0.00238
SoilPoro = 0.60, RegPoro = 0.45, FlyschPoro = 0.02
SoilAlpha = 2.4, RegAlpha = 1.1, FlyschAlpha = 4
SoilN = 2.67, RegN = 1.4, FlyschN = 2
SoilSRes = 0.04, RegSRes = 0.05, FlyschSRes = 0.04
SoilSSat = 0.9, RegSSat = 0.9, FlyschSSat = 0.9

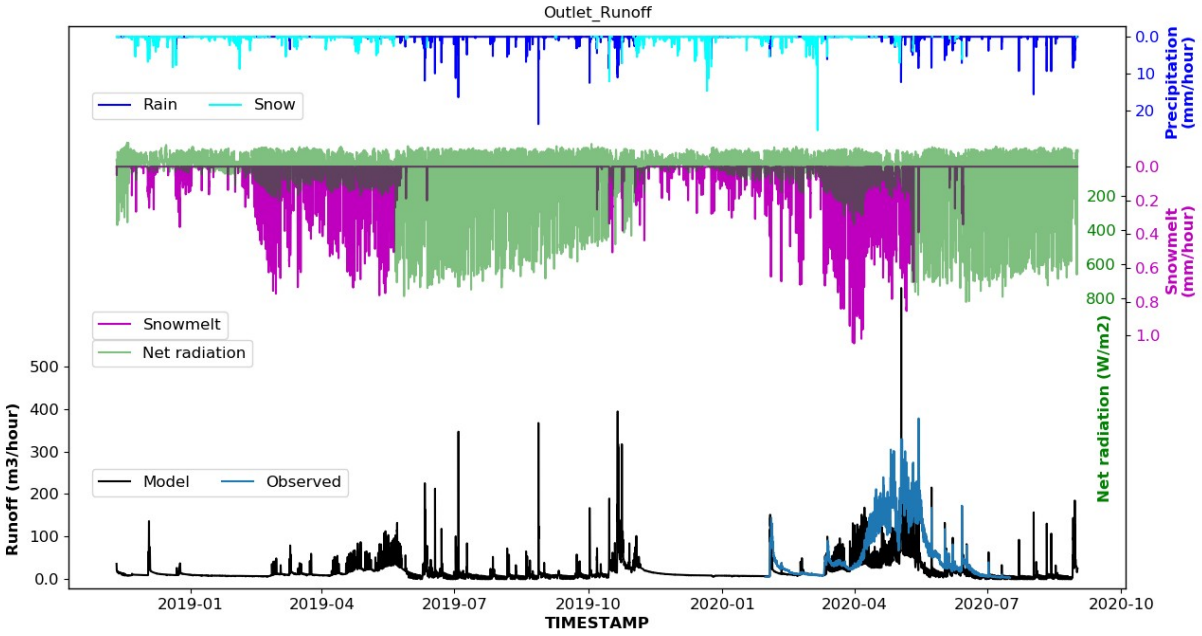

Part II

Simulations for Van-Genuchten parameter sensitivity

Parflow 2018-2019 simulations

Simulation name: Standard

SoilPerm = 0.237, RegPerm = 0.058, FlyschPerm = 0.00238
SoilPoro = 0.60, RegPoro = 0.45, FlyschPoro = 0.02
SoilAlpha = 2.4, RegAlpha = 0.16, FlyschAlpha = 4
SoilN = 2.67, RegN = 1.56, FlyschN = 2
SoilSRes = 0.04, RegSRes = 0.05, FlyschSRes = 0.04
SoilSSat = 0.9, RegSSat = 0.9, FlyschSSat = 0.9

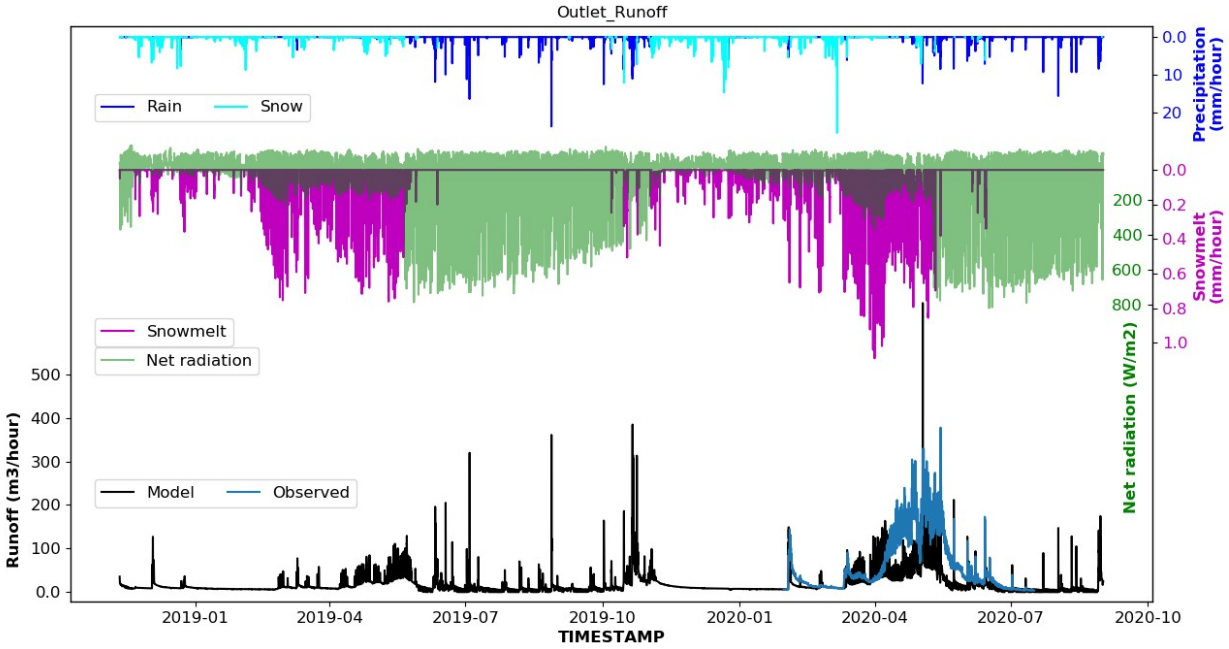

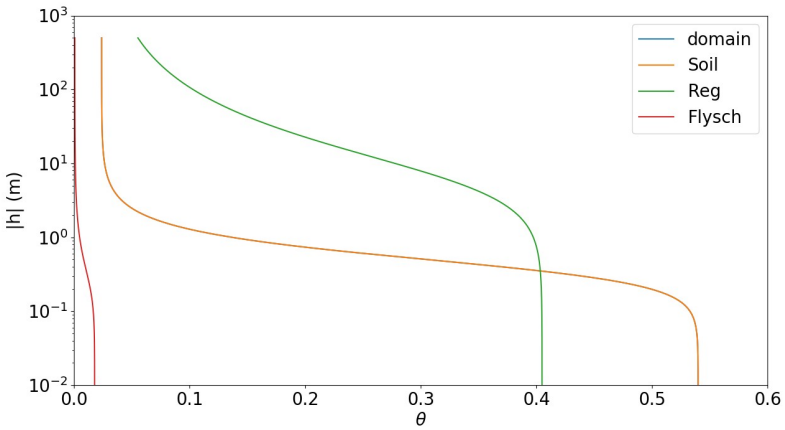

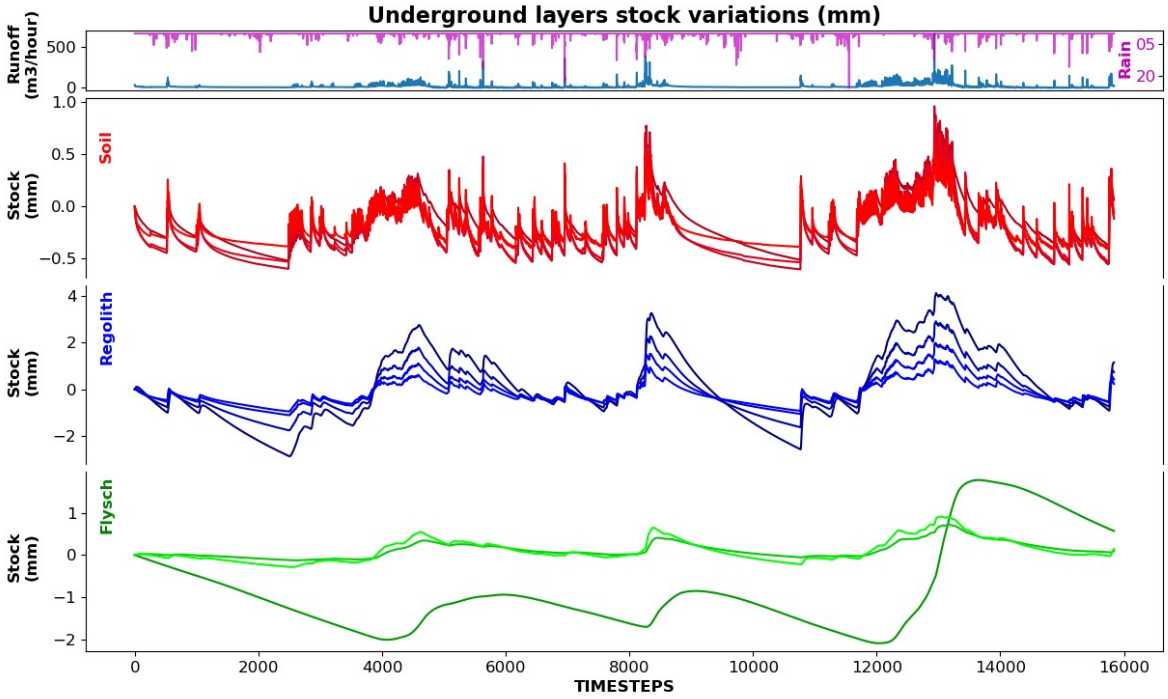
Underground layers stock variations (mm)
Runoff (m3/hour)
500
0
Rain
05
20
Soil
Stock (mm)
1.0
0.5
0.0
−0.5
Regolith
Stock (mm)
4
2
0
−2
Flysch
Stock (mm)
1
0
−1
−2
0
2000
4000
6000
8000
10000
12000
14000
16000
TIMESTEPS

Simulation name:
SoilRegSamePermFlyschPoro0.1HighRegAlphaNSoilAlpha0.5FlyschAlpha0.4

SoilPerm = 0.237, RegPerm = 0.237, FlyschPerm = 0.00238
SoilPoro = 0.60, RegPoro = 0.45, FlyschPoro = 0.1
SoilAlpha = 0.5, RegAlpha = 1.1, FlyschAlpha = 0.4
SoilN = 2.67, RegN = 1.4, FlyschN = 2
SoilSRes = 0.04, RegSRes = 0.04, FlyschSRes = 0.2
SoilSSat = 0.9, RegSSat = 0.9, FlyschSSat = 0.9

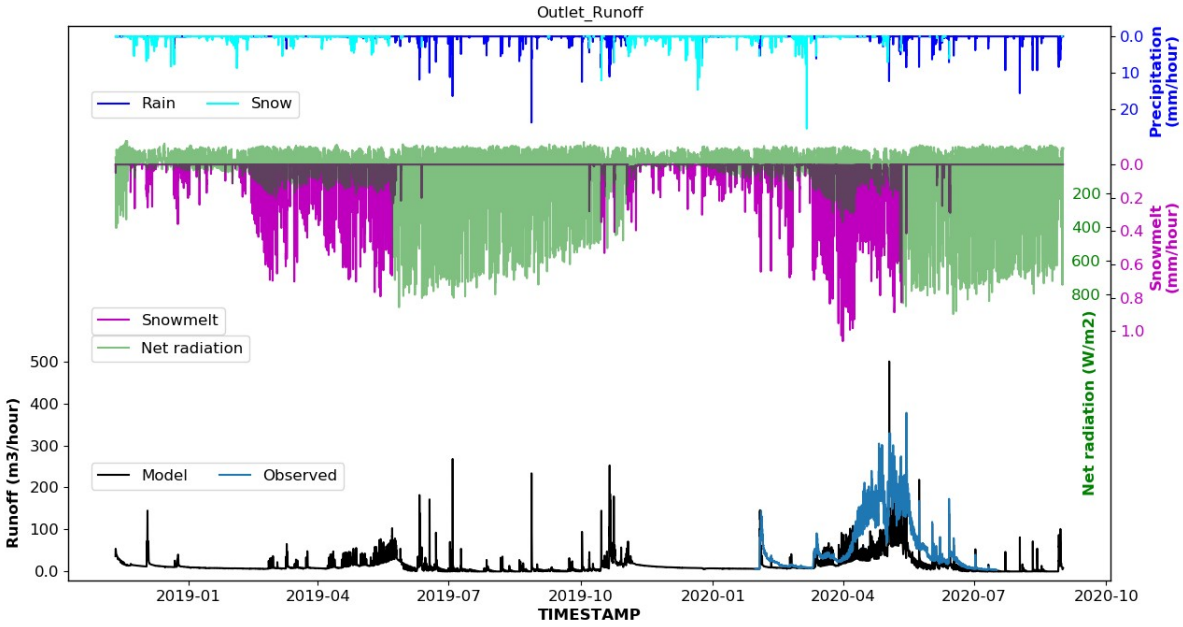

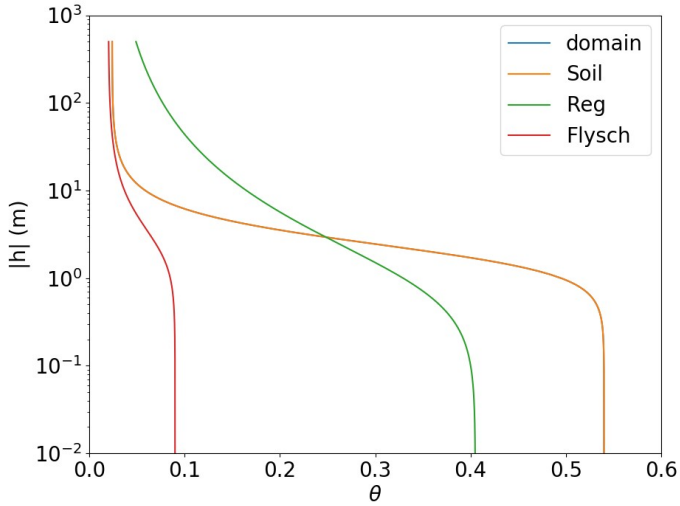

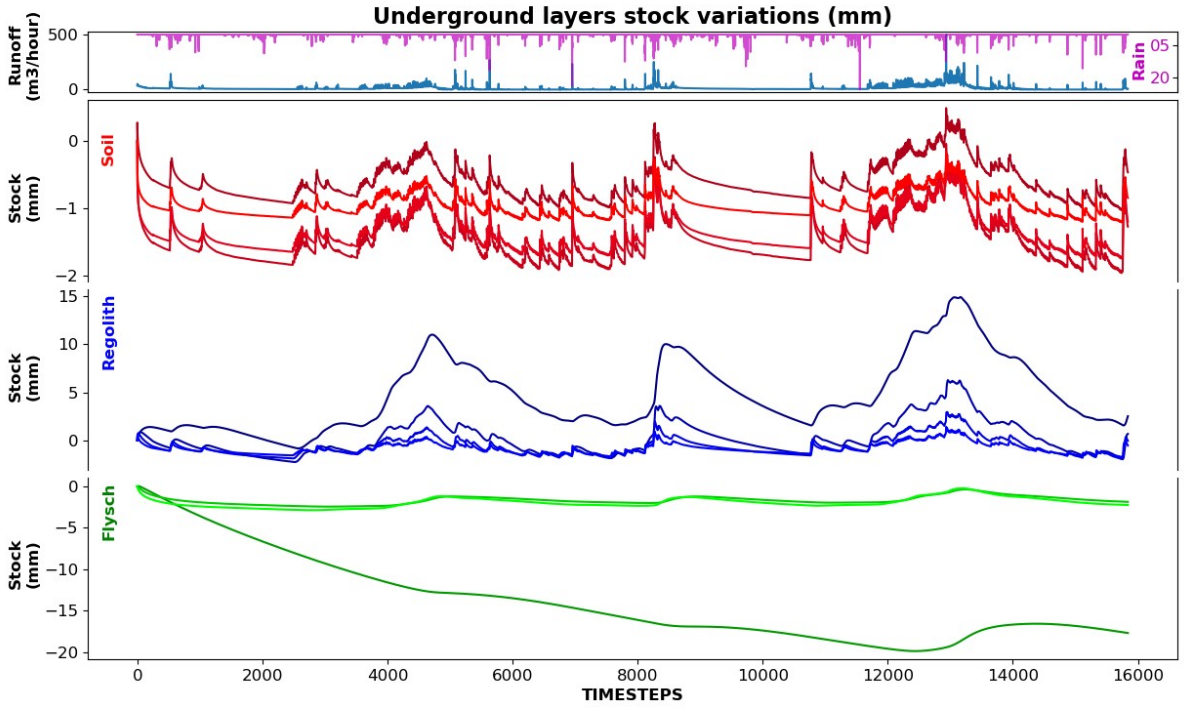
Underground layers stock variations (mm)
Runoff (m3/hour)
500
0
Rain
05
20
Soil
Stock (mm)
0
−1
−2
Regolith
Stock (mm)
15
10
5
0
Flysch
Stock (mm)
0
−5
−10
−15
−20
0
2000
4000
6000
8000
10000
12000
14000
16000
TIMESTEPS

Simulation name: SoilRegSamePermFlyschPoro0.1HighRegAlphaNSoilAlpha2.4RegAlpha4

SoilPerm = 0.237, RegPerm = 0.237, FlyschPerm = 0.00238
SoilPoro = 0.60, RegPoro = 0.45, FlyschPoro = 0.1
SoilAlpha = 2.4, RegAlpha = 4, FlyschAlpha = 0.4
SoilN = 2.67, RegN = 1.4, FlyschN = 2
SoilSRes = 0.04, RegSRes = 0.04, FlyschSRes = 0.2
SoilSSat = 0.9, RegSSat = 0.9, FlyschSSat = 0.9

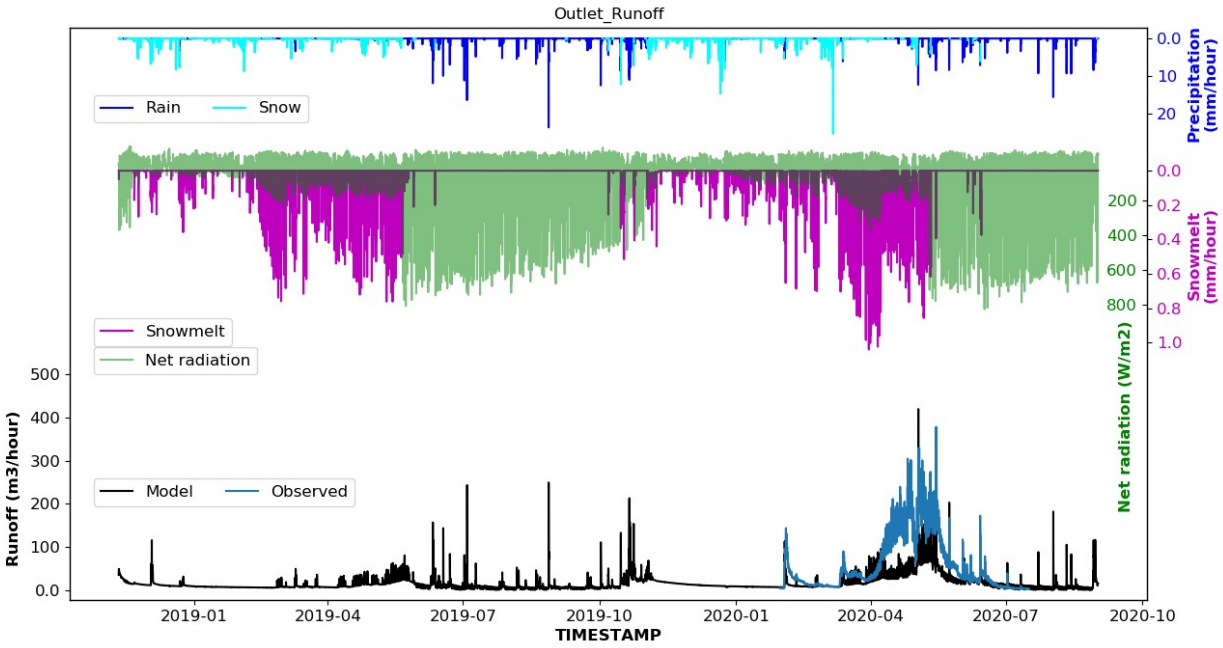

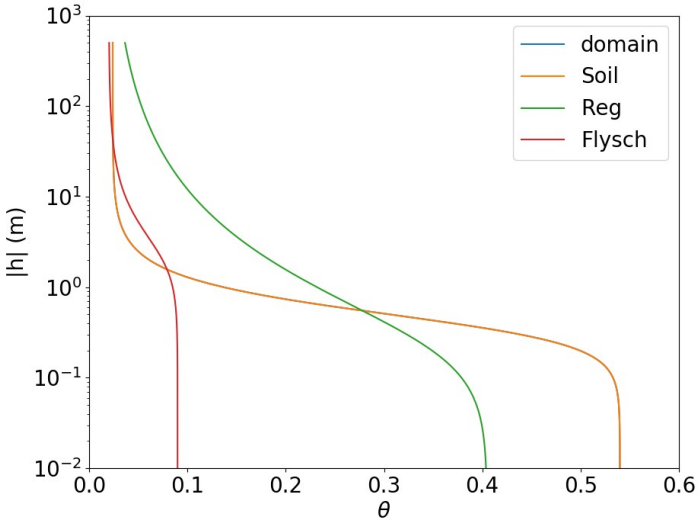

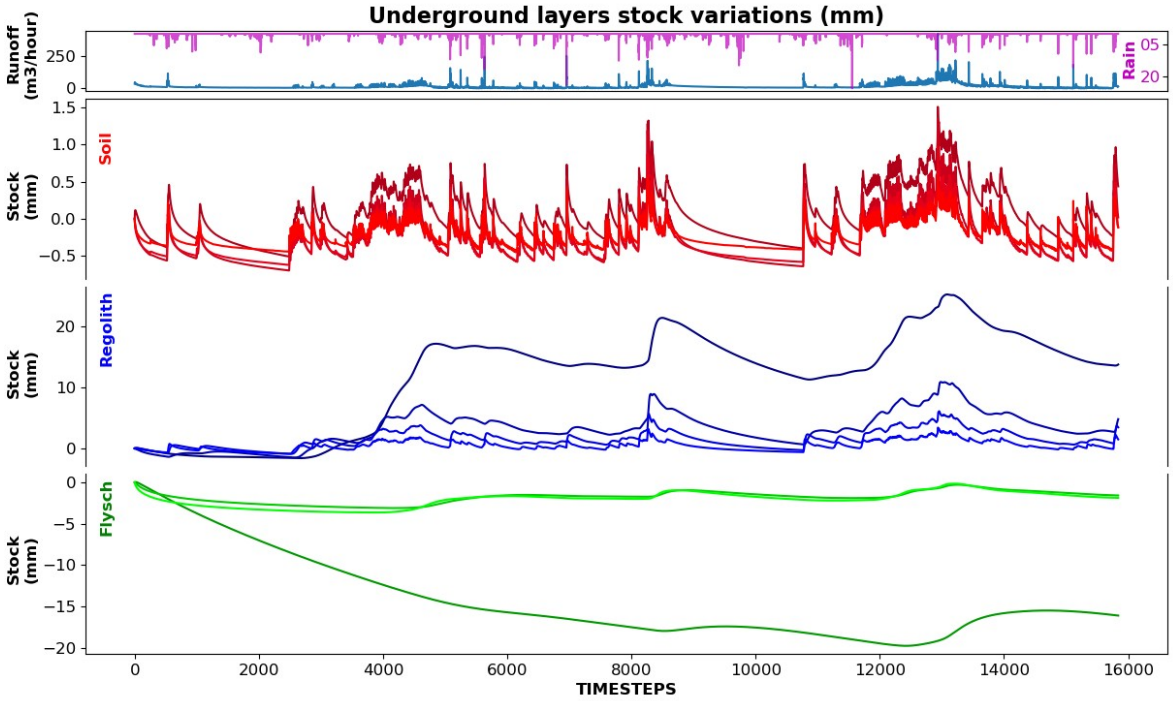
Underground layers stock variations (mm)
Runoff (m3/hour)
250
0
Rain
05
20
Soil
Stock (mm)
1.5
1.0
0.5
0.0
−0.5
Regolith
Stock (mm)
20
10
0
Flysch
Stock (mm)
0
−5
−10
−15
−20
0
2000
4000
6000
8000
10000
12000
14000
16000
TIMESTEPS

Simulation name: SoilRegSamePermFlyschPoro0.2HighRegAlphaNSoilAlpha2.4RegAlpha4 (*BEST FIT TILL NOW*)
SoilPerm = 0.237, RegPerm = 0.237, FlyschPerm = 0.00238
SoilPoro = 0.60, RegPoro = 0.45, FlyschPoro = 0.2
SoilAlpha = 2.4, RegAlpha = 4, FlyschAlpha = 0.4
SoilN = 2.67, RegN = 1.4, FlyschN = 2
SoilSRes = 0.04, RegSRes = 0.04, FlyschSRes = 0.2
SoilSSat = 0.9, RegSSat = 0.9, FlyschSSat = 0.9

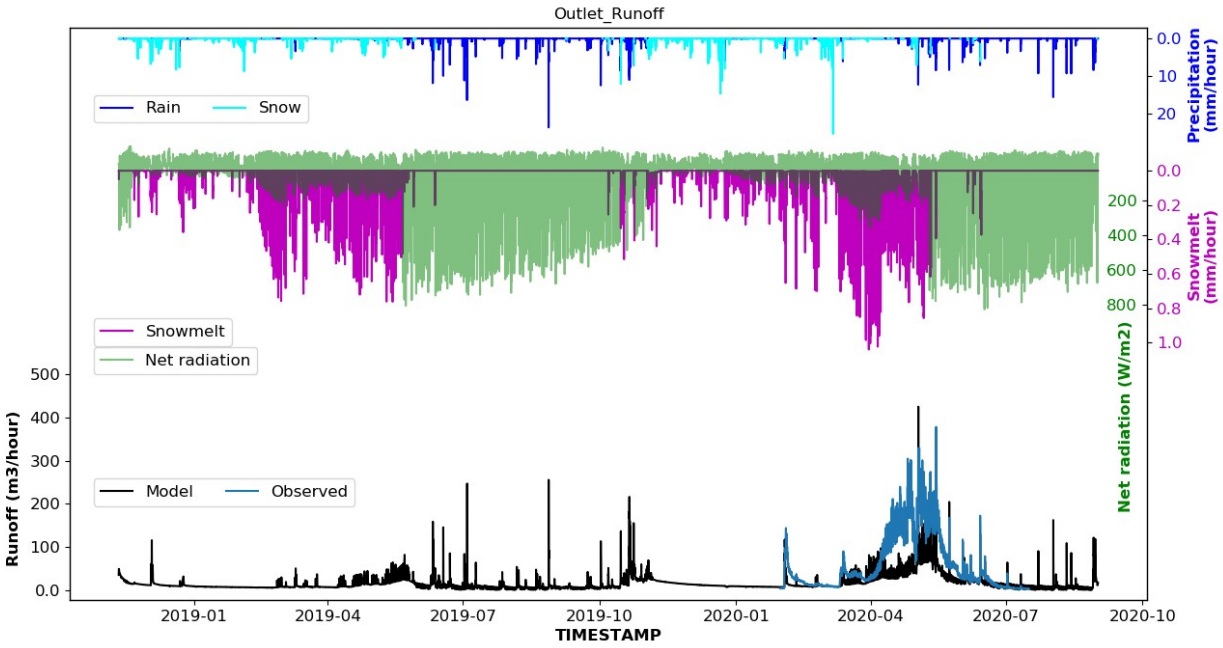

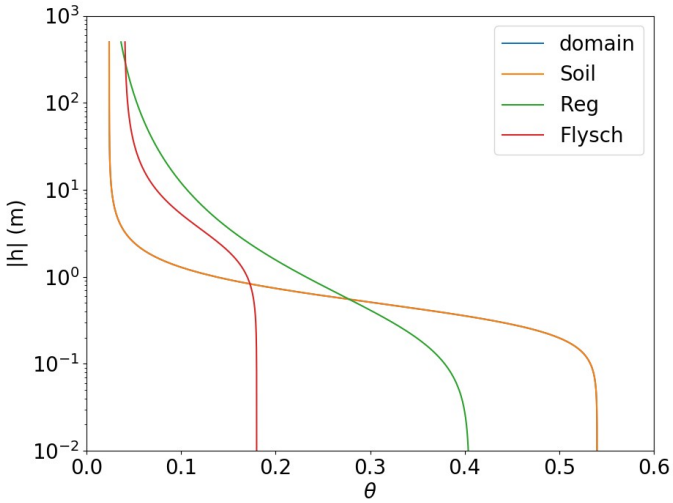

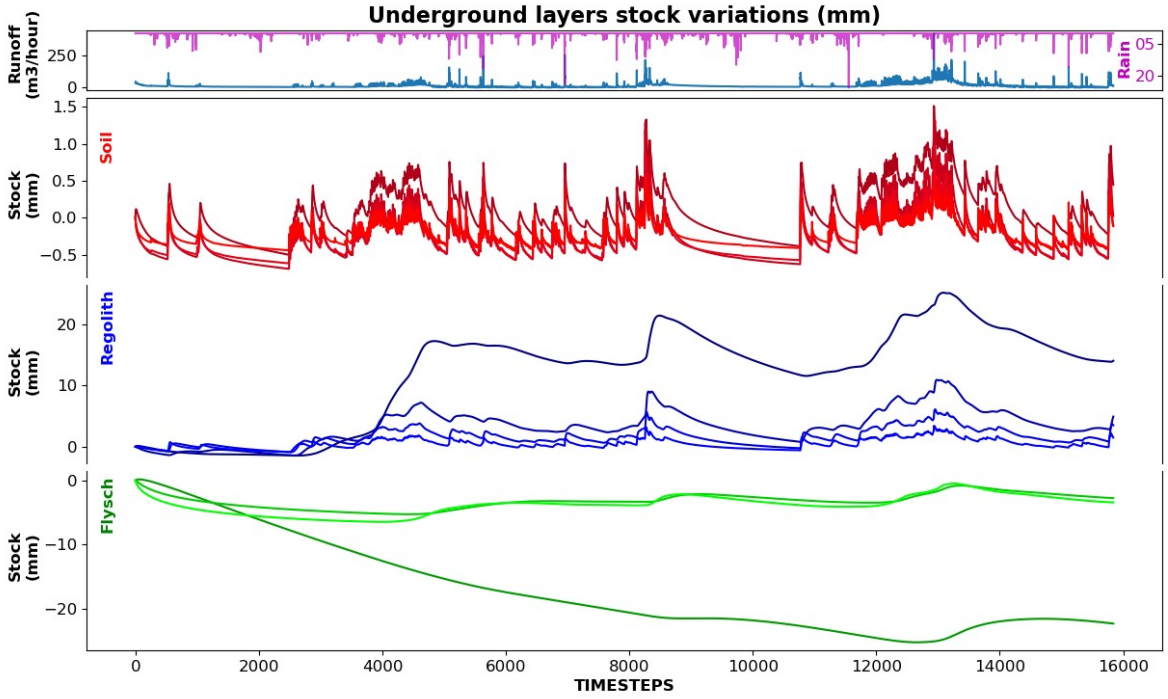
Underground layers stock variations (mm)
Runoff (m3/hour)
250
0
Rain
05
20
Soil
Stock (mm)
1.5
1.0
0.5
0.0
−0.5
Regolith
Stock (mm)
20
10
0
Flysch
Stock (mm)
0
−10
−20
0
2000
4000
6000
8000
10000
12000
14000
16000
TIMESTEPS

Simulation name: RegPerm0.148FlyschPoro0.1HighRegAlphaNSoilAlpha2.4RegAlpha4

SoilPerm = 0.237, RegPerm = 0.148, FlyschPerm = 0.00238
SoilPoro = 0.60, RegPoro = 0.45, FlyschPoro = 0.1
SoilAlpha = 2.4, RegAlpha = 4, FlyschAlpha = 0.4
SoilN = 2.67, RegN = 1.4, FlyschN = 2
SoilSRes = 0.04, RegSRes = 0.04, FlyschSRes = 0.2
SoilSSat = 0.9, RegSSat = 0.9, FlyschSSat = 0.9

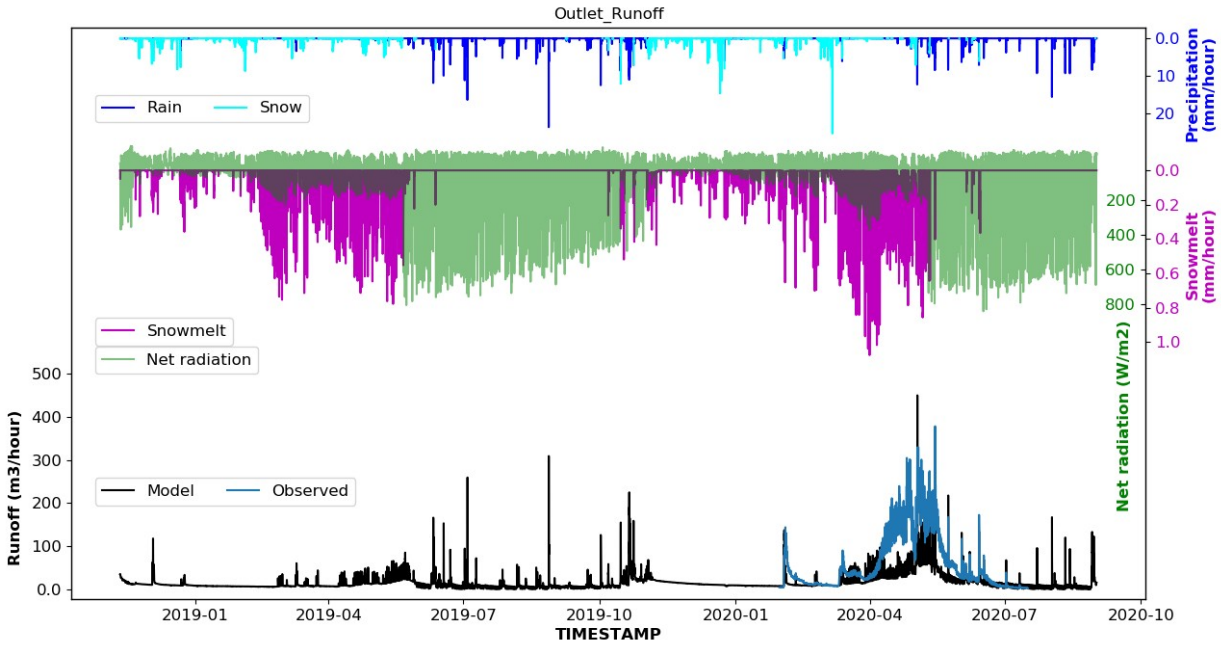

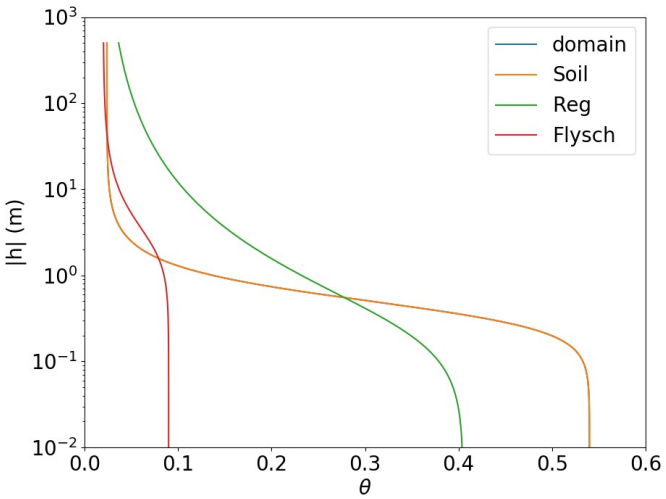

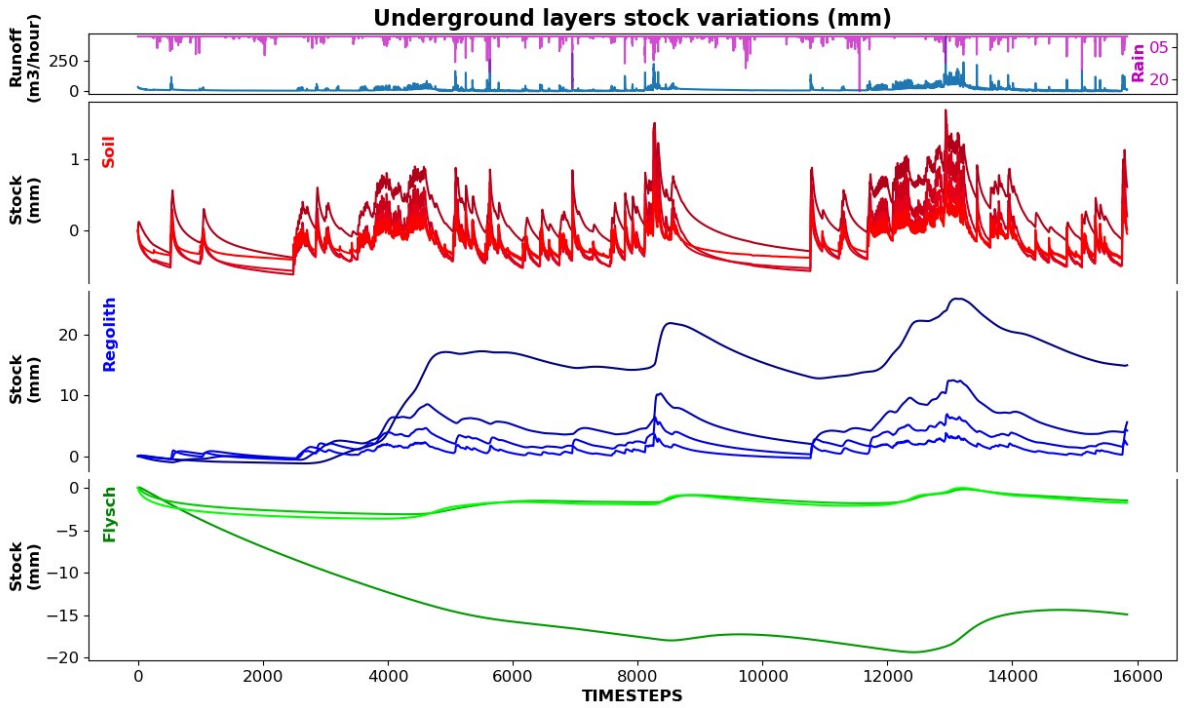
Underground layers stock variations (mm)
Runoff (m3/hour)
250
0
Rain
05
20
Stock (mm)
Soil
1
0
Stock (mm)
Regolith
20
10
0
Stock (mm)
Flysch
0
−5
−10
−15
−20
0
2000
4000
6000
8000
10000
12000
14000
16000
TIMESTEPS

Simulation name: RegPerm0.058FlyschPoro0.1HighRegAlphaNSoilAlpha2.4RegAlpha4

SoilPerm = 0.237, RegPerm = 0.058, FlyschPerm = 0.00238
SoilPoro = 0.60, RegPoro = 0.45, FlyschPoro = 0.1
SoilAlpha = 2.4, RegAlpha = 4, FlyschAlpha = 0.4
SoilN = 2.67, RegN = 1.4, FlyschN = 2
SoilSRes = 0.04, RegSRes = 0.04, FlyschSRes = 0.2
SoilSSat = 0.9, RegSSat = 0.9, FlyschSSat = 0.9

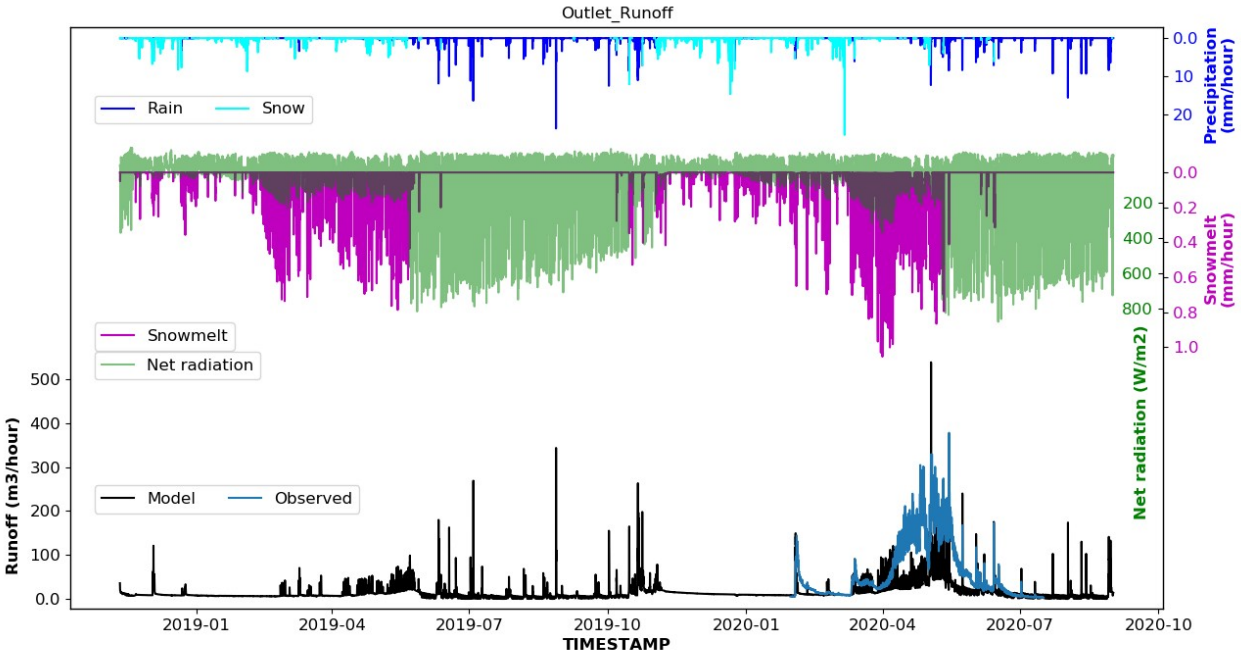

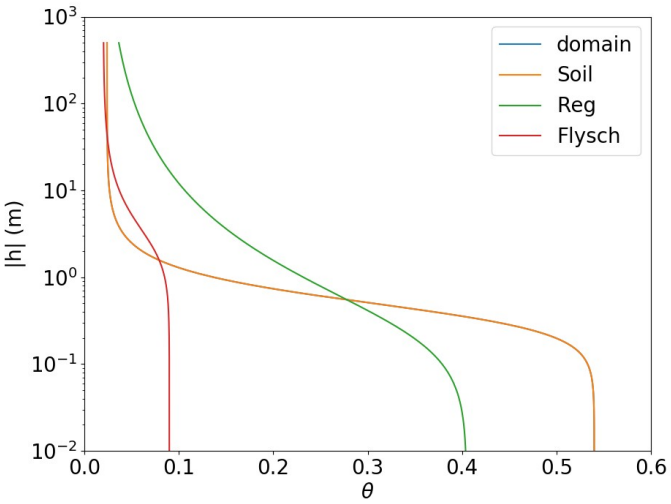

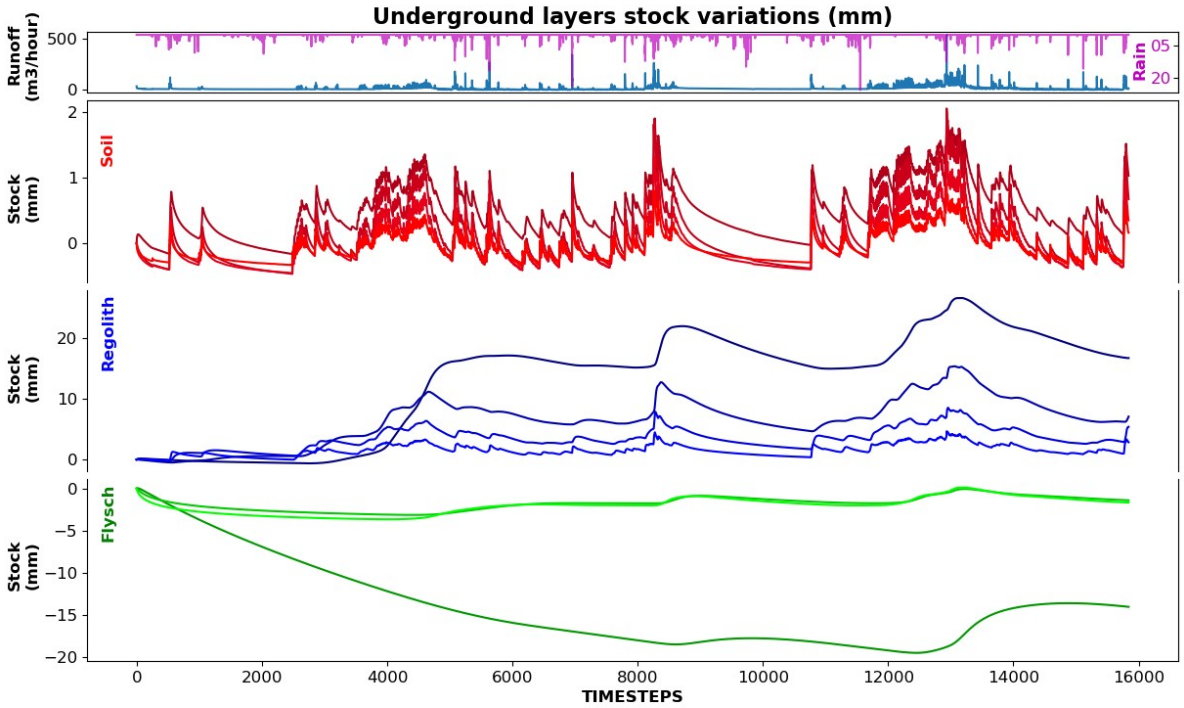
Underground layers stock variations (mm)
Runoff (m3/hour)
500
0
Rain
05
20
Soil
Stock (mm)
2
1
0
Regolith
Stock (mm)
20
10
0
Flysch
Stock (mm)
0
−5
−10
−15
−20
0
2000
4000
6000
8000
10000
12000
14000
16000
TIMESTEPS

Simulation name: SoilRegSamePermFlyschPoro0.2SoilAlpha0.5N1.4HighRegAlphaN

SoilPerm = 0.237, RegPerm = 0.237, FlyschPerm = 0.00238
SoilPoro = 0.60, RegPoro = 0.45, FlyschPoro = 0.2
SoilAlpha = 0.5, RegAlpha = 4, FlyschAlpha = 0.4
SoilN = 1.4, RegN = 1.4, FlyschN = 2
SoilSRes = 0.04, RegSRes = 0.04, FlyschSRes = 0.2
SoilSSat = 0.9, RegSSat = 0.9, FlyschSSat = 0.9

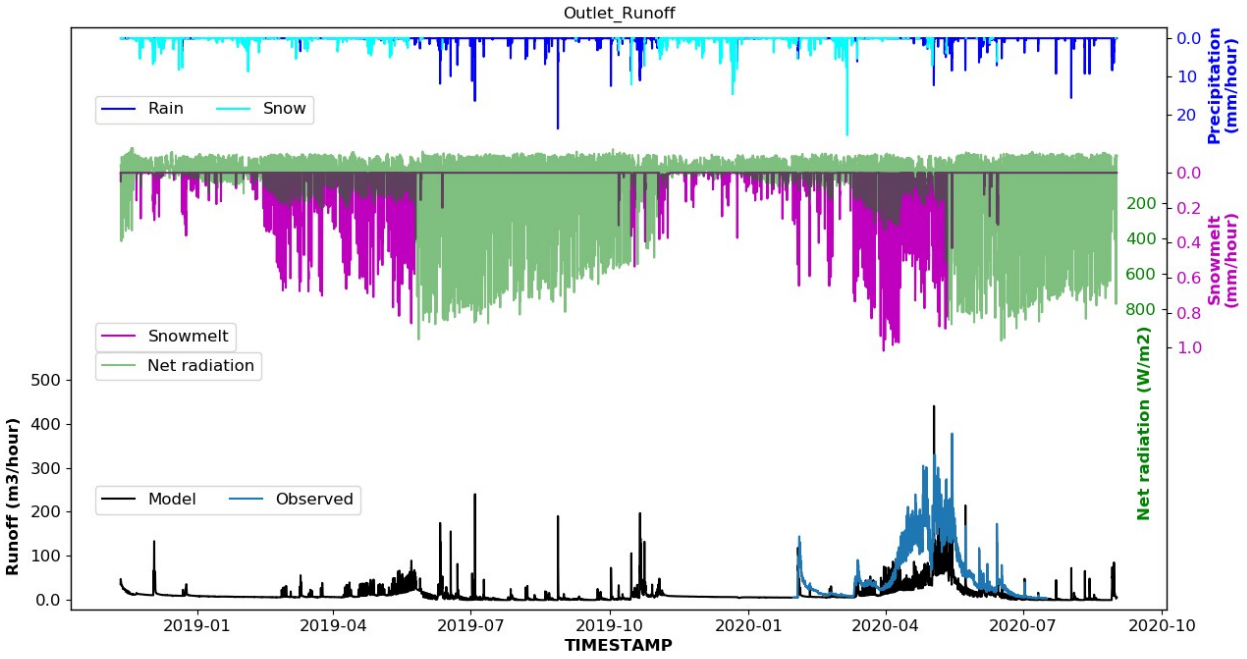

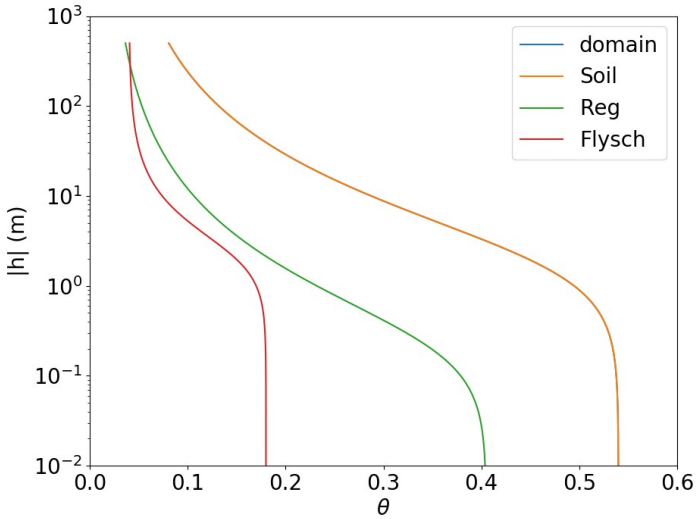

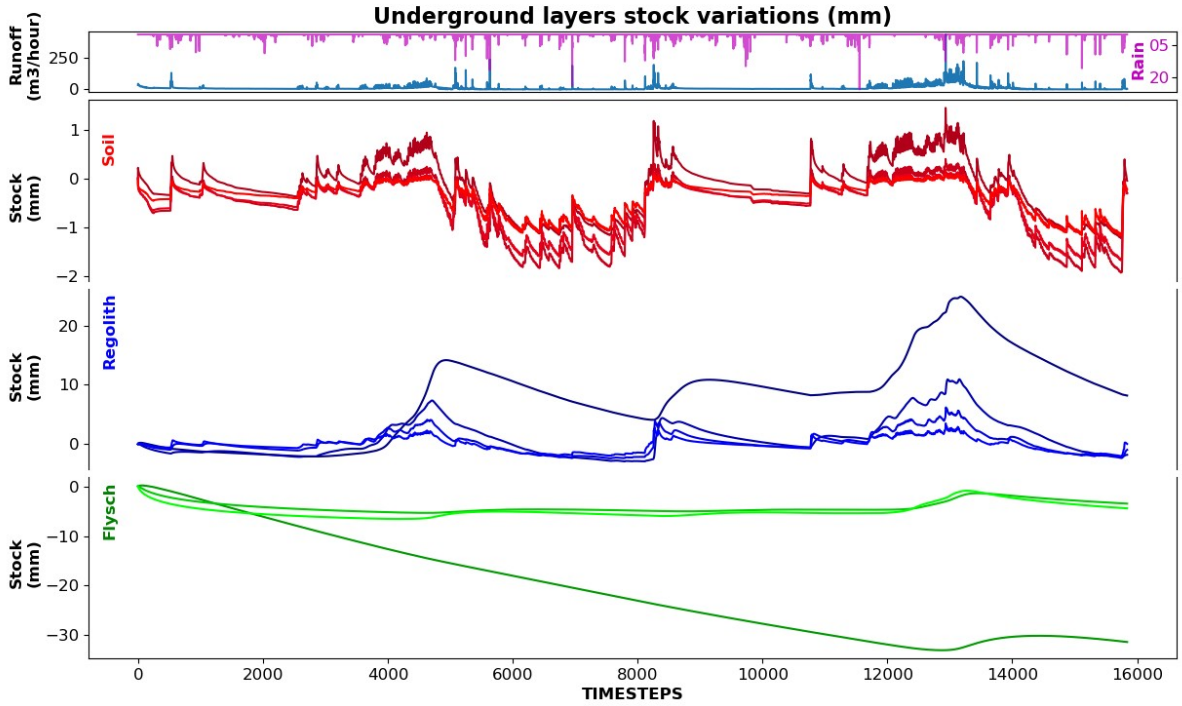
Underground layers stock variations (mm)
Runoff (m3/hour)
250
0
Rain
05
20
Soil
Stock (mm)
1
0
−1
−2
Regolith
Stock (mm)
20
10
0
Flysch
Stock (mm)
0
−10
−20
−30
0
2000
4000
6000
8000
10000
12000
14000
16000
TIMESTEPS

ONGOING SIMULATIONS

Simulation name: SoilRegSamePermFlyschPoro0.2SoilRegSameAlphaN

SoilPerm = 0.237, RegPerm = 0.237, FlyschPerm = 0.00238
SoilPoro = 0.60, RegPoro = 0.45, FlyschPoro = 0.2
SoilAlpha = 4, RegAlpha = 4, FlyschAlpha = 0.4
SoilN = 1.4, RegN = 1.4, FlyschN = 2
SoilSRes = 0.04, RegSRes = 0.04, FlyschSRes = 0.2
SoilSSat = 0.9, RegSSat = 0.9, FlyschSSat = 0.9

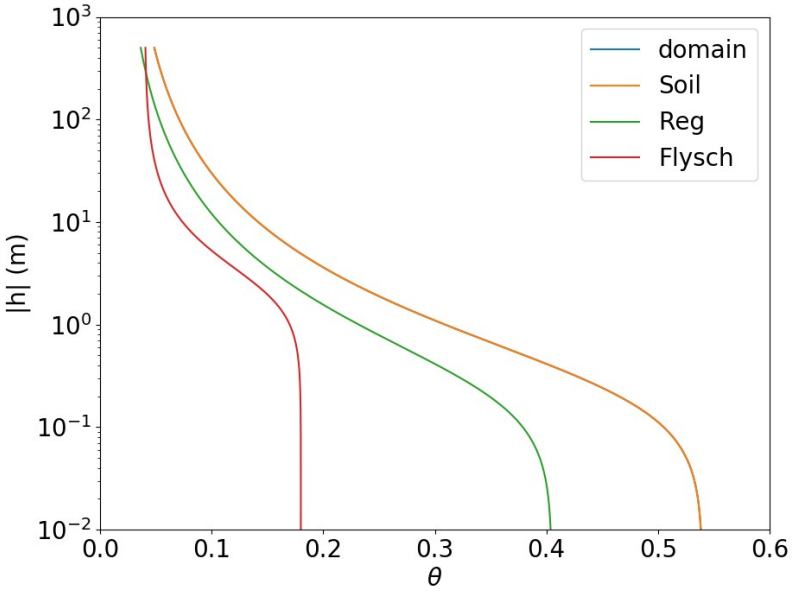

Simulation name: SoilRegSamePermFlyschPoro0.2SoilAlpha6N4HighRegAlphaN

SoilPerm = 0.237, RegPerm = 0.237, FlyschPerm = 0.00238
SoilPoro = 0.60, RegPoro = 0.45, FlyschPoro = 0.2
SoilAlpha = 6, RegAlpha = 4, FlyschAlpha = 0.4
SoilN = 4, RegN = 1.4, FlyschN = 2
SoilSRes = 0.04, RegSRes = 0.04, FlyschSRes = 0.2
SoilSSat = 0.9, RegSSat = 0.9, FlyschSSat = 0.9

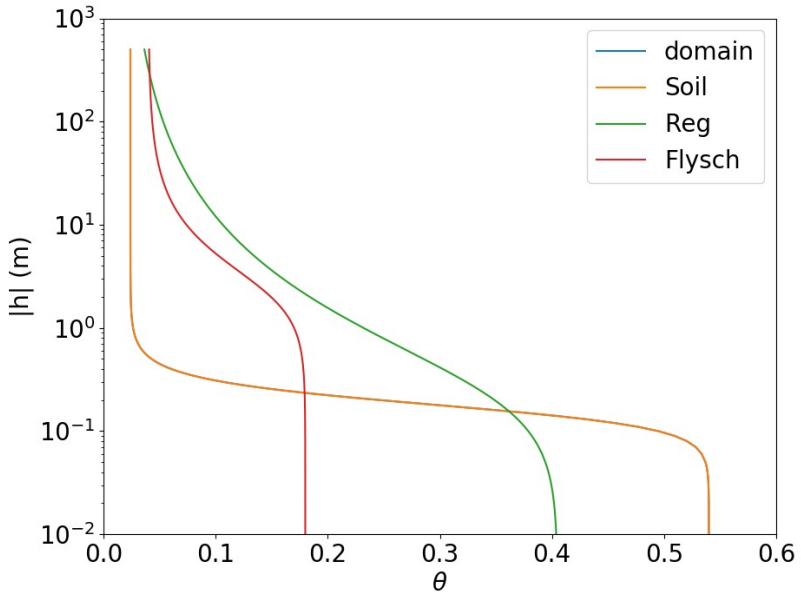

Simulation name: SoilRegSamePermFlyschPoro0.2SoilAlpha6N4RegAlpha4N4

SoilPerm = 0.237, RegPerm = 0.237, FlyschPerm = 0.00238
SoilPoro = 0.60, RegPoro = 0.45, FlyschPoro = 0.2
SoilAlpha = 6, RegAlpha = 4, FlyschAlpha = 0.4
SoilN = 4, RegN = 4, FlyschN = 2
SoilSRes = 0.04, RegSRes = 0.04, FlyschSRes = 0.2
SoilSSat = 0.9, RegSSat = 0.9, FlyschSSat = 0.9

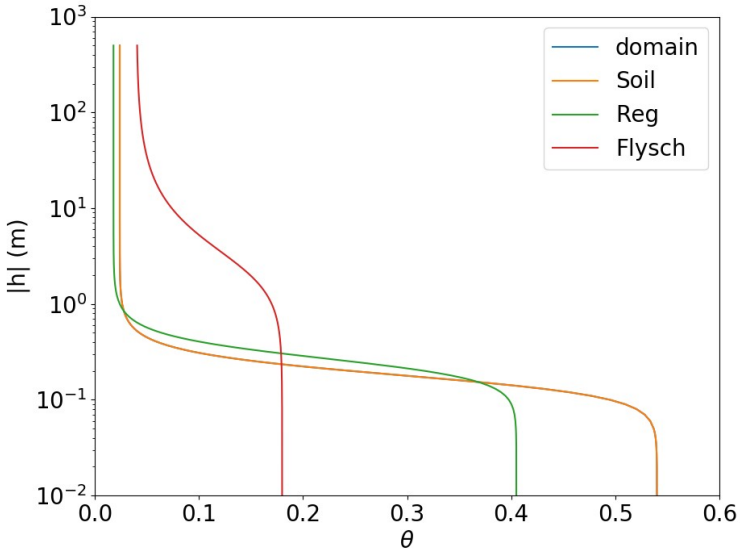

Part III

Subsurafce parameter sensitivity towards evapotranspiration and runoff

Spin-up table (all the runs are after running spin-up for 10 years for every single change, and changes are mainly done in the regolith parameters):
Unit in 'mm' (catchment average):
Default values:
Soil: Alpha=2.5 N=2
Regolith: Alpha=4 N=1.5
Flysch: Alpha=0.5 N=2

REGOLITH	Alpha	N	R	ET	SWE
1	0.2	2	974	280	23
2	0.5	2	1005	290	-do-
3	1.3	2	1009	315	-do-
4	1.5	2	1007	320	-do-
5	0.5	3	998	286	-do-
6	1.5	3	1006	318	-do-
7	1.5	2.5	1007	318	-do-
8	0.5	2 (Soi:3)	1051	199	-do-
9	0.2 (fly:0.1)	2	978	276	-do-
10	0.2 (fly:0.2)	2	975	278	-do-
11	0.5 (fly:0.2)	2	1007	289	-do-
12	3 (fly:2)	1.5 (fly:1.5)	987	352	-do-
13	3 (fly:2)	2.5 (fly:1.5)	984	352	-do-
14 (LowFlyPerm=0.00120)	3 (fly:2)	2.5 (fly:1.5)	1011	358	-do-
15 (SoilAlpha:3, N:2.5)	2.5 (fly:2)	1.5 (fly:1.5)	1073	257	-do-
16	3	2	990	349	-do-

Appendix C - ParFLOW-CLM and EcoSLIM spinup

This section shows the spinup of ParFlow-CLM and EcoSLIM.

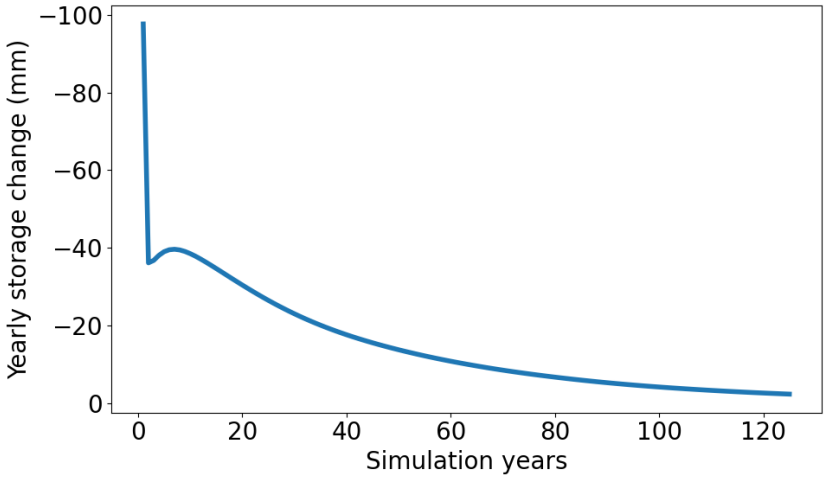

Figure C1: ParFlow spinup for the 125 years.

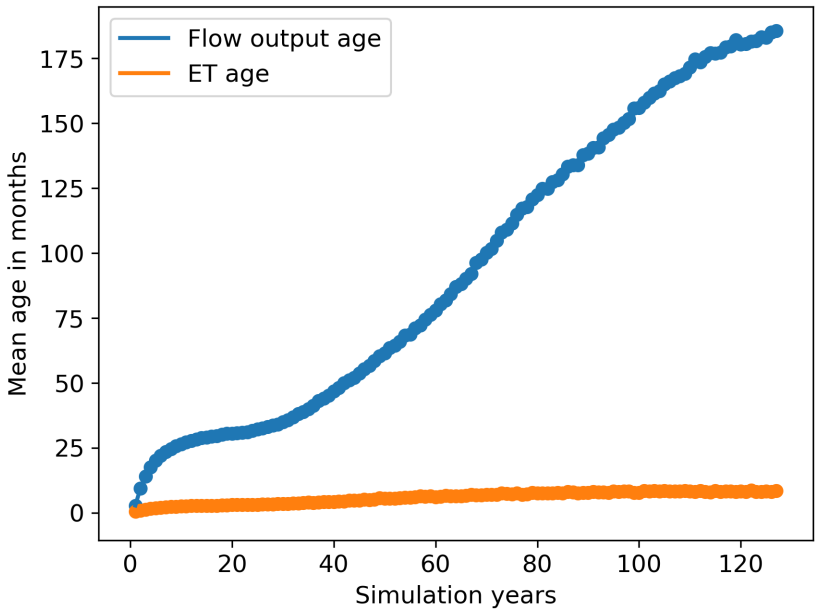

Figure C2: EcoSLIM spinup (125 years) for stabilizing the flow and evapotranspiration age.

References

Aguayo, M. A., Flores, A. N., McNamara, J. P., Marshall, H.-P., and Mead, J. (2020). Examining cross-scale influences of forcing resolutions in a hillslope-resolving, integrated hydrologic model. *Hydrology and Earth System Sciences Discussions*, pages 1–28. Publisher: Copernicus GmbH.

Ajami, H., McCabe, M. F., Evans, J. P., and Stisen, S. (2014). Assessing the impact of model spin-up on surface water-groundwater interactions using an integrated hydrologic model. *Water Resources Research*, 50(3):2636–2656. ISBN: 0043-1397 Publisher: Wiley Online Library.

Anderson, E. A. (1968). Development and testing of snow pack energy balance equations. *Water Resources Research*, 4(1):19–37. ISBN: 0043-1397 Publisher: Wiley Online Library.

Anderson, S. P., von Blanckenburg, F., and White, A. F. (2007). Physical and chemical controls on the critical zone. *Elements*, 3(5):315–319. ISBN: 1811-5209 Publisher: GeoScienceWorld.

Arora, B., Briggs, M. A., Zarnetske, J. P., Stegen, J., Gomez-Velez, J. D., Dwivedi, D., and Steefel, C. (2022). Hot spots and hot moments in the critical zone: identification of and incorporation into reactive transport models. In *Biogeochemistry of the Critical Zone*, pages 9–47. Springer.

Ashby, S. F. and Falgout, R. D. (1996). A parallel multigrid preconditioned conjugate gradient algorithm for groundwater flow simulations. *Nuclear science and engineering*, 124(1):145–159. ISBN: 0029-5639 Publisher: Taylor & Francis.

Atchley, A. L. and Maxwell, R. M. (2011). Influences of subsurface heterogeneity and vegetation cover on soil moisture, surface temperature and evapotranspiration at hillslope scales. *Hydrogeology Journal*, 19(2):289–305. ISBN: 1435-0157 Publisher: Springer.

Auken, E., Pellerin, L., Christensen, N. B., and Sørensen, K. (2006). A survey of current trends in near-surface electrical and electromagnetic methods. *Geophysics*, 71(5):G249–G260. ISBN: 0016-8033 Publisher: Society of Exploration Geophysicists.

Avanzi, F., Ercolani, G., Gabellani, S., Cremonese, E., Pogliotti, P., Filippa, G., Morra di Cella, U., Ratto, S., Stevenin, H., and Cauduro, M. (2021). Learning about precipitation lapse rates from snow course data improves water balance modeling. *Hydrology and Earth System Sciences*, 25(4):2109–2131. ISBN: 1027-5606 Publisher: Copernicus GmbH.

Aygün, O., Kinnard, C., and Campeau, S. (2020). Impacts of climate change on the hydrology of northern midlatitude cold regions. *Progress in Physical Geography: Earth and Environment*, 44(3):338–375. ISBN: 0309-1333 Publisher: SAGE Publications Sage UK: London, England.

Baba, M. W., Gascoin, S., Kinnard, C., Marchane, A., and Hanich, L. (2019). Effect of Digital Elevation Model Resolution on the Simulation of the Snow Cover Evolution in the High Atlas. *Water Resources Research*, 55(7):5360–5378. _eprint: https://onlinelibrary.wiley.com/doi/pdf/10.1029/2018WR023789.

Bales, R. C., Molotch, N. P., Painter, T. H., Dettinger, M. D., Rice, R., and Dozier, J. (2006). Mountain hydrology of the western United States. *Water Resources Research*, 42(8). ISBN: 0043-1397 Publisher: Wiley Online Library.

Barfod, A. A., Møller, I., and Christiansen, A. V. (2016). Compiling a national resistivity atlas of Denmark based on airborne and ground-based transient electromagnetic data. *Journal of Applied Geophysics*, 134:199–209. ISBN: 0926-9851 Publisher: Elsevier.

Barnhart, T. B., Molotch, N. P., Livneh, B., Harpold, A. A., Knowles, J. F., and Schneider, D. (2016). Snowmelt rate dictates streamflow. *Geophysical Research Letters*, 43(15):8006–8016. ISBN: 0094-8276 Publisher: Wiley Online Library.

Baroni, G., Schalge, B., Rakovec, O., Kumar, R., Schüler, L., Samaniego, L., Simmer, C., and Attinger, S. (2019). A comprehensive distributed hydrological modeling intercomparison to support process representation and data collection strategies. *Water Resources Research*, 55(2):990–1010. ISBN: 0043-1397 Publisher: Wiley Online Library.

Batlle-Aguilar, J., Schneider, S., Pessel, M., Tucholka, P., Coquet, Y., and Vachier, P. (2009). Axisymetrical infiltration in soil imaged by noninvasive electrical resistivimetry.

Soil Science Society of America Journal, 73(2):510–520. ISBN: 0361-5995 Publisher: Wiley Online Library.

Becker, R., Gebremichael, M., and Märker, M. (2018). Impact of soil surface and subsurface properties on soil saturated hydraulic conductivity in the semi-arid Walnut Gulch Experimental Watershed, Arizona, USA. *Geoderma*, 322:112–120. ISBN: 0016-7061 Publisher: Elsevier.

Beniston, M., Keller, F., Koffi, B., and Goyette, S. (2003). Estimates of snow accumulation and volume in the Swiss Alps under changing climatic conditions. *Theoretical and Applied Climatology*, 76(3):125–140. ISBN: 1434-4483 Publisher: Springer.

Beres Jr, M. and Haeni, F. P. (1991). Application of ground-penetrating-radar Methods in Hydrogeologie Studies. *Groundwater*, 29(3):375–386. ISBN: 0017-467X Publisher: Wiley Online Library.

Berghuijs, W. R., Woods, R. A., and Hrachowitz, M. (2014). A precipitation shift from snow towards rain leads to a decrease in streamflow. *Nature climate change*, 4(7):583–586. ISBN: 1758-6798 Publisher: Nature Publishing Group.

Bertoldi, G., Della Chiesa, S., Notarnicola, C., Pasolli, L., Niedrist, G., and Tappeiner, U. (2014). Estimation of soil moisture patterns in mountain grasslands by means of SAR RADARSAT2 images andhydrological modeling. *Journal of Hydrology*, 516:245–257.

Beven, K. J. (1990). A discussion of distributed hydrological modelling. In *Distributed hydrological modelling*, pages 255–278. Springer.

Biggs, T. W. and Whitaker, T. M. (2012). Critical elevation zones of snowmelt during peak discharges in a mountain river basin. *Journal of Hydrology*, 438:52–65. ISBN: 0022-1694 Publisher: Elsevier.

Binley, A., Elgy, J., and Beven, K. (1989). A physically based model of heterogeneous hillslopes: 1. Runoff production. *Water Resources Research*, 25(6):1219–1226. ISBN: 0043-1397 Publisher: Wiley Online Library.

Binley, A., Hubbard, S. S., Huisman, J. A., Revil, A., Robinson, D. A., Singha, K., and Slater, L. D. (2015). The emergence of hydrogeophysics for improved understanding of subsurface processes over multiple scales. *Water resources research*, 51(6):3837–3866. ISBN: 0043-1397 Publisher: Wiley Online Library.

Blume, T., Zehe, E., and Bronstert, A. (2009). Use of soil moisture dynamics and patterns at different spatio-temporal scales for the investigation of subsurface flow processes. *Hydrology and Earth System Sciences*, 13(7):1215–1233. ISBN: 1027-5606 Publisher: Copernicus GmbH.

Blöschl, G., Bierkens, M. F. P., Chambel, A., Cudennec, C., Destouni, G., Fiori, A., Kirchner, J. W., McDonnell, J. J., Savenije, H. H. G., Sivapalan, M., Stumpp, C., Toth, E., Volpi, E., Carr, G., Lupton, C., Salinas, J., Széles, B., Viglione, A., Aksoy, H., Allen, S. T., Amin, A., Andréassian, V., Arheimer, B., Aryal, S. K., Baker, V., Bardsley, E., Barendrecht, M. H., Bartosova, A., Batelaan, O., Berghuijs, W. R., Beven, K., Blume, T., Bogaard, T., Amorim, P. B. d., Böttcher, M. E., Boulet, G., Breinl, K., Brilly, M., Brocca, L., Buytaert, W., Castellarin, A., Castelletti, A., Chen, X., Chen, Y., Chen, Y., Chifflard, P., Claps, P., Clark, M. P., Collins, A. L., Croke, B., Dathe, A., David, P. C., Barros, F. P. J. d., Rooij, G. d., Baldassarre, G. D., Driscoll, J. M., Duethmann, D., Dwivedi, R., Eris, E., Farmer, W. H., Feiccabrino, J., Ferguson, G., Ferrari, E., Ferraris, S., Fersch, B., Finger, D., Foglia, L., Fowler, K., Gartsman, B., Gascoin, S., Gaume, E., Gelfan, A., Geris, J., Gharari, S., Gleeson, T., Glendell, M., Bevacqua, A. G., González-Dugo, M. P., Grimaldi, S., Gupta, A. B., Guse, B., Han, D., Hannah, D., Harpold, A., Haun, S., Heal, K., Helfricht, K., Herrnegger, M., Hipsey, M., Hlaváčiková, H., Hohmann, C., Holko, L., Hopkinson, C., Hrachowitz, M., Illangasekare, T. H., Inam, A., Innocente, C., Istanbulluoglu, E., Jarihani, B., Kalantari, Z., Kalvans, A., Khanal, S., Khatami, S., Kiesel, J., Kirkby, M., Knoben, W., Kochanek, K., Kohnová, S., Kolechkina, A., Krause, S., Kreamer, D., Kreibich, H., Kunstmann, H., Lange, H., Liberato, M. L. R., Lindquist, E., Link, T., Liu, J., Loucks, D. P., Luce, C., Mahé, G., Makarieva, O., Malard, J., Mashtayeva, S., Maskey, S., Mas-Pla, J., Mavrova-Guirguinova, M., Mazzoleni, M., Mernild, S., Misstear, B. D., Montanari, A., Müller-Thomy, H., Nabizadeh, A., Nardi, F., Neale, C., Nesterova, N., Nurtaev, B., Odongo,

V. O., Panda, S., Pande, S., Pang, Z., Papacharalampous, G., Perrin, C., Pfister, L., Pimentel, R., Polo, M. J., Post, D., Sierra, C. P., Ramos, M.-H., Renner, M., Reynolds, J. E., Ridolfi, E., Rigon, R., Riva, M., Robertson, D. E., Rosso, R., Roy, T., Sá, J. H. M., Salvadori, G., Sandells, M., Schaefli, B., Schumann, A., Scolobig, A., Seibert, J., Servat, E., Shafiei, M., Sharma, A., Sidibe, M., Sidle, R. C., Skaugen, T., Smith, H., Spiessl, S. M., Stein, L., Steinsland, I., Strasser, U., Su, B., Szolgay, J., Tarboton, D., Tauro, F., Thirel, G., Tian, F., Tong, R., Tussupova, K., Tyralis, H., Uijlenhoet, R., Beek, R. v., Ent, R. J. v. d., Ploeg, M. v. d., Loon, A. F. V., Meerveld, I. v., Nooijen, R. v., Oel, P. R. v., Vidal, J.-P., Freyberg, J. v., Vorogushyn, S., Wachniew, P., Wade, A. J., Ward, P., Westerberg, I. K., White, C., Wood, E. F., Woods, R., Xu, Z., Yilmaz, K. K., and Zhang, Y. (2019). Twenty-three unsolved problems in hydrology (UPH) – a community perspective. *Hydrological Sciences Journal*, 64(10):1141–1158. Publisher: Taylor & Francis _eprint: https://doi.org/10.1080/02626667.2019.1620507.

Bourgeois, I., Savarino, J., Caillon, N., Angot, H., Barbero, A., Delbart, F., Voisin, D., and Clement, J.-C. (2018a). Tracing the fate of atmospheric nitrate in a subalpine watershed using Δ17O. *Environmental science & technology*, 52(10):5561–5570. ISBN: 0013-936X Publisher: ACS Publications.

Bourgeois, I., Savarino, J., Némery, J., Caillon, N., Albertin, S., Delbart, F., Voisin, D., and Clement, J.-C. (2018b). Atmospheric nitrate export in streams along a montane to urban gradient. *Science of The Total Environment*, 633:329–340. ISBN: 0048-9697 Publisher: Elsevier.

Breiling, M. and Charamza, P. (1999). The impact of global warming on winter tourism and skiing: a regionalised model for Austrian snow conditions. *Regional Environmental Change*, 1(1):4–14. Publisher: Springer.

Brooks, P. D., Chorover, J., Fan, Y., Godsey, S. E., Maxwell, R. M., McNamara, J. P., and Tague, C. (2015). Hydrological partitioning in the critical zone: Recent advances and opportunities for developing transferable understanding of water cycle dynamics. *Water Resources Research*, 51(9):6973–6987. ISBN: 0043-1397 Publisher: Wiley Online Library.

Brutsaert, W. (1975). The roughness length for water vapor sensible heat, and other scalars. *Journal of the Atmospheric Sciences*, 32(10):2028–2031. ISBN: 0022-4928 Publisher: American Meteorological Society.

Brutsaert, W. (1982). The surface roughness parameterization. In *Evaporation into the Atmosphere*, pages 113–127. Springer.

Calamita, G., Serlenga, V., Stabile, T. A., Gallipoli, M. R., Bellanova, J., Bonano, M., Casu, F., Vignola, L., Piscitelli, S., and Perrone, A. (2019). An integrated geophysical approach for urban underground characterization: the Avigliano town (southern Italy) case study. *Geomatics, Natural Hazards and Risk*, 10(1):412–432. ISBN: 1947-5705 Publisher: Taylor & Francis.

Camporese, M., Paniconi, C., Putti, M., and Orlandini, S. (2010). Surface-subsurface flow modeling with path-based runoff routing, boundary condition-based coupling, and assimilation of multisource observation data. *Water Resources Research*, 46(2). ISBN: 0043-1397 Publisher: Wiley Online Library.

Carroll, R. W., Bearup, L. A., Brown, W., Dong, W., Bill, M., and Willlams, K. H. (2018). Factors controlling seasonal groundwater and solute flux from snow-dominated basins. *Hydrological Processes*, 32(14):2187–2202. ISBN: 0885-6087 Publisher: Wiley Online Library.

Carroll, R. W., Huntington, J. L., Snyder, K. A., Niswonger, R. G., Morton, C., and Stringham, T. K. (2017). Evaluating mountain meadow groundwater response to Pinyon-Juniper and temperature in a great basin watershed. *Ecohydrology*, 10(1):e1792. ISBN: 1936-0584 Publisher: Wiley Online Library.

Chen, L., Šimůnek, J., Bradford, S. A., Ajami, H., and Meles, M. B. (2022). A computationally efficient hydrologic modeling framework to simulate surface-subsurface hydrological processes at the hillslope scale. *Journal of Hydrology*, page 128539. ISBN: 0022-1694 Publisher: Elsevier.

Chorover, J., Troch, P. A., Rasmussen, C., Brooks, P. D., Pelletier, J. D., Breshears, D. D., Huxman, T. E., Kurc, S. A., Lohse, K. A., and McIntosh, J. C. (2011). How water,

carbon, and energy drive critical zone evolution: The Jemez–Santa Catalina Critical Zone Observatory. *Vadose Zone Journal*, 10(3):884–899. ISBN: 1539-1663 Publisher: Wiley Online Library.

Claes, N., Paige, G. B., Grana, D., and Parsekian, A. D. (2020). Parameterization of a hydrologic model with geophysical data to simulate observed subsurface return flow paths. *Vadose Zone Journal*, 19(1):e20024. _eprint: https://onlinelibrary.wiley.com/doi/pdf/10.1002/vzj2.20024.

Claes, N., Paige, G. B., and Parsekian, A. D. (2019). Uniform and lateral preferential flows under flood irrigation at field scale. *Hydrological Processes*, 33(15):2131–2147. ISBN: 0885-6087 Publisher: Wiley Online Library.

Clark, M. P., Fan, Y., Lawrence, D. M., Adam, J. C., Bolster, D., Gochis, D. J., Hooper, R. P., Kumar, M., Leung, L. R., Mackay, D. S., Maxwell, R. M., Shen, C., Swenson, S. C., and Zeng, X. (2015). Improving the representation of hydrologic processes in Earth System Models. *Water Resources Research*, 51(8):5929–5956. _eprint: https://onlinelibrary.wiley.com/doi/pdf/10.1002/2015WR017096.

Cohen, J. and Rind, D. (1991). The effect of snow cover on the climate. *Journal of Climate*, 4(7):689–706. ISBN: 1520-0442.

Condon, L. E., Markovich, K. H., Kelleher, C. A., McDonnell, J. J., Ferguson, G., and McIntosh, J. C. (2020). Where is the bottom of a watershed? *Water Resources Research*, 56(3):e2019WR026010. ISBN: 0043-1397 Publisher: Wiley Online Library.

Condon, L. E. and Maxwell, R. M. (2019). Modified priority flood and global slope enforcement algorithm for topographic processing in physically based hydrologic modeling applications. *Computers & Geosciences*, 126:73–83.

Costa, D., Shook, K., Spence, C., Elliott, J., Baulch, H., Wilson, H., and Pomeroy, J. W. (2020). Predicting Variable Contributing Areas, Hydrological Connectivity, and Solute Transport Pathways for a Canadian Prairie Basin. *Water Resources Research*, 56(12):e2020WR027984. Publisher: John Wiley & Sons, Ltd.

Crawford, N. H. and Linsley, R. K. (1966). Digital Simulation in Hydrology'Stanford Watershed Model 4.

Dahri, Z. H., Ludwig, F., Moors, E., Ahmad, B., Khan, A., and Kabat, P. (2016). An appraisal of precipitation distribution in the high-altitude catchments of the Indus basin. *Science of the Total Environment*, 548:289–306. ISBN: 0048-9697 Publisher: Elsevier.

Dai, Y., Zeng, X., Dickinson, R. E., Baker, I., Bonan, G. B., Bosilovich, M. G., Denning, A. S., Dirmeyer, P. A., Houser, P. R., Niu, G., Oleson, K. W., Schlosser, C. A., and Yang, Z.-L. (2003). The Common Land Model. *Bulletin of the American Meteorological Society*, 84(8):1013–1024. Publisher: American Meteorological Society Section: Bulletin of the American Meteorological Society.

Darcy, H. (1856). *Les fontaines publiques de la ville de Dijon: Exposition et application des principes à suivre et des formules à employer dans les questions de distribution d'eau: Ouvrage terminé par un appendice relatif aux fournitures d'eau de plusieurs villes, au filtrage des eaux et à la fabrication des tuyaux de fonte, de plomb, de tôle et de bitume*, volume 2. V. Dalmont.

Deming, D. (2005). Born to trouble: Bernard Palissy and the hydrologic cycle. *Groundwater*, 43(6):969–972. ISBN: 0017-467X Publisher: Blackwell Science Inc Oxford, UK; Malden, USA.

Deschamps-Berger, C., Gascoin, S., Berthier, E., Deems, J., Gutmann, E., Dehecq, A., Shean, D., and Dumont, M. (2020). Snow depth mapping from stereo satellite imagery in mountainous terrain: evaluation using airborne laser-scanning data. *The Cryosphere*, 14(9):2925–2940. ISBN: 1994-0416 Publisher: Copernicus GmbH.

Deschamps-Berger, C., Cluzet, B., Dumont, M., Lafaysse, M., Berthier, E., Fanise, P., and Gascoin, S. (2022). Improving the spatial distribution of snow cover simulations by assimilation of satellite stereoscopic imagery. *Water Resources Research*, 58(3):e2021WR030271. ISBN: 0043-1397 Publisher: Wiley Online Library.

Descloitres, M., Séguis, L., Legchenko, A., Wubda, M., Guyot, A., and Cohard, J. M. (2011). The contribution of MRS and resistivity methods to the interpretation of actual evapo-

transpiration measurements: a case study in metamorphic context in north Bénin. *Near Surface Geophysics*, 9(2):187–200. ISBN: 1569-4445 Publisher: European Association of Geoscientists & Engineers.

Dozier, J. (1989). Spectral signature of alpine snow cover from the Landsat Thematic Mapper. *Remote sensing of environment*, 28:9–22. ISBN: 0034-4257 Publisher: Elsevier.

Drusch, M., Del Bello, U., Carlier, S., Colin, O., Fernandez, V., Gascon, F., Hoersch, B., Isola, C., Laberinti, P., and Martimort, P. (2012). Sentinel-2: ESA's optical high-resolution mission for GMES operational services. *Remote sensing of Environment*, 120:25–36. ISBN: 0034-4257 Publisher: Elsevier.

Dumont, T., Schwartz, S., Guillot, S., Simon-Labric, T., Tricart, P., and Jourdan, S. (2012). Structural and sedimentary records of the Oligocene revolution in the Western Alpine arc. *Journal of Geodynamics*, 56:18–38. ISBN: 0264-3707 Publisher: Elsevier.

Dunne, T. (1983). Relation of field studies and modeling in the prediction of storm runoff. *Journal of Hydrology*, 65(1-3):25–48.

Emerson, D. W. (1990). Notes on mass properties of rocks ? density, porosity, permeability. *Exploration Geophysics*, 21(4):209–216. Publisher: CSIRO PUBLISHING.

Enzminger, T. L., Small, E. E., and Borsa, A. A. (2019). Subsurface water dominates Sierra Nevada seasonal hydrologic storage. *Geophysical Research Letters*, 46(21):11993–12001. ISBN: 0094-8276 Publisher: Wiley Online Library.

Esposito, A., Engel, M., Ciccazzo, S., Dapra, L., Penna, D., Comiti, F., Zerbe, S., and Brusetti, L. (2016). Spatial and temporal variability of bacterial communities in high alpine water spring sediments. *Research in microbiology*, 167(4):325–333. ISBN: 0923-2508 Publisher: Elsevier.

Fan, Y., Clark, M., Lawrence, D. M., Swenson, S., Band, L. E., Brantley, S. L., Brooks, P. D., Dietrich, W. E., Flores, A., Grant, G., Kirchner, J. W., Mackay, D. S., McDonnell, J. J., Milly, P. C. D., Sullivan, P. L., Tague, C., Ajami, H., Chaney, N., Hartmann, A., Hazenberg, P., McNamara, J., Pelletier, J., Perket, J.,

Rouholahnejad-Freund, E., Wagener, T., Zeng, X., Beighley, E., Buzan, J., Huang, M., Livneh, B., Mohanty, B. P., Nijssen, B., Safeeq, M., Shen, C., Verseveld, W. v., Volk, J., and Yamazaki, D. (2019). Hillslope Hydrology in Global Change Research and Earth System Modeling. *Water Resources Research*, 55(2):1737–1772. _eprint: https://onlinelibrary.wiley.com/doi/pdf/10.1029/2018WR023903.

Fang, X. and Pomeroy, J. W. (2020). Diagnosis of future changes in hydrology for a Canadian Rockies headwater basin. *Hydrology and Earth System Sciences*, 24(5):2731–2754. Publisher: Copernicus GmbH.

Flinchum, B. A., Holbrook, W. S., Grana, D., Parsekian, A. D., Carr, B. J., Hayes, J. L., and Jiao, J. (2018). Estimating the water holding capacity of the critical zone using near-surface geophysics. *Hydrological Processes*, 32(22):3308–3326. ISBN: 0885-6087 Publisher: Wiley Online Library.

Flügel, W.-A. (1995). Delineating hydrological response units by geographical information system analyses for regional hydrological modelling using PRMS/MMS in the drainage basin of the River Bröl, Germany. *Hydrological processes*, 9(3-4):423–436. ISBN: 0885-6087 Publisher: Wiley Online Library.

Foken, T., Wimmer, F., Mauder, M., Thomas, C., and Liebethal, C. (2006). Some aspects of the energy balance closure problem. *Atmospheric Chemistry and Physics*, 6(12):4395–4402. ISBN: 1680-7316 Publisher: Copernicus GmbH.

Fontrodona Bach, A., Van der Schrier, G., Melsen, L. A., Klein Tank, A. M. G., and Teuling, A. J. (2018). Widespread and accelerated decrease of observed mean and extreme snow depth over Europe. *Geophysical Research Letters*, 45(22):12,312–12,319. ISBN: 0094-8276 Publisher: Wiley Online Library.

Forrester, M. M. and Maxwell, R. M. (2020). Impact of lateral groundwater flow and subsurface lower boundary conditions on atmospheric boundary layer development over complex terrain. *Journal of Hydrometeorology*, 21(6):1133–1160. ISBN: 1525-755X.

Foster, J., Liston, G., Koster, R., Essery, R., Behr, H., Dumenil, L., Verseghy, D., Thompson, S., Pollard, D., and Cohen, J. (1996). Snow Cover and Snow Mass Intercomparisons

of General Circulation Models and Remotely Sensed Datasets. *Journal of Climate*, 9(2):409–426. Publisher: American Meteorological Society Section: Journal of Climate.

Francés, A. P., Lubczynski, M. W., Roy, J., Santos, F. A., and Ardekani, M. R. M. (2014). Hydrogeophysics and remote sensing for the design of hydrogeological conceptual models in hard rocks–Sardón catchment (Spain). *Journal of Applied Geophysics*, 110:63–81. ISBN: 0926-9851 Publisher: Elsevier.

Freeze, R. A. and Harlan, R. L. (1969). Blueprint for a physically-based, digitally-simulated hydrologic response model. *Journal of hydrology*, 9(3):237–258. ISBN: 0022-1694 Publisher: Elsevier.

Fuller, W. E. (1914). Flood flows. *Transactions of the American Society of Civil Engineers*, 77(1):564–617. ISBN: 0066-0604 Publisher: American Society of Civil Engineers.

Fullhart, A. T., Kelleners, T. J., Chandler, D. G., McNamara, J. P., and Seyfried, M. S. (2019). Bulk density optimization to determine subsurface hydraulic properties in Rocky Mountain catchments using the GEOtop model. *Hydrological Processes*, 33(17):2323–2336. ISBN: 0885-6087 Publisher: Wiley Online Library.

Gao, H., Fu, T., Liu, J., Liang, H., and Han, L. (2018). Ecosystem services management based on differentiation and regionalization along vertical gradient in Taihang Mountain, China. *Sustainability*, 10(4):986. ISBN: 2071-1050 Publisher: MDPI.

Gaur, S., Singh, B., Bandyopadhyay, A., Stisen, S., and Singh, R. (2022). Spatial pattern-based performance evaluation and uncertainty analysis of a distributed hydrological model. *Hydrological Processes*, page e14586. ISBN: 0885-6087 Publisher: Wiley Online Library.

Gilbert, J. M., Jefferson, J. L., Constantine, P. G., and Maxwell, R. M. (2016). Global spatial sensitivity of runoff to subsurface permeability using the active subspace method. *Advances in water resources*, 92:30–42. ISBN: 0309-1708 Publisher: Elsevier.

Gleick, P. H. (1993). *Water in crisis*, volume 100. New York: Oxford University Press.

Godsey, S. E., Marks, D., Kormos, P. R., Seyfried, M. S., Enslin, C. L., Winstral, A. H., McNamara, J. P., and Link, T. E. (2018). Eleven years of mountain weather, snow, soil moisture and streamflow data from the rain–snow transition zone–the Johnston Draw catchment, Reynolds Creek Experimental Watershed and Critical Zone Observatory, USA. *Earth System Science Data*, 10(3):1207–1216. ISBN: 1866-3508 Publisher: Copernicus GmbH.

Graham, S., Parkinson, C., and Chahine, M. (2010). The water cycle. *NASA Earth Observatory*.

Grant, G. E. and Dietrich, W. E. (2017). The frontier beneath our feet. *Water Resources Research*, 53(4):2605–2609. ISBN: 0043-1397 Publisher: Wiley Online Library.

Green, W. H. and Ampt, G. A. (1911). Studies on Soil Phyics. *The Journal of Agricultural Science*, 4(1):1–24. ISBN: 1469-5146 Publisher: Cambridge University Press.

Guo, L., Mount, G. J., Hudson, S., Lin, H., and Levia, D. (2020). Pairing geophysical techniques improves understanding of the near-surface Critical Zone: Visualization of preferential routing of stemflow along coarse roots. *Geoderma*, 357:113953. ISBN: 0016-7061 Publisher: Elsevier.

Gupta, A., Reverdy, A., Cohard, J.-M., Voisin, D., Hector, B., Descloitres, M., Vandervaere, J.-P., Coulaud, C., Biron, R., and Liger, L. (2022). Impact of distributed meteorological forcing on snow dynamic and induced water fluxes over a mid-elevation alpine micro-scale catchment. *Hydrology and Earth System Sciences Discussions*, pages 1–25. ISBN: 1027-5606 Publisher: Copernicus GmbH.

Günther, D., Marke, T., Essery, R., and Strasser, U. (2019). Uncertainties in Snowpack Simulations—Assessing the Impact of Model Structure, Parameter Choice, and Forcing Data Error on Point-Scale Energy Balance Snow Model Performance. *Water Resources Research*, 55(4):2779–2800. _eprint: https://onlinelibrary.wiley.com/doi/pdf/10.1029/2018WR023403.

Hammond, J. C., Harpold, A. A., Weiss, S., and Kampf, S. K. (2019). Partitioning snowmelt and rainfall in the critical zone: Effects of climate type and soil properties. *Hydrology*

and Earth System Sciences, 23(9):3553–3570. ISBN: 1027-5606 Publisher: Copernicus GmbH.

Hartmann, A., Gleeson, T., Wada, Y., and Wagener, T. (2017). Enhanced groundwater recharge rates and altered recharge sensitivity to climate variability through subsurface heterogeneity. *Proceedings of the National Academy of Sciences*, 114(11):2842–2847. ISBN: 0027-8424 Publisher: National Acad Sciences.

Hauck, C. (2013). New concepts in geophysical surveying and data interpretation for permafrost terrain. *Permafrost and Periglacial Processes*, 24(2):131–137. ISBN: 1045-6740 Publisher: Wiley Online Library.

Hector, B., Cohard, J.-M., Séguis, L., Galle, S., and Peugeot, C. (2018). Hydrological functioning of western African inland valleys explored with a critical zone model. *Hydrology and Earth System Sciences*, 22(11):5867–5888. ISBN: 1027-5606 Publisher: Copernicus GmbH.

Hector, B., Séguis, L., Hinderer, J., Cohard, J.-M., Wubda, M., Descloitres, M., Benarrosh, N., and Boy, J.-P. (2015). Water storage changes as a marker for base flow generation processes in a tropical humid basement catchment (Benin): Insights from hybrid gravimetry. *Water Resources Research*, 51(10):8331–8361. _eprint: https://onlinelibrary.wiley.com/doi/pdf/10.1002/2014WR015773.

Hellström, M., Vermeulen, A., Mirzov, O., Sabbatini, S., Vitale, D., Papale, D., Tarniewicz, J., Hazan, L., Rivier, L., and Jones, S. D. (2016). Near Real Time Data Processing In ICOS RI. In *2nd international workshop on interoperable infrastructures for interdisciplinary big data sciences (it4ris 16) in the context of ieee real-time system symposium (rtss)*.

Henriksen, H. J., Troldborg, L., Nyegaard, P., Sonnenborg, T. O., Refsgaard, J. C., and Madsen, B. (2003). Methodology for construction, calibration and validation of a national hydrological model for Denmark. *Journal of Hydrology*, 280(1-4):52–71. ISBN: 0022-1694 Publisher: Elsevier.

Hinnell, A. C., Ferré, T. P. A., Vrugt, J. A., Huisman, J. A., Moysey, S., Rings, J., and Kowalsky, M. B. (2010). Improved extraction of hydrologic information from geophysical data through coupled hydrogeophysical inversion. *Water resources research*, 46(4). ISBN: 0043-1397 Publisher: Wiley Online Library.

Hofmeister, F., Arias-Rodriguez, L. F., Premier, V., Marin, C., Notarnicola, C., Disse, M., and Chiogna, G. (2022). Intercomparison of Sentinel-2 and modelled snow cover maps in a high-elevation Alpine catchment. *Journal of Hydrology X*, 15:100123. ISBN: 2589-9155 Publisher: Elsevier.

Hojatimalekshah, A., Uhlmann, Z., Glenn, N. F., Hiemstra, C. A., Tennant, C. J., Graham, J. D., Spaete, L., Gelvin, A., Marshall, H.-P., and McNamara, J. P. (2021). Tree canopy and snow depth relationships at fine scales with terrestrial laser scanning. *The Cryosphere*, 15(5):2187–2209. ISBN: 1994-0416 Publisher: Copernicus GmbH.

Horton, R. E. (1933). The Rôle of infiltration in the hydrologic cycle. *Eos, Transactions American Geophysical Union*, 14(1):446–460. _eprint: https://onlinelibrary.wiley.com/doi/pdf/10.1029/TR014i001p00446.

Hubbard, S. S. and Rubin, Y. (2000). Hydrogeological parameter estimation using geophysical data: a review of selected techniques. *Journal of Contaminant Hydrology*, 45(1-2):3–34. ISBN: 0169-7722 Publisher: Elsevier.

Hurrell, J. W., Holland, M. M., Gent, P. R., Ghan, S., Kay, J. E., Kushner, P. J., Lamarque, J.-F., Large, W. G., Lawrence, D., Lindsay, K., Lipscomb, W. H., Long, M. C., Mahowald, N., Marsh, D. R., Neale, R. B., Rasch, P., Vavrus, S., Vertenstein, M., Bader, D., Collins, W. D., Hack, J. J., Kiehl, J., and Marshall, S. (2013). The Community Earth System Model: A Framework for Collaborative Research. *Bulletin of the American Meteorological Society*, 94(9):1339–1360. Publisher: American Meteorological Society Section: Bulletin of the American Meteorological Society.

Immerzeel, W. W., Lutz, A. F., Andrade, M., Bahl, A., Biemans, H., Bolch, T., Hyde, S., Brumby, S., Davies, B. J., and Elmore, A. C. (2020). Importance and vulnerability of the world's water towers. *Nature*, 577(7790):364–369. ISBN: 1476-4687 Publisher: Nature Publishing Group.

Iseri, Y., Diaz, A. J., Trinh, T., Kavvas, M. L., Ishida, K., Anderson, M. L., Ohara, N., and Snider, E. D. (2021). Dynamical downscaling of global reanalysis data for high-resolution spatial modeling of snow accumulation/melting at the central/southern Sierra Nevada watersheds. *Journal of Hydrology*, 598:126445. ISBN: 0022-1694 Publisher: Elsevier.

Jabot, E., Zin, I., Lebel, T., Gautheron, A., and Obled, C. (2012). Spatial interpolation of sub-daily air temperatures for snow and hydrologic applications in mesoscale Alpine catchments. *Hydrological processes*, 26(17):2618–2630. ISBN: 0885-6087 Publisher: Wiley Online Library.

Jacobs, J. M., Hunsaker, A. G., Sullivan, F. B., Palace, M., Burakowski, E. A., Herrick, C., and Cho, E. (2021). Snow depth mapping with unpiloted aerial system lidar observations: a case study in Durham, New Hampshire, United States. *The Cryosphere*, 15(3):1485–1500. ISBN: 1994-0416 Publisher: Copernicus GmbH.

Jasper, K., Calanca, P., Gyalistras, D., and Fuhrer, J. (2004). Differential impacts of climate change on the hydrology of two alpine river basins. *Climate Research*, 26(2):113–129. ISBN: 0936-577X.

Jefferson, J. L. and Maxwell, R. M. (2015). Evaluation of simple to complex parameterizations of bare ground evaporation. *Journal of Advances in Modeling Earth Systems*, 7(3):1075–1092. _eprint: https://onlinelibrary.wiley.com/doi/pdf/10.1002/2014MS000398.

Jewitt, G. (2006). Integrating blue and green water flows for water resources management and planning. *Physics and Chemistry of the Earth, Parts A/B/C*, 31(15-16):753–762. ISBN: 1474-7065 Publisher: Elsevier.

Jones, J. E. and Woodward, C. S. (2001). Newton–Krylov-multigrid solvers for large-scale, highly heterogeneous, variably saturated flow problems. *Advances in Water Resources*, 24(7):763–774. ISBN: 0309-1708 Publisher: Elsevier.

Kampf, S. K. and Burges, S. J. (2007). A framework for classifying and comparing distributed hillslope and catchment hydrologic models. *Water resources research*, 43(5). ISBN: 0043-1397 Publisher: Wiley Online Library.

Keck, J., Istanbulluoglu, E., Lundquist, J., Bandaragoda, C., Jaeger, K., Mauger, G., and Horner-Devine, A. (2022). How does precipitation variability control bedload response across a mountainous channel network in a maritime climate? *Water Resources Research*, 58(8):e2021WR030358. ISBN: 0043-1397 Publisher: Wiley Online Library.

Keller, F., Goyette, S., and Beniston, M. (2005). Sensitivity Analysis of Snow Cover to Climate Change Scenarios and Their Impact on Plant Habitats in Alpine Terrain. *Climatic Change*, 72(3):299–319.

Kirkby, M., Bracken, L., and Reaney, S. (2002). The influence of land use, soils and topography on the delivery of hillslope runoff to channels in SE Spain. *Earth Surface Processes and Landforms: The Journal of the British Geomorphological Research Group*, 27(13):1459–1473. ISBN: 0197-9337 Publisher: Wiley Online Library.

Kljun, N., Calanca, P., Rotach, M. W., and Schmid, H. P. (2004). A simple parameterisation for flux footprint predictions. *Boundary-Layer Meteorology*, 112(3):503–523. ISBN: 1573-1472 Publisher: Springer.

KLOK, E. J., JASPER, K., ROELOFSMA, K. P., GURTZ, J., and BADOUX, A. (2001). Distributed hydrological modelling of a heavily glaciated Alpine river basin. *Hydrological Sciences Journal*, 46(4):553–570. Publisher: Taylor & Francis _eprint: https://doi.org/10.1080/02626660109492850.

Knight, R., Walsh, D. O., Butler Jr, J. J., Grunewald, E., Liu, G., Parsekian, A. D., Reboulet, E. C., Knobbe, S., and Barrows, M. (2016). NMR logging to estimate hydraulic conductivity in unconsolidated aquifers. *Groundwater*, 54(1):104–114. ISBN: 0017-467X Publisher: Wiley Online Library.

Koch, J., Cornelissen, T., Fang, Z., Bogena, H., Diekkrüger, B., Kollet, S., and Stisen, S. (2016). Inter-comparison of three distributed hydrological models with respect to seasonal variability of soil moisture patterns at a small forested catchment. *Journal of hydrology*, 533:234–249. ISBN: 0022-1694 Publisher: Elsevier.

Kohler, T. and Maselli, D. (2009). *Mountains and climate change. From understanding to action*. Geographica Bernensia.

Kollet, S. J. and Maxwell, R. M. (2006). Integrated surface–groundwater flow modeling: A free-surface overland flow boundary condition in a parallel groundwater flow model. *Advances in Water Resources*, 29(7):945–958.

Kollet, S. J. and Maxwell, R. M. (2008). Capturing the influence of groundwater dynamics on land surface processes using an integrated, distributed watershed model. *Water Resources Research*, 44(2). _eprint: https://onlinelibrary.wiley.com/doi/pdf/10.1029/2007WR006004.

Kotlarski, S., Gobiet, A., Morin, S., Olefs, M., Rajczak, J., and Samacoïts, R. (2022). 21st Century alpine climate change. *Climate Dynamics*, pages 1–22. ISBN: 1432-0894 Publisher: Springer.

Koutsoyiannis, D. and Mamassis, N. (2021). From mythology to science: the development of scientific hydrological concepts in Greek antiquity and its relevance to modern hydrology. *Hydrology and Earth System Sciences*, 25(5):2419–2444. ISBN: 1027-5606 Publisher: Copernicus GmbH.

Kowalsky, M. B., Finsterle, S., Peterson, J., Hubbard, S., Rubin, Y., Majer, E., Ward, A., and Gee, G. (2005). Estimation of field-scale soil hydraulic and dielectric parameters through joint inversion of GPR and hydrological data. *Water Resources Research*, 41(11). ISBN: 0043-1397 Publisher: Wiley Online Library.

Kowalsky, M. B., Finsterle, S., and Rubin, Y. (2004). Estimating flow parameter distributions using ground-penetrating radar and hydrological measurements during transient flow in the vadose zone. *Advances in Water Resources*, 27(6):583–599. ISBN: 0309-1708 Publisher: Elsevier.

Kuffour, B. N. O., Engdahl, N. B., Woodward, C. S., Condon, L. E., Kollet, S., and Maxwell, R. M. (2020). Simulating coupled surface–subsurface flows with ParFlow v3.5.0: capabilities, applications, and ongoing development of an open-source, massively parallel, integrated hydrologic model. *Geoscientific Model Development*, 13(3):1373–1397. Publisher: Copernicus GmbH.

Kuntz, B. W., Rubin, S., Berkowitz, B., and Singha, K. (2011). Quantifying solute transport at the shale hills critical zone observatory. *Vadose Zone Journal*, 10(3):843–857. ISBN: 1539-1663 Publisher: Wiley Online Library.

Le Roux, G., Hansson, S. V., and Claustres, A. (2016). Inorganic chemistry in the mountain critical zone: are the mountain water towers of contemporary society under threat by trace contaminants? In *Developments in earth surface processes*, volume 21, pages 131–154. Elsevier.

Lehmann, P., Gambazzi, F., Suski, B., Baron, L., Askarinejad, A., Springman, S. M., Holliger, K., and Or, D. (2013). Evolution of soil wetting patterns preceding a hydrologically induced landslide inferred from electrical resistivity survey and point measurements of volumetric water content and pore water pressure. *Water Resources Research*, 49(12):7992–8004. ISBN: 0043-1397 Publisher: Wiley Online Library.

Lievens, H., Demuzere, M., Marshall, H.-P., Reichle, R. H., Brucker, L., Brangers, I., de Rosnay, P., Dumont, M., Girotto, M., and Immerzeel, W. W. (2019). Snow depth variability in the Northern Hemisphere mountains observed from space. *Nature communications*, 10(1):1–12. ISBN: 2041-1723 Publisher: Nature Publishing Group.

Liniger, H. and Weingartner, R. (1998). Mountains and freshwater supply. *Unasylva (FAO)*. ISBN: 0251-1053.

Liston, G. E. and Elder, K. (2006). A Meteorological Distribution System for High-Resolution Terrestrial Modeling (MicroMet). *Journal of Hydrometeorology*, 7(2):217–234. Publisher: American Meteorological Society Section: Journal of Hydrometeorology.

Liston, G. E., Perham, C. J., Shideler, R. T., and Cheuvront, A. N. (2016). Modeling snowdrift habitat for polar bear dens. *Ecological Modelling*, 320:114–134.

Liu, Q. Q., Chen, L., Li, J. C., and Singh, V. P. (2004). Two-dimensional kinematic wave model of overland-flow. *Journal of Hydrology*, 291(1):28–41.

Liu, X., Chen, J., Cui, X., Liu, Q., Cao, X., and Chen, X. (2019). Measurement of soil water content using ground-penetrating radar: a review of current methods. *International Journal of Digital Earth*, 12(1):95–118. ISBN: 1753-8947 Publisher: Taylor & Francis.

Liu, Y., Zhuang, Q., Pan, Z., Miralles, D., Tchebakova, N., Kicklighter, D., Chen, J., Sirin, A., He, Y., and Zhou, G. (2014). Response of evapotranspiration and water availability to the changing climate in Northern Eurasia. *Climatic change*, 126(3):413–427. ISBN: 1573-1480 Publisher: Springer.

Lofi, J., Pezard, P., Loggia, D., Garel, E., Gautier, S., Merry, C., and Bondabou, K. (2012). Geological discontinuities, main flow path and chemical alteration in a marly hill prone to slope instability: Assessment from petrophysical measurements and borehole image analysis. *Hydrological Processes*, 26(14):2071–2084. _eprint: https://onlinelibrary.wiley.com/doi/pdf/10.1002/hyp.7997.

Loritz, R., Hrachowitz, M., Neuper, M., and Zehe, E. (2021). The role and value of distributed precipitation data in hydrological models. *Hydrology and Earth System Sciences*, 25(1):147–167. Publisher: Copernicus GmbH.

Lv, Z., Pomeroy, J. W., and Fang, X. (2019). Evaluation of SNODAS snow water equivalent in western Canada and assimilation into a Cold Region Hydrological Model. *Water Resources Research*, 55(12):11166–11187. ISBN: 0043-1397 Publisher: Wiley Online Library.

Lyon, S. W., Walter, M. T., Gérard-Marchant, P., and Steenhuis, T. S. (2004). Using a topographic index to distribute variable source area runoff predicted with the SCS curve-number equation. *Hydrological processes*, 18(15):2757–2771. ISBN: 0885-6087 Publisher: Wiley Online Library.

Markovich, K. H., Manning, A. H., Condon, L. E., and McIntosh, J. C. (2019). Mountain-block recharge: A review of current understanding. *Water Resources Research*, 55(11):8278–8304. ISBN: 0043-1397 Publisher: Wiley Online Library.

Marsh, C. B., Pomeroy, J. W., Spiteri, R. J., and Wheater, H. S. (2020). A Finite Volume Blowing Snow Model for Use With Variable Resolution Meshes. *Water Resources Research*, 56(2):e2019WR025307. _eprint: https://onlinelibrary.wiley.com/doi/pdf/10.1029/2019WR025307.

Marshall, D. J. and Madden, T. R. (1959). Induced polarization, a study of its causes. *Geophysics*, 24(4):790–816. ISBN: 0016-8033 Publisher: Society of Exploration Geophysicists.

Martinec, J. (1960). The degree-day factor for snowmelt runoff forecasting. *IUGG General Assembly of Helsinki, IAHS Commission of Surface Waters*, 51:468–477. Publisher: IAHS Wallingford.

Marty, C., Schlögl, S., Bavay, M., and Lehning, M. (2017). How much can we save? Impact of different emission scenarios on future snow cover in the Alps. *The Cryosphere*, 11(1):517–529. ISBN: 1994-0416 Publisher: Copernicus GmbH.

Masaki, Y., Hanasaki, N., Biemans, H., Schmied, H. M., Tang, Q., Wada, Y., Gosling, S. N., Takahashi, K., and Hijioka, Y. (2017). Intercomparison of global river discharge simulations focusing on dam operation—multiple models analysis in two case-study river basins, Missouri–Mississippi and Green–Colorado. *Environmental Research Letters*, 12(5):055002. Publisher: IOP Publishing.

Matiu, M., Crespi, A., Bertoldi, G., Carmagnola, C. M., Marty, C., Morin, S., Schöner, W., Cat Berro, D., Chiogna, G., De Gregorio, L., Kotlarski, S., Majone, B., Resch, G., Terzago, S., Valt, M., Beozzo, W., Cianfarra, P., Gouttevin, I., Marcolini, G., Notarnicola, C., Petitta, M., Scherrer, S. C., Strasser, U., Winkler, M., Zebisch, M., Cicogna, A., Cremonini, R., Debernardi, A., Faletto, M., Gaddo, M., Giovannini, L., Mercalli, L., Soubeyroux, J.-M., Sušnik, A., Trenti, A., Urbani, S., and Weilguni, V. (2021). Observed snow depth trends in the European Alps: 1971 to 2019. *The Cryosphere*, 15(3):1343–1382. Publisher: Copernicus GmbH.

Maulé, C. P. and Stein, J. (1990). Hydrologic flow path definition and partitioning of spring meltwater. *Water Resources Research*, 26(12):2959–2970. ISBN: 0043-1397 Publisher: Wiley Online Library.

Maxwell, R. M. (2013). A terrain-following grid transform and preconditioner for parallel, large-scale, integrated hydrologic modeling. *Advances in Water Resources*, 53:109–117. ISBN: 0309-1708 Publisher: Elsevier.

Maxwell, R. M. and Condon, L. E. (2016). Connections between groundwater flow and transpiration partitioning. *Science*, 353(6297):377–380. Publisher: American Association for the Advancement of Science Section: Report.

Maxwell, R. M., Condon, L. E., Danesh-Yazdi, M., and Bearup, L. A. (2019). Exploring source water mixing and transient residence time distributions of outflow and evapotranspiration with an integrated hydrologic model and Lagrangian particle tracking approach. *Ecohydrology*, 12(1):e2042. _eprint: https://onlinelibrary.wiley.com/doi/pdf/10.1002/eco.2042.

Maxwell, R. M. and Miller, N. L. (2005). Development of a coupled land surface and groundwater model. *Journal of Hydrometeorology*, 6(3):233–247. ISBN: 1525-7541.

McDonnell, J. J. and Beven, K. (2014). Debates—The future of hydrological sciences: A (common) path forward? A call to action aimed at understanding velocities, celerities and residence time distributions of the headwater hydrograph. *Water Resources Research*, 50(6):5342–5350. ISBN: 0043-1397 Publisher: Citeseer.

McGuire, K. J. and McDonnell, J. J. (2010). Hydrological connectivity of hillslopes and streams: Characteristic time scales and nonlinearities. *Water Resources Research*, 46(10). ISBN: 0043-1397 Publisher: Wiley Online Library.

McGuire, K. J., McDonnell, J. J., Weiler, M., Kendall, C., McGlynn, B. L., Welker, J. M., and Seibert, J. (2005). The role of topography on catchment-scale water residence time. *Water Resources Research*, 41(5). ISBN: 0043-1397 Publisher: Wiley Online Library.

McLaughlin, B. C., Ackerly, D. D., Klos, P. Z., Natali, J., Dawson, T. E., and Thompson, S. E. (2017). Hydrologic refugia, plants, and climate change. *Global change biology*, 23(8):2941–2961. ISBN: 1354-1013 Publisher: Wiley Online Library.

McNeill, J. D. (1980). Electromagnetic terrain conductivity measurement at low induction numbers. Publisher: Geonics Limited Mississauga, ON, Canada.

Meerveld, H. J. T.-v., James, A. L., McDonnell, J. J., and Peters, N. E. (2008). A reference data set of hillslope rainfall-runoff response, Panola Mountain Re-

search Watershed, United States. *Water Resources Research*, 44(6). _eprint: https://onlinelibrary.wiley.com/doi/pdf/10.1029/2007WR006299.

Melton, F. S., Huntington, J., Grimm, R., Herring, J., Hall, M., Rollison, D., Erickson, T., Allen, R., Anderson, M., and Fisher, J. B. (2021). Openet: Filling a critical data gap in water management for the western united states. *JAWRA Journal of the American Water Resources Association*. ISBN: 1093-474X Publisher: Wiley Online Library.

Moghadas, D., Jadoon, K. Z., Vanderborght, J., Lambot, S., and Vereecken, H. (2013). Effects of near surface soil moisture profiles during evaporation on far-field ground-penetrating radar data: A numerical study. *Vadose Zone Journal*, 12(2):1–11. ISBN: 1539-1663 Publisher: Wiley Online Library.

Morin, S., Samacoïts, R., François, H., Carmagnola, C. M., Abegg, B., Demiroglu, O. C., Pons, M., Soubeyroux, J.-M., Lafaysse, M., and Franklin, S. (2021). Pan-European meteorological and snow indicators of climate change impact on ski tourism. *Climate Services*, 22:100215. ISBN: 2405-8807 Publisher: Elsevier.

Mulvaney, T. J. (1851). On the use of self-registering rain and flood gauges in making observations of the relations of rainfall and flood discharges in a given catchment. *Proceedings of the institution of Civil Engineers of Ireland*, 4:19–31.

Nijssen, B. and Lettenmaier, D. P. (1999). A simplified approach for predicting shortwave radiation transfer through boreal forest canopies. *Journal of Geophysical Research: Atmospheres*, 104(D22):27859–27868. _eprint: https://onlinelibrary.wiley.com/doi/pdf/10.1029/1999JD900377.

Notarnicola, C. (2020). Hotspots of snow cover changes in global mountain regions over 2000–2018. *Remote Sensing of Environment*, 243:111781. ISBN: 0034-4257 Publisher: Elsevier.

Obi, J. C., Ogban, P. I., Ituen, U. J., and Udoh, B. T. (2014). Development of pedotransfer functions for coastal plain soils using terrain attributes. *Catena*, 123:252–262. ISBN: 0341-8162 Publisher: Elsevier.

O'Geen, A., Safeeq, M., Wagenbrenner, J., Stacy, E., Hartsough, P., Devine, S., Tian, Z., Ferrell, R., Goulden, M., and Hopmans, J. W. (2018). Southern Sierra Critical Zone Observatory and Kings River Experimental Watersheds: A synthesis of measurements, new insights, and future directions. *Vadose Zone Journal*, 17(1):1–18. ISBN: 1539-1663 Publisher: Wiley Online Library.

Oishi, A. C., Oren, R., and Stoy, P. C. (2008). Estimating components of forest evapotranspiration: a footprint approach for scaling sap flux measurements. *agricultural and forest meteorology*, 148(11):1719–1732. ISBN: 0168-1923 Publisher: Elsevier.

Oleson, K. W., Dai, Y., Bonan, G., Bosilovich, M., Dickinson, R., Dirmeyer, P., Hoffman, F., Houser, P., Levis, S., and Niu, G.-Y. (2004). Technical description of the community land model (CLM). *Tech. Note NCAR/TN-461+ STR*.

Overgaard, J., Rosbjerg, D., and Butts, M. B. (2006). Land-surface modelling in hydrological perspective – a review. *Biogeosciences*, 3(2):229–241. Publisher: Copernicus GmbH.

Painter, T. H., Berisford, D. F., Boardman, J. W., Bormann, K. J., Deems, J. S., Gehrke, F., Hedrick, A., Joyce, M., Laidlaw, R., and Marks, D. (2016). The Airborne Snow Observatory: Fusion of scanning lidar, imaging spectrometer, and physically-based modeling for mapping snow water equivalent and snow albedo. *Remote Sensing of Environment*, 184:139–152. ISBN: 0034-4257 Publisher: Elsevier.

Parsekian, A. D., Grana, D., Neves, F. d. A., Pleasants, M. S., Seyfried, M., Moravec, B. G., Chorover, J., Moraes, A. M., Smeltz, N. Y., and Westenhoff, J. H. (2021). Hydrogeophysical comparison of hillslope critical zone architecture for different geologic substrates. *Geophysics*, 86(5):WB29–WB49. ISBN: 0016-8033 Publisher: Society of Exploration Geophysicists.

Parsekian, A. D., Singha, K., Minsley, B. J., Holbrook, W. S., and Slater, L. (2015). Multiscale geophysical imaging of the critical zone. *Reviews of Geophysics*, 53(1):1–26. ISBN: 8755-1209 Publisher: Wiley Online Library.

Pelletier, J. D., Barron-Gafford, G. A., Gutiérrez-Jurado, H., Hinckley, E.-L. S., Istanbulluoglu, E., McGuire, L. A., Niu, G.-Y., Poulos, M. J., Rasmussen, C., and Richardson, P.

(2018). Which way do you lean? Using slope aspect variations to understand Critical Zone processes and feedbacks. *Earth Surface Processes and Landforms*, 43(5):1133–1154. ISBN: 0197-9337 Publisher: Wiley Online Library.

Pfister, L., Savenije, H. H., and Fenicia, F. (2009). *Leonardo Da Vinci's water theory: on the origin and fate of water.* Iahs Press.

Pomeroy, J. W., Gray, D. M., Brown, T., Hedstrom, N. R., Quinton, W. L., Granger, R. J., and Carey, S. K. (2007). The cold regions hydrological model: a platform for basing process representation and model structure on physical evidence. *Hydrological Processes*, 21(19):2650–2667. _eprint: https://onlinelibrary.wiley.com/doi/pdf/10.1002/hyp.6787.

Pomeroy, J. W. and Li, L. (2000). Prairie and arctic areal snow cover mass balance using a blowing snow model. *Journal of Geophysical Research: Atmospheres*, 105(D21):26619–26634. _eprint: https://onlinelibrary.wiley.com/doi/pdf/10.1029/2000JD900149.

Pomeroy, J. W., Toth, B., Granger, R. J., Hedstrom, N. R., and Essery, R. L. H. (2003). Variation in Surface Energetics during Snowmelt in a Subarctic Mountain Catchment. *Journal of Hydrometeorology*, 4(4):702–719. Publisher: American Meteorological Society Section: Journal of Hydrometeorology.

Pradhananga, D. and Pomeroy, J. W. (2022). Diagnosing changes in glacier hydrology from physical principles using a hydrological model with snow redistribution, sublimation, firnification and energy balance ablation algorithms. *Journal of Hydrology*, 608:127545. ISBN: 0022-1694 Publisher: Elsevier.

Rains, M. C., Dahlgren, R. A., Fogg, G. E., Harter, T., and Williamson, R. J. (2008). Geological control of physical and chemical hydrology in California vernal pools. *Wetlands*, 28(2):347–362. ISBN: 1943-6246 Publisher: Springer.

Rapp, G. A., Condon, L. E., and Markovich, K. H. (2020). Sensitivity of simulated mountain block hydrology to subsurface conceptualization. *Water Resources Research*, 56(10):e2020WR027714. ISBN: 0043-1397 Publisher: Wiley Online Library.

Revuelto, J., Alonso-González, E., Gascoin, S., Rodríguez-López, G., and López-Moreno,

J. I. (2021a). Spatial Downscaling of MODIS Snow Cover Observations Using Sentinel-2 Snow Products. *Remote Sensing*, 13(22):4513. ISBN: 2072-4292 Publisher: MDPI.

Revuelto, J., Azorin-Molina, C., Alonso-González, E., Sanmiguel-Vallelado, A., Navarro-Serrano, F., Rico, I., and López-Moreno, J. I. (2017). Meteorological and snow distribution data in the Izas Experimental Catchment (Spanish Pyrenees) from 2011 to 2017. *Earth System Science Data*, 9(2):993–1005. Publisher: Copernicus GmbH.

Revuelto, J., Billecocq, P., Tuzet, F., Cluzet, B., Lamare, M., Larue, F., and Dumont, M. (2020). Random forests as a tool to understand the snow depth distribution and its evolution in mountain areas. *Hydrological Processes*, 34(26):5384–5401. _eprint: https://onlinelibrary.wiley.com/doi/pdf/10.1002/hyp.13951.

Revuelto, J., Cluzet, B., Duran, N., Fructus, M., Lafaysse, M., Cosme, E., and Dumont, M. (2021b). Assimilation of surface reflectance in snow simulations: Impact on bulk snow variables. *Journal of Hydrology*, 603:126966. ISBN: 0022-1694 Publisher: Elsevier.

Richards, L. A. (1931). Capillary conduction of liquids through porous mediums. *Physics*, 1(5):318–333. ISBN: 0148-6349 Publisher: American Institute of Physics.

Riggs, G., Hall, D., and Salomonson, V. (1994). A snow index for the Landsat Thematic Mapper and Moderate Resolution Imaging Spectroradiometer. In *Proceedings of IGARSS '94 - 1994 IEEE International Geoscience and Remote Sensing Symposium*, volume 4, pages 1942–1944 vol.4.

Robert, F. (2001). The origin of water on Earth. *Science*, 293(5532):1056–1058. ISBN: 0036-8075 Publisher: American Association for the Advancement of Science.

Robinson, D. A., Binley, A., Crook, N., Day-Lewis, F. D., Ferré, T. P. A., Grauch, V. J. S., Knight, R., Knoll, M., Lakshmi, V., and Miller, R. (2008). Advancing process-based watershed hydrological research using near-surface geophysics: A vision for, and review of, electrical and magnetic geophysical methods. *Hydrological Processes: An International Journal*, 22(18):3604–3635. ISBN: 0885-6087 Publisher: Wiley Online Library.

Rodda, J. C. (2006). On the British contribution to international hydrology—an historical perspective. *Hydrological sciences journal*, 51(6):1177–1193. ISBN: 0262-6667 Publisher: Taylor & Francis.

Rosbjerg, D. and Rodda, J. (2019). IAHS: a brief history of hydrology. *History of Geo-and Space Sciences*, 10(1):109–118. ISBN: 2190-5010 Publisher: Copernicus GmbH.

Rush, M., Rajaram, H., Anderson, R. S., and Anderson, S. P. (2021). Modeling Aspect-Controlled Evolution of Ground Thermal Regimes on Montane Hillslopes. *Journal of Geophysical Research: Earth Surface*, 126(8):e2021JF006126. ISBN: 2169-9003 Publisher: Wiley Online Library.

Réveillet, M., Dumont, M., Gascoin, S., Lafaysse, M., Nabat, P., Ribes, A., Nheili, R., Tuzet, F., Ménégoz, M., and Morin, S. (2022). Black carbon and dust alter the response of mountain snow cover under climate change. *Nature communications*, 13(1):1–12. ISBN: 2041-1723 Publisher: Nature Publishing Group.

Sampaio, R. J., Rodriguez, D. A., Von Randow, C., da Silva, F. P., de Araújo, A. A. M., and Filho, O. C. R. (2021). Sensible heat flux assessment in a complex coastal-mountain urban area in the metropolitan area of Rio de Janeiro, Brazil. *Meteorology and Atmospheric Physics*.

Schreiner-McGraw, A. P. and Ajami, H. (2020). Impact of uncertainty in precipitation forcing data sets on the hydrologic budget of an integrated hydrologic model in mountainous terrain. *Water Resources Research*, 56(12):e2020WR027639. ISBN: 0043-1397 Publisher: Wiley Online Library.

Sevruk, B. and WMO, G. (1986). Correction of precipitation measurements.(Proceedings). Publisher: Zuerich (Switzerland) ETH, Geographisches Inst.

Seyfried, M., Lohse, K., Marks, D., Flerchinger, G., Pierson, F., and Holbrook, W. S. (2018). Reynolds creek experimental watershed and critical zone observatory. *Vadose Zone Journal*, 17(1):1–20. ISBN: 1539-1663 Publisher: Wiley Online Library.

Shen, C. and Phanikumar, M. S. (2010). A process-based, distributed hydrologic model based

on a large-scale method for surface–subsurface coupling. *Advances in Water Resources*, 33(12):1524–1541. ISBN: 0309-1708 Publisher: Elsevier.

Sidle, R. C. (2006). Field observations and process understanding in hydrology: essential components in scaling. *Hydrological Processes*, 20(6):1439–1445. ISBN: 0885-6087 Publisher: John Wiley & Sons Ltd.

Sidle, R. C. (2021). Strategies for smarter catchment hydrology models: incorporating scaling and better process representation. *Geoscience Letters*, 8(1):1–14. ISBN: 2196-4092 Publisher: Springer.

Siirila-Woodburn, E. R., Rhoades, A. M., Hatchett, B. J., Huning, L. S., Szinai, J., Tague, C., Nico, P. S., Feldman, D. R., Jones, A. D., and Collins, W. D. (2021). A low-to-no snow future and its impacts on water resources in the western United States. *Nature Reviews Earth & Environment*, 2(11):800–819. ISBN: 2662-138X Publisher: Nature Publishing Group.

Silver, M., Karnieli, A., Ginat, H., Meiri, E., and Fredj, E. (2017). An innovative method for determining hydrological calibration parameters for the WRF-Hydro model in arid regions. *Environmental modelling & software*, 91:47–69. ISBN: 1364-8152 Publisher: Elsevier.

Singh, R. S., Reager, J. T., Miller, N. L., and Famiglietti, J. S. (2015). Toward hyper-resolution land-surface modeling: The effects of fine-scale topography and soil texture on CLM4.0 simulations over the Southwestern U.S. *Water Resources Research*, 51(4):2648–2667. _eprint: https://onlinelibrary.wiley.com/doi/pdf/10.1002/2014WR015686.

Sivapalan, M. and Blöschl, G. (2017). The growth of hydrological understanding: Technologies, ideas, and societal needs shape the field. *Water Resources Research*, 53(10):8137–8146. ISBN: 0043-1397 Publisher: Wiley Online Library.

Song, J., Miller, G. R., Cahill, A. T., Aparecido, L. M. T., and Moore, G. W. (2020). Modeling land surface processes over a mountainous rainforest in Costa Rica using CLM4.5 and CLM5. *Geoscientific Model Development*, 13(11):5147–5173. Publisher: Copernicus GmbH.

Soulsby, C., Birkel, C., Geris, J., Dick, J., Tunaley, C., and Tetzlaff, D. (2015). Stream water age distributions controlled by storage dynamics and nonlinear hydrologic connectivity: Modeling with high-resolution isotope data. *Water Resources Research*, 51(9):7759–7776. ISBN: 0043-1397 Publisher: Wiley Online Library.

Soulsby, C., Tetzlaff, D., Rodgers, P., Dunn, S., and Waldron, S. (2006). Runoff processes, stream water residence times and controlling landscape characteristics in a mesoscale catchment: An initial evaluation. *Journal of Hydrology*, 325(1-4):197–221. ISBN: 0022-1694 Publisher: Elsevier.

Spies, B. R. (1989). Depth of investigation in electromagnetic sounding methods. *Geophysics*, 54(7):872–888. ISBN: 0016-8033 Publisher: Society of Exploration Geophysicists.

Sprenger, M., Carroll, R. W., Dennedy-Frank, J., Siirila-Woodburn, E. R., Newcomer, M. E., Brown, W., Newman, A., Beutler, C., Bill, M., and Hubbard, S. S. (2022). Variability of snow and rainfall partitioning into evapotranspiration and summer runoff across nine mountainous catchments. *Geophysical Research Letters*, 49(13):e2022GL099324. ISBN: 0094-8276 Publisher: Wiley Online Library.

Stephenson, G. R. and Freeze, R. A. (1974). Mathematical simulation of subsurface flow contributions to snowmelt runoff, Reynolds Creek Watershed, Idaho. *Water Resources Research*, 10(2):284–294. ISBN: 0043-1397 Publisher: Wiley Online Library.

Stober, I. and Bucher, K. (1999). Deep groundwater in the crystalline basement of the Black Forest region. *Applied geochemistry*, 14(2):237–254. ISBN: 0883-2927 Publisher: Elsevier.

Su, H., Yang, Z.-L., Niu, G.-Y., and Dickinson, R. E. (2008). Enhancing the estimation of continental-scale snow water equivalent by assimilating MODIS snow cover with the ensemble Kalman filter. *Journal of Geophysical Research: Atmospheres*, 113(D8). _eprint: https://onlinelibrary.wiley.com/doi/pdf/10.1029/2007JD009232.

Sun, N., Wigmosta, M., Zhou, T., Lundquist, J., Dickerson-Lange, S., and Cristea, N. (2018). Evaluating the functionality and streamflow impacts of explicitly modelling forest–snow

interactions and canopy gaps in a distributed hydrologic model. *Hydrological Processes*, 32(13):2128–2140. _eprint: https://onlinelibrary.wiley.com/doi/pdf/10.1002/hyp.13150.

Terzago, S., Cassardo, C., Cremonini, R., and Fratianni, S. (2010). Snow precipitation and snow cover climatic variability for the period 1971–2009 in the southwestern Italian Alps: The 2008–2009 snow season case study. *Water*, 2(4):773–787. ISBN: 2073-4441 Publisher: MDPI.

Thayer, D., Parsekian, A. D., Hyde, K., Speckman, H., Beverly, D., Ewers, B., Covalt, M., Fantello, N., Kelleners, T., and Ohara, N. (2018). Geophysical measurements to determine the hydrologic partitioning of snowmelt on a snow-dominated subalpine hillslope. *Water Resources Research*, 54(6):3788–3808. ISBN: 0043-1397 Publisher: Wiley Online Library.

Tooth, S., McCarthy, T. S., Brandt, D., Hancox, P. J., and Morris, R. (2002). Geological controls on the formation of alluvial meanders and floodplain wetlands: the example of the Klip River, eastern Free State, South Africa. *Earth Surface Processes and Landforms: The Journal of the British Geomorphological Research Group*, 27(8):797–815. ISBN: 0197-9337 Publisher: Wiley Online Library.

Toth, J. (1971). Groundwater discharge: a common generator of diverse geologic and morphologic phenomena. *Hydrological Sciences Journal*, 16(1):7–24. ISBN: 0020-6024 Publisher: Taylor & Francis.

Tran, H., Zhang, J., Cohard, J.-M., Condon, L. E., and Maxwell, R. M. (2020). Simulating Groundwater-Streamflow Connections in the Upper Colorado River Basin. *Groundwater*, 58(3):392–405. _eprint: https://onlinelibrary.wiley.com/doi/pdf/10.1111/gwat.13000.

Tuzet, F., Dumont, M., Picard, G., Lamare, M., Voisin, D., Nabat, P., Lafaysse, M., Larue, F., Revuelto, J., and Arnaud, L. (2020). Quantification of the radiative impact of light-absorbing particles during two contrasted snow seasons at Col du Lautaret (2058 m a.s.l., French Alps). *The Cryosphere*, 14(12):4553–4579. Publisher: Copernicus GmbH.

van den Hurk, B., Best, M., Dirmeyer, P., Pitman, A., Polcher, J., and Santanello, J. (2011). ACCELERATION OF LAND SURFACE MODEL DEVELOPMENT OVER A DECADE OF GLASS. *Bulletin of the American Meteorological Society*, 92(12):1593–1600. Publisher: American Meteorological Society.

Van Genuchten, M. T. (1980). A closed-form equation for predicting the hydraulic conductivity of unsaturated soils. *Soil science society of America journal*, 44(5):892–898. ISBN: 0361-5995 Publisher: Wiley Online Library.

Vanham, D. (2012). The Alps under climate change: implications for water management in Europe. *Journal of Water and Climate Change*, 3(3):197–206.

Vanham, D. and Rauch, W. (2009). Climate change and its influence on mountain snow covers: implication for drinking water in the European Alps. *International Journal of Climate Change: Impacts and Responses*, 1(4):101–112. ISBN: 1835-7156 Publisher: Common Ground Publishing.

Vignoli, G., Cassiani, G., Rossi, M., Deiana, R., Boaga, J., and Fabbri, P. (2012). Geophysical characterization of a small pre-Alpine catchment. *Journal of applied geophysics*, 80:32–42. ISBN: 0926-9851 Publisher: Elsevier.

Vionnet, V., Brun, E., Morin, S., Boone, A., Faroux, S., Le Moigne, P., Martin, E., and Willemet, J.-M. (2012). The detailed snowpack scheme Crocus and its implementation in SURFEX v7.2. *Geoscientific Model Development*, 5(3):773–791.

Vionnet, V., Six, D., Auger, L., Dumont, M., Lafaysse, M., Quéno, L., Réveillet, M., Dombrowski-Etchevers, I., Thibert, E., and Vincent, C. (2019). Sub-kilometer precipitation datasets for snowpack and glacier modeling in alpine terrain. *Frontiers in Earth Science*, 7:182. ISBN: 2296-6463 Publisher: Frontiers Media SA.

Viviroli, D., Dürr, H. H., Messerli, B., Meybeck, M., and Weingartner, R. (2007). Mountains of the world, water towers for humanity: Typology, mapping, and global significance. *Water resources research*, 43(7). ISBN: 0043-1397 Publisher: Wiley Online Library.

Weiler, M., McDonnell, J. J., Tromp-van Meerveld, I., and Uchida, T. (2006). Subsurface stormflow. *Encyclopedia of hydrological sciences*. Publisher: Wiley Online Library.

Weingartner, R., Viviroli, D., and Schädler, B. (2007). Water resources in mountain regions: a methodological approach to assess the water balance in a highland-lowland-system. *Hydrological Processes: An International Journal*, 21(5):578–585. ISBN: 0885-6087 Publisher: Wiley Online Library.

Wenner, F. (1916). *A method of measuring earth resistivity*. US Government Printing Office. Issue: 258.

Wlostowski, A. N., Molotch, N., Anderson, S. P., Brantley, S. L., Chorover, J., Dralle, D., Kumar, P., Li, L., Lohse, K. A., and Mallard, J. M. (2021). Signatures of hydrologic function across the critical zone observatory network. *Water Resources Research*, 57(3):e2019WR026635. ISBN: 0043-1397 Publisher: Wiley Online Library.

Xi, Y., Peng, S., Ciais, P., and Chen, Y. (2021). Future impacts of climate change on inland Ramsar wetlands. *Nature Climate Change*, 11(1):45–51. ISBN: 1758-6798 Publisher: Nature Publishing Group.

Xiao, X., Zhang, X., Wu, H., Zhang, C., and Han, L. (2022). Stable isotopes of surface water and groundwater in a typical subtropical basin in south-central China: Insights into the young water fraction and its seasonal origin. *Hydrological Processes*, 36(4):e14574. ISBN: 0885-6087 Publisher: Wiley Online Library.

Xu, K., Daian, J.-F., and Quenard, D. (1997). Multiscale structures to describe porous media part II: transport properties and application to test materials. *Transport in Porous Media*, 26(3):319–338. ISBN: 1573-1634 Publisher: Springer.

Yan, R., Zhang, X., Yan, S., Zhang, J., and Chen, H. (2018). Spatial patterns of hydrological responses to land use/cover change in a catchment on the Loess Plateau, China. *Ecological Indicators*, 92:151–160. ISBN: 1470-160X Publisher: Elsevier.

Yang, T., Sun, F., Gentine, P., Liu, W., Wang, H., Yin, J., Du, M., and Liu, C. (2019). Evaluation and machine learning improvement of global hydrological model-based flood simulations. *Environmental Research Letters*, 14(11):114027. Publisher: IOP Publishing.

Zaremehrjardy, M. (2020). Modelling snow dynamics and groundwater-surface water interactions in mountainous, foothill and plain regions in North Saskatchewan River Basin, Canada.

Zhu, B., Xie, X., Lu, C., Lei, T., Wang, Y., Jia, K., and Yao, Y. (2021). Extensive evaluation of a continental-scale high-resolution hydrological model using remote sensing and ground-based observations. *Remote Sensing*, 13(7):1247. ISBN: 2072-4292 Publisher: MDPI.

Zhu, R., Zheng, H., and Liu, C. (2010). Estimation of groundwater residence time and recession rate in watershed of the Loess Plateau. *Journal of Geographical Sciences*, 20(2):273–282. ISBN: 1861-9568 Publisher: Springer.

Šimůnek, J., Van Genuchten, M. T., and Šejna, M. (2016). Recent developments and applications of the HYDRUS computer software packages. *Vadose Zone Journal*, 15(7). ISBN: 1539-1663 Publisher: GeoScienceWorld.